Cosmologies, singularities, quantum extremal surfaces, holographic complexity, and time entanglement and pseudo-entropy

By

Hitesh K. Saini

A thesis submitted in partial fulfillment of the requirements for the degree of Doctor of Philosophy

to

Chennai Mathematical Institute

July 2025

Plot-H1, SIPCOT IT Park,
Siruseri, Kelambakkam,
Tamil Nadu - 603103
India

Advisor:
Dr. K.Narayan, Chennai Mathematical Institute (CMI)

Doctoral Committee Members:

1. Dr. K G Arun, Chennai Mathematical Institute (CMI)
2. Dr. Dileep Jatkar, Harish-Chandra Research Institute (HRI)

Declaration

This thesis is a presentation of my original research work, carried out with my collaborators under the guidance of Dr. K. Narayan at Chennai Mathematical Institute (CMI). This work has not formed the basis for the award of any degree, diploma, associateship, fellowship or other titles in Chennai Mathematical Institute (CMI) or any other university or Institution of higher education.

Hitesh K. Saini
July 2025

In my capacity as the supervisor of the candidate's thesis, I certify that the above statements are true to the best of my knowledge.

K. Narayan
July 2025

Acknowledgments

I am deeply grateful to my advisor, Dr. K. Narayan, for his invaluable guidance, insightful discussions, and constructive feedback throughout my research. His intuition and profound understanding of the field have greatly influenced my work. I also sincerely appreciate his efforts in offering online courses on string theory and hosting extended discussion sessions during the pandemic.

I extend my gratitude to Dr. Dileep Jatkar at Harish-Chandra Research Institute (HRI) and Dr. K. G. Arun at Chennai Mathematical Institute (CMI) for serving as my doctoral committee members. Their thoughtful feedback and critical questions on my thesis draft have been instrumental in refining the draft.

I am also thankful to my collaborators, Kaberi Goswami, and Gopal Yadav, for their insightful discussions and valuable contributions during our collaborations.

Finally, I express my heartfelt appreciation to my family for always supporting and encouraging me throughout my studies. Their constant help and belief in me have made my academic journey possible.

List of publications

This thesis is based on the following publications.

1. K. Goswami, K. Narayan and H. K. Saini, Cosmologies, singularities and quantum extremal surfaces, JHEP **03**, 201 (2022) doi:10.1007/JHEP03(2022)201 [arXiv:2111.14906 [hep-th]].

2. K. Narayan, H. K. Saini and G. Yadav, Cosmological singularities, holographic complexity and entanglement, JHEP **07**, 125 (2024) doi:10.1007/JHEP07(2024)125 [arXiv:2404.00761 [hep-th]].

3. K. Narayan and Hitesh K. Saini, Notes on time entanglement and pseudo-entropy, Eur. Phys. J. C (2024) doi:10.1140/epjc/s10052-024-12855-x [arXiv:2303.01307 [hep-th]].

Contents

Acknowledgments **4**

List of publications **6**

1 Introduction **12**
1.1 AdS/CFT correspondence . . . 15
1.1.1 Maldacena's derivation of AdS/CFT correspondence . . . 15
1.1.2 AdS space . . . 17
1.1.3 Conformal Field Theory (CFT) . . . 18
1.1.4 AdS/CFT dictionary . . . 19
1.2 Entanglement . . . 23
1.2.1 Introduction to entanglement . . . 23
1.2.2 Entanglement entropy in field theory . . . 25
1.2.3 Holographic entanglement entropy . . . 26
1.2.4 RT/HRT surface in AdS Kasner cosmologies . . . 28
1.2.5 Entanglement wedge . . . 31
1.2.6 Corrections to the holographic entanglement entropy . . . 32
1.2.7 Quantum extremal surfaces . . . 32
1.3 Complexity . . . 35
1.3.1 K qubits and size of the space of states . . . 36
1.3.2 Circuit complexity . . . 36
1.3.3 Circuit complexity for coupled harmonic oscillators . . . 36
1.3.4 Circuit complexity in quantum field theories . . . 38
1.3.5 SU(2^K), unitaries, and complexity . . . 39
1.3.6 Holographic complexity . . . 42

2 Cosmologies, singularities and quantum extremal surfaces **50**
2.1 Review of quantum extremal surfaces in *AdS* Kasner cosmologies . . . 51
2.2 *AdS* Kasner, quantum extremal surfaces, regulated . . . 52
2.2.1 Searching for islands . . . 55

2.2.2 Appending a time-independent far region . . . 57
2.2.3 More general 2-dim cosmologies, QES, regulated . . . 58
2.3 Null cosmologies and quantum extremal surfaces . . . 60
2.4 Discussion . . . 65

3 Cosmological singularities, holographic complexity and entanglement 67
3.1 Higher dim volume complexity → 2-dims: generalities . . . 70
3.2 Complexity: AdS Kasner . . . 74
3.2.1 AdS_5-Kasner spacetime . . . 74
3.2.2 Holographic complexity of AdS_4-Kasner spacetime . . . 80
3.2.3 Holographic complexity of AdS_7-Kasner spacetime . . . 81
3.2.4 Numerical computation of complexity, AdS Kasner . . . 81
3.3 Complexity: hyperscaling violating cosmologies . . . 84
3.3.1 $d_i = 2,\ \theta = -\frac{1}{3}$ . . . 85
3.3.2 $d_i = 4,\ \theta = -1$ . . . 87
3.3.3 Numerical computation of complexity in hv cosmologies . . . 89
3.4 Complexity: isotropic Lifshitz Kasner cosmologies . . . 90
3.5 Holographic entanglement entropy: AdS Kasner etc . . . 92
3.6 Entanglement, AdS Kasner: numerical results . . . 94
3.6.1 Holographic entanglement entropy in AdS_5-Kasner . . . 94
3.6.2 Holographic entanglement entropy, AdS_7-Kasner . . . 95
3.6.3 Numerical computation of holographic entanglement entropy . . . 96
3.7 Discussion . . . 98

4 Time entanglement and pseudo-entropy 102
4.1 Review of extremal surfaces in de Sitter space . . . 105
4.1.1 dS extremal surfaces from I^+, and boundary conditions . . . 105
4.1.2 Future-past extremal surfaces in dS . . . 106
4.1.3 dS no-boundary surfaces . . . 108
4.1.4 dS_3 no-boundary surfaces, and pseudo entropy . . . 110
4.2 Review of time-entanglement in quantum mechanics . . . 111
4.3 Summary: time evolution and pseudo-entropy . . . 114
4.3.1 The time evolution operator and the transition matrix . . . 115
4.4 Time evolution operator, entanglement: examples . . . 116
4.4.1 2-qubit systems . . . 117
4.4.2 2-qutrit systems . . . 119
4.4.3 Two uncoupled oscillators . . . 119
4.5 The time evolution operator with projections . . . 120
4.5.1 Thermofield-double type states . . . 122

4.6 Time evolution operator, normalized at $t = 0$ . . . 123
4.7 2-dim CFTs and timelike intervals . . . 124
4.8 Time entanglement, time-dependent interactions . . . 126
4.9 Discussion . . . 130

5 Conclusion **134**

6 Appendix **138**
6.1 Computation of renormalized on-shell gravitational action for two-point correlators in AdS_{d+1} . . . 138
6.2 Black hole near-horizon geometry and Rindler time . . . 140
6.3 Some details: 2-dim gravity, extremal surfaces . . . 141
6.4 Some details on 2d CFT and entanglement entropy . . . 143
6.5 Holographic cosmologies $\to$ 2-dim . . . 143
6.6 g_i, s_i, y_i, v_i . . . 145
6.7 EE, finite subregions ($A \neq 0$), AdS_5 Kasner . . . 146
6.8 Time evolution, pseudo-entropy: special cases . . . 147
6.9 Qubit chains . . . 148
6.10 Two coupled oscillators . . . 151

Bibliography **156**

Chapter 1

Introduction

The maximum entropy of a gravitational region is proportional to its surface area; this is encapsulated in the Bekenstein bound. The Bekenstein-Hawking entropy [1] of a black hole is given by $\frac{A}{4G_N}$, where A represents the area of the black hole horizon. The holographic principle ([2], [3]) encapsulates this idea, suggesting that a volume in the real world can be described in the lower-dimensional space that lives on its boundary, encoding all the necessary degrees of freedom (information) to reconstruct a phenomenon within the volume. AdS/CFT correspondence is a realization of this idea, first proposed by Juan Maldacena in 1997 [4]. There are several comprehensive reviews on this correspondence ([5], [6], [7], [8]). AdS/CFT correspondence originally describes a duality between $\mathcal{N} = 4$ SU(N) gauge theory in four dimensions and type IIB superstring theory on the background of $AdS_5 \times S^5$. This framework extends to more general asymptotically AdS spacetimes, where $(d+1)$-dimensional asymptotic AdS_{d+1} gravitational theory is holographically dual to a d-dimensional Conformal Field Theory (CFT_d) living on the boundary of the AdS_{d+1} space. This correspondence represents a strong/weak duality, where the field theory is strongly coupled, while the dual gravitational theory is weakly coupled. The generalization of AdS/CFT correspondence is known as the gauge/gravity duality.

AdS/CFT correspondence has numerous applications, including strongly coupled condensed matter systems ([9], [10], [11],[12]), black-hole information paradox, and quark confinement in QCD. It plays a crucial role in computing quantities in strongly coupled quantum field theories, where direct computations are intractable. However, the dual gravitational theory simplifies the problem due to its weak coupling. Conversely, the field theory provides valuable insights into the quantum gravity.

In recent years, extensive studies have focused on resolving the black hole information paradox ([13]) using the island prescription ([14], [15], [16]), which involves Quantum Extremal Surfaces (QES). This approach relies primarily on a quantum information tool: entanglement entropy. Fur-

thermore, quantum information theory provides valuable insights into quantum gravity within the framework of gauge/gravity correspondence. Several powerful tools have emerged from quantum information theory, including entanglement, mutual information, and quantum complexity. Notably, entanglement entropy provides unique insights, including in quantum gravity, the black hole information paradox, and probing cosmological singularities.

For ground states and low-lying excited states in field theory, the entanglement entropy of a subregion is proportional to the area of its boundary. Similarly, the Bekenstein entropy of a black hole is proportional to the area of its gravitational horizon. This realization led to the Ryu-Takayanagi conjecture regarding the holographic entanglement entropy of boundary subregions. According to this conjecture, the entanglement entropy of a boundary subregion is obtained holographically by minimizing the area of a codimension-two surface in the bulk, homologous to the boundary subregion. The holographic entanglement entropy for a boundary subregion A is given by the Ryu-Takayanagi formula [17]: $S_A = min_{\partial\gamma=\partial A}[\frac{Area(\gamma)}{4G_N}]$, where γ is the codimension-two bulk surface that minimizes the area. For time-dependent geometries, the RT/HRT prescription [18] is used to define holographic entanglement entropy, which involves determining a codimension-two extremal surface in the bulk anchored to the boundary of subregion A. This surface, known as the RT/HRT surface, extends into the time direction as well. Holographic entanglement entropies satisfy several important properties, such as subadditivity and strong subadditivity. The RT/HRT surface also serves as a tool to probe the bulk geometry and its interior ([19], [20]), as well as cosmological singularities. A notable example of a simple cosmological geometry is the AdS Kasner, a time-dependent deformation of AdS, where the dual field theory resides on a time-dependent space with a time-dependent gauge coupling. Time-dependent AdS deformations exhibiting cosmological singularities have been studied extensively in ([21], [22], [23], [24]).

Holographic entanglement entropy can be used to probe the interior of a black hole. However, it has been noted that entanglement does not encode the full spacetime, as the entanglement surface cannot probe regions far beyond the black hole horizon [20]. From the perspective of the boundary theory, entanglement entropy fails to capture the complete evolution of a quantum system undergoing thermalization. In contrast, complexity continues to grow even after thermalization. Complexity quantifies how difficult a task is to accomplish, defined as the minimum number of steps required to obtain the target state from a reference state by using a set of unitary operations.

Several holographic proposals for defining complexity have been put forward, with prominent conjectures including complexity=volume ([25], [26]), complexity=action ([27], [28]), complexity=spacetime volume [29], and complexity=anything ([30], [31]). For an eternal black hole dual to the thermofield double (TFD) state, complexity is proportional to the spatial volume of the Einstein-Rosen bridge (wormhole). Moreover, complexity grows linearly with time, following

the relation $\frac{dC}{dt} \sim S\,T$, where S is the entropy and T is the black hole's temperature.

In this thesis, we employ the tools of quantum extremal surfaces (QES) and holographic volume complexity to investigate cosmologies exhibiting Big-Crunch singularities, all of which can be represented as two-dimensional models. The primary objective of these investigations is to gain insights into the behavior of these singular spacetimes through a systematic analysis of QES and holographic complexity. Additionally, we explore the structure of timelike entanglement by treating the time evolution operator as a density operator and investigating its connection with pseudo-entropy, providing deeper insights into quantum systems and their entanglement properties.

In Chapter 1, we provide a comprehensive overview of the AdS/CFT correspondence and entanglement entropy, with a focus on holographic entanglement entropy and quantum extremal surfaces. In Section 1.2.4 , we employ the RT/HRT surfaces to investigate AdS Kasner cosmologies for a strip-shaped boundary subregion. In Section 1.3, we review the concept of complexity, discussing various proposals for defining holographic complexity.

In Chapter 2, we analyze quantum extremal surfaces that are spacelike-separated from the observer's location in AdS Kasner cosmologies by introducing a spatial regulator. This approach establishes a relationship between the observer's time on the holographic boundary and the corresponding QES location in time. Additionally, we analyze a potential island-like solution by examining its boundary. To this end, we first derive the extremization equations from the generalized entropy and study their behavior in the vicinity of the proposed island boundary. However, a simultaneous solution to these equations is not achieved, indicating that the potential island solution is inconsistent. We extend our analysis to more general singularities with holographic interpretations, identifying similar behavior. Finally, we explore certain families of null Kasner Big-Crunch singularities, which can reach the null singularity.

In Chapter 3, we investigate the holographic volume complexity for several classes of holographic cosmologies with Kasner-like singularities, including AdS Kasner, hyperscaling-violating geometries, and Lifshitz geometries. Our analysis involves an extensive numerical study of the extremization equations derived from the volume functional, offering detailed insights into the behavior of the complexity surface. The results reveal that the complexity surface bends away from the singularity, undergoing a transition from spacelike near the boundary to lightlike in the interior. Notably, as the boundary anchoring time slice approaches the singularity, this transition becomes increasingly abrupt, with the spacelike region diminishing. In the vicinity of the singularity, the complexity approaches vanishingly small values, suggesting a dual Kasner state of minimal complexity and providing evidence for the effective degrees of freedom associated with the near-singularity region. For AdS and isotropic Lifshitz Kasner cosmologies, holographic complexity exhibits a linear scaling behavior with the anchoring time slice, t_0. In contrast, hyperscaling-violating geometries demonstrate a nonlinear dependence of holographic complexity on t_0, highlighting distinct scaling

properties across these families. Additionally, we refine prior investigations of extremal surfaces for holographic entanglement entropy, showing that their behavior in the infrared (IR) limit closely resembles the patterns observed in complexity.

In Chapter 4, we explore various aspects of time entanglement and its entanglement structure, treating the time evolution operator as a density operator. This approach has a close relation to the transition matrix and pseudo-entropy. We analyze several examples of simple quantum systems to investigate the time entanglement structure emerging from the time evolution operator. While the corresponding entanglement entropy is generally complex, specific subfamilies exhibit real values. Notably, time entanglement aligns with the finite-temperature entanglement entropy evaluated at an imaginary temperature, with $\beta \to it$, for systems characterized by time-independent interactions. Furthermore, we examine the entanglement structure of the time evolution operator when projected onto an initial state. In this case, the operator is precisely equivalent to the transition matrix, where the final state is obtained by time-evolving the initial state. The corresponding entanglement entropy in this context is identified as the pseudo-entropy. Finally, we extend our analysis to quantum systems with time-dependent interactions, which introduce a more intricate time entanglement structure.

Overall, this thesis leverages QES and holographic complexity to provide novel insights into cosmologies with Big-Crunch singularities, alongside a related study on the time evolution operator and pseudo-entropy in quantum systems. These investigations illuminate the interplay between geometry, entanglement, and complexity within holographic frameworks.

1.1 AdS/CFT correspondence

In this section, we first review the original Maldacena's derivation of AdS/CFT. We then introduce AdS space in different coordinate systems. Finally, we discuss several key entries in the AdS/CFT dictionary.

1.1.1 Maldacena's derivation of AdS/CFT correspondence

$\mathcal{N} = 4$, SU(N) gauge theory in $D = 4$ is dual to IIB superstring theory on the background $AdS_5 \times S^5$.

For the derivation of the conjecture above, we consider N coincident D3-branes in type IIB superstring theory. For $g_s N \ll 1$, the D3-branes live in 10-dimensions. For this system, open strings end on D3-branes, which describe the dynamics of D3-branes and closed strings propagate in the bulk. At low-energies, we only consider massless string states described by low-energy effective action. The massless states of open string comprise $\mathcal{N} = 4$ vector multiplet in four dimensions, and their low-energy effective action is described by $\mathcal{N} = 4$, U(N) super-Yang-Mills in four dimensions.

The closed string states comprise of both massless states, represented by graviton supermultiplet, and massive states in ten dimensions. At low-energies, massive states become irrelevant, and their low-energy effective action is then described by IIB supergravity theory in ten dimensional flat space. Moreover, the interaction between the brane and the bulk vanishes, which leads to two decoupled theories: $\mathcal{N} = 4$, U(N) super-Yang-Mills in four dimensions, and IIB supergravity in ten dimensions.

We now consider a different regime $g_sN \gg 1$. Now the D3-branes gravitate and source an extremal black 3-brane supergravity solution:

$$\begin{aligned} ds^2 &= f(r)^{-\frac{1}{2}}\,\eta_{\mu\nu}dx^\mu dx^\nu + f(r)^{\frac{1}{2}}(dr^2 + r^2 d\Omega_5^2)\,, \quad f(r) = 1 + 4\pi g_s N\,\frac{l_s^4}{r^4} \\ F_5 &= (1+*)\,dt dx_1 dx_2 dx_3 df^{-1}\,, \end{aligned} \tag{1.1}$$

the notation x^μ, where $\mu = 0, 1, 2, 3$, denotes coordinates along the D3-brane world-volume. $d\Omega^5$ is the metric on a unit five sphere, and F_5 is a 5-form self-dual field strength, which has flux on the S^5.

There are two types of low energy excitations from the point of view of an observer at infinity. First one is any finite energy excitation near the horizon which would appear strongly redshifted to the asymptotic observer, and the second one is the massless excitation in the bulk. Both excitations decouple in the low-energy limit. The massless excitations propagating in the asymptotic region of (1.1) decouple from the near horizon region because the absorption scattering cross-section vanishes as $\sigma \sim \omega^3 R^8$, where ω is the energy of an excitation. The redshifted excitations near the horizon can not escape to the asymptotic region due to presence of gravitational potential. So we have two decoupled sectors: type IIB superstring theory on the near horizon geometry and a free supergravity theory (type IIB) in ten-dimensional flat space. We now focus on the near horizon geometry, we see that $r \to 0$ near the horizon. In this limit, $f(r)$ can be approximated as $f(r) \simeq \frac{R^4}{r^4}$, where $R^4 = 4\pi g_s N\, l_s^4$. Now the background (1.1) in the near-horizon limit becomes

$$ds^2 = \frac{r^2}{R^2}\,\eta_{\mu\nu}dx^\mu dx^\nu + \frac{R^2}{r^2}dr^2 + R^2 d\Omega_5^2\,. \tag{1.2}$$

This reveals that the near-horizon geometry is $\mathrm{AdS}_5 \times S^5$. The first term represents the metric for the AdS_5 geometry in Poincaré coordinates, with $r = \frac{R^2}{z}$, while the last term corresponds to the metric on the five-sphere (S^5). The low-energy behavior of D3-branes reveals two decoupled systems in both regimes: $g_sN \ll 1$ and $g_sN \gg 1$. In both cases, supergravity in ten-dimensional flat space emerges as a common decoupled system. The other decoupled systems are $\mathcal{N} = 4$ U(N) super-Yang-Mills gauge theory and superstring theory on $\mathrm{AdS}_5 \times S^5$. These systems remain decoupled and well-defined for any value of the coupling g_sN in the low-energy limit. This establishes the equivalence between $\mathcal{N} = 4$ U(N) super-Yang-Mills theory in four dimensions and type IIB superstring theory on the $\mathrm{AdS}_5 \times S^5$ background. Furthermore, U(N) gauge theory can be decomposed

into SU(N) gauge theory and a U(1) vector multiplet, with some identification $\mathbb{Z}_N$. The SU(N) component corresponds to the AdS theory in the bulk, while the U(1) degrees of freedom represent zero modes that reside at the AdS boundary. Therefore, we conclude that $\mathcal{N} = 4$ SU(N) super-Yang-Mills theory in four dimensions is equivalent to type IIB superstring theory on $\mathrm{AdS}_5 \times S^5$.

We now look for the validity of a classical gravity description within AdS/CFT correspondence. Stringy corrections should be suppressed for the gravity description. For this purpose, we rewrite the curvature scale R in terms of string length l_s as $R = (4\pi g_s N)^{\frac{1}{4}} l_s$, and from D3-branes description we have $g_{YM}^2 = 4\pi g_s$. By combining these two we have $\frac{R}{l_s} = (g_{YM}^2 N)^{\frac{1}{4}} = \lambda^{\frac{1}{4}}$, where $\lambda = g_{YM}^2 N$ is 't Hooft coupling. Stringy effects are suppressed for $\frac{R}{l_s} \gg 1$, which implies $\lambda \gg 1$. Therefore, the gauge theory must be strongly coupled in order to have a dual gravitational description. We now write the ten dimensional Newton's constant in terms of string coupling g_s as $G_N = l_p^8 \sim g_s^2 l_s^8$. This combined with $R = (4\pi g_s N)^{\frac{1}{4}} l_s$, leads $\frac{R}{l_p} \sim N^{\frac{1}{4}}$. To suppress any quantum corrections to the geometry, we must have $\frac{R}{l_p} \gg 1$, which implies $N \gg 1$. The large N limit ($N \to \infty$) corresponds to 't Hooft limit with a fixed value of λ, where the dominant contribution comes from planar Feynman diagrams. Therefore, the classical gravity description is reliable in the regime $\lambda \gg 1$ and $N \gg 1$. However, it is believed that AdS/CFT correspondence holds even at finite λ and N.

1.1.2 AdS space

AdS_{d+1} can be considered as a hyperboloid in the embedding space $\mathbb{R}^{2,d}$. The hyperboloid is given by

$$-X_0^2 - X_{d+1}^2 + X_1^2 + X_2^2 + ... + X_d^2 = -R^2\,, \tag{1.3}$$

where $X_0, X_1 ... X_{d+1}$ are embedding coordinates of the hyperboloid. This geometry (1.3) is invariant under SO(d,2) group. The metric reads as:

$$ds^2 = -dX_0^2 - dX_{d+1}^2 + dX_1^2 + dX_2^2 + ... + dX_d^2\,. \tag{1.4}$$

One can choose the embedding coordinates in terms of the intrinsic coordinates (τ, ρ, Ω_i) as follows:

$$\begin{aligned} X_0 &= R\,\cos\tau \cosh\rho \quad ; \quad X_{d+1} = R\,\sin\tau\cosh\rho \\ X_i &= R\,\Omega_i \sinh\rho\,, \end{aligned} \tag{1.5}$$

where the index i runs from 1 to d, and $\sum_i \Omega_i^2 = 1$. Substituting these embedding coordinates in (1.4), we obtain an induced metric on the hyperboloid as

$$ds_{d+1}^2 = R^2\left(-\cosh^2\rho\, d\tau^2 + d\rho^2 + \sinh^2\rho\, d\Omega_{d-1}^2\right)\,. \tag{1.6}$$

Here, the coordinate τ lies on a circle S^1, i.e, $0 \le \tau < 2\pi$. To get the causal structure of AdS, we unwrap the circle and allow $-\infty < \tau < \infty$. The metric (1.6) now represents AdS space in global

coordinates, and $\rho = \infty$ represents the boundary of AdS. We may choose the Poincare coordinates as

$$\begin{aligned} X_0 &= \frac{1}{2z}\left(R^2 + z^2 + x^2\right) \\ X_i &= \frac{R}{z}x_i \qquad , \qquad i = 1, 2, ..., (d-1) \\ X_d &= \frac{1}{2z}\left(-R^2 + z^2 + x^2\right) \\ X_{d+1} &= \frac{R}{z}\,t\,. \end{aligned} \tag{1.7}$$

Subsequently, we obtain AdS metric in Poincare coordinates as

$$ds^2_{d+1} = \frac{R^2}{z^2}\left(dz^2 - dt^2 + dx_1^2 + ... + dx_{d-1}^2\right)\,, \tag{1.8}$$

where $z = 0$ represents the boundary of AdS in poincare patch. This patch only covers a half of the full AdS space. The metric solution (1.8) satisfies the following equation:

$$R_{\mu\nu} - \frac{\mathsf{R}}{2}\,g_{\mu\nu} = -\Lambda g_{\mu\nu}\,. \tag{1.9}$$

We compute the Ricci tensor as $R_{\mu\nu} = -\frac{d}{R^2}g_{\mu\nu}$. This implies that $\Lambda = -\frac{d(d-1)}{2R^2}$. Therefore, AdS is the solution of Einstein's equation of motion with negative constant curvature and negative cosmological constant (Λ).

1.1.3 Conformal Field Theory (CFT)

Quantum field theories typically exhibit Poincare symmetry, which includes translation and Lorentz transformation. However, some field theories possess additional symmetries, such as $\mathcal{N} = 4$ super Yang-Mills theory in four dimensions, exhibiting scale invariance. A field theory which is invariant under conformal transformations is known as conformal field theory (CFT). Conformal transformations include translation, Lorentz transformation, scaling, and special conformal transformation. Here, we discuss conformal transformations in higher dimensions, i.e., $d > 2$.

The metric remains invariant up to a scale factor under a conformal transformation $x^\mu \to x'^\mu$, the transformed metric is given as:

$$g'_{\mu\nu}(x') = \frac{\partial x^\rho}{\partial x'^\mu}\frac{\partial x^\sigma}{\partial x'^\nu}\,g_{\rho\sigma}(x) = \Omega(x) g_{\mu\nu}(x)\,. \tag{1.10}$$

For a Minkowski space with $d > 2$, the metric $ds^2 = \eta_{\mu\nu}dx^\mu dx^\nu$ transforms under the conformal transformation $x^\mu \to x^\mu + \epsilon^\mu(x)$ as follows:

$$ds^2 \to ds^2 + (\partial_\mu\epsilon_\nu + \partial_\nu\epsilon_\mu)dx^\mu dx^\nu\,. \tag{1.11}$$

For the metric ds^2 to be scale invariant, the following condition must hold

$$\partial_\mu \epsilon_\nu + \partial_\nu \epsilon_\mu = \frac{2}{d}\left(\partial_\rho \epsilon^\rho\right)\eta_{\mu\nu} \quad ; \quad \Omega(x) = 1 + \frac{2}{d}\left(\partial_\rho \epsilon^\rho\right). \tag{1.12}$$

The infinitesimal conformal transformations satisfying (1.12) are as follows:

$$\begin{aligned}
&x^\mu \to x^\mu + a^\mu && : \quad \text{Translation} \\
&x^\mu \to x^\mu + \Lambda^\mu_\nu x^\nu && : \quad \text{Lorentz transformation} \\
&x^\mu \to \lambda x^\mu && : \quad \text{Scaling} \\
&x^\mu \to x^\mu + b^\mu x^2 - 2(b\cdot x)x^\mu && : \quad \text{Special Conformal Transformation}
\end{aligned}$$

The finite special conformal transformation is given as $x \to x' = \frac{x+bx^2}{1+2b\cdot x+b^2x^2}$. The total number of independent parameters is given by $\frac{(d+2)(d+1)}{2}$, and the conformal group is SO(d,2). The generators for the conformal transformations (translation, lorentz transformation, scaling, and special conformal transformation, respectively) are given as:

$$\begin{aligned}
P_\mu &= -i\partial_\mu \\
M_{\mu\nu} &= i(x_\mu\partial_\nu - x_\nu\partial_\mu) \\
D &= -ix^\mu\partial_\mu \\
K_\mu &= i(x^2\partial_\mu - 2x_\mu x^\nu\partial_\nu).
\end{aligned} \tag{1.13}$$

A quasi-primary operator O of scaling dimension Δ transforms under the conformal transformation $x \to x'$ as follows:

$$\mathcal{O}'(x') = \left|\frac{\partial x}{\partial x'}\right|^{\frac{\Delta}{d}} \mathcal{O}(x). \tag{1.14}$$

In two dimensions, the conformal group is infinite dimensional, and each holomorphic transformation: $z \to f(z)$ is a conformal transformation.

1.1.4 AdS/CFT dictionary

Several entries in the AdS/CFT dictionary have been established over the years. We will discuss some of the key entries in the dictionary.

Global symmetries

AdS_5 has SO(4,2) global symmetry. This symmetry is manifest when we consider the geometry in an embedding space, and the five-sphere has SO(6) rotational symmetry group. Therefore, the isometry group of $AdS_5 \times S^5$ is SO(4,2) $\times$ SO(6). In the dual field theory, we have the SO(2,4) conformal group which corresponds to the isometry of AdS_5. Additionally, there are six scalars which transform in the fundamental representation of SO(6). This group represents the R-symmetry of super-Yang-Mills theory, and it corresponds to the isometry group of five-sphere. The isometry

group SO(4,2) × SO(6) is the bosonic subgroup of the superconformal group for SYM theory. More generally, AdS_{d+1} possesses an SO(d,2) isometry group, which coincides with the global conformal group SO(d,2) of the CFT_d.

Parameters

There are parameters g^2_{YM} and λ on the field theory side. Which are related to the parameters on the gravity side as follows: $g^2_{YM} = 4\pi g_s$ and $\lambda = \frac{R^4}{\alpha'^2}$, where $\alpha' = l_s^2$.

IR/UV connection

To illustrate the IR/UV connection, consider Poincare patch for AdS. The AdS boundary is situated at $z = 0$, and $z = \infty$ represents the deep bulk of AdS. These correspond to the IR and UV cutoffs of AdS gravity, respectively. We now consider a geodesic anchoring at the boundary of an interval of length l in conformal field theory (CFT), the geodesic extends up to the point $z = z_*(l)$ in the bulk, and returns to the boundary. It turns out that $z_* \sim l$. Therefore, for a UV cutoff $l = \epsilon$ (with the energy cutoff $E_{YM} \sim 1/z$), $z_* \sim \epsilon$. This suggests that the UV regime of CFT corresponds to the IR regime in AdS, and the IR cutoff $l \to \infty$ corresponds to UV regime of AdS. Thus, moving from boundary to the deep bulk ($z = 0$ to $z = \infty$) , represents transitioning from UV to IR regime in the dual field theory (CFT). Therefore, the extra-dimension z can be interpreted as representing the energy scale for the boundary theory.

A scalar field in AdS

We consider a free massive scalar field ϕ on AdS background in poincare corrdinates, the action for the scalar field is given as:

$$S_{matter} = -\frac{1}{2}\int d^{d+1}x\sqrt{-g}\,\left(\partial_M\phi\partial^M\phi + m^2\phi^2\right)\,. \tag{1.15}$$

The equation of motion for ϕ is given as:

$$\frac{1}{\sqrt{-g}}\,\partial_M\left(\sqrt{-g}g^{MN}\partial_N\phi\right) - m^2\phi = 0\,. \tag{1.16}$$

By utilising the various metric components, this simplifies to

$$z^{d+1}\partial_z\left(z^{1-d}\partial_z\phi\right) + z^2\partial_\mu\partial^\mu\phi - m^2R^2\phi = 0\,. \tag{1.17}$$

The scalar field ϕ is the function of z and x^μ : $\phi = \phi(z, x^\mu)$. The Poincare metric has the translation invariance along x^μ directions, therefore, we can write an ansatz for the scalar field $\phi(z, x^\mu)$ as:

$$\phi(z, x^\mu) = \int \frac{d^dK}{(2\pi)^d}\,e^{iK.x}\phi_K(z)\,, \tag{1.18}$$

where $K^\mu = (\omega, \vec{k})$, and $K^2 = -\omega^2 + \vec{k}^2$. By implementing (1.18) into (1.17), we obtain

$$z^{d+1}\partial_z\left(z^{1-d}\partial_z\phi_K\right) - z^2K^2\phi_K - m^2R^2\phi_K = 0\,. \tag{1.19}$$

We now analyse this equation near the boundary $z \to 0$, the term involving K^2 vanishes. Therefore, eq(1.19) simplifies to

$$z^{d+1}\partial_z \left(z^{1-d}\partial_z \phi_K \right) - m^2 R^2 \phi_K = 0 \,. \tag{1.20}$$

We now consider the following ansatz for $\phi_K(z)$ as: $\phi_K(z) \sim z^\beta$. Eq(1.20) along with this leads to:

$$\beta^2 - \beta d - m^2 = 0 \,. \tag{1.21}$$

The solution of the above quadratic equation is:

$$\beta = \frac{d \pm \sqrt{d^2 + 4m^2R^2}}{2} = \frac{d}{2} \pm \nu \,, \tag{1.22}$$

where $\nu = \sqrt{\frac{d^2}{4} + m^2R^2}$. Let us consider $\Delta = \frac{d}{2} + \nu$, then the solution for $\phi_K(z)$ is given as:

$$\phi_K(z) = A(K)\, z^{d-\Delta} + B(K)\, z^\Delta \,. \tag{1.23}$$

This combined with (1.18) gives the asymptotic behaviour of ϕ as:

$$\phi(z, x^\mu) = A(x)\, z^{d-\Delta} + B(x)\, z^\Delta \,. \tag{1.24}$$

For $\nu \geq 0$, $\Delta \geq \frac{d}{2}$ is real. This constraint gives $m^2R^2 > -\frac{d^2}{4}$, this condition is known as BF bound. $(d - \Delta)$ is negative for $m^2 > 0$, this implies that the field $\phi(z, x^\mu)$ diverges as $z \to 0$ near the boundary.

We would now like to identify normalizable and non-normalizable modes, remember the inner product of two scalar fields which satisfy Klein-Gordon equation, is defined as

$$(\phi_1, \phi_2) = -i \int_{\Sigma_t} dz d^d x \, \sqrt{-g} g^{tt} \left(\phi_1^* \partial_t \phi_2 - \phi_2 \partial_t \phi_1^* \right) \,. \tag{1.25}$$

We focus on near the boundary region $z \to 0$, considering the following ansatz $\phi_K(z) \sim z^\beta$ near the boundary. We now evaluate $\int d^d x \sqrt{-g} g^{tt} \left(\phi^* \partial_t \phi - \phi \partial_t \phi^* \right) \sim z^{1-d+2\beta}$. Then $\int dz\, z^{1-d+2\beta} \sim z^{2-d+2\beta}$. In order to have finite norm we must have $2 - d + 2\beta > 0$. Let us first consider the mode $B(x)\, z^\Delta$, we note that $\beta = \Delta$ for this mode. Then $2 - d + 2\beta = 2(1 + \nu)$, this is always positive since $\nu \geq 0$. Therefore, the mode $B(x)\, z^\Delta$ is always normalizable. We now consider the another mode $A(x)\, z^{d-\Delta}$, for this mode $\beta = d - \Delta$, Now $2 - d + 2\beta = 2(1 - \nu)$, therefore, $\nu \leq 1$ for this mode to be normalizable. This means that for $-\frac{d^2}{4} < m^2R^2 < -\frac{d^2}{4} + 1$, the mode is normalizable, infact both modes are normalizable in this range of m^2R^2. Additionally, for $m^2R^2 \geq -\frac{d^2}{4} + 1$, the mode $A(x) z^{d-\Delta}$ is non-normalizable. Normalizable modes are part of the bulk Hilbert space, and it corresponds to a state in the holographic field theory. Non-normalizable modes are not the part of the bulk Hilbert space, and they provide sources for the operators in the field theory. The source modifies the state of the field theory, since it modifies the boundary action as follows: $S_{bdy} \sim \int d^d x\, \phi_0(x) O(x)$, where $\phi_0(x)$ is a source for an operator O in the boundary theory. we expect that source $\phi_0(x)$ is finite, therefore, we remove the divergent part to obtain the finite

quantity for source. Then the source $\phi_0(x)$ is given as: $\phi_0(x) = \lim_{z\to 0} z^{\Delta-d}\phi(z,x) = A(x)$. It turns out that Δ is exactly equal to the scaling dimension of the operator O in the dual conformal field theory. The Poincare AdS metric exhibits the isometry $x \to x^{'} = \lambda x$ and $z \to z^{'} = \lambda z$. We now consider the fields $\phi(z,x)$ and $\tilde{\phi}(z^{'},x^{'})$ related by the above scaling isometry. Since ϕ is scalar field : $\phi(z,x) = \tilde{\phi}(z^{'},x^{'})$. This leads $\tilde{\phi}_0(x^{'}) = \lambda^{\Delta-d}\phi_0(x)$. We expect that the boundary action $S_{bdy} \sim \int d^dx\, \phi_0(x)O(x)$ is conformal invariant. Therefore, $\int d^dx\, \phi_0(x)O(x) = \int d^dx^{'}\, \tilde{\phi}_0(x^{'})\tilde{O}(x^{'})$. We now combine this with $\tilde{\phi}_0(x^{'}) = \lambda^{\Delta-d}\phi_0(x)$, leads to $\tilde{O}(x^{'}) = \lambda^{-\Delta}O(x)$. This shows that Δ is the scaling dimension of the operator $O(x)$.

States and geometries

The ground state in a Conformal Field Theory (CFT) corresponds to pure Anti-de Sitter (AdS) geometry. Excited states in a CFT correspond to asymptotically AdS geometries, and a thermal state in a CFT corresponds to a black hole in AdS space.

Correlators

We can utilise AdS/CFT correspondence to compute the correlation function of the field theory operators by performing calculations in the bulk. AdS/CFT correspondence suggests that the generating functional of CFT is equal to the partition function of gravity, i.e., $Z_{CFT}[\phi] = Z_{gravity}[\Phi|_{\partial AdS} = \phi]$, where $\phi(x)$ is the source for an operator O in CFT. As discussed earlier, the non-normalizable modes in bulk leads to the source in the field theory, thereby modifying the boundary theory. This is expressed as $\phi(x) = \lim_{z\to 0} z^{\Delta-d}\Phi(z,x)$, where $\Phi(z,x)$ is a massive scalar field propagating in Euclidean AdS background, with the matter action as $S_{matter} = -\frac{1}{2}\int d^{d+1}x\sqrt{g}\left(\partial_M\Phi\partial^M\Phi + m^2\Phi^2\right)$. Recall that the 2-point correlation function in CFT is given by:

$$\langle O_1(x_1)O_2(x_2)\rangle = \frac{\delta^2 \log Z^{ren.}_{CFT}}{\delta\phi_1(x_1)\delta\phi_2(x_2)}\bigg|_{\phi=0}, \tag{1.26}$$

where $Z^{ren.}_{CFT}$ is a renormalised generating functional of CFT. To compute the gravity partition function, consider a scalar field Φ in the Euclidean AdS background. The classical gravity partition function can be evaluated using the saddle point approximation, yielding $Z_{gravity} \sim e^{S_{os}[\Phi_c]}$. Here, Φ_c is the classical solution for the scalar field which behaves $\Phi_c(z,x) \to z^{d-\Delta}\,\phi(x)$ as $z \to 0$, and $S_{os}[\Phi_c]$ is the on-shell gravitational action. Therefore, using the arguments above, we find $\log Z_{CFT} \sim S_{os}[\Phi_c]$. We note that $S_{os}[\Phi_c]$ contains local divergences near the boundary. To address this, we introduce a regulator $z = \epsilon$ and add a local counterterm to cancel the divergences in the on-shell action. Following renormalisation procedure, we obtain $\log Z^{ren.}_{CFT} \sim S^{ren.}_{os}[\Phi_c]$. The two-point correlator (1.26) can be expressed as:

$$\langle O_1(x_1)O_2(x_2)\rangle = \frac{\delta^2 S^{ren.}_{os}[\Phi_c]}{\delta\phi_1(x_1)\delta\phi_2(x_2)}\bigg|_{\phi=0}. \tag{1.27}$$

The detailed computation of $S^{ren.}_{os}[\Phi_c]$ can be found in Appendix 6.1, the 2-point correlation function

is then expressed by:

$$\langle O(k)O(-k))\rangle \sim k^{2\nu}\,, \tag{1.28}$$

where $\nu = \Delta - \frac{d}{2}$. In the position space, the 2-point correlation function becomes

$$\langle O(x)O(0))\rangle \sim \frac{1}{|x|^{2\Delta}}\,. \tag{1.29}$$

This result precisely matches the two-point correlator of the operators with scaling dimension Δ in the conformal field theory (CFT).

Quantum information tools

Quantum information theory provides valuable insights into the study of quantum gravity within the framework of gauge/gravity correspondence. Quantum information tools offer profound insights into black hole physics, addressing fundamental puzzles like the black hole information paradox. Over the years, several powerful quantum information tools have been developed, including entanglement, mutual information, and quantum complexity. Entanglement plays a crucial role in understanding the geometry of the spacetime, encapsulating an idea 'entanglement builds the spacetime' ([32], [33]). Holographic entanglement entropy proposal is crucial in this context. On the other hand, complexity plays crucial role in understanding the growth of interior of the black hole at very late times. We will discuss these topics in the next section.

1.2 Entanglement

In this section, we first introduce entangled and non-entangled states, followed by a brief discussion of several measures used to quantify entanglement. Notable studies on these topics include ([34], [35], [36], [37], [38], [39], [40]). We then present the RT/HRT prescription, which is used to compute the entanglement entropy of a boundary subregion holographically. Specifically, we use the RT prescription to compute the entanglement entropy of a strip-shaped boundary subregion in d-dimensional Conformal Field Theory (CFT_d). In a later subsection, we employ RT/HRT surfaces to probe Big-crunch singularities in AdS Kasner cosmologies and study quantum extremal surfaces in dimensionally reduced two-dimensional dilaton gravity backgrounds.

1.2.1 Introduction to entanglement

We consider a quantum bipartite system consists of subsystems A and B with the state $|\Psi\rangle$ in the Hilbert space $\mathcal{H}_A \otimes \mathcal{H}_B$. This state is separable if it can be expressed as the tensor product of states from subsystems A and B, i.e.,$|\Psi\rangle = |\Psi\rangle_A \otimes |\Psi\rangle_B$. In this case, there is no entanglement between subsystems A and B. Conversely, the state $|\Psi\rangle$ is inseparable if it cannot be represented as a simple tensor product, specifically if it takes the form $|\Psi\rangle = \sum_{i,j} C_{ij} |i\rangle_A |j\rangle_B \neq |\Psi\rangle_A \otimes |\Psi\rangle_B$. In such

cases, there is entanglement between the subsystems A and B. For instance, in a two qubit system, the states $\frac{1}{\sqrt{2}}\left(|00\rangle \pm |11\rangle\right)$, $\frac{1}{\sqrt{2}}\left(|01\rangle \pm |10\rangle\right)$ are maximally entangled. These states are referred to as Bell states.

The entanglement in a quantum system is quantified using entanglement entropy, von Neumann measure is a prominent measure for defining entanglement entropy. Consider a quantum system described by a pure state $|\Psi\rangle$, the density matrix is given as $\rho = |\Psi\rangle\langle\Psi|$. We now decompose the Hilbert space as $\mathcal{H} = \mathcal{H}_A \otimes \mathcal{H}_B$, then reduced density matrix is obtained as $\rho_A = tr_B(\rho)$ by tracing out the degrees of freedoms associated with subsystem B. The von Neumann entropy of subsystem A is then given by

$$S_A = -tr_A(\rho_A \log \rho_A)\,. \tag{1.30}$$

Let us first consider a Bell state $|\Psi\rangle = \frac{1}{\sqrt{2}}\left(|00\rangle + |11\rangle\right)$ to perform explicit calculations. The density matrix is given by:

$$\rho = |\Psi\rangle\langle\Psi| = \frac{1}{2}\left(|00\rangle\langle 00| + |00\rangle\langle 11| + |11\rangle\langle 00| + |11\rangle\langle 11|\right)\,. \tag{1.31}$$

The reduced density matrix ρ_A for the first qubit 'A' is obtained by tracing out the second qubit 'B'. This yields:

$$\rho_A = \frac{1}{2}\left(|0\rangle\langle 0| + |1\rangle\langle 1|\right)\,. \tag{1.32}$$

The von Neumann entropy of the first qubit 'A' is then calculated as:

$$S_A = -\sum_{i=1,2} \lambda_i \log \lambda_i = \log 2\,, \tag{1.33}$$

where λ_i's are the eigenvalues of the reduced density matrix ρ_A. Similarly, we obtain $S_B = \log 2$. We note that $S_A = S_B$, this is expected because the total system is in a pure state. We also observe that both ρ_A and ρ_B represent mixed states.

Now, let's consider another example of an entangled state, the well-known Thermo Field Double (TFD) state, in the Hilbert space $\mathcal{H}_A \otimes \mathcal{H}_B$:

$$|TFD\rangle = \frac{1}{\sqrt{Z}} \sum_n e^{-\frac{\beta E_n}{2}}\ |n\rangle_A \otimes |n\rangle_B\ , \tag{1.34}$$

where $Z = e^{-\beta E_n}$ is the partition function, and subsystem 'B' is identical to subsystem 'A'. The density matrix is given as $\rho = |TFD\rangle\langle TFD|$, then the reduced density matrix ρ_A is obtained by tracing out the subsystem B:

$$\rho_A = \frac{1}{Z} \sum_n e^{-\beta E_n}\ |n\rangle_A \langle n|_A\ . \tag{1.35}$$

This is exactly equal to thermal density matrix $\frac{1}{Z}\, e^{-\beta H}$, where E_n are the eigenvalues of the Hamiltonian H. Therefore, $\rho_A = \frac{1}{Z}\, e^{-\beta H}$ describes a thermal density matrix. This indicates that a

thermal density matrix ρ_A can be purified by considering a pure Thermo Field Double state $|TFD\rangle$ in an enlarged Hilbert space $\mathcal{H}_A \otimes \mathcal{H}_B$, where Hilbert space $\mathcal{H}_B$ is identical to $\mathcal{H}_A$.

We mention here a few important properties: The density matrix $\rho = |\Psi\rangle \langle\Psi|$ is a projection operator, Hermitian, and positive semi-definite. Consequently, the von Neumann entropy is real and non-negative. For a pure state, entanglement entropy of a subsystem 'A' is same as the entanglement entropy of its compliment subsystem 'B', i.e., $S_A = S_B$, and $S_{A\cup B} = 0$. Besides, von Neumann entropy satisfies the inequality $S_A + S_B \geq S_{A\cup B}$.

There are various other measures used to quantify entanglement, such as mutual information, relative entropy, and Rényi entropy. The mutual information of systems 'A' and 'B' is defined as $I(A,B) = S_A + S_B - S_{A\cup B}$. Mutual information satisfies the property $I(A,B) \geq 0$, this is known as subadditivity identity. Mutual information $I(A,B)$ measures the correlation between subsystems 'A' and 'B'. Relative entropy is defined as $S(\rho||\sigma) = tr(\rho\,(\log\ \rho - \log\ \sigma))$. It measure the distance between the two states described by ρ and σ. Relative entropy is always non-negative, i.e., $S(\rho||\sigma) \geq 0$. The Rényi entropy is defined as $S_n(A) = \frac{1}{1-n}\log\left(tr_A(\rho_A^n)\right)$. Rényi entropy is the generalisation of von Neumann entropy with replica number n, and It reduces to the von Neumann entropy as $n \to 1$, i.e., $S_A = \lim_{n\to 1} S_n(A)$. We now look at two crucial identities: subadditivity and strong subadditivity, the subadditivity is given as

$$S_A + S_B - S_{A\cup B} \geq 0 \quad \Leftrightarrow \quad I(A,B) \geq 0\,, \tag{1.36}$$

and the strong subadditivity is given as

$$S_{A\cup B\cup C} + S_B \leq S_{A\cup B} + S_{B\cup C} \quad \Leftrightarrow \quad I(A, B\cup C) \geq I(A,B)\,. \tag{1.37}$$

1.2.2 Entanglement entropy in field theory

Consider a spatial subregion 'A' in a d-dimensional field theory. Decomposing the total Hilbert space of the field theory as $\mathcal{H}_A \otimes \mathcal{H}_{A^C}$ by considering the field theory on a lattice with a lattice spacing ϵ (we recover the original field theory with the continuum limit of the lattice system, i.e., $\epsilon \to 0$). When the total system in a pure state (either in ground state or low-lying excited state), the entanglement entropy of the subregion 'A' is given by the following area law

$$S_A = \frac{Area(\partial A)}{\epsilon^{d-2}} + \ldots\,. \tag{1.38}$$

Here, ϵ is the UV cutoff, and $Area(\partial A)$ is the area of the entangling surface (∂A) . The first term in S_A is a leading ultraviolet divergent term which arises from the short-distance correlations, and the dotted terms may be finite or divergent depending on the specific theory. It tuns out that area law (1.38) only holds for $d > 2$, and the entropy S_A scales as volume for the random states in field theory.

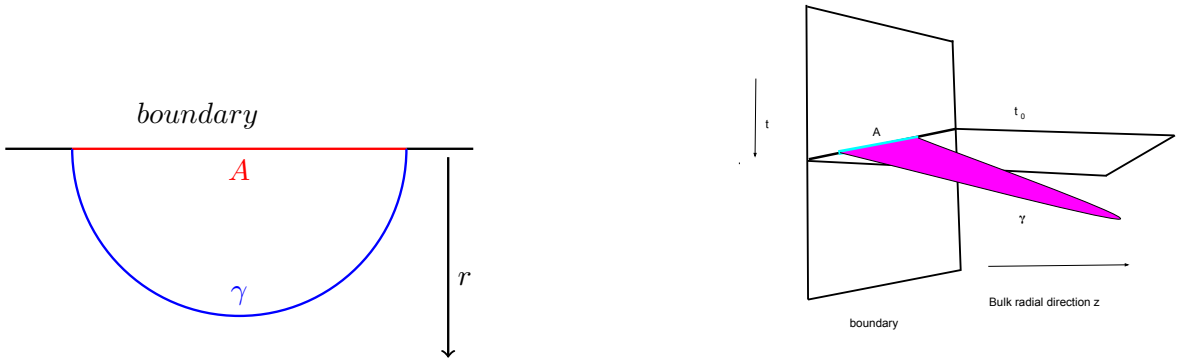

(a) (b)

Figure 1.1: Left panel: Minimal surface (Ryu-Takayanagi surface) γ (blue) anchored at the boundary of subregion A (red) in time-independent AdS geometries. Right panel: γ represents the RT/HRT surface anchored at the boundary of subregion A at a constant time slice t_0 in time-dependent AdS geometries

For an interval l within two-dimensional Conformal Field Theory (CFT_2) that is in its ground state , the entanglement entropy of the interval is given as $S_A = \frac{c}{3}\log\frac{l}{\epsilon}$, where c is the central charge of CFT_2. This is well-known as Calabrese-Cardy formula ([36]), which can be derived using replica trick.

1.2.3 Holographic entanglement entropy

Holographic entanglement entropy of a boundary subregion can be computed using RT/HRT prescription. According to Ryu-Takayanagi's proposal the entanglement entropy of a boundary subregion is obtained holographically by using a codimension-two minimal surface in the bulk which is homologous to the boundary subregion (see Figure 1.1a). The holographic entanglement entropy is given by the Ryu-Takayanagi formula [17]: $S_A = \frac{Area(\gamma)}{4G_N}$, where γ is the codimension-two minimal bulk surface anchoring at the boundary of subregion A. For the time dependent geometries, we employ RT/HRT prescription [18] to define the holographic entanglement entropy. This prescription involves determining a codimension-two extremal surface within the bulk, anchored at the boundary of subregion A. This surface is known as the RT/HRT surface, extends into the time direction as well as illustrated in Figure 1.1b. Some of notable reviews are ([41], [42]).

Consider AdS_{d+1} metric in Poincare coordinates:

$$ds^2_{d+1} = \frac{R^2}{z^2}\left(dz^2 - dt^2 + d\vec{x}^2\right), \tag{1.39}$$

where R is the AdS radius, z is the radial bulk coordinate, t is the time coordinate, and $\vec{x}$ represents the spatial coordinates. To study the entanglement entropy of a subsystem in the boundary theory, consider a strip-shaped region A with finite width l along the $x_1 = x$ direction and infinite extent in the other spatial directions. The area functional for a codimension-two bulk surface anchored to the boundary of the subregion 'A' is given by:

$$A = V_{d-2} R^{d-1} \int dz \, \frac{1}{z^{d-1}} \sqrt{1 + x'(z)^2} \,, \tag{1.40}$$

where V_{d-2} represents the transverse IR regulated volume (along the remaining spatial directions), and the codimension-two minimal surface lies on a constant time slice. The minimization of the area functional (1.40) yields,

$$x'(z) = \frac{z^{d-1}}{\sqrt{z_*^{2(d-1)} - z^{2(d-1)}}} \,, \tag{1.41}$$

where z_* is a turning point of the minimal surface, representing the deepest point in the bulk that the minimal surface can reach.

For the simplest case of AdS_3 (d=2) space. The solution to eq.(1.41) is:

$$x(z) = \pm\sqrt{z_*^2 - z^2} + C \,. \tag{1.42}$$

We now require that the minimal surface anchors at the boundary $z = 0$, i.e., $x(0) = \pm\frac{l}{2}$. This implies $C = 0$, the minimal surface then represents a semi-circle $x^2 + z^2 = (\frac{l}{2})^2$ with radius $z_* = \frac{l}{2}$. The area functional for the minimal surface then becomes:

$$A = Rl \int_{z=\epsilon}^{z_*=\frac{l}{2}} \frac{dz}{z} \, \frac{1}{\sqrt{(\frac{l}{2})^2 - z^2}} \,, \tag{1.43}$$

we introduce a cutoff $z = \epsilon$ to regulate the divergence near $z = 0$. After evaluating the integral, we find:

$$A = 2R \, \log \frac{l}{\epsilon} \,. \tag{1.44}$$

The entropy of boundary subregion is then evaluated using Ryu-Takayanagi's formula as

$$S_A = \frac{A}{4G_N} = \frac{R}{2G_N} \, \log \frac{l}{\epsilon} \,. \tag{1.45}$$

Identifying the central charge of CFT as $c = \frac{3R}{2G_N}$, the entropy S_A can be recast as:

$$S_A = \frac{c}{3} \, \log \frac{l}{\epsilon} \,. \tag{1.46}$$

This result is in agreement with the known expression for the entanglement entropy of a boundary subregion A in two-dimensional Conformal Field Theory (CFT_2).

For general values of d, we substitute Eq.(1.41) into (1.40) . The area functional becomes

$$A = 2V_{d-2}R^{d-1}Z_*^{d-1}\int_{z=\epsilon}^{z=z_*}\frac{dz}{z^{d-1}}\frac{1}{\sqrt{z_*^{2(d-1)}-z^{2(d-1)}}}\,. \tag{1.47}$$

The width of the boundary subregion l along x direction is related to the turning point z_* as follows:

$$\frac{l}{2} = \int_\epsilon^{z_*} dz \frac{z^{d-1}}{\sqrt{z_*^{2(d-1)}-z^{2(d-1)}}} = z_*\sqrt{\pi}\,\frac{\Gamma\left(\frac{d}{2(d-1)}\right)}{\Gamma\left(\frac{1}{2(d-1)}\right)}\,. \tag{1.48}$$

This implies

$$z_* = \frac{l}{2\sqrt{\pi}}\,\frac{\Gamma\left(\frac{1}{2(d-1)}\right)}{\Gamma\left(\frac{d}{2(d-1)}\right)}\,. \tag{1.49}$$

The area functional (1.47) after evaluating the integral becomes

$$A = \frac{2V_{d-2}R^{d-1}}{d-2}\left[\frac{1}{\epsilon^{d-2}} - \frac{\sqrt{\pi}}{z_*^{d-2}}\,\frac{\Gamma\left(\frac{d}{2(d-1)}\right)}{\Gamma\left(\frac{1}{2(d-1)}\right)}\right]\,. \tag{1.50}$$

Utilizing (1.49) into (1.50), we obtain the holographic entanglement entropy of boundary subregion A as

$$S_A = \frac{V_{d-2}R^{d-1}}{(d-2)2G_N}\left[\frac{1}{\epsilon^{d-2}} - \frac{(l/2)}{z_*^{d-1}}\right]\,. \tag{1.51}$$

The diverging part has a leading contribution to the entanglement entropy which scales as $S_A \sim \frac{1}{\epsilon^{d-2}}$, while the second part of S_A is finite and depends on the finite width of the subregion A along x-direction. In the IR limit of the subregion A, i.e., $l \to \infty$ ($z_* \to \infty$), the finite term vanishes in S_A.

1.2.4 RT/HRT surface in AdS Kasner cosmologies

[43] explores RT/HRT surfaces in AdS Kasner cosmologies in great detail. In this section, we review the key aspects of that study here. AdS Kasner cosmologies are time-dependent deformation of AdS, where the dual field theory resides on a time-dependent space with a time-dependent gauge coupling. One might expect that the RT/HRT surfaces could be used to probe the cosmological singularities such as Big-Crunch. However, it turns out that the RT/HRT surfaces cannot probe regions near-singularity in AdS Kasner cosmologies. Instead, they avoid near-singularity regions as illustrated in Figure 1.2.

Consider the $(d+2)$-dimensional Isotropic AdS Kasner metric:

$$ds_{d+2}^2 = \frac{e^f}{\phi^{\frac{(d-1)}{d}}}\left(-dt^2+dr^2\right) + \phi^{\frac{2}{d}}\,dx_i^2\,. \tag{1.52}$$

The dimensionally reduced 2-dim background is given by:

$$ds^2 = \frac{t^{\frac{(d-1)}{d}}}{r^{d+1}}\left(-dt^2 + dr^2\right) \quad ; \quad \phi = \frac{t}{r^d}\,. \tag{1.53}$$

We notice that $e^f = \frac{t^{\frac{(d-1)}{d}}}{r^{d+1}}$, and the geometry described by the metric (1.52) possess Big-crunch singularity at $t = 0$.

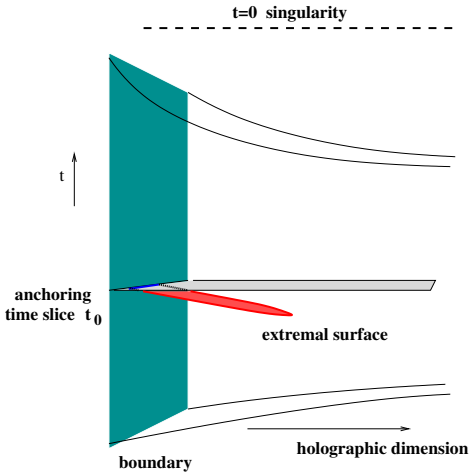

Figure 1.2: Cartoon of extremal surfaces in *AdS* Kasner spacetime, anchored on a boundary time slice t_0. The extremal surface (red) bends away from the singularity at $t = 0$ (dotted line), *i.e.* $t_* > t_0$, with (t_*, r_*) the turning point.

Now, consider a strip-shaped spatial subregion A with finite width along $x_1 = x$ and infinite extent along the remaining spatial directions, situated on the regulated boundary of (1.52) at the boundary time slice $t = t_0$. We note that the geometry is time-dependent, therefore, we utilze RT/HRT prescription to find a codimension-two extremal surface in the bulk, the surface anchors on the boundary of subregion A. The codimension-two surface can be specified by $(x(r), t(r))$, the area functional of the codimension-two surface is then given by:

$$\mathcal{A} = V_{d-1}\int dr\,\phi^{\frac{(d-1)}{d}}\sqrt{\frac{e^f}{\phi^{\frac{(d-1)}{d}}}\left(1 - t'(r)^2\right) + \phi^{\frac{2}{d}}\,x'(r)^2}\,, \tag{1.54}$$

where $t'(r) \equiv \frac{dt}{dr}$, $x'(r) \equiv \frac{dx}{dr}$, and $V_{d-1} = \int dx_2 ... dx_d$ is the regulated volume. The above expression simplifies to:

$$\mathcal{A} = V_{d-1}\int dr\,\phi\sqrt{\frac{e^f}{\phi^{\frac{(d+1)}{d}}}\left(1 - t'(r)^2\right) + x'(r)^2}\,. \tag{1.55}$$

Extremizing the area functional (1.55) with respect to $x(r)$ yields x-extremization equation as:

$$x'(r)^2 = A^2\,\frac{e^f}{\phi^{\frac{(d+1)}{d}}}\,\frac{\left(1 - t'(r)^2\right)}{\left(\phi^2 - A^2\right)}\,, \tag{1.56}$$

here, A is a constant. Utilising the above equation in (1.55), the area functional becomes:

$$\mathcal{A} = V_{d-1}\int dr\,e^{\frac{f}{2}}\,\frac{\phi^{\left(3-\frac{1}{d}\right)/2}}{\sqrt{\phi^2 - A^2}}\sqrt{1 - t'(r)^2}\,. \tag{1.57}$$

The extremal surface possess a turning point (r_*, t_*) as $x'(r)^2 \to \infty$. At the turning point, $\phi_* = A$, therefore the constant A is given by:

$$A = \phi_* = \frac{t_*}{r_*^d}\,, \tag{1.58}$$

where $t_* = t(r_*)$. The turning point (r_*, t_*) depends on the values of t_0 (anchoring time) and the width l for a fixed value of A. The relation between r_* and the width of the subregion A is:

$$\frac{l}{2} = \int_{r=0}^{r=r_*} dr\, x'(r) = A \int_0^{r_*} dr\, \frac{e^{\frac{f}{2}}}{\phi^{\frac{(d+1)}{2d}}} \sqrt{\frac{(1-t'(r)^2)}{(\phi^2 - A^2)}} = r_* \int_0^1 du\, t(u)^{-\frac{1}{d}} \sqrt{\frac{(1-t'(u)^2)}{\frac{\phi^2}{A^2} - 1}}\,. \tag{1.59}$$

We observe the scaling as $l \sim r_*$, therefore $A \sim \frac{t_*}{l^d}$. This indicates that for a small subregion width l, r_* is small, the extremal surface returns to the boundary after approaching the turning point. However, for a larger subregion width, r_* is large, this indicates that the extremal surface can go deeper into the bulk. Moreover, $r_* \to \infty$ (the surface dipping deeper into the bulk) in the IR limit of the subregion ($l \to \infty$).

We observe that the factor $\frac{e^f}{\phi^{(d+1)/d}}$ in (1.56) includes a term proportional to $t^{-\#}$, which suggests the presence of a distinct turning point localized at the singularity $t_* = 0$. However, this branch of extremal surfaces appears to be disconnected from the branch that remains continuously connected to the AdS-like branch in the region far from the singularity. Notably, such a branch with $t_* = 0$ exists only in the limit of infinite strip width, i.e., the infrared (IR) limit, where no parameter (such as A) enables deformation away from the $t_* = 0$ locus. This implies that the branch is inaccessible from the classical region far from the singularity. Moreover, the vicinity of the singularity at $t = 0$ is a regime where quantum gravity effects are expected to dominate. A classical RT/HRT extremal surface localized in this region, with no means of deformation toward a well-defined classical region, is therefore unreliable. For this reason, we discard this branch of extremal surfaces. Additionally, for $(\partial_r x)^2 > 0$ to be well-defined, we require $(\partial_r t)^2 < 1$, ensuring that $|\partial_r t|$ remains bounded. For small strip widths, the extremal surface lies on an almost constant-time slice, i.e., $(\partial_r t)^2 \ll 1$. This condition, $(\partial_r t)^2 < 1$, is consistent with the surface being spacelike everywhere under our boundary conditions.

The above analysis does not reveal the full characteristics of the solution $t(r)$ and the turning points t_* and r_*. To address this, we derive the differential equation for $t(r)$ by extremizing the area functional, as discussed below. Extremizing the area functional (1.55) with respect to $t(r)$ and utilizing the x-extremization equation (1.56) yields the t-extremization equation:

$$(1-t'(r)^2)\left(d^2t'(r) + \frac{r(t(r)^2 - A^2r^{2d})}{t(r)^3} - \frac{dr}{t(r)}\right) - \left(t(r)^2 - A^2r^{2d}\right)\frac{drt''(r)}{t(r)^2} = 0\,. \tag{1.60}$$

Consider an ansatz for $t(r)$ as:

$$t(r) = t_0 + \sum_{n\geq 1} c_n r^n \quad ; \quad c_n \sim \frac{1}{t_0^{n-1}} \quad \to \quad t_* > t_0\,. \tag{1.61}$$

The perturbative solution for $t(r)$ reads as:

$$t(r) = t_0 + \frac{r^2}{12t_0} - \frac{r^4}{432t_0^3} + \frac{r^6}{7776t_0^5} + \left(\frac{A^2}{160t_0^3} - \frac{17}{7776.240t_0^7}\right) r^8 + \dots \tag{1.62}$$

This indicates that $t(r) \geq t_0$, meaning the extremal surface dips away from the anchoring time slice t_0, avoiding the near-singularity region, as depicted in Figure 1.2. Next, we examine the validity of the perturbative solution (1.62). The condition $r \leq t_0$ must hold to ensure the perturbative solution is well-defined. Thus, the perturbative solution is valid for small subregions with $l \leq t_0$. Additionally, we observe that the condition $t'(r) \ll 1$ is satisfied for the perturbative solution.

The IR limit, where the strip width is large, corresponds to $\frac{t_*}{r_*^d} = A \sim \frac{1}{l^d} \to 0$. In this limit, Eq. (1.60) becomes:

$$d^2t^3t' + rt^2 - drt^2 - t^2drt'' = 0.$$

Analyzing this via a power series in Mathematica for AdS_5 Kasner ($d = 3$), we find:

$$t(r) = t_0 + \frac{1}{12\,t_0}\, r^2 - \frac{1}{432\,t_0^3}\, r^4 + \frac{1}{7776\,t_0^5}\, r^6 - \frac{17}{1866240\,t_0^7}\, r^8 + \frac{247}{335923200\,t_0^9}\, r^{10} + \dots \tag{1.63}$$

The series here is more delicate, as the surface extends fully into the bulk with $r_* \to \infty$. Thus, the entire r-series becomes significant. The limit $A \to 0$ implies $A \lesssim \frac{1}{t_0^2}$ when compared with the scale t_0, which further requires:

$$r_* \to \infty\,, \quad t_0 \to \infty\,, \qquad \frac{t_0}{r_*} \lesssim 1\,. \tag{1.64}$$

This describes the reliable semiclassical regime far from the singularity. In this regime, the series defining the time behavior of the surface remains well-defined, though delicate: the surface is anchored on a slice far from $t = 0$. While it dips deep into the bulk, its time dependence is mild, with $t'^2 \ll 1$ everywhere. The perturbative solution (1.63) breaks down beyond a certain r, and therefore it does not capture the full RT/HRT surface in the region $r > t_0$. For this regime, numerical methods must be employed to solve the t-extremization equation (1.60) directly. In [44], we perform a numerical analysis of the IR limit of the boundary subregion. Our results indicate that the codimension-two extremal surface originates from the boundary, bending away from the singularity region, and eventually becomes light-like beyond a certain r. The extremal surface extends up to $r \to \infty$.

1.2.5 Entanglement wedge

The RT/HRT proposal suggests that the codimension-2 extremal surface γ is homologous to the boundary subregion A, meaning there exists a bulk region $\mathcal{R}$ such that $\partial\mathcal{R} = A \cup \gamma$. The surface $\mathcal{R}$, referred to as the homology surface, is a codimension-one surface in the bulk. The entanglement wedge of the boundary subregion A is defined as the domain of dependence of the homology surface $\mathcal{R}$, denoted as $\mathcal{D}[\mathcal{R}] = \mathcal{W}_\gamma[A]$. This entanglement wedge corresponds to a codimension-zero region in the bulk.

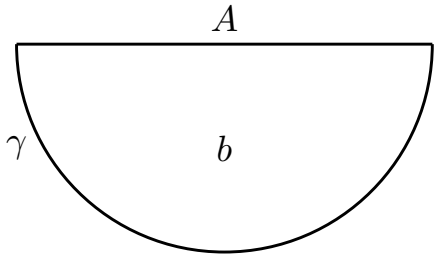

Figure 1.3: The figure shows a minimal surface γ anchoring at the boundary of the subregion 'A' and b represents the bulk region surrounded by γ and A

1.2.6 Corrections to the holographic entanglement entropy

The holographic entanglement entropy obtained using Ryu-Takayanagi (RT) or Hubeny-Rangamani-Takayanagi (HRT) prescription only holds at order $O(\frac{1}{G_N})$ (or $O(N^2)$ in the boundary theory). This entropy can receive corrections from quantum mechanical effects in the bulk. Faulkner, Lewkowycz and Juan Maldacena ([45]) found that the quantum corrections at $O(G_N^0)$ (or $O(N^0)$ in the boundary theory) to the holographic entanglement entropy are given by incorporating the bulk entanglement entropy. The corrected holographic entropy of the boundary subregion A is then given by:

$$S_A = \frac{Area(\gamma)}{4G_N} + S_{bulk}(b) + counterterms\,, \tag{1.65}$$

where the first term represents a classical term: area of the codimension-two minimal surface, while the second term represents a quantum term: bulk entanglement entropy of the region b (surrounded by the boundary subregion and the minimal surface γ as illustrated in Figure 1.3). The term S_{bulk} is UV divergent, but these divergences can be absorbed by adding counterterms. The combination $(S_{bulk} + counterterms)$ is then finite.

1.2.7 Quantum extremal surfaces

The von Neumann entropy of a boundary subregion at all orders in $1/N^2$ (or G_N) can be holographically obtained by extremizing generalised entropy ([46]). The generalised entropy is defined as:

$$S_{gen} = \frac{Area(\gamma)}{4G_N} + S_{bulk}\,, \tag{1.66}$$

where γ is a codimension-two bulk surface that anchors at the boundary of the subregion A, and S_{bulk} is entanglement entropy of the bulk region surrounded by boundary subregion A and the surface γ. The extremization of (1.66) provides quantum extremal surface (QES), and the generalised entropy evaluated at the quantum extremal surface gives the von Neumann entropy of the boundary subregion A. If there are multiple quantum extremal surfaces, the one that provides minimum S_{gen} is considered. This can be summarized as

$$S_A = min\left\{ext\left[\frac{Area(\gamma)}{4G_N} + S_{bulk}\right]\right\}. \tag{1.67}$$

The term S_{bulk} involves area-like UV divergences in d-dimensions ($d > 2$), these divergences can be absorbed by the renormalisation of Newton's constants. The renormalised Newton's constant is given by:

$$\frac{1}{4G_N^r} = \frac{1}{4G_N} + \frac{1}{\epsilon^{d-2}}. \tag{1.68}$$

The explicit computation of S_{bulk} is challenging in general dimensions. However, for two-dimensional conformal field theories (CFT_2), it can be calculated explicitly using the Cardy-Calabrese formula. Therefore, we focus on theories in two dimensions or those obtained by dimensionally reducing higher-dimensional theories to two dimensions. Additionally, we assume that the bulk matter is described by two-dimensional conformal field theory (CFT_2) in its ground state, especially for the explicit computations. We further assume that $\frac{1}{G_N} \gg c \gg 1$ to avoid back-reaction on the classical geometry due to strong quantum effects, where c is the central charge of CFT_2. For two-dim dilaton gravity theories the QES and boundary subregions are just points. Therefore, the generalised entropy is given by:

$$S_{gen} = \frac{\phi}{4G_N} + \frac{c}{12}\log\left(\Delta^2 e^f\right), \tag{1.69}$$

where ϕ represents dilaton profile, and e^f is the conformal factor appearing in the conformally flat two-dimensional metric background. Here, $\Delta^2 = r^2 - (t - t_0)^2$, where t_0 is the time slice at the location of boundary subregion.

The entropy functional involved in the RT/HRT prescription under the IR limit of a boundary subregion of a higher-dimensional theory ($d > 2$) gives the classical term (dilaton ϕ term) in the generalised entropy (1.69). This can be seen explicitly by considering the higher-dimensional AdS_{d+2} background as

$$ds^2 = \phi^{\frac{2}{d}}\left(-dt^2 + dr^2\right) + \phi^{\frac{2}{d}} d\vec{x}^2, \tag{1.70}$$

where $\phi = \frac{1}{r^d}$. We first assume that the boundary subregion has finite length l along $x_1 = x$ direction. Later, we consider the IR limit as $l \to \infty$. The entropy functional for the boundary subregion is:

$$S = \frac{V_{d-1}}{4G_{d+2}} \int dr\, \phi(r)\sqrt{1 + x'(r)^2}, \tag{1.71}$$

In the IR limit, S is given as:

$$S = \frac{V_{d-1}}{4G_{d+2}} \int dr\, \phi(r) x'(r) \sim \frac{\phi(r)}{4G_2}\,, \tag{1.72}$$

where two-dimensional Newton's constant is given as $\frac{1}{G_2} \sim \frac{V_d}{G_{d+2}}$.

Quantum extremal surface in AdS_2-dilaton gravity theory

The 2-dimensional dilaton gravity solution is given by:

$$ds^2 = \frac{1}{r^2}\left(-dt^2 + dr^2\right) \quad ; \quad \phi = \frac{\phi_r}{r}\,. \tag{1.73}$$

The generalised entropy is then given as:

$$S_{gen} = \frac{\phi_r}{4G_N}\frac{1}{r} + \frac{c}{6}\log\left(r\frac{1}{r}\right) \quad , \quad \partial_r S_{gen} = -\frac{\phi_r}{4G_N}\frac{1}{r^2}\,. \tag{1.74}$$

The extremization of the generalised entropy, as shown in (1.74), gives the quantum extremal surface at $r_* \to \infty$. This indicates that the entanglement wedge is the entire Poincaré patch, as expected.

Quantum extremal surfaces in AdS_{d+2} dimensionally reduced theories

The 2-dimensional background is given by:

$$ds^2 = \frac{1}{r^{d+1}}\left(-dt^2 + dr^2\right) \quad ; \quad \phi = \frac{\phi_r}{r^d}\,. \tag{1.75}$$

The generalised entropy is given as:

$$S_{gen} = \frac{\phi_r}{4G_N}\frac{1}{r^d} + \frac{c}{6}\log\left(\frac{r}{r^{\frac{(d+1)}{2}}}\right) \quad , \quad \partial_r S_{gen} = -\frac{\phi_r}{4G_N}\frac{d}{r^{d+1}} - \frac{c}{6}\frac{(d-1)}{2r}\,. \tag{1.76}$$

The extremization of the generalised entropy gives the location of quantum extremal surface (QES) at $r_* \to \infty$ again. This suggest that the entanglement wedge is the entire Poincaré patch, as expected. The generalised entropy (1.76) can be recast as:

$$S_{gen} = \frac{\phi}{4G} + \frac{c}{12}\frac{(d-1)}{d}\log\phi\,. \tag{1.77}$$

In summary, for the simple 2-dimensional dilaton gravity backgrounds considered, the QES is located at infinity, i.e., $r_* \to \infty$, and the entanglement wedge is the entire Poincaré patch, as expected.

1.3 Complexity

In computer science, computational complexity measures the difficulty of performing a task, often in terms of the resources required, such as the amount of time needed to complete a task or the memory necessary to store information. As computing evolved, this concept naturally extended to quantum systems, where representing and processing quantum information posed unique challenges. The transition from classical to quantum circuit complexity builds upon the foundational work of early computing pioneers. Claude Shannon's introduction of Boolean circuits [47] in 1948 laid the groundwork for representing logical operations, a concept that would later be adapted to quantum systems. Richard Feynman [48] and David Deutsch [49] took this further by proposing that quantum systems could be simulated using quantum circuits. Deutsch also formalized the concept of a quantum Turing machine, which provided a theoretical framework for quantum computation. This led to the introduction of quantum gates—unitary operations that form the building blocks of quantum circuits. The power of quantum circuits was dramatically illustrated by Peter Shor's quantum factoring algorithm [50] in 1994, which showed that quantum circuits could outperform classical circuits for certain problems. In 1995, Adriano Barenco and colleagues [51] demonstrated that a universal set of quantum gates, such as Hadamard and CNOT, could generate any quantum operation, solidifying the idea that arbitrary quantum states could be represented as circuits. These ideas culminated in Michael Nielsen and Isaac Chuang's Quantum Computation and Quantum Information [52], which provided a comprehensive framework for quantum circuits. Their work formalized the use of quantum gates to represent arbitrary unitary transformations, demonstrating that any quantum operation, and by extension any quantum state, could be represented by a quantum circuit. Mathematically, this is expressed as $|\psi\rangle = U\,|\psi\rangle_I$, where $|\psi\rangle_I$ denotes the initial state and U is a unitary operator implemented via quantum gates. This integrated approach became the standard model for quantum computation, illustrating how complex quantum systems could be simulated and manipulated through the careful arrangement of quantum gates.

With these developments, the computational complexity landscape expanded, and the concept of quantum circuit complexity emerged as a critical framework for understanding the power and limitations of quantum computation.

Beyond computation, quantum circuit complxity is used in studying the dynamics of quantum systems, including quantum chaos and black hole physics. In this section, we review circuit complexity for states and operators in quantum mechanics and quantum field theories. Additionally, we examine various holographic proposals to compute circuit complexity. The textbook [52] provides a comprehensive introduction to quantum information and quantum computation, encompassing topics such as classical and quantum computational complexity. Furthermore, numerous studies [25], [53]–[75] have investigated complexity in the contexts of quantum field theory (QFT) and holography. A comprehensive review of circuit complexity can be found in [76].

1.3.1 K qubits and size of the space of states

For K qubits, the dimension of Hilbert space is 2^K. A general state can be expressed by:

$$|\Psi\rangle = \sum_{i=1}^{2^K} \alpha_i |i\rangle \tag{1.78}$$

In general, the coefficients α_i are arbitrary complex numbers, which result in an infinite number of state vectors (distinct from the basis vectors). To regulate the space of states, each α_i can be constrained to take m-discrete values. Under this restriction, the total number of states is given by:

$$\Omega = m^{2^K} . \tag{1.79}$$

The logarithm of this quantity is:

$$\log \Omega = 2^K \log m. \tag{1.80}$$

For $K = m = 4$, the total number of states is $\Omega = 4,294,967,296$, illustrating the immense state space, with $\log \Omega \sim 22.18$. Furthermore, the expression in Eq. 1.80 demonstrates that $\log \Omega$ depends strongly on the number of qubits K, while its dependence on the regulating parameter m is comparatively weak, varying only logarithmically.

1.3.2 Circuit complexity

Circuit complexity is defined as the minimum number of elementary gates (unitary operations) to construct a target state $|\psi\rangle_T$ from a reference state. The target state is obtained as $|\psi\rangle_T = U\,|\psi\rangle_R$, where the unitary operator U is constructed from a simple set of elementary gates. There could be many circuits to construct U using the same set of elementary gates, we consider the one with minimum number of elementary gates. We can introduce a tolerance ϵ for constructing the target state $|\psi\rangle_T$ with a desired precision:

$$\| |\psi_T\rangle - U|\psi_R\rangle \| \leq \epsilon \, . \tag{1.81}$$

For n qubits, the maximum complexity scales as $\mathcal{C}_{max} \sim 2^n$. The circuit complexity $C(U)$ of a unitary operator U is defined as the minimum number of elementary gates U_i to construct U with a tolerance ϵ, expressed as

$$\left\| U - \prod_{i=1}^{n} U_i \right\| < \epsilon \, . \tag{1.82}$$

1.3.3 Circuit complexity for coupled harmonic oscillators

[72] investigates circuit complexity in the context of coupled harmonic oscillators and quantum field theories. In this section, we review the key aspects of circuit complexity for a system of two coupled harmonic oscillators with the Hamiltonian:

$$\mathcal{H} = \frac{1}{2}\,(p_1^2 + p_2^2) + \frac{\omega^2}{2}\,(x_1^2 + x_2^2) + \frac{\Omega^2}{2}\,(x_1 - x_2)^2 \, . \tag{1.83}$$

We can recast the above Hamiltonian (1.83) in a different basis $\{y_1, y_2\}$, as follows:

$$\begin{aligned}
&\mathcal{H} = \frac{1}{2}(P_1^2 + P_2^2) + \frac{\Omega_1^2 y_1^2}{2} + \frac{\Omega_2^2 y_2^2}{2}\,, \\
&y_1 = \frac{1}{\sqrt{2}}\,(x_1 + x_2) \quad ; \quad y_2 = \frac{1}{\sqrt{2}}\,(x_1 - x_2)
\end{aligned} \tag{1.84}$$

where $\Omega_1 = \omega$, and $\Omega_2 = \sqrt{\omega^2 + 2\Omega^2}$.

The ground state wave function in this new basis is given by:

$$\Psi(y_1, y_2) = \frac{(\Omega_1\Omega_2)^{\frac{1}{4}}}{\pi^{\frac{1}{2}}}\, e^{-\left(\frac{\Omega_1 y_1^2}{2} + \frac{\Omega_2 y_2^2}{2}\right)}\,. \tag{1.85}$$

Transforming back to the original coordinates (x_1, x_2), the ground state wave function becomes:

$$\Psi(x_1, x_2) = \frac{(\omega_1\omega_2 - \beta^2)^{\frac{1}{4}}}{\pi^{\frac{1}{2}}}\, e^{-\left(\frac{\omega_1 x_1^2}{2} + \frac{\omega_2 x_2^2}{2} + \beta x_1 x_2\right)}\,, \tag{1.86}$$

where $\omega_1 = \omega_2 = \frac{(\Omega_1 + \Omega_2)}{2}$, and $\beta = \frac{(\Omega_1 - \Omega_2)}{2}$.

Assuming the target state is the ground state (1.86), i.e., $\Psi_T = \Psi(x_1, x_2)$, and the reference state is:

$$\Psi_R = \frac{(\omega_0)^{\frac{1}{2}}}{\pi^{\frac{1}{2}}}\, e^{-\frac{\omega_0}{2}\left(x_1^2 + x_2^2\right)}\,. \tag{1.87}$$

The target state Ψ_T can be constructed by applying a sequence of elementary gates to the reference state, such that $\Psi_T = U\Psi_R$. Here, U is a unitary operator composed of the following elementary gates:

$$\begin{aligned}
&H = e^{i\epsilon x_0 p_0} \quad ; \quad J_a = e^{i\epsilon x_0 p_a} \quad ; \quad K_a = e^{i\epsilon x_a p_0} \\
&Q_{ab} = e^{i\epsilon x_a p_b} \quad (a \neq b) \quad ; \quad Q_{aa} = e^{i\epsilon\, \frac{(x_a p_a + p_a x_a)}{2}} = e^{\frac{\epsilon}{2}}\, e^{i\epsilon x_a p_a}\,,
\end{aligned} \tag{1.88}$$

where x_0 and p_0 are constants, and $a, b \in 1, 2$. The action of these gates on a wave function $\psi(x_1, x_2)$ is as follows:

$$\begin{aligned}
&H\psi(x_1, x_2) = e^{i\epsilon x_0 p_0}\, \psi(x_1, x_2) && \text{Constant phase change} \\
&J_1\psi(x_1, x_2) = \psi(x_1 + \epsilon x_0, x_2) && \text{Shifting } x_1 \text{ by } \epsilon x_0 \\
&K_a\psi(x_1, x_2) = e^{i\epsilon x_a p_0}\, \psi(x_1, x_2) && \text{Shifting momentum } p_a \text{ by } \epsilon p_0 \\
&Q_{21}\psi(x_1, x_2) = \psi(x_1 + \epsilon x_2, x_2) && \text{Shifting } x_1 \text{ by } \epsilon x_2 \text{ (entangling gate)} \\
&Q_{11}\psi(x_1, x_2) = e^{\frac{\epsilon}{2}}\, \psi(e^{\epsilon} x_1, x_2) && \text{Scaling } x_1 \text{ by } e^{\epsilon} x_1 \text{ (scaling gate)}
\end{aligned} \tag{1.89}$$

Consider a circuit defined as $\Psi_T = Q_{22}^{\alpha_3} Q_{21}^{\alpha_2} Q_{11}^{\alpha_1}\, \Psi_R$, where Q_{11} acts on Ψ_R for α_1 times, followed by Q_{21} and Q_{22} for α_2 and α_3 times respectively. The total number of elementary gates defines the

depth of the circuit (each depth has a single elementary gate), given by

$$D = \alpha_1 + \alpha_2 + \alpha_3 = \frac{1}{\epsilon}\left[\frac{1}{2}\log\left(\frac{\omega_1\omega_2 - \beta^2}{\omega_0^2}\right) + \sqrt{\frac{\omega_0}{\omega_1}}\frac{|\beta|}{\sqrt{\omega_1\omega_2 - \beta^2}}\right], \tag{1.90}$$

where the parameters are

$$\alpha_1 = \frac{1}{2\epsilon}\log\left(\frac{\omega_1}{\omega_0}\right),\ \alpha_2 = \frac{1}{\epsilon}\sqrt{\frac{\omega_0}{\omega_1}}\frac{|\beta|}{\sqrt{\omega_1\omega_2 - \beta^2}},\ \alpha_3 = \frac{1}{2\epsilon}\log\left(\frac{\omega_1\omega_2 - \beta^2}{\omega_0\omega_1}\right). \tag{1.91}$$

To determine the circuit complexity for the given reference state Ψ_R, target state Ψ_T, and the set of elementary gates, we seek the optimal circuit—the one that uses the fewest elementary gates to construct Ψ_T from Ψ_R. Neilsen's geometric approach ([77], [78], [79]) can be employed to find the optimal circuit.

1.3.4 Circuit complexity in quantum field theories

We now aim to compute the circuit complexity in quantum field theories (QFT). For simplicity, we consider a free scalar field theory with the Hamiltonian:

$$H = \int d^{d-1}x\left[\frac{\pi^2}{2} + \frac{1}{2}(\nabla\phi)^2 + \frac{1}{2}m^2\phi^2\right]. \tag{1.92}$$

The QFT can be reformulated as an infinite set of coupled harmonic oscillators by discretizing space into a lattice. In this formulation, each lattice point corresponds to a degree of freedom, behaving as a harmonic oscillator, as illustrated below. This approach transforms the problem of computing the complexity in QFT into that of coupled harmonic oscillators. For a scalar field $\phi(x)$ in d-dimensional spacetime, the Hamiltonian in Eq. (1.92) can be rewritten in the discretized lattice with spacing δ as follows:

$$H = \delta^{d-1}\sum_i\left[\frac{\pi_i^2}{2} + \frac{1}{2}m^2\phi_i^2 + \frac{1}{2\delta^2}\sum_{j\in\text{neighbor}(i)}(\phi_i - \phi_j)^2\right], \tag{1.93}$$

where π_i is the conjugate momentum at lattice site i, m is the mass of the field, and δ is the lattice spacing.

In the continuum limit ($\delta \to 0$), the discrete sum transitions to an integral over the $(d-1)$-dimensional spatial coordinates, and the Hamiltonian reduces to Eq. (1.92).

To further simplify, we redefine the scalar field and parameters as follows:

$$\Phi_i = \delta^{\frac{d}{2}}\phi_i, \quad M = \frac{1}{\delta}, \quad \omega = m, \quad \Omega = \frac{1}{\delta}.$$

Under this redefinition, the Hamiltonian in Eq. (1.93) becomes:

$$H = \frac{1}{2M}\sum_i \Pi_i^2 + \frac{M\omega^2}{2}\sum_i \Phi_i^2 + \frac{M\Omega^2}{2}\sum_{i,j\in\text{neighbor}(i)}(\Phi_i - \Phi_j)^2, \tag{1.94}$$

where Π_i is the conjugate momentum associated with Φ_i. This Hamiltonian describes an infinite set of coupled harmonic oscillators.

To calculate the circuit complexity, the ground state of the uncoupled oscillators is chosen as the reference state, while the ground state of the full coupled Hamiltonian is selected as the target state. Using Nielsen's geometric approach [77, 78, 79], the complexity is determined by considering a path in the space of unitary transformations that connects the reference and target states.

The complexity is defined as the geodesic distance along this path:

$$C = \int_0^1 ds \sqrt{G_{ab} \frac{dY^a}{ds} \frac{dY^b}{ds}}, \tag{1.95}$$

where $Y^a(s)$ parameterizes the path in the space of unitary transformations, and G_{ab} represents the metric on the space of unitaries (a Riemannian manifold). For detailed computations, refer to [72].

1.3.5 SU(2^K), unitaries, and complexity

Consider a quantum system of K qubits, where the Hilbert space is 2^K dimensional. A special unitary operator can be expressed as:

$$U = \sum_{ij} U_{ij} \ |i\rangle \langle j| \ , \tag{1.96}$$

where indices i and j takes values from 1 to 2^K, and the unitary operator U has $4^K - 1$ independent real parameters. If each independent parameter is restricted to take m discrete values, the total number of distinct unitary operators is given by:

$$n = m^{4^K - 1} \quad \rightarrow \quad \log n = (4^K - 1) \log m \, . \tag{1.97}$$

This result reveals a similar pattern to that of the states (discussed in 1.3.1), but with a 4^K factor instead of the 2^K.

The volume of SU(N) [1] is given by:

$$V\left(SU(N)\right) = 2 \, \frac{\pi^{\frac{(N-1)(N+2)}{2}}}{1!2!...(N-1)!} \, . \tag{1.98}$$

For $N \gg 1$, this can be approximated using Stirling's formula as:

$$V\left(SU(N)\right) \sim \frac{\pi^{\frac{N^2}{2}}}{N^{\frac{N^2}{2}}} \, . \tag{1.99}$$

[1] The formula for the volume of $SU(N)$ is derived by calculating its invariant volume, leveraging its recursive relationship with spheres (S^{2N-1}) and the subgroups $SU(N-1)$. This formula encapsulates the intricate geometric and topological structure of $SU(N)$, as thoroughly examined in the iterative approach presented in arXiv:math-ph/0210033. It provides a foundational measure of $SU(N)$'s compact manifold, with significant applications in representation theory, quantum physics, and related fields.

The volume of (N^2-1)-dimensional ball of radius ϵ is given by:

$$V(\epsilon) = \frac{\pi^{\frac{N^2-1}{2}}\epsilon^{N^2-1}}{\Gamma(\frac{N^2+1}{2})} \sim \frac{\pi^{\frac{N^2}{2}}\epsilon^{N^2}}{N^{N^2}}\,, \tag{1.100}$$

where Stirling's approximation for $N = 2^K \gg 1$ has been used. The number of unitaries $n = \frac{V(SU(N))}{V(\epsilon)}$ is then given by:

$$n \sim \left(\frac{N}{\epsilon^2}\right)^{\frac{N^2}{2}} \rightarrow \log n = K\frac{4^K}{2}\log 2 + 4^K \log\left(\frac{1}{\epsilon}\right). \tag{1.101}$$

We now introduce K-local, all-to-all circuits. A K-local circuit involves up to K qubits at once.

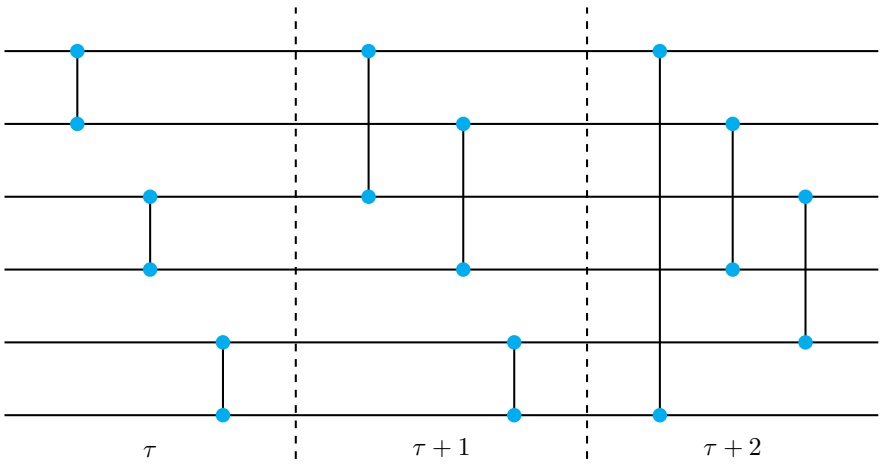

Figure 1.4: Standard architecture for a K-local all-to-all circuit. The first depth is labeled with the circuit time τ, and the time increases by one unit with each subsequent depth

All-to-all connectivity means that any qubit can pair with any other qubit. The Figure 1.4 shows the standard architecture of a K-local all-to-all circuit with 6 qubits and $K = 2$.

Let's now discuss a circuit graph, which is a graph describing a circuit. For the illustration, we assume elementary gates acting on two qubits, with $\frac{K}{2}$ gates operating at a particular depth. The total number of ways to construct $\frac{K}{2}$ pairs from K qubits is given by:

$$d = \frac{K!}{2^{\frac{K}{2}}\left(\frac{K}{2}!\right)} \sim K^{\frac{K}{2}}\,. \tag{1.102}$$

Therefore, there are d possible circuits/configurations at each depth, each corresponding to a unitary operator in $SU(2^K)$ space. This suggests that each depth may yield one of these d unitary

operators. For the visualisation, the decision-tree is embedded in $SU(2^K)$ space, as shown in Figure 1.5. The Figure 1.5a illustrates a depth one tree with a central vertex representing the identity operator I. Eight branches emerge from this vertex, each corresponding to one of $d = 8$ circuit configuration choices. Each leaf of the tree represents a unitary operator. By adding another depth, we obtain the embedded graph shown in Figure 1.5b , where each vertex and leaf represents a unitary operator. At the second depth, we consider only $(d-1)$ circuit configurations, as discussed in [76]. For large K, this approximation does not significantly impact the results but simplifies the technical details.

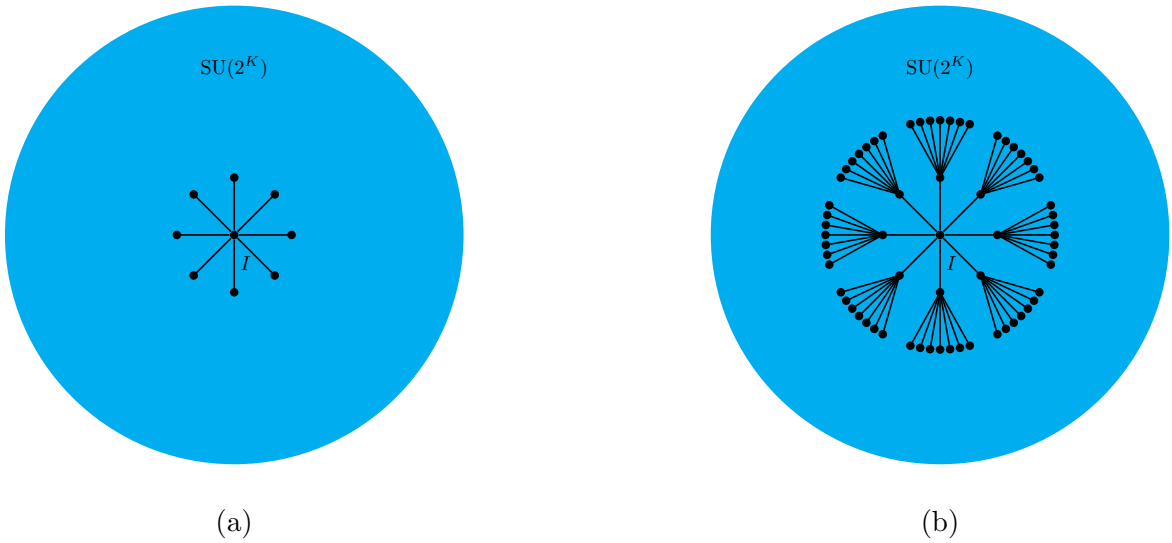

(a) (b)

Figure 1.5: Tree graph with $d = 8$ and depth $D = 1$. Right panel: Tree graph with $d = 8$ and depth $D = 2$.

The circuit time, denoted by τ, increases as the circuit depth D increases, expressed as $\tau \propto D$. The rate of complexity with respect to circuit time τ is given by:

$$\frac{d\mathcal{C}}{d\tau} = \frac{K}{2} \,. \tag{1.103}$$

This shows the linear growth of the circuit complexity $\mathcal{C}$ with respect to circuit time τ. The total complexity at depth D is $\mathcal{C} = \frac{KD}{2}$, and the number of unitaries at depth D is:

$$\mathcal{N} = d^D \sim K^{\frac{KD}{2}} \,. \tag{1.104}$$

According to the no-collision theorem, different circuits at each depth generate distinct unitary operators, meaning two circuits do not produce the same operator. However, collisions may occur after the system reaches the maximum complexity, $\mathcal{C}_{\text{max}}$. The total number of unitaries $\mathcal{N}_{\text{total}}$ corresponds to this maximum complexity, implying $\mathcal{N}_{\text{total}} \sim K^{\mathcal{C}_{\text{max}}}$. Using equation (1.101), the maximum complexity evaluates to $\mathcal{C}_{\text{max}} \sim 4^K$. After reaching maximum complexity, loops may form. See [76] for further details.

1.3.6 Holographic complexity

It is well known that the black hole interior grows with time, while the entanglement entropy saturates after thermalization. This naturally raises the question: which boundary quantity represents the growth of the black hole interior? Susskind provided an answer in [25], suggesting that complexity is the boundary dual representing this growth. We review Susskind's arguments on how complexity captures the black hole interior's growth and various conjectures about holographic complexity.

The black hole interior growth

Consider an eternal AdS black hole geometry, which is dual to the Thermo Field Double (TFD) state. In this context, the maximum volume spatial slice connecting the two asymptotic boundaries is diffeomorphism invariant (coordinate-independent). This spatial slice Σ_t is a codimension-one surface that represents the growth of the black hole interior as follows:

$$\frac{dV}{dt} \sim A_H T \, l_{ads} \,, \tag{1.105}$$

where t denotes the anchoring time, A_H represents the horizon area of the black hole , T is the temperature, and l_{ads} is AdS length scale. The maximal slice Σ_t represents the Einstein-Rosen bridge connecting the two boundaries at anchoring time t as illustrated in Figure 1.6 with $t_L = t_R = t$.

We define a dimensionless quantity as follows:

$$C = \frac{V(\Sigma_t)}{G_N \, l_{ads}} \,, \tag{1.106}$$

where $V(\Sigma_t)$ is the volume of the maximal spatial slice Σ_t, and G_N is the Newton's constant. The growth of C with respect to time t is given by:

$$\frac{dC}{dt} \sim S \, T \,. \tag{1.107}$$

where S is the entropy and T is the temperature of the black hole. The Rindler time τ is related to t as $\tau = 2\pi \, T \, t$, the growth of C with respect to the Rindler time τ is:

$$\frac{dC}{d\tau} \sim S \,. \tag{1.108}$$

The black hole-quantum circuit correspondence

To describe a black hole in terms of a qubit system, the first question is: how many qubits are required? The answer is simple: a minimum of S qubits, where S represents the black hole's entropy.

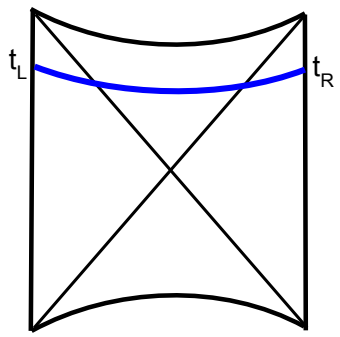

Figure 1.6: Illustration of the maximal spatial slice (blue), anchored at times t_L and t_R on the left and right boundaries, respectively, in an eternal AdS black hole

Thus, the number of qubits K can be identified with the entropy, i.e., $K \sim S$. In this context, a K-local all-to-all quantum circuit corresponds to a K-local Hamiltonian[2]. This means that any qubit in the system can interact with any other qubit at any given time. This behaviour is consistent with the black hole's scrambling properties, where information becomes rapidly distributed across the system. To complete the analogy, we need a dimensionless time parameter in the black hole's geometry that corresponds to the circuit time. In the context of black holes, the Rindler time τ serves as this dimensionless parameter, as discussed in detail in Appendix 6.2. Therefore, we identify the circuit time τ with the Rindler time τ. The correspondence between the quantum circuit and the black hole can be summarized as follows:

$$\begin{array}{lcl} \text{Number of qubits } K & \leftrightarrow & \text{Black hole entropy } S \\ K\text{-local circuit} & \leftrightarrow & K\text{-local Hamiltonian} \\ \text{Circuit time } \tau & \leftrightarrow & \text{Rindler time } \tau \end{array} \tag{1.109}$$

[2] A K-local Hamiltonian refers to a quantum Hamiltonian that consists of a sum of terms, each of which involves interactions between at most K qubits. The "K-local" property indicates that the interactions described by each term are limited to subsets of at most K qubits. This terminology arises because the interaction is limited to smaller subsets of qubits, and the interactions are "localized" within these subsets, as opposed to acting globally on the entire system. Formally, a K-local Hamiltonian can be written as

$$H = \sum_{i_1<i_2<\cdots<i_K} H_{i_1 i_2 \ldots i_K},$$

where each $H_{i_1 i_2 \ldots i_K}$ represents an interaction term acting on the subset of qubits $i_1, i_2, \ldots, i_K$.

Complexity representing black hole interior growth

Applying the black hole-quantum circuit correspondence (1.109) to the black hole, we find that the quantity C appearing in (1.108) corresponds to the circuit complexity $\mathcal{C}$ appearing in eq. (1.103). Additionally, eq.(1.106) defines the holographic complexity according to complexity=volume proposal. The complexity $\mathcal{C}$ represents the circuit complexity of the boundary state Σ_{CFT} with $\Sigma_{CFT} = \partial\Sigma_t$.

Classically, the Einstein-Rosen bridge grows indefinitely, as described by Eq. (1.105). However, quantum mechanics imposes a bound on this growth. Consider the equal-time two-point correlation between the left and right CFTs living on the boundaries, expressed in terms of the wormhole length $L(t)$ as follows:

$$\langle \phi_L \phi_R \rangle = e^{-\frac{L(t)}{l_{AdS}}} , \tag{1.110}$$

where ϕ_L and ϕ_R are operators associated with the left and right CFTs, respectively. As the Einstein-Rosen bridge (wormhole) grows, the wormhole length $L(t)$ increases, leading to a decrease in the correlation between the left and right CFTs. This decrease corresponds to a linear growth in the complexity. When the correlation between the CFTs approaches zero, the complexity saturates. This occurs at a time on the order of $t \sim e^S$, at which point all elementary gates have been used to construct a new state. At this time, the wormhole has stretched to its maximal length, and further evolution results in small fluctuations around this maximum. It is important to note that the saturation of the wormhole length ultimately arises from the finite nature of black hole entropy, a quantum effect. This contrasts with classical entropy S, which is theoretically infinite. Consequently, the finiteness of black hole entropy is the underlying reason for the saturation of complexity.

Moreover, according to the quantum recurrence theorem[3], the system's state is quasi-periodic. After a doubly exponential time $t \sim exp(expS)$, the system will return to a state that is nearly identical to its initial configuration.

Holographic complexity: conjectures

Several proposals aim to define complexity holographically, prominent conjectures include complexity=volume (CV), complexity=action (CA), complexity=spacetime volume (CV2.0), and complexity=anything. Complexity=volume conjecture embrace the formula for the complexity of the dual quantum state, which is given by

$$\mathcal{C}_V \sim \frac{V(\Sigma_t)}{G_N R} , \tag{1.111}$$

where Σ_t is the codimension-one maximal surface in the bulk with the property: $\partial\Sigma_t = \Sigma_{CFT}$, where Σ_{CFT} represents the boundary time slice and $V(\Sigma_t)$ represents the volume of the surface

[3]The Quantum Recurrence Theorem states that for a finite quantum system evolving under unitary time evolution, the system returns arbitrarily close to its initial state after a long time.

Σ_t. Here G_N is Newton's constant, and R is AdS curvature radius. For eternal black hole dual to thermo field double state, holographic complexity is proportional to the spatial volume of the Einstein-Rosen bridge connecting the two boundaries. Figure 1.6 illustrates the maximal spatial surface Σ_t, anchored at the two boundaries, with $t_L = t_R = t$.

Let's now explore the original motivation for the complexity=action (CA) proposal. The complexity obtained using the volume proposal can be rewritten as:

$$\mathcal{C} \sim \frac{V(t_L, t_R)R}{G_N R^2}\,, \tag{1.112}$$

where t_L and t_R represents anchoring time slices of the wormhole at the left and right boundaries, respectively. To obtain this expression, we multiply both the numerator and denominator of the complexity=volume conjecture by the AdS curvature scale R. At late times, the spatial volume of the Einstein-Rosen bridge can be approximated as $V(\Sigma_t) \sim GS\,(t_R + t_L)$, where GS represents the cross-sectional area of the wormhole. Hence, the world volume of the wormhole can be approximated as $|\mathcal{W}| \sim GS\,(t_R + t_L)\,R$, where the AdS curvature scale R represents the time duration. This world volume can be interpreted as a tube of length $(t_L + t_R)$. By combining this approximation with the expression for complexity, we obtain:

$$\mathcal{C} \sim \frac{|\mathcal{W}|}{G_N R^2}\,. \tag{1.113}$$

Since $\frac{1}{R^2}$ is proportional to the cosmological constant Λ, this expression suggests that complexity corresponds to a gravitational action in the presence of a negative cosmological constant. This observation motivates the complexity=action proposal.

The Complexity=action proposal postulates that holographic complexity is defined as the on-shell gravitational action evaluated on the Wheeler-DeWitt patch (WDW), divided by $\pi\hbar$, expressed as

$$\mathcal{C}_A = \frac{I_{\mathcal{W}}}{\pi\hbar}\,, \tag{1.114}$$

where $I_{\mathcal{W}}$ represents the on-shell gravitational action evaluated on the WDW patch. This patch is bounded by the null rays emerging from the boundaries as illustrated in Figure 1.7 and is the union of all space-like surfaces anchored at the boundary time slice Σ_{CFT}. Unlike the complexity=volume proposal, which selects a single space-like surface, the complexity=action proposal requires the action to be evaluated on the entire WDW patch, encapsulating all space-like surfaces anchored at Σ_{CFT}.

Consider a D-dimensional AdS black hole metric given by:

$$ds^2 = -f(r)dt^2 + \frac{dr^2}{f(r)} + r^2 d\Omega^2_{D-2}\,, \tag{1.115}$$

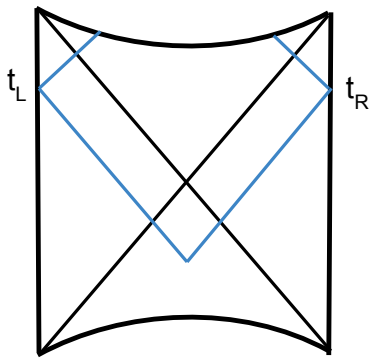

Figure 1.7: Illustration of Wheeler-DeWitt patch enclosed by null rays (blue) , anchored at times t_L and t_R on the left and right boundaries, respectively, in an eternal AdS black hole

where $d\Omega_{D-2}^2$ represents the metric on a $(D-2)$-dimensional unit sphere and the blackening function $f(r)$ reads as:

$$f(r) = 1 - \frac{16\pi G_D M}{(D-2)\Omega_{D-2} r^{D-3}} + \frac{r^2}{L^2}\,, \tag{1.116}$$

with Ω_{D-2} denoting the volume of $(D-2)$-dimensional unit sphere.

The Gravitational action for the eternal AdS black hole geometry is given by:

$$S_{\text{grav}} = \frac{1}{16\pi G_D}\left[\int_{\mathcal{M}} d^D x\,\sqrt{-g}\,(R - 2\Lambda) + 2\int_{\partial\mathcal{M}} d^{D-1}x\,\sqrt{-h}\,K\right], \tag{1.117}$$

where the first term represents the bulk Einstein-Hilbert action, and the second term is the Gibbons-Hawking-York boundary term. For a charged black hole, the geometry is described by the Reissner-Nordström-AdS metric, and an additional term, Maxwell's action, contributes to the gravitational action:

$$S_{\text{Maxwell}} = -\frac{1}{4}\int_{\mathcal{M}} d^D x\,\sqrt{-g}\,F_{\mu\nu}F^{\mu\nu}\,. \tag{1.118}$$

The WDW patch is anchored at the boundaries with $t_L = t_R = t$, computing the gravitation action (1.117) on this patch leads to:

$$\frac{d\mathcal{I}_{\mathcal{W}}}{dt} = 2M \qquad \rightarrow \qquad \frac{d\mathcal{C}_A}{dt} = \frac{2M}{\pi\hbar}\,. \tag{1.119}$$

This expression for the complexity $\mathcal{C}_A$ holds for an uncharged AdS black hole of any size. However, for a charged black hole, the action complexity is bounded by this value. The result (1.119) reflects the expected linear growth of complexity, consistent with the linear growth of the wormhole in the AdS black hole geometry.

The Complexity= spacetime volume (CV2.0) proposal suggests that the holographic complexity is defined as the volume of Wheeler-DeWitt (WDW) patch divided by $G_N R^2$, represented as $C_{SV} = \frac{V_{\mathcal{W}}}{G_N R^2}$.

Complexity involves inherent ambiguities stemming from the choice of a reference state and the set of unitary gates used to prepare a target state. [30, 31] highlight that these ambiguities are expected to manifest in the gravitational bulk as well. The authors argue that there is an infinite class of gravitational observables in AdS black hole geometry that exhibit universal features: linear growth with time at late times and switchback effect, making them plausible candidates for defining holographic complexity. These gravitational observables are defined in a diffeomorphism-invariant manner and may be associated with either codimension-zero or codimension-one regions. This approach to defining holographic complexity is known as the complexity=anything proposal. A number of studies have explored this proposal in detail [80, 81, 82, 83, 84, 85, 86, 87, 88, 89].

The codimension-one observables [30] are defined as:

$$O_{F_1,\Sigma_{F_2}} = \frac{1}{G_N R} \int_{\Sigma_{F_2}} d^d\sigma \sqrt{h}\, F_1(g_{\mu\nu}; X^\mu)\,, \tag{1.120}$$

where F_1 and F_2 are scalar functions of the metric $g_{\mu\nu}$ and the embedding coordinates $X^\mu(\sigma^a)$. Here, σ^a denotes the intrinsic coordinates on a codimension-one hypersurface, and h is the determinant of the induced metric h_{ab} on this hypersurface. The integral is evaluated over the codimension-one hypersurface Σ_{F_2}, which is determined by extremizing the generalized volume functional:

$$V_{gen} = \int d^d\sigma \sqrt{h}\, F_2(g_{\mu\nu}; X^\mu)\,, \tag{1.121}$$

with the condition that the extremal hypersurface anchors at the boundary time slice Σ_{CFT}, meaning $\partial\Sigma_{F_2} = \Sigma_{CFT}$. For $F_1 = F_2 = F$, the gravitational observables are referred to as generalized complexity ([30]):

$$C_{gen} = \frac{1}{G_N R} \int_{\Sigma_F} d^d\sigma \sqrt{h}\, F(g_{\mu\nu}; X^\mu)\,. \tag{1.122}$$

Generalized complexity extends the CV proposal, where setting $F = 1$ reduces to the holographic complexity defined in the CV proposal.

In the context of the thermofield double (TFD) state dual to an eternal black hole, the observables $O_{F_1,\Sigma_{F_2}}$ exhibit two universal characteristics:

1. Linear growth at late times: As time progresses towards infinity, these observables grow linearly:
$$\lim_{t\to\infty} O_{F_1,\Sigma_{F_2}}(t) \propto t\,. \tag{1.123}$$
2. Switchback effect: These observables also exhibit a universal time delay in response to perturbations or shockwaves. This phenomenon, known as the switchback effect, has been identified

in studies of holographic complexity, where a characteristic delay in the growth of complexity is observed following a perturbation.

These properties make $O_{F_1,\Sigma_{F_2}}$ (defined by 1.120) plausible candidates for holographic complexity.

Chapter 2

Cosmologies, singularities and quantum extremal surfaces

Recent years have witnessed significant progress on the black hole information paradox [14, 15, 16, 90, 91]. These advancements rely on the island prescription, embracing the study of entanglement and quantum extremal surfaces. Several papers have appeared on various aspects of these issues, as reviewed in, e.g., [92, 93, 94, 95]. Quantum extremal surfaces are the extrema of the generalized entropy [45, 46], obtained by incorporating the bulk entanglement entropy of matter and the classical area of the entangling RT/HRT surface [17, 42, 96, 97]. These developments have led to various new insights on black holes. Explicit calculations can be performed in effective two-dimensional models, where the bulk entanglement entropy is studied through two-dimensional CFT techniques.

It is interesting to ask whether quantum extremal surfaces might be used to probe cosmological singularities—whether of the Big-Crunch or Big-Bang type. While the vicinity of the singularity is expected to be dominated by severe stringy or quantum gravity effects, one may hope to gain some insight into how these extremal surfaces probe such singularities. [43] examines aspects of entanglement and quantum extremal surfaces (QES) in various families of holographic spacetimes that exhibit cosmological singularities. Some interesting recent work on QES and cosmologies appears in [98]–[127].

The investigations in [43] focused on various Big-Crunch singularities, in particular the isotropic AdS Kasner spacetime. These spacetimes lack horizons and significant entropy, distinguishing them from black hole horizons. Moreover, the authors consider closed universes that are not entangled with any external regions (e.g., other universes). One of the objectives here is to understand how quantum extremal surfaces probe such spacetime singularities in closed universes that do not possess horizons or external entanglement. The time-dependence implies that the classical extremal RT/HRT surface dips into the bulk radial and as well as time directions. Explicitly analysing the extremization equations in the semiclassical region far from the singularity can be carried out in detail: we find the surface bends in the direction away from the singularity. In the 2-dim cosmologies

[113] obtained by dimensional reduction of these and other singularities, quantum extremal surfaces can be studied by extremizing the generalized entropy, with the bulk matter taken to be in the ground state (which is reasonable in the semiclassical region far from the singularity). The resulting extremization shows the quantum extremal surfaces to always be driven to the semiclassical region far from the singularity. In sec. 1.2.7, we reviewed the analysis in [43]. The 2-dim dilaton gravity theories in these cases are somewhat more complicated than Jackiw-Teitelboim gravity and are not "near JT" in essential ways. The cosmological solutions here are sourced by an extra scalar which descends from the scalar in the higher dimensional theory. These theories capture a subset of the observables of the higher dimensional theory and so are best regarded as models of "effective holography" [112], UV-incomplete in totality but adequate for capturing various aspects including entanglement. Since the quantum extremal surfaces are driven to the semiclassical region far from the singularity, the approximation of using the 2-dimensional theory is consistent and the other higher dimensional modes do not make any significant contribution.

This chapter is based on [127] and builds upon the investigations of [43]. We further develop these studies by analyzing quantum extremal surfaces (QES), with a particular focus on those that remain spacelike-separated from the observer's location whenever possible. We begin with a detailed analysis of QES in AdS Kasner cosmologies (Section 2.2), introducing a spatial regulator. This approach allows us to relate the temporal positions of the observer on the holographic boundary and the QES to the bulk matter central charge and the regulator. In the semiclassical regime, our analysis reveals that the quantum extremal surface lags behind the observer (in the direction away from the singularity). A potential island-like region, upon analysing in detail near the island boundary, turns out to be inconsistent. We then generalize our investigation to include other singularities with holographic interpretations, which exhibit similar behavior. In Section 2.3, we analyze certain families of null Kasner Big-Crunch singularities. These display a form of "holomorphy" due to special properties of null backgrounds, and they also differ in the behavior of the QES, which can now reach the singularity (although the generalized entropy remains singular).

2.1 Review of quantum extremal surfaces in AdS Kasner cosmologies

Various families of cosmologies with Big-crunch singularities and their dimensional reduction have been studied in [113]. Consider the higher dimensional space and its reduction ansatz as:

$$ds_D^2 = g^{(2)}_{\mu\nu} dx^\mu dx^\nu + \phi^{\frac{2}{d}}\, d\sigma_d^2 \quad , \quad g_{\mu\nu} = \phi^{\frac{d-1}{d}} g^{(2)}_{\mu\nu} \quad , \quad D = d+2\,. \tag{2.1}$$

d is the number of the transverse dimensions. The two dimensional action after the Weyl transformation, is given by:

$$S = \frac{1}{16\pi G_2} \int d^2x\sqrt{-g}\left(\phi R - U(\phi,\psi) - \frac{1}{2}\phi(\partial\psi)^2\right)\,. \tag{2.2}$$

The dilaton potential $U(\phi,\psi)$ is the function of the dialton field ϕ and an extra scalar field ψ. The scalar field ψ controls the gauge coupling as $g_{YM}^2 = e^{\psi}$. The power-law scaling ansatz for the two-dimensional fields and the corresponding higher-dimensional spacetimes can be expressed as:

$$\phi = t^k r^m, \quad e^f = t^a r^b, \quad e^{\Psi} = t^{\alpha} r^{\beta} \quad \rightarrow \quad ds_D^2 = \frac{e^f}{\phi^{(d_i-1)/d_i}}\big(-dt^2+dr^2\big) + \phi^{2/d_i} dx_i^2 \,. \tag{2.3}$$

The solution of the two-dimensional dilaton gravity theory described in [113] (see Eq. 2.2) is given by:

$$\begin{aligned} ds_{d+2}^2 &= \frac{R^2}{r^2}\left(-dt^2+dr^2\right) + \frac{t^{\frac{2}{d}}R^2}{r^2}\, dx_i^2 \,, \\ \phi &= \frac{tR^d}{r^d} \quad , \quad ds^2 = \frac{t^{\frac{d-1}{d}}R^{d+1}}{r^{d+1}}(-dt^2+dr^2) \quad , \quad e^{\psi} = t^{\sqrt{\frac{2(d-1)}{d}}} \,. \end{aligned} \tag{2.4}$$

R is the AdS length scale. Consider a scenario where the bulk matter is described by a conformal field theory (CFT_2) in its ground state. This is a reasonable assumption far from the singularity at $t = 0$ in the semi-classical regime. Additionally, we assume that the quantum extremal surface lies on the same time slice as the observer, i.e., $t = t_0$. The generalized entropy is then derived using Eqs. (1.69) and (2.4), expressed as:

$$S_{gen} = \frac{\phi_r}{4G}\frac{tR^d}{r^d} + \frac{c}{12}\log\left(\frac{t^{\frac{(d-1)}{d}}}{r^{d-1}}\right) = \frac{\phi_r}{4G}\,\phi + \frac{c}{12}\,\frac{d-1}{d}\log(\phi)\,. \tag{2.5}$$

The extremization equations are given by:

$$\begin{aligned} \partial_r S_{gen} &= -\left[\frac{\phi_r}{4G}\frac{dtR^d}{r^{d+1}} + \frac{c}{12}\frac{(d-1)}{r}\right] = 0\,, \\ \partial_t S_{gen} &= \quad \frac{\phi_r}{4G}\frac{R^d}{r^d} + \frac{c}{12}\frac{(d-1)}{dt} = 0\,. \end{aligned} \tag{2.6}$$

We observe that both terms in the extremization equations have the same sign for $c > 0$ and $d > 1$. Therefore, each term must individually equal zero in both extremization equations. This leads to the quantum extremal surface (QES) solution [43], denoted as (r_*, t_*), given by:

$$t_* = t_0 \quad , \quad r \equiv r_* \to \infty \quad , \quad t \equiv t_* \to \infty \quad , \quad t_* \le r_* \,. \tag{2.7}$$

This suggests that the quantum extremal surface (QES) is driven to the semi-classical region, away from the singularity at $t = 0$. Consequently, island solutions are absent in AdS Kasner cosmologies under the assumption $t = t_0$.

2.2 *AdS* Kasner, quantum extremal surfaces, regulated

We study various two-dimensional backgrounds characterized by the dilaton and the two-dimensional metric , analyzing quantum extremal surfaces obtained from extremizing the generalized entropy (1.69):

$$S_{gen} = \frac{\phi}{4G} + \frac{c}{12}\log\Big(\Delta^2 e^f|_{(t,r)}\Big), \qquad \Delta^2 = r^2 - (t-t_0)^2. \tag{2.8}$$

The extremization equations, retaining only the relevant terms, are given by:

$$\frac{\partial_r\phi}{4G}+\frac{c}{6}\frac{r}{\Delta^2}+\frac{c}{12}\partial_r f=0\,,\ \frac{\partial_t\phi}{4G}-\frac{c}{6}\frac{t-t_0}{\Delta^2}+\frac{c}{12}\partial_t f=0\,. \tag{2.9}$$

We seek to understand the dependence of the quantum extremal surface (t_*, r_*) on the observer's location $(t_0, r_0) \equiv (t_0, 0)$. Specifically, we focus on an observer at the holographic boundary. Our analysis considers the AdS Kasner case, where we explicitly restore the AdS scale and the Kasner scale from (2.4) to ensure that length scales remain manifest. The dilaton and two-dimensional metric then take the form:

$$\phi=\frac{t/t_K}{(r/R)^{d_i}}\,,\qquad ds^2=\frac{(t/t_K)^{(d_i-1)/d_i}}{(r/R)^{d_i+1}}(-dt^2+dr^2)\ . \tag{2.10}$$

Towards understanding quantum extremal surfaces, let us study (2.8) with the scales put in explicitly as in (2.10). If we assume $t = t_0$, we obtain (2.6), (2.7), which are structurally similar to the AdS case (1.76). We will instead attempt solving for t as a function of t_0. Then the extremization equations are (introducing ϕ_r as bookkeeping for now)

$$\frac{c}{6}\frac{r}{\Delta^2}=\frac{\phi_r}{4G}\frac{d_i\,t/t_K}{r^{d_i+1}/R^{d_i}}+\frac{c}{12}\frac{d_i+1}{r}\,,\qquad \frac{c}{6}\frac{t-t_0}{\Delta^2}=\frac{\phi_r}{4G}\frac{1/t_K}{r^{d_i}/R^{d_i}}+\frac{c}{12}\frac{d_i-1}{d_i\,t}\ . \tag{2.11}$$

Note that each term now has dimensions of inverse length manifestly. In the parametrization of these cosmologies (2.4), the singularity is at $t = 0$: regarding this as a Big-Crunch, we take the time coordinate t to represent $|t|$ so that $t > 0$ in our entire discussion.

We require that the QES is spacelike-separated from the observer, consistent with the interpretation of these extremal surfaces as holographic entanglement. This implies

$$\Delta^2>0\quad\Rightarrow\quad t_*>t_0\ ,\qquad\qquad [\Delta^2=r^2-(\Delta t)^2] \tag{2.12}$$

from the t-equation in (2.11). This means that the QES always lags behind the observer, in the direction away from the singularity ($t = 0$).

Let us now look in more detail at QES solutions near the semiclassical solution (2.7), where $\Delta t \sim 0$ and $r, t \to \infty$. Let us first rewrite the r-extremization equation in (2.11) as

$$\frac{3\phi_r}{Gc}\frac{d_i\,t/t_K}{r^{d_i+1}/R^{d_i}}+\Big(\frac{d_i+1}{r}-\frac{2r}{\Delta^2}\Big)=\frac{3\phi_r}{Gc}\frac{d_i\,t/t_K}{r^{d_i+1}/R^{d_i}}+\frac{d_i+1}{r}\Big(\frac{\frac{d_i-1}{d_i+1}r^2-(\Delta t)^2}{r^2-(\Delta t)^2}\Big)=0 \tag{2.13}$$

As long as Δt is small, *i.e.* $\Delta^2 \sim r^2$, the second term is positive: thus both terms are positive, the only solution to this being $r \equiv r_* \to \infty$. This is very similar to the time-independent AdS case in (1.76), giving the entire Poincare wedge as the entanglement wedge: there are no islands.

Analysing the t-extremization equation is rendered tricky with $r_* \to \infty$ strictly. Towards obtaining insight into the t_0 dependence of t_*, let us regulate as $r_* = R_c \sim \infty$ with some large but finite spatial cutoff R_c that represents the boundary of the entanglement wedge. Then the t-equation in (2.11) becomes

$$\frac{\Delta t}{R_c^2-(\Delta t)^2}=\frac{1}{2K_c}+\frac{d_i-1}{2d_i\,t}\ ,\qquad\qquad \frac{1}{K_c}=\frac{3\phi_r}{Gc}\frac{1/t_K}{R_c^{d_i}/R^{d_i}}\ . \tag{2.14}$$

This expression is manifestly satisfied semiclassically as in (2.7). Taking these regulated equations as containing finite terms we can solve for t_* : with $\Delta t \ll R_c$, we obtain the approximate regulated expression

$$\frac{\Delta t}{R_c^2} \sim \frac{1}{2K_c} + \frac{d_i - 1}{2d_i\, t_0} \ , \qquad \Delta t = t_* - t_0 \ , \tag{2.15}$$

where we have approximated $\Delta^2 \sim R_c^2$ and set $t \sim t_0$ in the last expression (with t_0 large, as in (2.7)). We see that the QES (2.15) lags behind the observer, in the direction away from the singularity. We now see that as t_0 decreases, Δt increases, *i.e.* the lag of the QES is increasing: see the top part of Figure 2.1 for a heuristic depiction (the lag is exaggerated!).

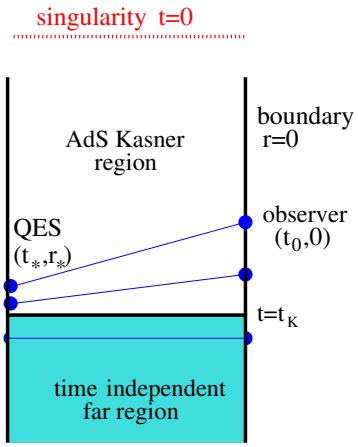

Figure 2.1: Cartoon of the 2-dim *AdS* Kasner geometry (singularity at $t = 0$), the holographic boundary at $r = 0$ and the QES at (t_*, r_*), with a time-independent *AdS* space appended for $t > t_K$. The boundary observer $(t_0, 0)$ moves in time from the time-independent region to the *AdS* Kasner region. The QES lags behind in time, *i.e.* $t_* > t_0$, when t_0 is in the Kasner region.

The on-shell generalized entropy (2.8) in the semiclassical regime where $\Delta^2 \sim R_c^2$ becomes

$$S_{gen}^{o.s.} \sim \frac{\phi_r}{4G} \frac{t_*/t_K}{(R_c/R)^{d_i}} + \frac{c}{12} \log \left(\frac{R_c^2}{\epsilon_{UV}^2} \frac{(t_*/t_K)^{(d_i-1)/d_i}}{(R_c/R)^{d_i+1}} \right) \ , \tag{2.16}$$

with t_* in (2.15). Since $t_* \gtrsim t_0$ and R_c is large, $S_{gen}^{o.s.}$ is not dramatically different structurally from the *AdS* value (1.76), without the t_*/t_K factors. In more detail, we see that the on-shell *AdS* expression (1.76) with $r_* = R_c$ and $\phi|_{r_*} = \phi_*$ becomes $S^{o.s.} = \frac{\phi_*}{4G} + \frac{c}{12} \log \left(\frac{R^2}{\epsilon_{UV}^2} \left(\frac{\phi_*}{\phi_r} \right)^{(d_i-1)/d_i} \right)$ so the log vanishes when its argument becomes $O(1)$, *i.e.* when ϕ_* is sufficiently small. At this point, $S^{o.s.} \sim \frac{\phi_*}{4G} \sim 0$, in accord with the physical expectation that the *AdS* ground state has zero entropy. In this sense the spatial regulator R_c has physical meaning as the effective physical boundary of the entanglement wedge, where ϕ_* becomes small enough to be comparable with $(\frac{\epsilon_{UV}}{R})^{\#}$. Note that we can recast $S^{o.s.}$ as (1.77) exactly setting $\frac{1}{\phi_r^{(d_i-1)/d_i}} \frac{R^2}{\epsilon_{UV}^2} \sim 1$ thus fixing ϕ_r, which can possibly be regarded as renormalizing $\frac{\phi_r}{G} \equiv \frac{1}{G_r}$ (and rendering S_{gen} finite). The above expression (2.16) is similar when the t_*/t_K factors are $O(1)$ so the above arguments apply, and the overall entropy is not appreciable.

As a further check, note that this QES solution vindicates the maximin property[1].

[1]In the semiclassical regime, the second derivatives $\partial_t^2 S_{gen}|_* \sim -\frac{c}{12} \frac{d_i - 1}{d_i\, t_*^2} - \frac{c}{6} \frac{1}{\Delta_*^2} - \frac{c}{3} \frac{(t_* - t_0)^2}{\Delta_*^4} < 0$ and

Naively it appears that $\frac{\Delta t}{R_c^2} \sim \frac{1}{t_0}$ shows a growth as t_0 decreases. Rewriting (2.14) and solving as a quadratic, taking $\Delta t > 0$, gives

$$\frac{\Delta t}{R_c} = \frac{1}{R_c}\left(\sqrt{\frac{1}{(\frac{1}{K_c}+\frac{d_i-1}{d_i\, t})^2}+R_c^2} \;-\; \frac{1}{\frac{1}{K_c}+\frac{d_i-1}{d_i\, t}}\right) , \tag{2.17}$$

showing a slow growth in Δt as t decreases, for fixed regulator R_c. Extrapolating and setting $t_0 = 0$ shows that $t = 0$ is not a solution (this can also be seen in (2.11)).

We consider our analysis to be most valid within the semiclassical regime, far from the singularity, where bulk matter is approximated to be in its ground state. Nevertheless, the qualitative behavior of the quantum extremal surfaces and the associated entanglement wedge—excluding the near-singularity region (schematically depicted in the top AdS Kasner part of Figure 2.1)—may persist as a reliable result even with improved near-singularity bulk entropy models.

We observe that the semiclassical generalized entropy, (2.16), decreases over time as the singularity is approached. This behavior is reminiscent of findings in [128, 129], which suggest low complexity in such singularities. Expressing this semiclassical value in the form (1.77), we find that as long as ϕ remains sufficiently large, the bulk entropy term remains subleading to the area term. Consequently, the Bekenstein bound is upheld, preventing the formation of spatially disconnected islands akin to those found in black holes. From a qualitative perspective, one might interpret the excluded near-singularity region as a timelike-separated, island-like domain. Further investigation into this interpretation could provide deeper insights.

2.2.1 Searching for islands

Examining (2.13), we observe that in the regime

$$\frac{d_i-1}{d_i+1} r^2 < (\Delta t)^2 < r^2, \tag{2.18}$$

a spacelike-separated island appears to emerge. This behavior contrasts with the semiclassical region with $\Delta t \ll r$ (where both terms are the same sign), as the numerator in the bracketed term of (2.13) changes sign, leading to a large but finite $r \sim (\frac{\phi_r}{Gc})^{\#}$ solution, indicating a disconnected region. This bears some structural resemblance to the discussion in [125].

To explore this in detail, we rewrite the ∂_r-equation in (2.11) as:

$$\Delta^2 = \frac{2r^2}{d_i+1}\,\frac{1}{1+\frac{d_i}{d_i+1}\frac{t}{K}} , \qquad \frac{1}{K} = \frac{3\phi_r}{Gc}\,\frac{1/t_K}{r^{d_i}/R^{d_i}} , \tag{2.19}$$

so

$$\Delta^2 = r^2 - (\Delta t)^2 \quad \Rightarrow \quad \frac{\Delta t}{r} = \sqrt{\frac{\frac{d_i-1}{d_i+1} \;+\; \frac{d_i}{d_i+1}\frac{t}{K}}{1 \;+\; \frac{d_i}{d_i+1}\frac{t}{K}}} . \tag{2.20}$$

$\partial_r^2 S_{gen}|_* \sim \frac{\phi_r}{4G}\,\frac{d_i\,(d_i+1)\,t_*\,R_i^d}{t_k\,R_c^{d_i+2}} + \frac{c}{12}\,\frac{d_i+1}{R_c^2} + \frac{c}{6}\,\frac{1}{\Delta_*^2}\,(1-\frac{2R_c^2}{\Delta_*^2}) > 0$ confirm time-maximization and spatial minimization, with the regulator R_c finite.

The potential island arises at large finite r in (2.13) when

$$(\Delta t)^2 \gtrsim \frac{d_i - 1}{d_i + 1} r^2 \tag{2.21}$$

so that Δt is not small but in fact scales as r which is large. Expanding (2.20) in the vicinity of (2.21) gives

$$\frac{\Delta t}{r^2} \sim \sqrt{\frac{d_i - 1}{d_i + 1}} \frac{1}{r} \left(1 + \frac{d_i}{d_i^2 - 1} \frac{t}{K} + \dots \right). \tag{2.22}$$

Now the ∂_t-equation (2.11) as an exact quadratic can be solved to obtain (choosing $\Delta t > 0$)

$$\frac{\Delta t}{r} = \sqrt{\frac{\frac{d_i^2}{(d_i-1)^2} \frac{t^2}{r^2}}{(\frac{d_i}{d_i-1}\frac{t}{K} + 1)^2} + 1} \; - \; \frac{\frac{d_i}{d_i-1}\frac{t}{r}}{\frac{d_i}{d_i-1}\frac{t}{K} + 1} \; , \tag{2.23}$$

with K defined in (2.19). For a nontrivial island-like solution, this expression for $\frac{\Delta t}{r}$ must match that in (2.20) in the vicinity of the island boundary (2.21). With $\frac{t}{K} \sim \epsilon$ being small, we expand and obtain at leading order

$$\sqrt{1 + x^2} - x = \sqrt{\frac{d_i - 1}{d_i + 1}} \quad \xrightarrow{solving} \quad x \equiv \frac{d_i}{d_i - 1} \frac{t}{r} = \frac{1}{\sqrt{d_i^2 - 1}} \tag{2.24}$$

This gives

$$\Delta t \gtrsim \sqrt{\frac{d_i - 1}{d_i + 1}} \, r \sim d_i \, t \; . \tag{2.25}$$

The last condition $\Delta t \gtrsim d_i \, t$ is clearly impossible with $\Delta t = t - t_0$ for any $d_i > 1$.

In addition, using the leading term matching condition (2.25) and expanding (2.23) about the potential island boundary (2.21) shows that the first subleading term in $\frac{t}{K}$ is $\frac{1}{d_i}\sqrt{\frac{d_i+1}{d_i-1}}\frac{t}{K}$ which does not match the first subleading term in (2.22).

We have investigated an island-like solution near the potential island boundary (2.21), emerging continuously from the semiclassical region where $r_* \to \infty$, as discussed after (2.13). However, a simultaneous solution to the extremization equations (2.11), rewritten as (2.20) and (2.23), is not achieved near (2.21). Consequently, this potential island solution is inconsistent. One might question whether nontrivial islands exist further towards the singularity (though they may not be physically reliable). Expressing and expanding the extremization equations (2.13) and (2.14) yields two cubic equations in t. However, solving these equations simultaneously (e.g., by eliminating the term t^3) suggests the absence of consistent finite solutions, implying that no islands exist.

Moreover, our current treatment of potential island-like solution is semiclassical, based on a fixed classical background geometry and a quantum field theory in the bulk. In this framework, the generalized entropy includes only the leading-order quantum correction term, S_{bulk}, at $\mathcal{O}(G_N^0)$, and does not account for higher-order quantum gravitational corrections. Nonetheless, the generalized entropy formula encapsulates results—such as the quantum extremal surfaces (QES) and the emergence of island-like regions—at all orders in G_N, provided the background geometry is held

fixed. This approach, while not fully non-perturbative, may be regarded as a semi-non-perturbative framework, as it extends beyond leading-order perturbation theory but still fundamentally relies on the semiclassical description. A genuinely non-perturbative formulation of quantum gravity must incorporate both all-order perturbative corrections in G_N and intrinsically non-perturbative effects, such as those arising from stringy dynamics or gravitational instantons. Establishing a rigorous, fully non-perturbative derivation of island phenomena would require computing the full quantum gravity path integral within a more complete framework—such as string theory. This remains an open problem and is left for future investigation.

2.2.2 Appending a time-independent far region

Let us now consider appending the AdS Kasner space with a time-independent AdS region far from the singularity, joined at the Kasner scale $t = t_K$. See Figure 2.1. Thus, we have AdS Kasner region for $t < t_K$ and a time-independent AdS space for $t > t_K$, i.e.,

$$\begin{aligned} \phi &= \frac{t/t_K}{(r/R)^{d_i}}\,, \qquad ds^2 = \frac{(t/t_K)^{(d_i-1)/d_i}}{(r/R)^{d_i+1}}(-dt^2+dr^2) \qquad [t<t_K]\,, \\ \phi &= \frac{1}{(r/R)^{d_i}}\,, \qquad ds^2 = \frac{1}{(r/R)^{d_i+1}}(-dt^2+dr^2) \qquad [t>t_K]\,. \end{aligned} \tag{2.26}$$

The two regions are continuously joined at $t = t_K$, though the joining is not smooth. The extremization equations must now be analyzed separately as the observer at t_0 moves through each region. Applying the generalized entropy and its extremization (2.8) to the background profiles (2.26) in both regions yields:

$$\begin{aligned} t_0 > t_K: &\quad \frac{c}{6}\frac{r}{\Delta^2} = \frac{\phi_r}{4G}\frac{d_i}{r^{d_i+1}/R^{d_i}} + \frac{c}{12}\frac{d_i+1}{r}\,, \qquad \frac{c}{6}\frac{t-t_0}{\Delta^2} = 0\,; \\ t_0 < t_K: &\quad \frac{c}{6}\frac{r}{\Delta^2} = \frac{\phi_r}{4G}\frac{d_i\,t/t_K}{r^{d_i+1}/R^{d_i}} + \frac{c}{12}\frac{d_i+1}{r}\,, \qquad \frac{c}{6}\frac{t-t_0}{\Delta^2} = \frac{\phi_r}{4G}\frac{1/t_K}{r^{d_i}/R^{d_i}} + \frac{c}{12}\frac{d_i-1}{d_i\,t}\,. \end{aligned} \tag{2.27}$$

In the time-independent region $t > t_K$, it is physically reasonable to set $t_* = t_0$, *i.e.*, the QES lies on the same time slice as the observer. This follows from time-translation invariance in that region, at least for $t_0 \gg t_K$ (sufficiently far from the junction at t_K). Since the joining slice $t = t_K$ lies in the semiclassical region, far from the singularity, it is appropriate to use (2.15) with the regulator to study the QES's time evolution in the Kasner region. The lagging (or repulsive) behavior of the QES thus begins when the observer enters the Kasner region. However, due to the sharp transition at t_K, this lag does not evolve smoothly.

To see this in more detail, consider the time $t_0 = t_K - \delta t_0$ when the observer is just entering the Kasner region: then we expect that the quantum extremal surface is just a little away from the observer time slice t_0. To quantify this, let us compare δt_* in (2.15) with δt_0 (and K_c defined in (2.14)): we have

$$\delta t_0 = t_K - t_0 > 0\,; \qquad \frac{\delta t_*}{R_c^2} = \frac{t_* - t_0}{R_c^2} \sim \frac{1}{2K_c} + \frac{d_i-1}{2d_i\,t_K}\Big(1+\frac{\delta t_0}{t_K}\Big), \tag{2.28}$$

so that for small δt_0 *i.e.* $t_0 \sim t_K$, the quantum extremal surface ends up being pushed to the time-independent region ($t_* > t_K$). Of course as the observer moves in time further, the QES enters the Kasner region as well. To see this further, let us compare the QES location with the Kasner scale: with $t_0 \lesssim t_K$, we have

$$t_* \lesssim t_K \qquad \Rightarrow \qquad \frac{t_K - t_0}{R_c^2} \gtrsim \frac{1}{2K_c} + \frac{d_i - 1}{2d_i\, t_0} \tag{2.29}$$

In other words, the quantum extremal surface is within the Kasner region if the observer is sufficiently further within. The cross-over of the QES to the Kasner region occurs when $t_* \sim t_K$, *i.e.* when the above inequality is saturated (giving $\frac{t_0 - t_K}{R_c^2} \sim -\frac{1}{2K_c} - \frac{d_i - 1}{2d_i t_K}$).

The model (2.26) serves as a simple toy model to gain insight into the evolution of the quantum extremal surface as the observer moves from the time-independent far region into the time-dependent *AdS* Kasner region toward the singularity. The presence of the time-independent far region suggests that the initial state can be prepared as a ground state via a Euclidean continuation. However, placing this on firmer footing is more subtle. A discontinuity arises at the $t = t_K$ slice, likely reflecting that the Kasner time dependence does not simply switch off at t_K. This raises potential concerns regarding smooth time evolution into the Kasner region, particularly in the absence of any external energy-momentum inflow. A more detailed analysis would require a careful examination of the junction conditions governing the transition at t_K. Rather than a sharp time slice at t_K, it may be more physical to consider a thickened spacetime region that interpolates smoothly between the time-independent far region and the Kasner region. In such a scenario, the QES lag would likely evolve more smoothly. We leave these questions for future investigation.

2.2.3 More general 2-dim cosmologies, QES, regulated

In the previous subsections, we examined *AdS*-Kasner cosmologies, their 2-dimensional reductions (2.4), and quantum extremal surfaces. We now extend this analysis to more general 2-dimensional cosmologies:

$$\phi = t^k r^m \quad , \quad e^f = t^a r^b \quad , \quad ds^2_{d+2} = \frac{e^f}{\phi^{\frac{(d-1)}{d}}} \left(-dt^2 + dr^2\right) + \phi^{\frac{2}{d}}\, dx_i^2 \,. \tag{2.30}$$

The corresponding 2-dimensional dilaton and metric fields take the form:

$$\phi = t r^m \,, \quad e^f = t^a r^b \,, \qquad a > 0, \quad m < 0, \quad b < 0 \,. \tag{2.31}$$

Note that we have taken the time exponent of the dilaton in accord with the universality of the near singularity region found in [113]. We take $a > 0$ to simulate a Big-Crunch singularity at $t = 0$. Further we assume $m, b < 0$ in accord with the intuition that the dilaton and the 2-dim metric grow towards the holographic boundary at $r = 0$.

The generalized entropy (2.8) and its extremization with r, t, give

$$\frac{c}{6}\frac{r}{\Delta^2} = \frac{\phi_r}{4G}\frac{|m|t}{r^{|m|+1}} + \frac{c}{12}\frac{|b|}{r} \,, \qquad \frac{c}{6}\frac{t - t_0}{\Delta^2} = \frac{\phi_r}{4G}\frac{1}{r^{|m|}} + \frac{c}{12}\frac{a}{t} \,, \tag{2.32}$$

analogous to (2.11), except that we have suppressed length scales analogous to R, t_K here. Firstly, requiring the spacelike condition $\Delta^2 > 0$ implies $t_* > t_0$, analogous to (2.12): this means the QES lags behind the observer, in the direction away from the singularity at $t = 0$.

As noted already in [43], it is clear that the QES solution to these extremization equations is again of the form (2.7), *i.e.* $r_* \to \infty,\ t_* \sim t_0 \to \infty$ with $t_* \lesssim r_*$. In the vicinity of the semiclassical region, analogous to the AdS Kasner case (2.13) we can recast the r-equation as

$$\frac{3\phi_r}{Gc}\frac{|m|t}{r^{|m|+1}} + \Big(\frac{|b|}{r} - \frac{2r}{\Delta^2}\Big) = \frac{3\phi_r}{Gc}\frac{|m|t}{r^{|m|+1}} + \frac{|b|}{r}\Big(\frac{\frac{|b|-2}{|b|}\,r^2 - (\Delta t)^2}{r^2 - (\Delta t)^2}\Big) = 0\ . \tag{2.33}$$

As in that case, with Δt small, *i.e.* $\Delta^2 \sim r^2$, both terms are positive and the only solution to this is $r_* \to \infty$, giving the entire Poincare wedge as the entanglement wedge: there are no islands. Now, the t-equation becomes

$$\frac{\Delta t}{R_c^2 - (\Delta t)^2} = \frac{3\phi_r}{2Gc}\frac{1/t_K}{R_c^{d_i}/R^{d_i}} + \frac{d_i - 1}{2d_i\, t}\ , \tag{2.34}$$

analogous to (2.14). As before, we are regulating the QES solution as $r_* = R_c \sim \infty$ with some large but finite spatial cutoff R_c representing the boundary of the entanglement wedge. Taking these regulated equations as containing finite terms we can solve for t_*, obtaining an approximate regulated expression analogous to (2.15) after setting $\Delta^2 \sim R_c^2$ and $t \sim t_0$. The resulting semiclassical picture is similar to the discussion in the AdS Kasner case, with the QES lag increasing as t_0 decreases.

Now let us look for island-like solutions in these more general holographic cosmologies, analogous to Sec. 2.2.1. The corresponding island boundary here, analogous to (2.21), is

$$(\Delta t)^2 \gtrsim \frac{|b| - 2}{|b|} r^2\ . \tag{2.35}$$

Analogous to (2.20) and (2.23) in the AdS Kasner case, we obtain, respectively,

$$\Delta^2 = r^2 - (\Delta t)^2 \quad \Rightarrow \quad \frac{\Delta t}{r} = \sqrt{\frac{\frac{|b|-2}{|b|} \ + \ \frac{|m|}{|b|}\frac{t}{K}}{1 \ + \ \frac{|m|}{|b|}\frac{t}{K}}}\ , \qquad \frac{1}{K} = \frac{3\phi_r}{Gc}\frac{1}{r^{|m|}}\ , \tag{2.36}$$

rearranging (2.33), and

$$\frac{\Delta t}{r} = \sqrt{\frac{\frac{1}{a^2}\frac{t^2}{r^2}}{(\frac{1}{a}\frac{t}{K} + 1)^2} + 1} \ - \ \frac{\frac{1}{a}\frac{t}{r}}{\frac{1}{a}\frac{t}{K} + 1}\ , \tag{2.37}$$

from the ∂_t-equation in (2.32) regarded as a quadratic, choosing $\Delta t > 0$.

For a nontrivial island-like solution emerging in the vicinity of (2.35), these two expressions for $\frac{\Delta t}{r}$ must match: expanding, the leading order terms give

$$x \equiv \frac{1}{a}\frac{t}{r}\ : \quad \sqrt{1 + x^2} - x = \sqrt{\frac{|b| - 2}{|b|}} \quad \xrightarrow{solving} \quad \frac{t}{r} = \frac{a}{\sqrt{|b|(|b| - 2)}}\ , \tag{2.38}$$

while matching the first subleading terms requires

$$\frac{1}{a\sqrt{|b|(|b|-2)}}\Big(1-\frac{1}{\sqrt{|b|(|b|-2)+1}}\Big)\,\frac{t}{K}=\frac{|m|/|b|}{\sqrt{|b|(|b|-2)}}\,\frac{t}{K} \tag{2.39}$$

i.e.

$$\frac{a|m|}{|b|}=1-\frac{1}{\sqrt{|b|(|b|-2)+1}} \tag{2.40}$$

For the AdS Kasner values $a=\frac{d_i-1}{d_i}\,,\ m=-d_i\,,\ b=-(d_i+1)$, these agree with the conditions obtained in Sec. 2.2.1, which were not consistent as we saw. The condition (2.38) gives $\Delta t=\frac{|b|-2}{a}t$: this is impossible in the AdS Kasner case (2.25) as we saw. For the hyperscaling violating cosmologies (6.33), this condition can again be shown to be impossible to satisfy (a takes its maximum value for $\gamma=0$). The hyperscaling violating Lifshitz cosmologies in [113] require $a=|b|-2\,,\ m=-1$ (reviewed very briefly after (6.33)). This gives $\Delta t=\frac{|b|-2}{a}t=t\,$, which is satisfied for $t_0=0$, but this is the location of the singularity which is unreliable (the condition (2.40) becomes $\frac{2}{b}=\frac{1}{\sqrt{|b|(|b|-2)+1}}$ giving $b=-2, a=0$). Thus overall, these more general holographic cosmologies appear qualitatively similar to the AdS Kasner case.

The conditions (2.31) on the exponents are motivated by the broader investigations of 2-dimensional cosmologies in [113]. These studies adopt fairly general and minimal assumptions about the effective action governing such cosmological spacetimes, revealing a remarkably rich space of solutions. This includes cosmologies with nonrelativistic asymptotics, such as hyperscaling-violating Lifshitz spacetimes, and various boundary conditions—all of which satisfy the conditions (2.31). However, it would be interesting to further explore this landscape of cosmologies, potentially extending it beyond those that reduce to two dimensions. A broader classification could provide deeper insights into the behavior of quantum extremal surfaces, particularly in relation to the Big-Crunch (or Big-Bang) singularities they may exhibit.

2.3 Null cosmologies and quantum extremal surfaces

In this section, we consider cosmological spacetimes with null time dependence, drawing parallels with the discussions in [22, 115, 116] as well as, for example, [130, 131, 132, 133, 134]. If we further impose that the higher-dimensional spacetime allows for dimensional reduction via (2.1) to two dimensions, the resulting backgrounds take a restricted form:

$$ds^2=-dx^+dx^-\,,\qquad \phi=\phi(x^+)\,,\qquad \Psi=\Psi(x^+)\,,\qquad x^\pm=t\pm r\,. \tag{2.41}$$

Since the two-dimensional metric depends only on x^+, it can always be transformed to a flat form via a coordinate redefinition, provided that ϕ and e^f in the reduction ansatz (2.1) also depend solely on x^+. This leads to the simplified expression above. Consequently, the higher-dimensional spacetime corresponding to (2.30) takes the form:

$$ds^2 = -\phi^{-(d_i-1)/d_i} dx^+ dx^- + \phi^{2/d_i} dy_i^2 \,, \qquad x_i = \{r, y_i\} \,. \tag{2.42}$$

This comprises various higher dimensional backgrounds with null singularities *e.g.*

$$ds^2 = (x^+)^a(-dx^+dx^-) + (x^+)^b dy_i^2 \tag{2.43}$$

which however are somewhat special, given the restriction to the 2-dimensional reduction ansatz (2.1): thus it also does not include the null holographic AdS cosmologies in [22, 115, 132, 133] which are of the form $ds^2 = \frac{R^2}{r^2}[e^{f(x^+)}(-dx^+dx^- + dx_i^2) + dr^2]$. There are qualitative parallels however. The exponents a, b in (2.43) are related by the Einstein equations. These are a bit similar to the null Kasner backgrounds considered in [116], except that the 2-dim restriction implies that $e^f \equiv (x^+)^a$ can be absorbed by redefining the null time variable $x^+ \to X^+ = \int e^f dx^+$. In writing the 2-dim backgrounds (2.41) we have effectively redefined the lightcone variables $x^\pm$ in this manner. These backgrounds are likely supersymmetric.

Now the equations of motion (6.29) simplify tremendously since there is only null-time dependence in the background ansatze (2.41): for instance all nontrivial contractions of the form $g^{\mu\nu}\partial_\mu\Psi\partial_\nu\Psi \sim g^{+-}\partial_+\Psi\partial_-\Psi$ vanish since there is no x^--dependence. We also have $\mathcal{R} = 0$ since the 2-dim space is flat. Thus the equations of motion give

$$\begin{aligned} (++): \qquad & -\partial_+^2\phi - \frac{\phi}{2}(\partial_+\Psi)^2 = 0 \,; \\ (\phi): \quad \frac{\partial U}{\partial\phi} = \mathcal{R} - \frac{1}{2}(\partial\Psi)^2 = 0 \,; \qquad & (\Psi): \quad \frac{\partial U}{\partial\Psi} = \partial_\mu(\phi g^{\mu\nu}\partial_\nu\Psi) = 0 \,. \end{aligned} \tag{2.44}$$

These imply that the dilaton potential is trivial and give a single nontrivial condition from the $(++)$ equation relating ϕ, Ψ. We want to consider a Big-Crunch singularity arising at $x^+ = 0$ as a future null singularity, so we take $x^+ < 0$ in our entire discussion below. Then

$$\begin{aligned} & \phi = (-x^+)^k \,, \quad \Psi = \Psi(x^+) \quad \Rightarrow \quad (\partial_+\Psi)^2 = -2\frac{\partial_+^2\phi}{\phi} = -\frac{2k(k-1)}{(x^+)^2} \,, \\ & \Rightarrow \quad 0 < k \leq 1 \,, \qquad \phi = (-x^+)^k \,, \qquad e^\Psi = (-x^+)^{\pm\sqrt{2k(1-k)}} \,. \end{aligned} \tag{2.45}$$

While $k > 0$ gives vanishing dilaton as $x^+ \to 0$, the exponent of e^Ψ could have either sign. The single ϕ, Ψ-relation allows extrapolating ϕ, Ψ above to asymptotically constant functions *i.e.* flat space. This 2-dim background implies the upstairs background (2.42) with ϕ as above: this is of the form (2.43) with $a = -\frac{k(d_i-1)}{d_i}$ and $b = \frac{2k}{d_i}$. These have $R^i{}_{+i+} = \frac{k(1-k)}{d_i\,(x^+)^2}$ so tidal forces diverge (all curvature invariants vanish due to the null nature of the backgrounds). To see this in more detail, consider a null geodesic congruence propagating along x^+ with cross-section along some y^i-direction: the geodesic equation then gives

$$\frac{dx^+}{d\lambda^2} + \Gamma^+_{++}\Big(\frac{dx^+}{d\lambda}\Big)^2 = 0 \quad \to \quad \lambda = \frac{(x^+)^{a+1}}{a+1} \,, \tag{2.46}$$

where $\Gamma^+_{++} = \frac{a}{x^+}$ is the only nonvanishing Γ^+_{ij} component. Solving this leads to the affine parameter above and the tangent vector becomes $\xi = \partial_\lambda = (\frac{dx^+}{d\lambda})\partial_+$ so $\xi^+ = (x^+)^a$. The relative acceleration of neighbouring geodesics then is $a^M = R^M{}_{CDB}\xi^C\xi^D n^B$ with $n = n^B\partial_B$ the unit normalized cross-sectional separation vector. Then it can be seen that $a^i = R^i{}_{+i+}(\xi^+)^2 n^i$ so $|a^i|^2$ diverges for all $0 < k < 1$ leading to diverging tidal forces, somewhat similar to the corresponding discussion in [116]. For $k = 1$ the spacetimes (2.42) have all Riemann components vanishing: these can be recast as $ds^2 = -dX^+dx^- + (X^+)^2 dy_i^2$ which can be shown to be flat space in null Milne coordinates (redefining $Y_i = X^+ y_i\,,\ y^- = x^- + y_i^2 X^+$).

Now we analyze quantum extremal surfaces. These cosmologies have no holographic boundary: introducing a bookkeeping ϕ_r, the generalized entropy (Appendix 6.4) is

$$S_{gen} = \frac{\phi_r}{4G}(-x^+)^k + \frac{c}{6}\log\big(-\Delta x^+\Delta x^-\big)\ , \tag{2.47}$$

where $\Delta x^\pm = x^\pm - x_0^\pm$ characterizes the spacetime interval between the observer O and the QES (see Figure 2.2). Strictly speaking, there is a null Kasner scale t_N here appearing as $\phi = (\frac{-x^+}{t_N})^k$ so ϕ is dimensionless: however since the 2-dim metric is flat in these variables, t_N can be absorbed into the definition of ϕ_r above: so we will suppress this (unlike the spacelike cases in sec. 2.2 earlier). The extremization with respect to x^- and x^+ gives

$$\partial_- S_{gen} = \frac{c}{6}\frac{-\Delta x^+}{-\Delta x^+\Delta x^-} = 0\,, \qquad \partial_+ S_{gen} = -\frac{\phi_r}{4G}\,\frac{k}{(-x^+)^{1-k}} + \frac{c}{6}\frac{\partial_+\Delta^2}{\Delta^2} = 0\,. \tag{2.48}$$

With $0 < k < 1$, the classical extremization ($c = 0$) gives $x^+ \to \infty$: in full, we have

$$\Delta^2 = -\Delta x^+\Delta x^- > 0\,, \quad \Delta x^- = x^- - x_0^- \to -\infty\,, \quad -\frac{1}{(-x^+)^{1-k}} + \frac{2Gc}{3\phi_r k}\,\frac{1}{x^+ - x_0^+} = 0\ , \tag{2.49}$$

so

$$\Delta x^+ > 0, \quad x_*^+ = x_0^+ + \frac{2Gc}{3k\phi_r}(-x_*^+)^{1-k} > x_0^+\ ; \qquad \Delta x^- < 0, \quad x_*^- \to X_c^- \sim -\infty\ . \tag{2.50}$$

This is best visualized as in Figure 2.2: we describe this further below. From (2.8), we have $Gc \ll 1$ so that $x^+ \sim x_0^+$ upto small corrections (with $k \neq 0$). Thus employing perturbation theory in Gc, we obtain

$$x_*^+ \sim x_0^+ + \frac{2Gc}{3k\phi_r}(-x_0^+)^{1-k}\ , \tag{2.51}$$

i.e. the QES is almost on the same null-time (x^+) slice as the observer, but just a little *towards* the null singularity (using absolute values gives $|x^+| - |x_0^+| \sim -\frac{2Gc}{3k\phi_r}|x_0^+|^{1-k}$). The location of the QES as being towards the singularity rather than away as in the spacelike cases may look surprising at first sight. However from Figure 2.2, drawing constant x^+ and x^- slices, it is clear that the location of the QES with $\Delta x^+ > 0$ and $\Delta x^- \to -\infty$ is geometrically reasonable and expected if the QES and the observer are to be spacelike separated ($\Delta x^+ < 0$ gives timelike separation between the QES and the observer). In terms of the (t, r)-coordinates (2.41), Figure 2.2 can be taken to depict

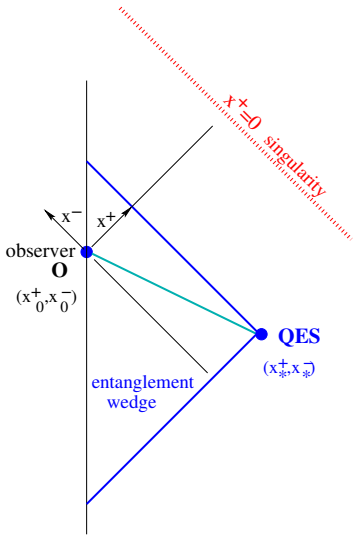

Figure 2.2: Cartoon of the 2-dim geometry with the null singularity at $x^+ = 0$, the worldline (x_0^+, x_0^-) of a timelike observer (vertical trajectory, representing for simplicity a fixed spatial location), and the quantum extremal surface at (x_*^+, x_*^-). As can be seen, the QES is spacelike separated from the observer ($\Delta^2 > 0$) if $\Delta x^+ > 0$ and $\Delta x^- \sim -\infty$, and lies towards the singularity in terms of x^+-slices. The entanglement wedge defined by the QES is shown as the blue wedge.

the region with $x^+ = t + r < 0$ in the (t, r)-plane, with the singularity locus being $t + r = 0$ and the timelike observer worldline having some fixed r_0 with $t_0 < 0$. The description in Figure 2.2 continues to hold as long as the observer remains timelike: it also holds if the observer is moving along a null trajectory along x^+ with fixed x^-. As a further check, we see that this extremization exhibits time-maximization with null time (x^+): we have, using (2.50),

$$\partial_+^2 S_{gen} = -k(1-k)\frac{\phi_r}{4G}(-x^+)^{k-2} - \frac{c}{6}\frac{1}{(x^+ - x_0^+)^2} \quad \to \quad \partial_+^2 S_{gen}|_* < 0 \ . \tag{2.52}$$

Note however that $\partial_-^2 S_{gen} = -\frac{c}{6}\frac{1}{(\Delta x^-)^2} \to 0^-$ from (2.48). This should not be surprising: the 2-dim space here is flat and the absence of the bulk gravitational field makes it quite different from AdS-like spaces (*e.g.* an expression like $S \sim \log r$ gives $\partial_r^2 S \sim -\frac{1}{r^2} \to 0^-$).

As examples of (2.47), we see that for a nearly smooth space *e.g.* with $k = \epsilon \ll 1$, (2.50) gives $x_*^+ \sim (1 - \frac{2Gc}{3\epsilon\phi_r})x_0^+$. The case $k = \frac{2}{3}$ gives the cubic

$$x_*^+ = -t^3 \ : \qquad t^3 + \frac{Gc}{\phi_r}\, t - |x_0^+| = 0 \ , \tag{2.53}$$

which can be shown to have one real root which satisfies $\Delta x^+ > 0$ and agrees with (2.51) in perturbation theory in Gc. For generic k values, recasting using $x^+ = -y^{\frac{1}{1-k}}$, it can be seen numerically that there is one real root satisfying $\Delta x^+ > 0$. Along these lines, for values such as $k = \frac{1}{2}$ we choose the positive root of the resulting quadratic in continuity with neighbouring k values, which then again gives $\Delta x^+ > 0$.

Note that these null cosmological singularities differ somewhat from spacelike ones. In particular, the extremization (2.50) shows that the singularity locus $x^+ = 0$ is an allowed QES solution when $x_0^+ = 0$. The behavior near $x^+ = 0$ can be explicitly examined in examples such as (2.53), e.g., numerically. Thus, these null singularities do not appear to be excluded from the observer's

entanglement wedge. However, the on-shell generalized entropy (2.47) remains singular in the vicinity of the singularity:

$$S_{gen}^{o.s.} = \frac{\phi_r}{4G}(-x_*^+)^k + \frac{c}{6}\log\left(\frac{2Gc}{3k\phi_r}\,\frac{(-x_*^+)^{1-k}\,|X_c^-|}{\epsilon_{UV}^2}\right) \ . \tag{2.54}$$

Thus although formal extrapolation to the singularity appears possible, the above implies that the QES (2.50) is only reliable in the semiclassical regime with large x_*^+ and $Gc \ll 1$ (where the Bekenstein bound does not appear violated). Also since $S_{gen}^{o.s.}$ appears singular, further subleading contributions beyond the bulk entropy term presumably also must be considered. It was observed in [116] that strings become highly excited in the vicinity of a null Kasner Big-Crunch singularity (see also [130, 134]). It is likely that this will be true for (2.43) as well. In this regard, note that the backgrounds (2.41) necessarily require the extra scalar e^Ψ to be nontrivial: interpreting this as the string coupling $g_s = e^\Psi$ and choosing the negative sign exponent for e^Ψ in (2.45) suggests large string interactions in the vicinity of the singularity $x^+ = 0$. It is conceivable however that in some appropriate double-scaling limit $x_*^+ \to 0$, $X_c^- \to -\infty$, with $\frac{2Gc}{3k\phi_r}\,\frac{(-x_*^+)^{1-k}\,|X_c^-|}{\epsilon_{UV}}$ held fixed, the generalized entropy can be rendered nonsingular. It would be nice to explore this more carefully, perhaps dovetailing with the positive sign exponent for e^Ψ in (2.45) and suppressed string interactions.

It is interesting to note that there exists an entire function-worth of nontrivial null backgrounds in (2.41), as shown by (2.44). This is a special feature of 2-dimensional spacetimes with a "holomorphic" structure, as is the case here with sole dependence on x^+. For instance, the backgrounds (2.43) can be recast by redefining the null-time variable to obtain (2.41), such that the 2-dimensional metric becomes flat in these $x^\pm$-coordinates.[2] In contrast, spacelike cosmological singularities generally do not exhibit such "holomorphy" and cannot typically be recast in flat coordinates—hence, the metric factor e^f persists. This holomorphicity manifests in the extremization equations (2.48), (2.50), where the $x^\pm$ sectors decouple—unlike, for instance, (2.11) in the AdS Kasner case and, more generally, (2.8). Indeed, for generic 2-dimensional backgrounds (2.41), extremizing the generalized entropy yields

$$\partial_+ S_{gen} = 0 \quad \to \quad \partial_+\phi + \frac{2Gc}{3\phi_r}\frac{1}{x^+ - x_0^+} = 0 \quad \to \quad x^+ - x_0^+ = -\frac{2Gc}{3\phi_r}\frac{1}{\partial_+\phi} \ , \tag{2.55}$$

once again reflecting this holomorphicity. From the reasoning in Figure 2.2, with $\Delta^2 > 0$ and $\Delta x^+ > 0$, we find $\Delta x^- \to -\infty$, implying that the quantum extremal surface must lie in the direction of decreasing dilaton, i.e., $\partial_+\phi < 0$. This is consistent with our earlier discussion since the

[2]Instead of these "flat" variables, had we taken the background to be

$$e^f = (X^+)^\alpha \ , \quad \phi = (X^+)^K \ , \quad \to \quad (\partial_+\Psi)^2 = \frac{2K(\alpha - K + 1)}{(X^+)^2} \quad \to \quad 0 < K \leq \alpha + 1 \ .$$

In other words, the exponent k from earlier relates as $k = \frac{K}{\alpha+1}$. Now, the generalized entropy contains the metric factor $e^{f/2}|_*$, thus appearing singular.

dilaton undergoes a crunch toward decreasing x^+.

2.4 Discussion

We have examined quantum extremal surfaces in a variety of cosmological spacetimes exhibiting Big-Crunch singularities, building upon the investigations in [43]. In this context, the generalized entropy is analyzed within two-dimensional cosmologies that can, in part, be derived from the dimensional reduction of higher-dimensional cosmologies. The bulk matter is assumed to be in the ground state, which is a reasonable approximation in the semiclassical regime far from the singularity. We first focused on the isotropic AdS Kasner spacetime and its reduction to two dimensions. In [43], the quantum extremal surfaces were found to be driven into the semiclassical region, located infinitely far from the Big-Crunch singularities present in these backgrounds (the classical RT/HRT surfaces for finite subregion sizes bend away from the singularity, as illustrated in Figure 1.2). Furthermore, an analysis of the spatial extremization equation (2.13) reveals that, in the semiclassical region, the QES location extends over the entire Poincaré wedge, leaving no room for island-like regions. Introducing a spatial regulator in the time extremization equation (2.14) enables understanding the dependence of the QES on the observer's location in time. This shows that the QES lags behind the observer location, in the direction away from the singularity, as in Figure 2.1. The lag can be seen to increase slowly as the observer evolves towards the singularity: extrapolating shows that the singularity $t = 0$ is not a solution to the extremization equations. Thus the entanglement wedge appears to exclude the near singularity region. Removing the regulator recovers the results in [43]. The spatial extremization equation (2.13) shows an island-like region emerging for (2.21). However analysing carefully the extremization equations recast as (2.20), (2.23), in the vicinity of this island boundary reveals that the potential island-like solution is in fact inconsistent. Appending a time-independent far region joined with the AdS Kasner region at the time slice $t = t_K$ as in (2.26) gives further insight on the QES behaviour. This QES analysis in the AdS Kasner case extends to more general singularities admitting a holographic interpretation, with similar QES behaviour (2.33), (2.34), in the semiclassical region, and inconsistencies near a potential island boundary (2.35). These cosmologies include nonrelativistic asymptotics: the assumptions on the exponents (2.31) are fairly general.

In Section 2.3, we investigated families of null Big-Crunch singularities that exhibit a form of holomorphy owing to the unique properties of null backgrounds. Notably, the behavior of the quantum extremal surfaces in these cases (see Figure 2.2) is distinct, as they can now reach the singularity. However, the on-shell generalized entropy remains singular, rendering the vicinity of the singularity unreliable. In all instances, the QES is clearly spacelike-separated from the observer (e.g., see (2.12) and (2.49)), which is consistent with its interpretation as holographic entanglement.

Our investigation focused on employing quantum extremal surfaces to gain insights into cosmo-

logical spacetimes that contain Big-Crunch singularities. These spacetimes can all be expressed as two-dimensional cosmologies, thereby excluding more general cosmologies that do not allow such a reduction. Our discussion primarily considers the bulk matter in its ground state—a reasonable assumption in regions far from the singularities encountered in these cosmologies. Overall, the cosmologies examined are closed universes with no horizons, negligible entropy, and no additional non-gravitating bath regions; consequently, islands are not generic in these settings (see, e.g., [126]). This observation aligns with previous studies of closed universes that lack entanglement with external regions, which could act as purifiers for mixed states. As a result, the Bekenstein bound is not violated, meaning that the bulk entropy does not overwhelm the classical area term in the generalized entropy.

Perhaps the most intriguing question involves exploring more sophisticated models for bulk matter in the near-singularity spacetime region, where the matter is expected to become highly excited. Incorporating analogs of more "stringy" physics or quantum entanglement may provide deeper insights into how the near-singularity region becomes accessible via entanglement (with the null singularities perhaps more tractable).

At a broad level, cosmological singularities in holography are, in several respects, qualitatively different from black holes. They seem to require nontrivial, non-generic initial conditions: generic time-dependent deformations of the CFT vacuum are expected to thermalize over long timescales, leading to black hole formation in the bulk rather than a Big-Crunch. This observation is consistent with our finding that, for example, the AdS Kasner and other holographic cosmological singularities remain inaccessible via entanglement with conventional ground state bulk matter—perhaps corroborating the expectation of non-generic holographic dual states (see the discussion following (3.13) and related studies such as [128, 129] on these singularities and complexity). It would be interesting to further explore the roles of holographic entanglement, quantum extremal surfaces, and islands in cosmology more broadly.

Chapter 3

Cosmological singularities, holographic complexity and entanglement

Building on our analysis of quantum extremal surfaces in cosmological backgrounds with Big-Crunch singularities in Chapter 2, we now turn to another key aspect of holography—*holographic complexity*. The QES framework provides valuable insights by incorporating the structure of entanglement; however, studies suggest that entanglement may not probe the deep interior of a black hole at very late times. In contrast, complexity-based approaches have proven effective in capturing the late-time dynamics of black holes and their interior growth. Consequently, it is natural to ask what insights holographic complexity can offer for cosmologies exhibiting Big-Crunch singularities.

Recent advancements in quantum information theory have further enriched our understanding of black hole physics and holography, especially in addressing the black hole information paradox. Within this framework, *complexity* emerges as a fundamental tool that quantifies the difficulty of preparing a target quantum state from a given reference state. In the context of holography, complexity is intimately connected with the growth of the black hole interior. For eternal black holes dual to thermofield double states, the ER=EPR conjecture [135] suggests that the linear growth of the spatial volume of the Einstein-Rosen bridge over time corresponds to the linear time growth of complexity in the dual field theory [25, 26, 136, 137, 138]. This relationship is encapsulated in the expression:

$$C(t) \sim \frac{\mathrm{Vol}(\Sigma_t)}{G_N R}, \tag{3.1}$$

where $C(t)$ denotes the holographic complexity, Σ_t is a codimension-1 spacelike extremal slice anchored at time t, G_N is the Newton constant, and R is the AdS scale. The precise proportionality factors are not canonical and depend on the specific details of the system. In time-independent scenarios, the extremal codimension-1 surface volumes receive dominant contributions from the

near-boundary region, leading to the scaling:

$$C(t) \propto \frac{R^{d_i+1}}{G_{d_i+2}R}\frac{V_{d_i}}{\epsilon^{d_i}} \equiv N_{\rm dof}V_{d_i}\Lambda_{\rm UV}^{d_i}, \tag{3.2}$$

where ϵ is a cutoff, d_i represents the spatial dimensions, $N_{\rm dof}$ corresponds to the number of degrees of freedom in the dual field theory, and $\Lambda_{\rm UV}$ is the UV cutoff scale. This reflects that complexity scales with both the number of degrees of freedom in the dual field theory and the spatial volume (measured in units of the UV cutoff). Extensive studies of holographic complexity, including alternative proposals such as complexity-equals-action, complexity-equals-anything, and path integral complexity, have been explored, with particular relevance to cosmological contexts [139]–[197]. For a comprehensive review of complexity, see Sec. 1.3 and [70].

The application of quantum information tools to investigate cosmological singularities is a captivating pursuit, as these singularities continue to pose profound and enigmatic challenges. In this work, we employ the "complexity equals volume" proposal (3.1) to study these phenomena. It is natural to expect significant stringy and quantum effects to play a critical role in this context. Within the framework of holography, severe time-dependent deformations of the conformal field theory (CFT) may provide insights into Big Bang or Big Crunch singularities. A prototypical example is the AdS_5 Kasner background, where the dual Super Yang-Mills CFT undergoes severe time-dependent deformations affecting both the gauge coupling and the spatial manifold on which the CFT resides [22, 23, 24, 115]. Further discussions on this subject can be found in [117, 118, 119, 120], as well as reviews on Big Bang/Crunch singularities and string theory in [121, 122]. These cosmological singularities are likely qualitatively distinct from bulk black holes, which, being dual to thermal states, are often regarded as natural endpoints of generic time-dependent perturbations that thermalize over long timescales. In contrast, the dual state to a Big Bang or Big Crunch singularity appears to be highly non-generic. For instance, studies on volume complexity in AdS-Kasner singularities indicate that complexity becomes vanishingly low [128] (see also [129]). This observation aligns with investigations of classical and quantum codimension-2 extremal surfaces and holographic entanglement entropy in AdS-Kasner and other singular backgrounds [43, 127]. Specifically, for spacelike singularities, entangling surfaces are driven away from the near-singularity region. These results suggest that the effective number of qubits corresponding to the near-singularity region is vanishingly small, resulting in low complexity for the "dual Kasner state," independent of the reference state, as well as low entanglement. The bulk singularity in these cases corresponds to a Big Bang or Big Crunch scenario, where spatial volumes—and consequently, the number of degrees of freedom—become vanishingly small. This contrasts with the colloquial perception of a Big Bang as a "hot dense mess" and instead reflects that these holographic singularities correspond to low-entropy configurations. It is worth noting that, in the eternal AdS black hole, the extremal surfaces associated with complexity avoid the black hole singularity. Instead, they approach a limiting surface as time progresses to infinity, $t \to \infty$, analogous to the behavior of holographic entanglement entropy surfaces described in [20] (see also [17, 42, 96, 97]). This aligns

with the observation that the black hole interior itself is a cosmological region with a spacelike Big Crunch singularity.

This study is based on [44] and builds upon previous investigations to study holographic complexity and entanglement in greater depth. As detailed in Sec. 3.2.1 and Sec. 3.2.4, we find that the codimension-1 complexity extremal surface anchored at a boundary time slice t, located at a finite temporal distance from the singularity at $t = 0$, initially emerges as a spacelike surface near the boundary. This surface bends away from the singularity and transitions towards a lightlike trajectory in the (t, r)-plane, where r represents the bulk holographic direction. As the anchoring time slice t decreases, moving closer to the singularity, the surface transitions more rapidly from spacelike to the lightlike limit. The lightlike portion of the surface has a vanishing volume, causing the complexity volume functional to diminish as t approaches zero. Eventually, this functional becomes vanishingly small as $t \to 0$, nearing the singularity. This behavior appears to be universal across various classes of Big Bang/Crunch singularities, including AdS Kasner, hyperscaling-violating Kasner, and Lifshitz-Kasner geometries. For AdS-Kasner and Lifshitz-Kasner backgrounds, the complexity decreases linearly with the boundary anchoring time slice t as $t \to 0$. In contrast, for hyperscaling-violating Kasner backgrounds, the decrease in complexity is nonlinear with respect to t, reflecting the nontrivial effective spatial dimension of the dual field theories. Overall, our results on complexity corroborate previous findings on AdS Kasner complexity discussed in [128]. However, our analysis, particularly the extensive numerical studies, adds greater detail to these discussions. The complexity results for other cosmological backgrounds presented here are new but align with those observed for AdS Kasner geometries.

Our technical analysis of complexity exhibits several parallels with the study of holographic entanglement entropy presented in [43], which builds on foundational work in [17, 42, 96, 97]. Specifically, in the semiclassical regime far from the singularity. We extend this analysis numerically, applying the methods used for volume complexity, as described above, to the study of entanglement. The codimension-2 area functional associated with holographic entanglement entropy shares many technical similarities with the codimension-1 volume complexity functional. Consequently, we observe analogous results in the infrared (IR) limit, where large subregions effectively covers the whole space. In this regime, the extremal surfaces transition from spacelike near the boundary to lightlike deeper in the interior. As the anchoring time slice t approaches the singularity, this transition becomes increasingly rapid. Ultimately, as $t \to 0$, the entanglement entropy diminishes and asymptotically approaches zero.

The vanishingly low complexity and entanglement observed as time approaches the singularity reflects the fact that spatial volumes crunch at the singularity, resulting in an effectively negligible number of degrees of freedom near this region. From the perspective of constructing the dual "Kasner" state from a reference state, this behavior suggests that the number of effective qubits in the vicinity of the singularity becomes vanishingly small, irrespective of the choice of the initial reference state. Consequently, the complexity is low in this regime.

The cosmological backgrounds under consideration are predominantly isotropic. As a result, the complexity volume functional can be reformulated in an effective two-dimensional framework, consistent with the dimensional reduction of all boundary spatial dimensions. This reformulation yields a relatively simple expression for complexity in terms of the variables characterizing the effective two-dimensional dilaton gravity theory. Specifically, these variables include the two-dimensional metric and the dilaton, the latter corresponding to the transverse area in the higher-dimensional spacetime. It may be of interest to interpret this effective two-dimensional holographic complexity in the context of suitable dual effective one-dimensional qubit models.

This Chapter is organized as follows: In Sec. 3.1, we argue that volume complexity in higher-dimensional theories can be reformulated as complexity in effective two-dimensional theories, which can be understood as arising via dimensional reduction. Sec. 3.2 focuses on the holographic complexity of AdS Kasner spacetimes. Specifically: In Sec. 3.2.1, Sec. 3.2.2, and Sec. 3.2.3, we derive solutions to the equations of motion for complexity surfaces in $AdS_{5,4,7}$ Kasner spacetimes. In Sec. 3.2.4, we numerically compute the holographic complexity of these spacetimes. Sec. 3.3 explores holographic complexity in hyperscaling-violating cosmologies: We focus on the cases $d_i = 2,\ \theta = -\frac{1}{3}$ (Sec. 3.3.1) and $d_i = 4,\ \theta = -1$ (Sec. 3.3.2). Numerical computations of holographic complexity for these cosmologies are presented in Sec. 3.3.3. In Sec. 3.4, we compute the holographic complexity of isotropic Lifshitz-Kasner cosmologies. Sec. 3.5 provides a review of holographic entanglement entropy studies from [43], focusing on RT/HRT surfaces in AdS Kasner spacetimes: Sec. 3.6.1 addresses AdS_5 Kasner, and Sec. 3.6.2 discusses AdS_7 Kasner. Numerical results for holographic entanglement entropy in $AdS_{5,7}$ Kasner spacetimes are presented in Sec. 3.6.3.

Appendices provide supplementary material: In Appendix 6.5, we briefly review prior studies on holographic cosmologies and their two-dimensional reductions. Appendix 6.6 lists coefficients appearing in the perturbative solutions for AdS-Kasner and hyperscaling-violating cosmologies. In Appendix 6.7, we outline our numerical methods for entanglement entropy calculations in finite subregions, with results that support our overall analysis.

3.1 Higher dim volume complexity → 2-dims: generalities

The metric for an eternal AdS_{d_i+2} Schwarzschild black hole (with transverse space $d\sigma_{d_i}^2$) is given by

$$ds^2 = \frac{R^2}{r^2}\Big(- H(r)dt^2 + \frac{dr^2}{H(r)} + d\sigma_{d_i}^2\Big)\,. \tag{3.3}$$

Then, the complexity volume functional given by the volume of the Einstein-Rosen bridge is

$$C_D = \frac{V_{d_i}}{G_{d_i+2}R}\int dr \frac{R^{d_i+1}}{r^{d_i+1}}\sqrt{\frac{1}{H(r)} - H(r)t'(r)^2}\,. \tag{3.4}$$

Since the transverse space (which the codimension-1 extremal surface wraps) appears in a straightforward manner in this expression, the complexity functional effectively reduces to a 2-dimensional form. This allows it to be explicitly recast in terms of the complexity of an effective 2-dimensional dilaton gravity theory, obtained via dimensional reduction over the transverse space $d\sigma_{d_i}^2$. This formulation is quite general and applies to a broad class of backgrounds that are predominantly isotropic. The 2-dimensional dilaton gravity theory, in many cases, serves as an effective description encapsulating the essential features of the higher-dimensional gravity theory [112]. We will find this perspective particularly useful in the following sections, where we investigate holographic backgrounds featuring cosmological singularities, with a focus on those examined in [113]. A brief review of these studies and holographic cosmologies is provided in App. 6.5.

Consider the general ansatz for a $D = d_i + 2$ dimensional gravity background

$$\begin{aligned} ds_D^2 &= g_{\mu\nu}^{(2)} dx^\mu dx^\nu + \phi^{2/d_i} d\sigma_{d_i}^2 = \frac{e^f}{\phi^{(d_i-1)/d_i}}(-dt^2 + dr^2) + \phi^{2/d_i} d\sigma_{d_i}^2 \,, \\ ds^2 &= g_{\mu\nu} dx^\mu dx^\nu = e^f \left(-dt^2 + dr^2\right), \qquad g_{\mu\nu} = \phi^{(d_i-1)/d_i} g_{\mu\nu}^{(2)} \,. \end{aligned} \tag{3.5}$$

Reviewing [112] and [113], performing a dimensional reduction over the transverse space $d\sigma_{d_i}^2$ gives rise to a 2-dim dilaton gravity theory. With the given parametrization, the higher-dimensional transverse area corresponds to the 2-dimensional dilaton ϕ. The Weyl transformation $g_{\mu\nu} = \phi^{(d_i-1)/d_i} g_{\mu\nu}^{(2)}$ absorbs the dilaton kinetic energy into the curvature $R^{(2)}$ and the 2-dim action becomes

$$S = \frac{1}{16\pi G_2} \int d^2x \sqrt{-g} \left(\phi \mathcal{R} - U(\phi, \Psi) - \frac{1}{2} \phi (\partial \Psi)^2 \right), \tag{3.6}$$

with the dilaton potential $U(\phi, \Psi)$ potentially coupling ϕ to another scalar Ψ which is a minimal massless scalar in the higher dimensional theory (see App. 6.5). The dilaton factor in the Ψ kinetic energy arises from the reduction to 2-dimensions. These models with various kinds of dilaton potentials encapsulate large families of nontrivial higher dimensional gravity theories with spacelike Big-Bang/Crunch type cosmological singularities. In the vicinity of the singularity, the 2-dim fields have power-law scaling behaviour of the form (setting dimensionful scales to unity)

$$\phi = t^k r^m \,, \qquad e^f = t^a r^b \,, \qquad e^\Psi = t^\alpha r^\beta \,, \tag{3.7}$$

and the forms of e^f, ϕ then translate to the higher dimensional cosmological background profile containing the singularities. The 2-dimensional formulation simplifies the structure of these backgrounds and highlights certain noteworthy features. In particular, the severe time dependence near the singularity implies that time derivative terms dominate, while other terms, especially those related to the dilaton potential, become negligible. This leads to the emergence of a "universal" subsector with $k = 1$,

$$\phi \sim t \,, \qquad e^f \sim t^a \,, \qquad e^\Psi \sim t^\alpha \,; \qquad a = \frac{\alpha^2}{2} \,. \tag{3.8}$$

A prototypical example is AdS Kasner [22] and its reduction to 2-dimensions,

$$ds^2 = \frac{R^2}{r^2}(-dt^2+dr^2) + \frac{t^{2/d_i}\,R^2}{r^2}dx_i^2\,, \qquad e^{\Psi} = t^{\sqrt{2(d_i-1)/d_i}}\,, \qquad \Lambda = -\frac{d_i(d_i+1)}{2R^2}\,,$$
$$\rightarrow \qquad \phi = \frac{t\,R^{d_i}}{r^{d_i}}\,, \qquad ds^2 = \frac{t^{(d_i-1)/d_i}\,R^{d_i+1}}{r^{d_i+1}}(-dt^2+dr^2)\,, \qquad U = 2\Lambda\phi^{1/d_i}\,. \tag{3.9}$$

The isotropic restriction from general AdS Kasner (A1) alongwith the Kasner exponent relation $\sum_i p_i = 1$ implies a single Kasner exponent $p = \frac{1}{d_i}$. R is the AdS length scale. We are suppressing an implicit Kasner scale t_K: *e.g.* $t^{2p} \to (t/t_K)^{2p}$. We will reinstate this as required. There are several more general families of such backgrounds with Big-Bang/Crunch singularities, including nonrelativistic ones such as hyperscaling violating (conformally AdS) theories, and those with nontrivial Lifshitz scaling, as we will discuss in what follows, and summarized in the Table 3.1.

Cosmologies	k	m	$a = \frac{\alpha^2}{2}$	b
AdS Kasner cosmology	1	$-d_i$	$\frac{d_i-1}{d_i}$	$-(d_i+1)$
Hv cosmology ($z=1,\ \theta\neq 0$)	1	$-(d_i-\theta)$	$\left(\sqrt{\frac{d_i-\theta-1}{d_i-\theta}} - \sqrt{\frac{(-\theta)}{d_i(d_i-\theta)}}\right)^2$	$-\frac{(d_i-\theta)(1+d_i)}{d_i}$
Lif cosmology ($z=d_i,\ \theta=0$)	1	-1	$\frac{d_i-1}{d_i}$	$-3+\frac{1}{d_i}$

Table 3.1: Exponents for 2-dim cosmologies.

The time dependence in these backgrounds does not switch off asymptotically, making simple interpretations in terms of deformations of a vacuum state challenging. Instead, these backgrounds are likely best understood as dual to a nontrivial, nongeneric state in the dual field theory. This aligns with the expectation that generic, severe time-dependent CFT deformations will lead to thermalization and, consequently, correspond to black hole formation in the bulk. Further discussions on this perspective appear throughout the study, building on [22, 23, 24, 115] and [43, 127].

We now turn to complexity. We mostly consider the transverse space to be planar, so $d\sigma_{d_i}^2 = \sum_i dx_i^2$. Then, in terms of 2-dim variables (3.5) the complexity volume functional becomes

$$\begin{aligned} C &= \frac{1}{G_{d_i+2}R}\int\prod_{j=1}^{d_i}\left(\phi^{1/d_i}dx_j\right)\sqrt{\frac{e^f}{\phi^{(d_i-1)/d_i}}(-dt^2+dr^2)} \\ &= \frac{V_{d_i}}{G_{d_i+2}R}\int_\epsilon dr\ \phi^{\frac{(d_i+1)}{2d_i}}\,e^{f/2}\sqrt{1-t'(r)^2} \;=\; \frac{1}{G_2R}\int_\epsilon dr\ \phi^{\frac{(d_i+1)}{2d_i}}\,e^{f/2}\sqrt{1-t'(r)^2}\,, \end{aligned} \tag{3.10}$$

with $G_2 = \frac{G_{d_i+2}}{V_{d_i}}$ the 2-dimensional Newton constant after reduction, and $r=\epsilon$ the holographic boundary. The higher dimensional curvature scale (*e.g.* R in (3.9)) continues as the 2-dim curvature scale. Also, $t' \equiv \frac{dt}{dr}$ is the r-derivative of the time coordinate as a function $t(r)$ of the holographic radial coordinate.

The last expression in (3.10) above can be interpreted as the complexity volume functional in the 2-dim dilaton gravity theory intrinsically. It would then be interesting to ask for dual 1-dimensional effective qubit models whose complexity can be understood as this.

Sticking in the power-law ansatze (3.7) above, we obtain

$$C = \frac{V_{d_i}}{G_{d_i+2}R}\int_\epsilon dr\ \ t(r)^{\left(k\left(\frac{(d_i+1)}{2d_i}\right)+\frac{a}{2}\right)}\ r^{\left(m\left(\frac{(d_i+1)}{2d_i}\right)+\frac{b}{2}\right)}\ \sqrt{1-t'(r)^2}\ \equiv\ \frac{V_{d_i}}{G_{d_i+2}R}\int_\epsilon dr\,\mathcal{L}\,, \qquad (3.11)$$

with $\mathcal{L}\equiv\mathcal{L}\left(r,t(r),t'(r)\right)$ the effective Lagrangian. Extremizing for the complexity surface $t(r)$ leads to the Euler-Lagrange equation $\frac{d}{dr}\left(\frac{\partial\mathcal{L}}{\partial t'(r)}\right)-\frac{\partial\mathcal{L}}{\partial t(r)}=0$. Simplifying this gives the equation of motion for the complexity surface $t(r)$ in (3.11)

$$2d_i r\,t\,t''+r\left(ad_i+d_i+1\right)\left(1-(t')^2\right)+\left(bd_i+d_im+m\right)t\,t'\left(1-(t')^2\right)=0\,, \qquad (3.12)$$

abbreviating notation with $t\equiv t(r),\ t'\equiv\frac{dt}{dr}\,,\ t''\equiv\frac{d^2t}{dr^2}$, and we have used the universality result $k=1$ in (3.8).

Now we solve equation (3.12) perturbatively and numerically for AdS Kasner, hyperscaling violating and Lifshitz cosmologies, and thereby compute holographic complexity for these cosmologies in sections 3.2 and 3.3.

Methodology: We outline our techniques and methods here:

1. For a given background, first, we solve (3.12) semiclassically in perturbation theory using an ansatz of the form $t(r)=\sum_{n\in\mathbb{Z}_+}c_nr^n$ for the complexity surfaces $t(r)$, as functions of the radial coordinate r for various anchoring time slices t_0 which define boundary conditions at $r=0$. The perturbative solutions are valid only in a certain r-regime, *i.e.* upto a cut-off r_Λ (roughly $r_\Lambda\lesssim t_0$). Thus these cannot encapsulate the entire bulk geometry.

2. To overcome this and obtain a global picture of the bulk, we solve (3.12) numerically (in Mathematica). For this purpose, we need two initial conditions which we extract from the perturbative solutions for $t(r)$ above and their derivatives $t'(r)$, setting the boundary value $r=\epsilon=10^{-2}$ and t_0 as the numerical value of a specific anchoring time slice (with all other dimensionful scales set to unity). This allows us to obtain numerical solutions for the complexity surfaces, which then reveal nontrivial bulk features such as lightlike limits and the transition thereto, from spacelike regimes near the boundary. This then allows us to numerically evaluate holographic volume complexity and plot it against t_0 for various backgrounds.

3. We then employ similar algorithms more broadly for holographic entanglement entropy.

4. Some numerical issues persist for certain backgrounds, as we outline below, and we omit detailed discussions in these cases.

3.2 Complexity: AdS Kasner

The isotropic AdS_{d_i+2} Kasner spacetime (3.9), expressed in terms of the reduction ansatz (3.5) along with its 2-dimensional exponents (3.7), is:

$$\begin{aligned} ds^2 &= \frac{R^2}{r^2}(-dt^2+dr^2)+\frac{t^{2/d_i}\,R^2}{r^2}dx_i^2\,, \qquad e^{\Psi}=t^{\sqrt{2(d_i-1)/d_i}}\,, \qquad \Lambda=-\frac{d_i(d_i+1)}{2R^2}\,, \\ \phi &= \frac{t\,R^{d_i}}{r^{d_i}}\,, \qquad ds^2=\frac{t^{(d_i-1)/d_i}\,R^{d_i+1}}{r^{d_i+1}}(-dt^2+dr^2)\,, \qquad U=2\Lambda\phi^{1/d_i}\,, \\ k&=1\,, \qquad m=-d_i\,, \qquad a=\frac{d_i-1}{d_i}\,, \qquad b=-(d_i+1)\,, \qquad \alpha=\sqrt{\frac{2(d_i-1)}{d_i}}\,. \end{aligned} \tag{3.13}$$

The single Kasner exponent $p=\frac{1}{d_i}$ arises due to the isotropic restriction in (A1). R is the AdS length scale. We are suppressing an implicit Kasner scale t_K: *e.g.* $t^{2p}\to(t/t_K)^{2p}$.

Then the $t(r)$ extremization equation (3.12) becomes

$$r\,t(r)\,t''(r)-(d_i+1)\,t(r)\,t'(r)\,\left(1-t'(r)^2\right)+r\,\left(1-t'(r)^2\right)=0\,. \tag{3.14}$$

We discuss the solution of (3.14) for $AdS_{5,4,7}$-Kasner spacetimes in sec. 3.2.1, 3.2.2, and 3.2.3.

3.2.1 AdS_5-Kasner spacetime

For AdS_5-Kasner spacetime, we have $d_i=3$: then (3.14) simplifies to

$$r\,t(r)\,t''(r)-4t(r)\,t'(r)\,\left(1-t'(r)^2\right)+r\,\left(1-t'(r)^2\right)=0\,. \tag{3.15}$$

First we note that with $t',t''=0$, the equation above is not satisfied except for $r\sim 0$, so that $t(r)=const$ is not a solution: the surface always bends in the time direction due to the time dependence of the background. When the complexity surface $t(r)$ has weak r-dependence, *i.e.* it is almost constant with $t(r)\sim t_0$, we can analyze the above equation in perturbation theory in r, by considering the following ansatz for $t(r)$:

$$t(r)=t_0+\sum_{n\in\mathbb{Z}_+}c_n r^n\,. \tag{3.16}$$

Inputting this ansatz (3.16) in (3.15) and solving for the coefficients iteratively, we found the solution up to $\mathcal{O}(r^{30})$. Up to $O(r^4)$, this is

$$t(r)=t_0+\frac{r^2}{6t_0}-\frac{7r^4}{216t_0^3}\,. \tag{3.17}$$

We have truncated the solution (3.17) up to $O(r^4)$ here for brevity of the series expansion (this is $O(r^3)$ in $t'(r)$ in (3.23)). A more detailed iterative version of (3.17) up to $O(r^{30})$ appears in (B1). Likewise, truncated solutions are displayed elsewhere in the paper, *e.g.* (3.19), (3.31), (3.42),

(3.44), (3.49), (3.51) and (3.61). The numerical analysis described in what follows is based on the more detailed expansion up to $O(r^{30})$. However we find that the numerical plots do not change much with the truncated solutions such as (3.17): the qualitative features of the extremal surfaces are the same. So we will continue to display the truncated solutions alone in the rest of the paper for compactness.

The solution $t(r)$ in (B1) and its derivative $t'(r)$ are plotted in Fig. 3.1 for various t_0-values[1].

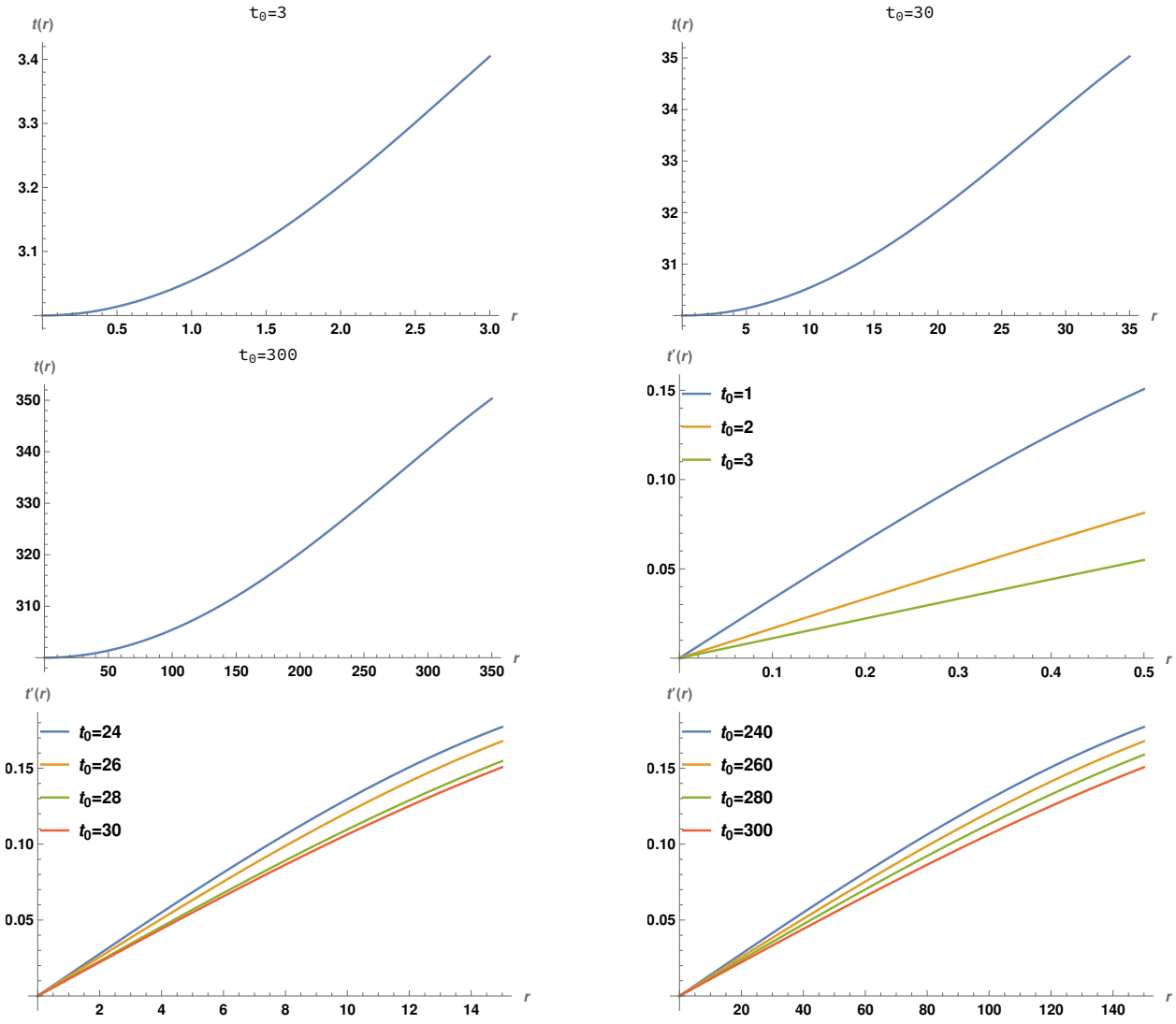

Figure 3.1: Variation with r of the semiclassical (perturbative) complexity surfaces $t(r)$ and their derivatives $t'(r)$ for various values of the anchoring time slice t_0.

[1]We obtain similar qualitative behaviour for the variation of complexity surfaces and their derivatives in other backgrounds, so we will not display them, in favour of the plots of numerical solutions which are more instructive.

From Fig. 3.1, we see that the complexity surface varies approximately linearly with r in the regime roughly $r \sim t_0$ and $t'(r)$ reaches its maximum value about $t'(r) \lesssim 0.2$, which vindicates the mild bending of the surface $t(r)$ in the radial direction. Of course this perturbative solution has clear limitations, expressed as it is here by a finite power series. However it is of great value to display the behaviour of the complexity surface near the boundary $r = 0$.

We expect that when the anchoring time slice t_0 is far from the singularity at $t = 0$, the above perturbative solution remains reasonable, at least in the vicinity of the boundary. A closely related analysis was performed in [43], demonstrating that the RT/HRT surface in the semiclassical regime far from the singularity bends away from it. We will later study this numerically to extract further insights.

A further check of the above series solution is that in the semiclassical limit, when we ignore the higher order terms in $t'(r)$ (*i.e.* $t'(r) \ll 1$), then (3.15) reduces to

$$t(r)\left(rt''(r) - 4t'(r)\right) + r = 0\,. \tag{3.18}$$

Solving (3.18) with the ansatz (3.16), we obtain up to $\mathcal{O}(r^4)$:

$$t(r) = t_0 + \frac{r^2}{6t_0} - \frac{r^4}{24t_0^3}\,. \tag{3.19}$$

Plotting (3.19) and its r-derivative reveals that the behaviour of the complexity surface $t(r)$ and its derivative is qualitatively similar to that in Fig. 3.1. This vindicates the fact that $t'(r)$ is indeed small in this regime.

Holographic complexity of AdS$_5$-Kasner spacetime: The holographic volume complexity (3.11) for the AdS_5-Kasner spacetime (3.13) with $d_i = 3$ simplifies to

$$C = \frac{V_3 R^3}{G_5}\int_\epsilon dr\left(\frac{t(r)\sqrt{(1-t'(r)^2)}}{r^4}\right). \tag{3.20}$$

Now we compute this for the solutions (3.19) and (3.17).

The semiclassical solution (3.19) was obtained with $t'(r) \ll 1$ so we can approximate the complexity functional (3.20) as:

$$C \sim \frac{V_3 R^3}{G_5}\int_\epsilon^{r_\Lambda} dr\left(\frac{t(r)\left(1-\frac{t'(r)^2}{2}\right)}{r^4}\right). \tag{3.21}$$

We have inserted a cut-off r_Λ in (3.21) because the perturbative solution is only valid upto some $r_\Lambda \lesssim t_0$, and so this only covers part of the full complexity surface. Beyond this we require additional analysis, which we carry out numerically later.

Substituting the semiclassical solution $t(r)$ from (3.19) into (3.21) and integrating gives complexity as (writing only terms up to next-to-leading order in t_0 for simplicity)

$$C(t_0, r_\Lambda, \epsilon) \approx \frac{V_3 R^3}{G_5}\left[t_0\left(\frac{0.3}{\epsilon^3} - \frac{0.3}{r_\Lambda^3}\right) + \frac{1}{t_0}\left(\frac{0.1}{\epsilon} - \frac{0.1}{r_\Lambda}\right) + O\left(\left(\frac{1}{t_0}\right)^3\right)\right]. \tag{3.22}$$

For the more general solution (3.17) obtained retaining all the nonlinear terms in (3.15), we find $t'(r)$ as:

$$t'(r) \approx \frac{0.3r}{t_0} - \frac{0.1r^3}{t_0^3}. \tag{3.23}$$

Thus we see that $t'(r) \ll 1$ provided $r \lesssim t_0$. In this approximation, we can evaluate complexity as (3.21) with the solution (3.17). Then holographic complexity is the same as (3.22) upto next-to-leading-order in t_0.

Going beyond perturbation theory fascinatingly shows that the complexity surface becomes lightlike in the interior, as first noted in [128]. This can be seen right away by noting that (3.15) is in fact satisfied identically when $t'(r) = 1$ and $t''(r) = 0$, *i.e.* with $t(r) \sim r$ being lightlike independent of the anchoring time slice t_0.

Towards identifying this in the AdS_5-Kasner spacetime, consider the following ansatz for $t(r)$ around the lightlike limit with $f(r)$ a small deviation:

$$t(r) = t_0 + r + f(r)\,. \tag{3.24}$$

This ansatz simplifies (3.15) to

$$-r\left(f'(r)+1\right)^2 + \left(f(r)+r+t_0\right)\left(rf''(r) + 4f'(r)\left(f'(r)+1\right)\left(f'(r)+2\right)\right) + r = 0\,. \tag{3.25}$$

Linearizing the above equation, *i.e.* ignoring higher order terms in $f'(r)$, gives

$$r^2 f''(r) + rt_0 f''(r) + 8t_0 f'(r) + 6rf'(r) = 0\,, \tag{3.26}$$

which can be solved as

$$f(r) = c_1\left(-\frac{t_0^2}{7r^7} - \frac{t_0}{3r^6} - \frac{1}{5r^5}\right) + c_2\,, \tag{3.27}$$

where c_1, c_2 are constants. This gives the solution for $t(r)$ as

$$t(r) = t_0 + r + c_1\left(-\frac{t_0^2}{7r^7} - \frac{t_0}{3r^6} - \frac{1}{5r^5}\right) + c_2\,. \tag{3.28}$$

The above solution is not well-behaved when extrapolated all the way to the boundary $r = 0$ but it indicates the existence of the neighbourhood of a lightlike surface. We now look for the lightlike solution numerically.

Lightlike limits of complexity surfaces, numerically

Now we solve equation (3.15) numerically. Since this is a second-order nonlinear differential equation, we need two initial conditions for a numerical solution. One trivial initial condition is $t(r = 0) = t_0$, leaving the question of the initial condition for $t'(r = 0)$. Since we have solved (3.15) perturbatively obtaining (3.17), we can obtain the initial condition $t'(r = 0)$ by evaluating

the r-derivative thereof. We regulate the holographic boundary $r = \epsilon \sim 0$ by choosing $\epsilon = 10^{-2}$ as the boundary point. For a specific slice t_0, we can obtain initial conditions $t(r = 0.01)$ and $t'(r = 0.01)$ by substituting $r = 0.01$ and the value of t_0 in the solution (3.17) and its r-derivative[2]. The numerical computations were performed using Mathematica, with careful tuning of parameters such as setting WorkingPrecision to MachinePrecision and PrecisionGoal to Infinity in NDSolve to ensure stable solutions for the chosen initial conditions. The results have also been partially cross-validated using independent Python implementations. The Mathematica files are available upon request.

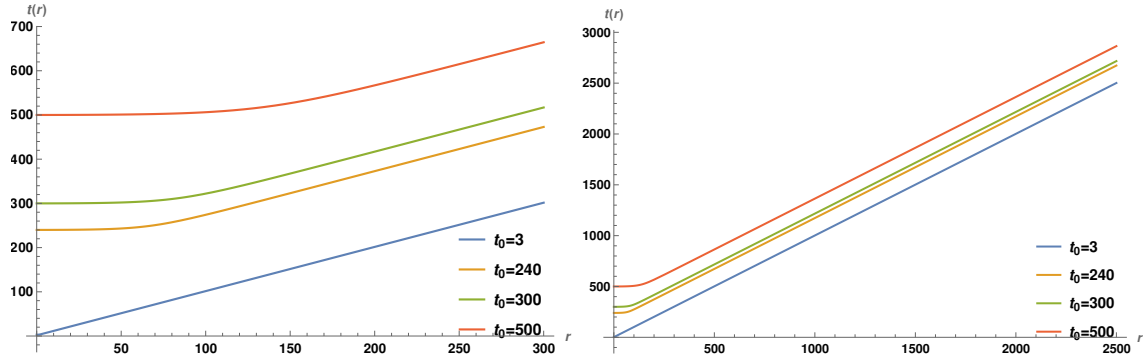

Figure 3.2: Numerical plots of the complexity surface versus r in AdS_5-Kasner spacetime for different slices of t_0. In the right Figure, we have extended the range of radial coordinate.

The numerical solutions of (3.15) for the complexity surface $t(r)$ and their derivatives $t'(r)$ for different t_0 slices are plotted in Fig. 3.2 and Fig. 3.3 respectively. Some striking points to note are:

- In Fig. 3.2, we remind the reader that $t(r)$ corresponds to $|t(r)|$ so the singularity is at $t = 0$ (the horizontal axis at the bottom). Thus all complexity surfaces bend away from the neighbourhood of the singularity, which correlates with $t'(r) > 0$.

- From Fig. 3.2, the complexity surfaces become lightlike after a certain value of r for any anchoring time slice t_0.

- The surfaces with lower t_0 (*i.e.* closer to the singularity) become lightlike earlier (at smaller r) than those with larger t_0. This is also vindicated in Fig. 3.3, where we have numerically plotted $t'(r)$ with r. All the complexity surfaces $t(r)$ approach $t'(r) = 1$ eventually, *i.e.* a lightlike regime.

- The lightlike regime $t'(r) = 1$ implies vanishing holographic complexity here from the $\sqrt{1 - t'(r)^2}$ factor in (3.20). Thus, numerically we see that complexity picks up finite contributions only

[2]We have used this method in obtaining the numerical solution of the equation of motion associated with complexity/entanglement surfaces throughout the paper for different backgrounds. Therefore, we will not repeat this again: we will simply quote the results for different backgrounds.

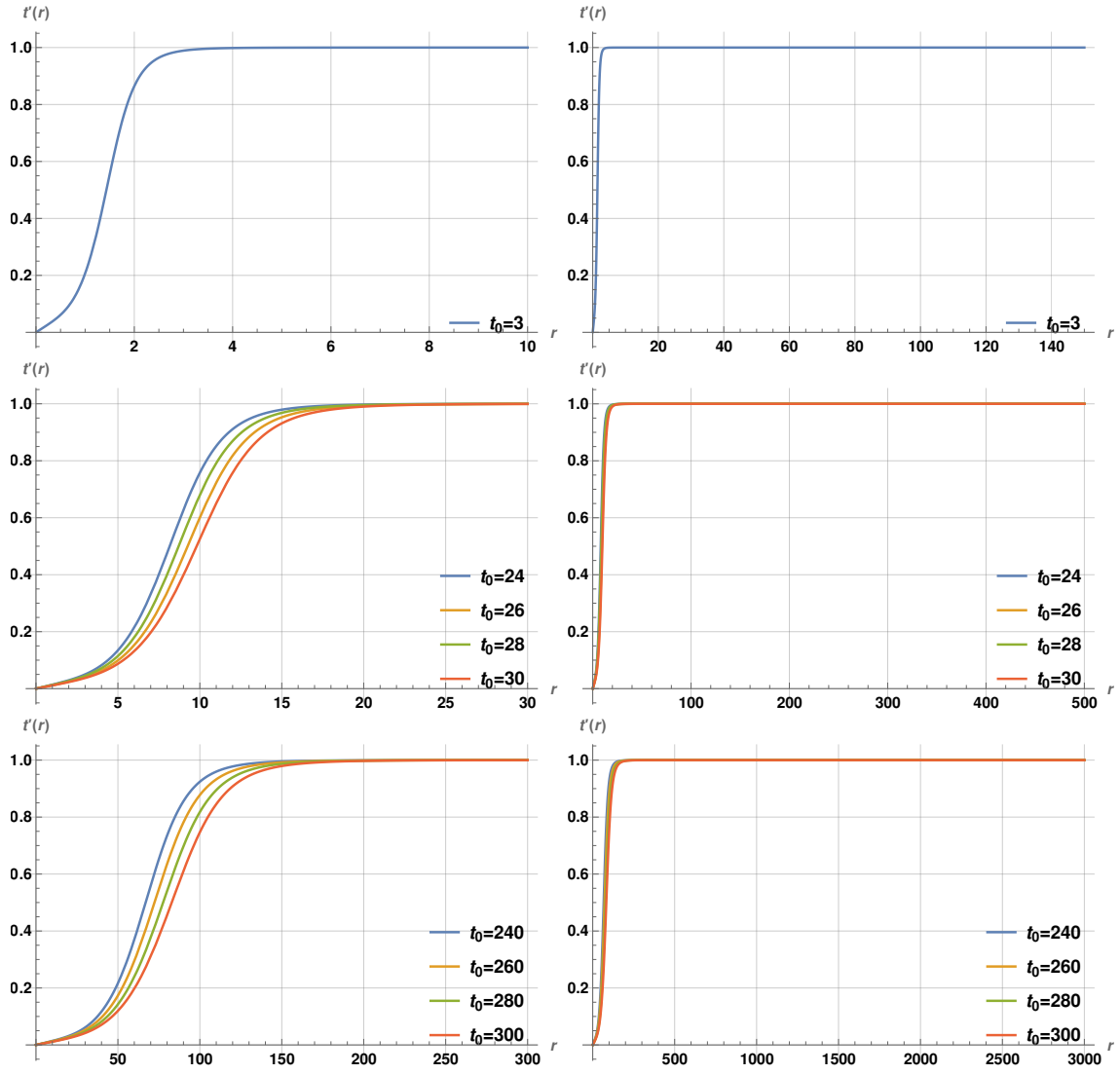

Figure 3.3: Numerical plots of $t'(r)$ versus r in AdS_5-Kasner spacetime for different t_0 slices. In the right Figures, we have extended the range of the radial coordinate.

from the near-boundary spacelike part of the complexity surfaces, beyond which it has negligible value where the complexity surfaces are lightlike.

- The above two points imply that as the anchoring time slice approaches the singularity location $t_0 \to 0$, the complexity surface is almost entirely lightlike: thus as $t_0 \to 0$ the holographic volume complexity becomes vanishingly small. We verify this later by numerical evaluation of the volume complexity integral in sec. 3.2.4.

- These numerical plots and this analysis only makes sense for t_0 not strictly vanishing (*e.g.* we require $t_0 \gtrsim \epsilon$). In close proximity to the singularity, the semiclassical gravity framework here and our analysis breaks down.

In Figs. 3.2 and 3.3, we have shown the behaviour of $t(r)$ and $t'(r)$ with r for both limited range (left side plots) and extended range of the radial coordinate in these Figures (right side plots). We obtain similar behavior for other cases later. So we will not show the counterparts of the right side plots (extended r-range) in Figs. 3.2-3.3 in order to display our results succinctly in subsequent data

3.2.2 Holographic complexity of AdS_4-Kasner spacetime

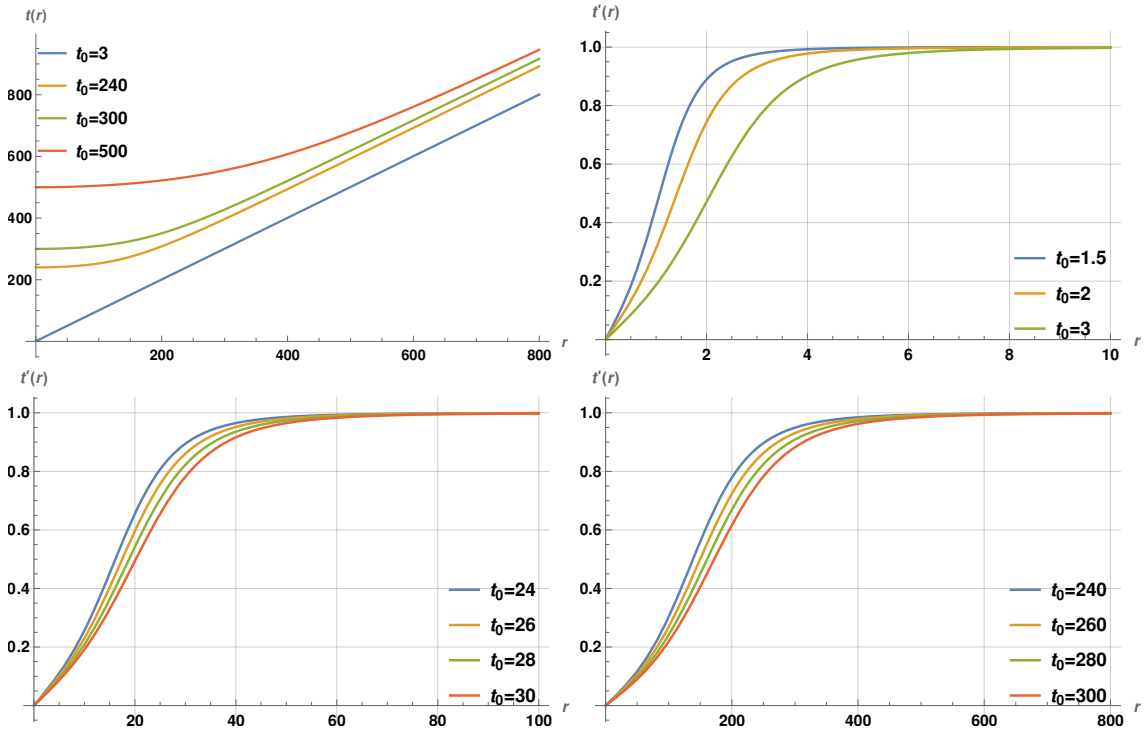

Figure 3.4: Plots of $t(r)$ with r and $t'(r)$ with r in AdS_4-Kasner spacetime for various t_0 slices.

For the AdS_4-Kasner spacetime with $d_i = 2$, the equation of motion (3.14) for the complexity surface $t(r)$ becomes

$$r\, t(r)\, t''(r) - 3t(r)\, t'(r)\left(1 - t'(r)^2\right) + r\left(1 - t'(r)^2\right) = 0\,. \tag{3.29}$$

Numerical results: The perturbative solution of (3.29) is obtained only up to $O(r^2)$ unfortunately, *i.e.* $t(r) = t_0 + \frac{r^2}{4t_0}$, beyond which the numerics appear problematic. However, we find that this $O(r^2)$ perturbative solution is adequate in extracting the initial conditions for numerical solutions.

Using these initial conditions, the numerical solution of (3.29) for $t(r)$ and its derivative $t'(r)$ are obtained along the same lines as in AdS_5-Kasner. These are plotted in Fig. 3.4, which reveal that the behaviour of the complexity surfaces $t(r)$ and their derivatives are similar to those in AdS_5-Kasner.

3.2.3 Holographic complexity of AdS_7-Kasner spacetime

The equation of motion for the complexity surface $t(r)$ for AdS_7-Kasner spacetime using $d_i = 5$ in (3.14) becomes

$$r\, t(r)\, t''(r) - 6t(r)\, t'(r)\left(1 - t'(r)^2\right) + r\left(1 - t'(r)^2\right) = 0\,. \tag{3.30}$$

As in AdS_5-Kasner spacetime, we solve this perturbatively and numerically.

Perturbative results: The perturbative solution of (3.30) for the ansatz $t(r) = t_0 + \sum_{\mathbf{n}\in\mathbb{Z}_+} c_n r^n$ is given as:

$$t(r) = t_0 + \frac{r^2}{10t_0} - \frac{23r^4}{3000t_0^3}. \tag{3.31}$$

The solution (3.31) for $t(r)$ and its derivative $t'(r)$ for AdS_7-Kasner are qualitatively similar to those in AdS_5-Kasner.

Numerical results: Using the above, we can pin down boundary conditions near the boundary and then solve (3.30) numerically. This is similar to the analysis in AdS_5-Kasner and the solution $t(r)$ of (3.30) and its derivative $t'(r)$ are plotted in Fig. 3.5. We see that the AdS_7-Kasner spacetime gives similar results.

3.2.4 Numerical computation of complexity, AdS Kasner

We evaluate holographic complexity of $AdS_{5,4,7}$-Kasner spacetime numerically using the numerical solutions discussed above and performing the numerical integration in C. The expression of holographic complexity for AdS_5, AdS_4 and AdS_7-Kasner spacetimes are given as:

$$(\mathrm{AdS}_{\mathrm{d_i}+2}\ \text{Kasner}) \qquad C = \frac{V_{d_i} R^{d_i}}{G_{d_i+2}} \int_\epsilon dr \left(\frac{t(r)\ \sqrt{1 - t'(r)^2}}{r^{d_i+1}}\right). \tag{3.32}$$

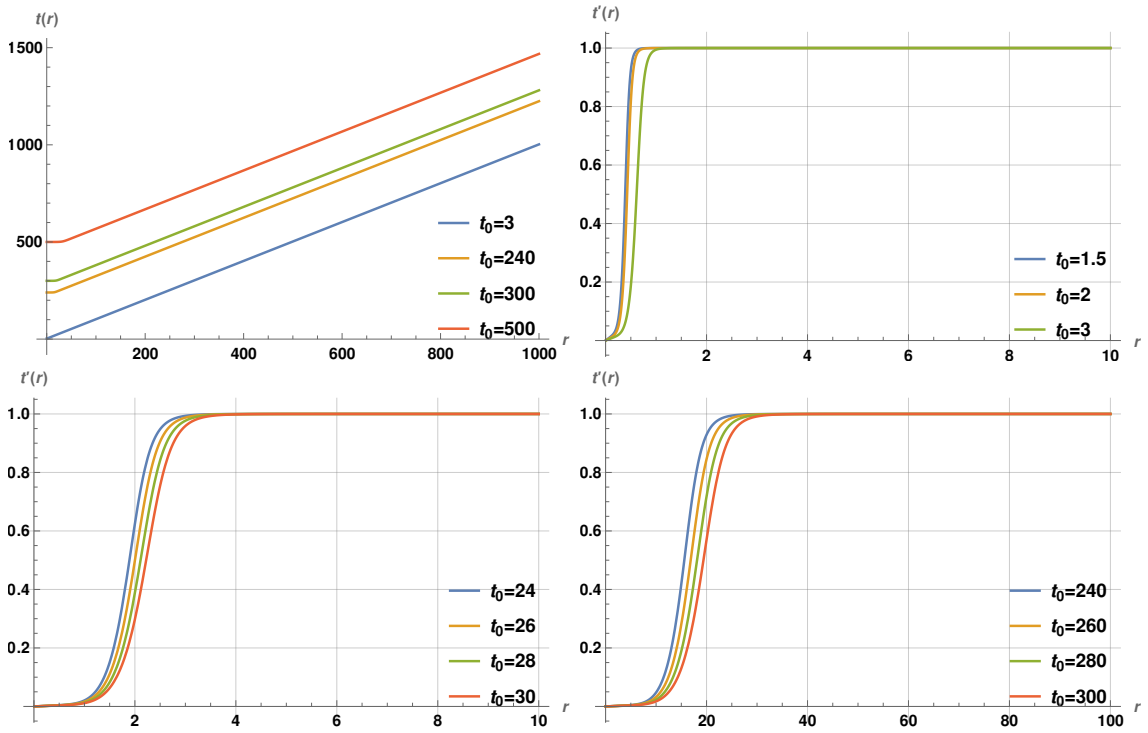

Figure 3.5: Plots of $t(r)$ with r and $t'(r)$ with r in AdS_7-Kasner spacetime for different t_0 slices.

To perform the integrals numerically, we set the lengthscales V_{d_i}, R^{d_i}, G_{d_i+2} to unity and take $\epsilon = 10^{-2}$ at the lower end. The upper end of the integration domain is irrelevant since the complexity surfaces become lightlike eventually as r increases so the complexity integral has negligible contribution there, as stated in sec. 3.2.1. Then as an order-of-magnitude estimate, $t_0 \sim 100$ gives $C \sim \frac{t_0}{\epsilon^{d_i}} \sim 10^{2d_i+2}$ which corroborates with the scales in Fig. 3.6 which displays the variation of complexity with t_0 in AdS-Kasner spacetime. From the Figure, we see that holographic volume complexity decreases linearly as the anchoring time slice approaches the vicinity of the singularity, *i.e.* as $t_0 \to 0$. Thus the dual Kasner state appears to be of vanishingly low complexity, independent of the reference state.

It is worth making a few comparisons on holographic complexity across $AdS_{5,7,4}$ Kasner spacetimes, based on the numerical results in Fig. 3.2, Fig. 3.3 (AdS_5-K), Fig. 3.5 (AdS_7-K), and Fig. 3.4 (AdS_4-K). Relative to AdS_5-Kasner, we see that the complexity surfaces become lightlike at smaller r-values in AdS_7-Kasner. Thus complexity of AdS_7-Kasner acquires vanishing contributions at smaller r-values relative to AdS_5-Kasner. Likewise, we see that the AdS_5-Kasner displays the lightlike regime at smaller r-values than AdS_4-Kasner. Thus complexity surfaces in higher dimensional AdS-Kasner acquire lightlike regimes earlier than those in lower dimensional ones. However it is clear that the leading divergence behaviour is larger for higher dimensions, since the extremal codim-1 surface volumes have dominant contributions from the near boundary region. With cutoff

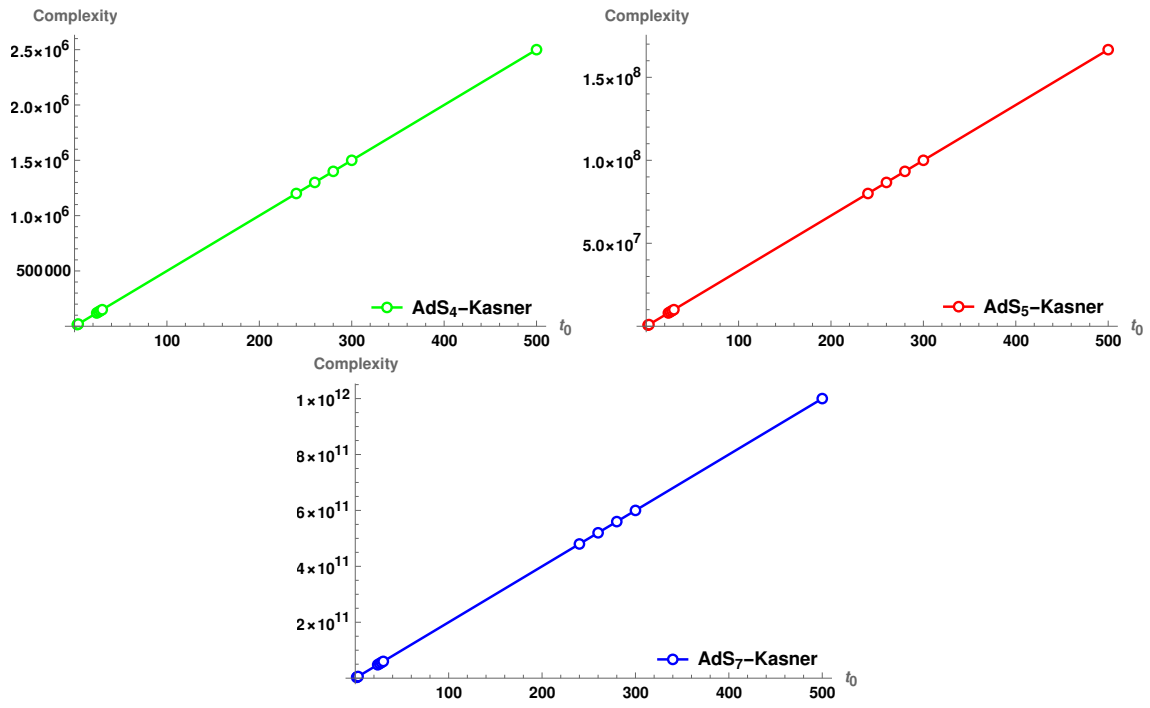

Figure 3.6: Numerical plots of holographic volume complexity with t_0 in $AdS_{4,5,7}$-Kasner spacetimes.

$\epsilon \equiv \Lambda_{UV}^{-1}$ we have the scaling

$$C \sim \frac{R^{d_i+1}}{G_{d_i+2}\, R}\, \frac{V_{d_i}}{\epsilon^{d_i}}\, t_0 \equiv N_{dof}\, V_{d_i} \Lambda_{UV}^{d_i}\, t_0\,, \tag{3.33}$$

reflecting the fact that complexity scales with the number of degrees of freedom in the dual field theory and with spatial volume in units of the UV cutoff. Some intuition for this can be obtained from the form of the complexity volume functional (3.32) where the $\sqrt{1-(t')^2}$ factor is amplified by the $\frac{1}{r^{d_i}}$-factor. Both the spacelike part ($t' \ll 1$) of the complexity surface and the transition to the lightlike part (where t' is changing) are amplified by the $\frac{1}{r^{d_i}}$-factor to a greater degree at larger d_i. Thus higher dimensional AdS-Kasner hits the lightlike regime and vanishing complexity at smaller r-values relative to lower dimensions.

Overall from (3.33) we see that

$$\frac{dC}{dt_0} \sim N_{dof}\, V_{d_i} \Lambda_{UV}^{d_i}\,. \tag{3.34}$$

This arises from the near-boundary UV part of the complexity surface, with the lightlike component contributing negligibly. This is consistent with complexity scaling as the number of microscopic degrees of freedom in (a lattice approximation of) the CFT. In this context, it appears that near the singularity, there is a reduction in the effective number of degrees of freedom. As $t_0 \to 0$, space completely crunches, and there are no effective qubits, leading to the vanishing of complexity.

3.3 Complexity: hyperscaling violating cosmologies

Various cosmological deformations of conformally AdS or hyperscaling-violating theories were identified in [113] (see Appendix 6.5). The two-dimensional form of these backgrounds can be described using the two-dimensional dilaton gravity action (3.6), along with the corresponding dilaton potential, parameters, and the (t, r)-scaling exponents in (3.7). Additionally, the higher-dimensional cosmology is:

$$
\begin{aligned}
&U = 2\Lambda\phi^{1/d_i}\, e^{\gamma\Psi}\,, \qquad 2\Lambda = -(d_i+1-\theta)(d_i-\theta)\,, \qquad \gamma = \frac{-2\theta}{\sqrt{2d_i(d_i-\theta)(-\theta)}}\,,\\
&ds^2 = \frac{R^2 r^{\frac{2\theta}{d_i}}}{r^2}\left(\frac{-dt^2+dr^2}{t^{\gamma\alpha}} + t^{2/d_i}dx_i^2\right), \quad e^{\Psi} = t^{\alpha} r^{\sqrt{2(d_i-\theta)\frac{(-\theta)}{d_i}}}\,,\\
&k=1\,, \quad m=-(d_i-\theta)\,, \quad a=\frac{\alpha^2}{2}\,, \quad \alpha = -\gamma \pm \sqrt{\gamma^2+\frac{2(d_i-1)}{d_i}}\,,\\
&b = -\frac{(d_i-\theta)(d_i+1)}{d_i}\,, \quad \beta = \sqrt{\frac{2(d_i-\theta)(-\theta)}{d_i}}\,.
\end{aligned}
\tag{3.35}
$$

With α taken positive, $e^{\Psi} \to 0$ as $t \to 0$ and we obtain

$$
\alpha = -\gamma + \sqrt{\gamma^2+\frac{2(d_i-1)}{d_i}} \quad \to \quad a = \left(\sqrt{\frac{d_i-\theta-1}{d_i-\theta}} - \sqrt{\frac{(-\theta)}{d_i(d_i-\theta)}}\right)^2 . \tag{3.36}
$$

In this section, we restrict to Lorentz invariance: the Lifshitz exponent is $z = 1$. Then the null energy conditions [198] implies that the hyperscaling violating exponent θ is constrained as

$$
(d_i-\theta)(d_i(z-1)-\theta) \geq 0\,, \qquad (z-1)(d_i+z-\theta) \geq 0 \quad \xrightarrow{z=1} \quad \theta \leq 0\,. \tag{3.37}
$$

The other possibility $\theta > d_i$ has undesirable properties suggesting instabilities [198].

Time-independent backgrounds of this sort appear in the dimensional reduction [198] over the transverse spheres of nonconformal Dp-branes [199], and the θ-exponent is then related to the nontrivial running of the gauge coupling. Reductions of nonconformal Dp-branes over the transverse spheres and over the brane spatial dimensions leads to 2-dim dilaton gravity theories [200] with dilaton potentials as in (3.35) above, and the 2-dim dilaton then leads to a holographic c-function encoding the nontrivial renormalization group flows. Some of the analysis there, as well as in [198], may be helpful to keep in mind in our discussions here. In particular, the D2-brane and D4-brane supergravity phases give rise to $d_i = 2,\ \theta = -\frac{1}{3}$ and $d_i = 4,\ \theta = -1$, respectively, both with $z = 1$. In these cases, the Big-Bang/Crunch singularities may be interpreted as appropriate Kasner-like deformations of the nonconformal Dp-brane backgrounds, although again the time-dependence does not switch off asymptotically with corresponding difficulties in interpretation as severe time-dependent deformations of some vacuum state.

We will focus on studying the Big-Bang/Crunch hyperscaling-violating cosmological backgrounds in (3.35) above and explore the holographic complexity associated with them. The calculations are broadly similar to those in AdS Kasner spacetimes earlier, but with noteworthy detailed differences. Using the exponents in (3.35), (3.36), the holographic volume complexity (3.11) simplifies to

$$C = \frac{V_{d_i} R^{d_i}}{G_{d_i+2}} \int_\epsilon dr \left(r^{\frac{(d_i+1)(\theta-d_i)}{d_i}} t(r)^{\frac{1}{2}\left(\left(\sqrt{\frac{d_i-\theta-1}{d_i-\theta}}-\sqrt{\frac{(-\theta)}{d_i(d_i-\theta)}}\right)^2+\frac{1}{d_i}+1\right)} \sqrt{1-t'(r)^2} \right). \tag{3.38}$$

Extremizing with $t(r)$, we obtain the Euler-Lagrange equation of motion for the complexity surface $t(r)$ as

$$\begin{aligned} & r\left(d_i\left(\sqrt{\frac{d_i-\theta-1}{d_i-\theta}}-\sqrt{\frac{(-\theta)}{d_i(d_i-\theta)}}\right)^2+d_i+1\right)\left(1-t'(r)^2\right) \\ & \quad + 2d_i\, r\, t(r)\, t''(r) - 2(d_i+1)(d_i-\theta)\, t(r)\, t'(r)\left(1-t'(r)^2\right) = 0\,. \end{aligned} \tag{3.39}$$

In the semiclassical limit ($t'(r) \ll 1$), we can ignore terms like $t'(r)^2, t'(r)^3$ in the equation of motion (3.39), which then simplifies to

$$t(r)\left(2(d_i+1)(d_i-\theta)t'(r) - 2d_i r t''(r)\right) - r\left(d_i\left(\sqrt{\frac{d_i-\theta-1}{d_i-\theta}}-\sqrt{\frac{(-\theta)}{d_i(d_i-\theta)}}\right)^2+d_i+1\right) = 0. \tag{3.40}$$

Now, we solve equations (3.39) and (3.40) perturbatively using ansatze similar to those in the AdS-Kasner spacetime, *i.e.* $t(r) = t_0 + \sum_{n\in\mathbb{Z}_+} c_n r^n$. We illustrate this in detail by analysing holographic volume complexity for two cases: (i) $d_i = 2,\ \theta = -1/3$ in sec. 3.3.1, and (ii) $d_i = 4,\ \theta = -1$ in sec. 3.3.2. Analysing other cases reveals similar results. To differentiate between the different solutions, we will use different coefficients for the different cases, e.g., g_n, s_n etc.

3.3.1 $d_i = 2,\ \theta = -\frac{1}{3}$

This case is related to the $D2$-brane supergravity phase as stated earlier, and we analyze the perturbative and numerical solutions now.

The equation of motion (3.39) with exponents (3.35), (3.36), for this case simplifies to

$$14r\, t(r)\, t''(r) - \left(2\sqrt{2}-15\right) r\left(1-t'(r)^2\right) - 49 t(r)\, t'(r)\left(1-t'(r)^2\right) = 0\,. \tag{3.41}$$

The solution $t(r)$ up to $\mathcal{O}(r^4)$ is given as

$$t(r) = t_0 + g_2 r^2 + g_4 r^4\,, \tag{3.42}$$

with g_i in (B2). The behaviour of the complexity surfaces (3.42) with r for different t_0 values is qualitatively similar to those in AdS-Kasner (see Fig. 3.1) so we will not display the plots.

When $t'(r) \ll 1$, we can ignore the higher order terms in (3.41) to obtain

$$2\left(2\sqrt{2}-15\right) r - 14t(r)\left(2rt''(r) - 7t'(r)\right) = 0. \tag{3.43}$$

This has solution up to $\mathcal{O}(r^4)$ given as

$$t(r) = t_0 + s_2 r^2 + s_4 r^4\,, \tag{3.44}$$

with s_i in (B3). The behaviour of (3.44) is qualitatively similar to that in AdS-Kasner.

Solving (3.41) numerically along similar lines as in AdS-Kasner, we obtain the variation of the complexity surfaces and their derivatives with r: this is shown in Fig. 3.7.

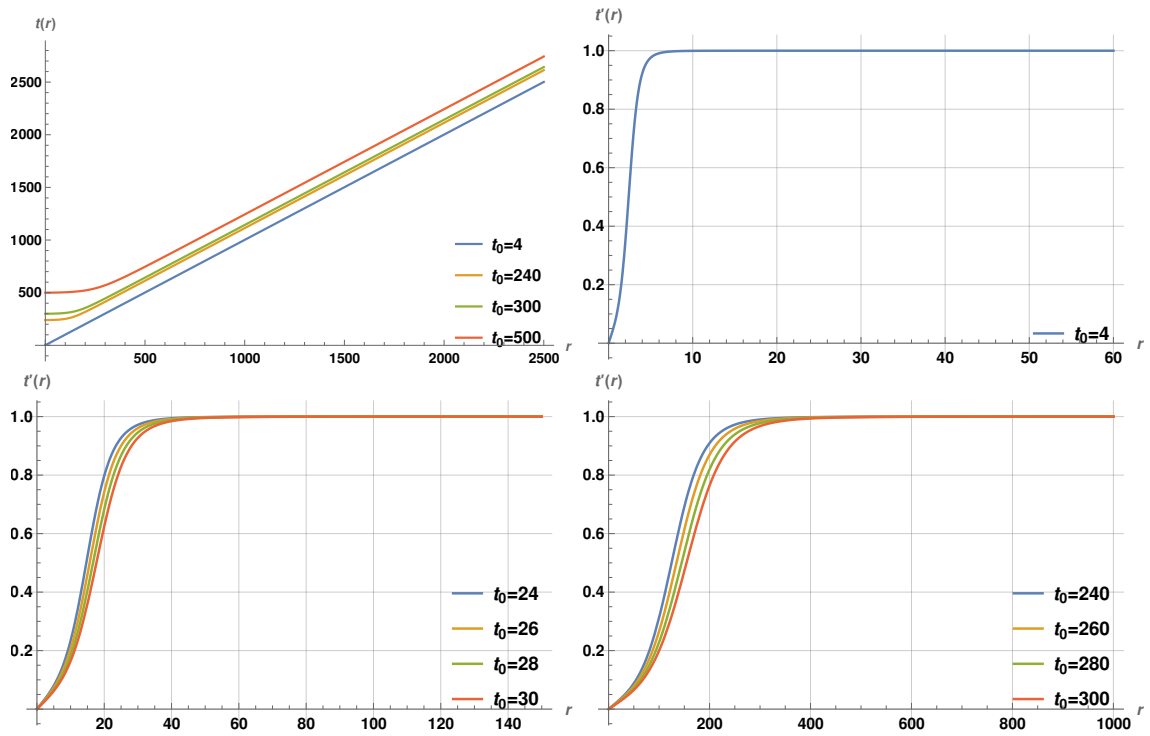

Figure 3.7: Numerical plots of $t(r)$ versus r and $t'(r)$ versus r for $d_i = 2$ and $\theta = -1/3$ in hv cosmology.

Holographic complexity: With $d_i = 2,\ \theta = -\frac{1}{3}$ in (3.38) gives

$$C = \frac{V_2 R^2}{G_4}\int_\epsilon dr \left(\frac{t(r)^{\frac{15}{14}-\frac{\sqrt{2}}{7}}\sqrt{1-t'(r)^2}}{r^{7/2}}\right). \tag{3.45}$$

Restricting to the regime $t'(r) \ll 1$, we perform this integral rewriting as

$$C = \frac{V_2 R^2}{G_4}\int_\epsilon^{r_\Lambda} dr \left(\frac{t(r)^{\frac{15}{14}-\frac{\sqrt{2}}{7}}\left(1-\frac{t'(r)^2}{2}\right)}{r^{7/2}}\right). \tag{3.46}$$

Then using (3.44) truncating to $t(r) = t_0 + s_2 r^2 + s_4 r^4$ using (B3), the complexity (3.46) up to next-to-leading-order in t_0 is obtained as

$$C = \frac{V_2 R^2}{G_4}\left(\frac{2}{5}t_0^{\frac{15}{14}-\frac{\sqrt{2}}{7}}\left(\frac{1}{\epsilon^{5/2}}-\frac{1}{r_\Lambda^{5/2}}\right)-\frac{2883\left(\frac{1}{t_0}\right)^{\frac{13}{14}+\frac{\sqrt{2}}{7}}\left(\frac{1}{\sqrt{r_\Lambda}}-\frac{1}{\sqrt{\epsilon}}\right)}{50\left(233+60\sqrt{2}\right)}\right). \tag{3.47}$$

3.3.2 $d_i = 4,\ \theta = -1$

This is related to the $D4$-brane supergravity phase as stated earlier.

For $d_i = 4$ and $\theta = -1$, the equation of motion (3.39) becomes

$$20\, r\, t(r)\, t''(r) + 17\, r\left(1 - t'(r)^2\right) - 125\, t(r)\, t'(r)\left(1 - t'(r)^2\right) = 0\,. \tag{3.48}$$

Using the ansatz $t(r) = t_0 + \sum_{n\in\mathbb{Z}_+} y_n r^n$, we obtain the following solution to (3.48):

$$t(r) = t_0 + y_2 r^2 + y_4 r^4\,, \tag{3.49}$$

with y_i given in (B4). The plots of the solution (3.49) and its derivatives are qualitatively similar to those in AdS-Kasner spacetimes and the $d_i = 2, \theta = -\frac{1}{3}$ hv-cosmology. Ignoring higher order terms in (3.48), we obtain

$$-34r + 5t(r)\left(-8rt''(r) + 50t'(r)\right) = 0\,. \tag{3.50}$$

Solving this with the ansatz $t(r) = t_0 + \sum_{n\in\mathbb{Z}_+} v_n r^n$ gives the qualitatively similar complexity surface (with v_i in (B5)):

$$t(r) = t_0 + v_2 r^2 + v_4 r^4\,. \tag{3.51}$$

Solving the nonlinear equation (3.48) numerically as in AdS-Kasner gives numerical solutions for the complexity surfaces $t(r)$ and their derivatives. These are shown in Fig. 3.8.

Holographic complexity: Substituting $d_i = 4,\ \theta = -1$ in (3.38) gives

$$C = \frac{V_4 R^4}{G_6}\int_\epsilon dr\left(\frac{t(r)^{17/20}\sqrt{1-t'(r)^2}}{r^{25/4}}\right) \sim \frac{V_4 R^4}{G_6}\int_\epsilon^{r_\Lambda} dr\left(\frac{t(r)^{17/20}\left(1-\frac{t'(r)^2}{2}\right)}{r^{25/4}}\right). \tag{3.52}$$

Similar to the discussion for $d_i = 2, \theta = -\frac{1}{3}$, we approximate as $t(r) = t_0 + v_2 r^2 + v_4 r^4$ (with v_2, v_4 in (B5)) and simplify (3.52). The calculations are similar to the earlier case: complexity up to next-to-leading-order in t_0 is

$$C = \frac{V_4 R^4}{G_6}\left[t_0^{17/20}\left(\frac{4}{21\epsilon^{21/4}}-\frac{4}{21{r_\Lambda}^{21/4}}\right) + \left(\frac{1}{t_0}\right)^{23/20}\left(\frac{4913}{525\left(\sqrt{715}-13\right)\left(13+\sqrt{715}\right)\epsilon^{13/4}}-\frac{4913}{525\left(\sqrt{715}-13\right)\left(13+\sqrt{715}\right){r_\Lambda}^{13/4}}\right)\right]. \tag{3.53}$$

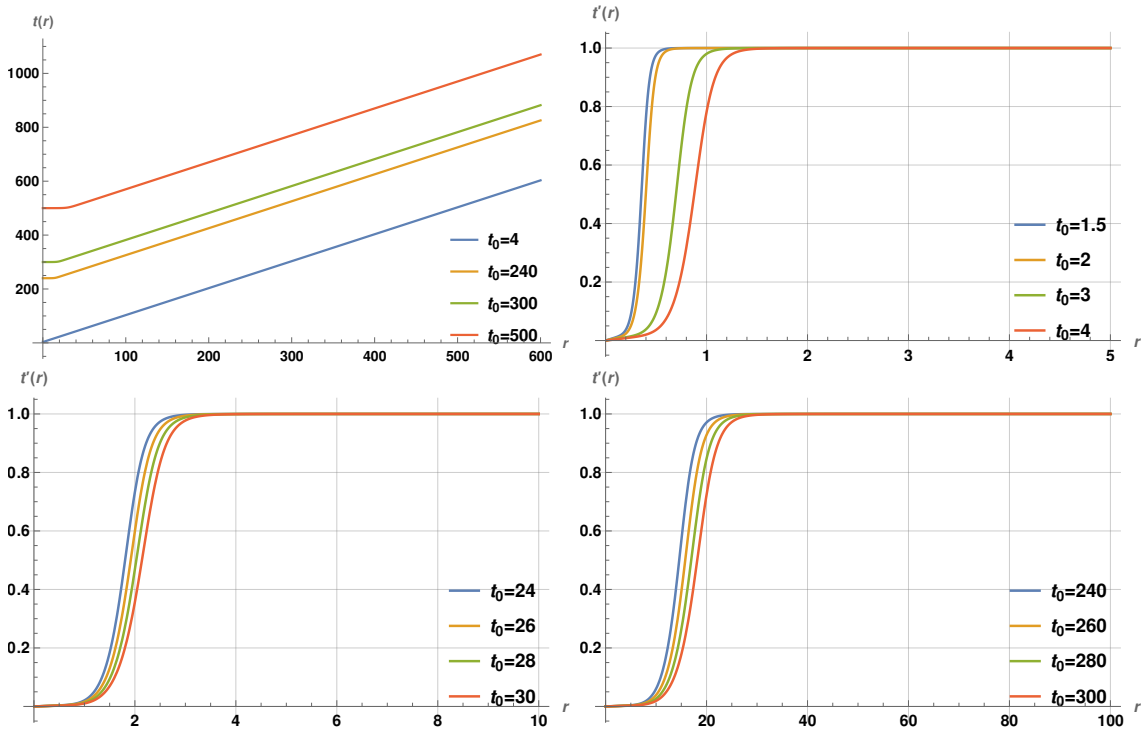

Figure 3.8: Plots of complexity surface versus r and $t'(r)$ versus r for $d_i = 4$ and $\theta = -1$ in hyperscaling violating cosmology.

$\{d_i = 2,\ \theta = -\frac{1}{3}\}$ vs $\{d_i = 4,\ \theta = -1\}$ hv-cosmologies: Comparing Fig. 3.7 and Fig. 3.8, we see that the numerical solution of $d_i = 4,\ \theta = -1$ hv-cosmology becomes lightlike for a smaller r-value relative to that for $d_i = 2,\ \theta = -\frac{1}{3}$. The $\sqrt{1 - t'(r)^2}$ factor in the volume complexity expression implies $d_i = 4,\ \theta = -1$ complexity vanishing earlier relative to that in $d_i = 2,\ \theta = -\frac{1}{3}$. These theories have effective space dimension $d_{eff} = d_i - \theta$ so the effective dimensions are $d_{eff} = 5$ and $d_{eff} = \frac{7}{3}$ respectively: so the larger effective dimension case acquires vanishing complexity at smaller r-values. This is similar to the observations in AdS-Kasner discussed in sec. 3.2.4.

Let us summarize the results for complexity in AdS_5-Kasner and hyperscaling violating cosmologies up to next-to-leading-order in t_0 (the results to this order are the same whether we use

the linearized equation ignoring higher order terms in $t'(r)$, or the full nonlinear one):

$$
\begin{aligned}
&(\mathrm{AdS}_5-\mathrm{Kasner}) \qquad C \approx \frac{V_3R^3}{G_5}\left[t_0\left(\frac{0.3}{\epsilon^3}-\frac{0.3}{r_\Lambda^3}\right)+\frac{1}{t_0}\left(\frac{0.1}{\epsilon}-\frac{0.1}{r_\Lambda}\right)+O\left(\left(\frac{1}{t_0}\right)^3\right)\right],\\
&\left(d_i=2,\ \theta=-\frac{1}{3}\right) \qquad C \approx \frac{V_2R^2}{G_4}\left(\frac{2}{5}t_0^{\frac{15}{14}-\frac{\sqrt{2}}{7}}\left(\frac{1}{\epsilon^{5/2}}-\frac{1}{r_\Lambda^{5/2}}\right)-\frac{2883\left(\frac{1}{t_0}\right)^{\frac{13}{14}+\frac{\sqrt{2}}{7}}\left(\frac{1}{\sqrt{r_\Lambda}}-\frac{1}{\sqrt{\epsilon}}\right)}{50\left(233+60\sqrt{2}\right)}\right),\\
&(d_i=4,\ \theta=-1) \qquad C \approx \frac{V_4R^4}{G_6}\left[t_0^{17/20}\left(\frac{4}{21\epsilon^{21/4}}-\frac{4}{21{r_\Lambda}^{21/4}}\right)\right.\\
&\left.+\left(\frac{1}{t_0}\right)^{23/20}\left(\frac{4913}{525\left(\sqrt{715}-13\right)\left(13+\sqrt{715}\right)\epsilon^{13/4}}-\frac{4913}{525\left(\sqrt{715}-13\right)\left(13+\sqrt{715}\right){r_\Lambda}^{13/4}}\right)\right].
\end{aligned}
\tag{3.54}
$$

The leading divergence of complexity from above is $C=\frac{V_2R^2}{G_4\epsilon^{5/2}}\,t_0^{\frac{15-2\sqrt{2}}{14}}$ for $d_i=2,\theta=-\frac{1}{3}$, and $C=\frac{V_4R^4}{G_6\epsilon^{21/4}}\,t_0^{17/20}$ for $d_i=4,\theta=-1$. Overall, at leading order in (3.54), we see that the holographic complexity of AdS_5-Kasner spacetime is linearly proportional to t_0 whereas in hyperscaling violating cosmologies, complexity is proportional to $t_0^{0.9}$ and $t_0^{0.85}$ summarized below:

$$
\begin{aligned}
&(\mathrm{AdS}_5-\mathrm{Kasner}) \qquad C\propto t_0\,,\\
&\left(d_i=2,\ \theta=-\frac{1}{3}\right) \qquad C\propto t_0^{0.9}\,, \qquad (d_i=4,\ \theta=-1) \qquad C\propto t_0^{0.85}\,.
\end{aligned}
\tag{3.55}
$$

The complexity scaling in hyperscaling-violating cosmologies reflects the fact that the dual theories reside in an effective space dimension, $d_{eff}=d_i-\theta$. It may be interesting to investigate the underlying effective lattice qubit models that simulate this behavior, which could potentially differ from relativistic CFTs, considering the general arguments in [25].

3.3.3 Numerical computation of complexity in hv cosmologies

We now compute holographic complexity of hyperscaling violating cosmologies, for $d_i=2,\ \theta=-\frac{1}{3}$, and $d_i=4,\ \theta=-1$, as for *AdS*-Kasner spacetimes in sec. 3.2.4. For this purpose, we use the numerical solutions of the cosmologies as discussed earlier, and numerically perform the integrations appearing in the complexity expressions in (3.45) for $d_i=2,\ \theta=-\frac{1}{3}$, and (3.52) for $d_i=4,\ \theta=-1$ (using the full nonlinear expression). The variation of holographic complexity with t_0 in these backgrounds is shown in Fig. 3.9.

As shown in (3.55), the complexity of hyperscaling-violating cosmologies does not scale linearly with t_0 , in contrast to the scaling observed in *AdS* Kasner spacetimes. However, the exponents remain positive, so complexity continues to decrease as t_0 approaches the singularity, becoming vanishingly small as $t_0\to 0$. Thus, the dual Kasner state continues to exhibit low complexity, as illustrated in Fig. 3.9.

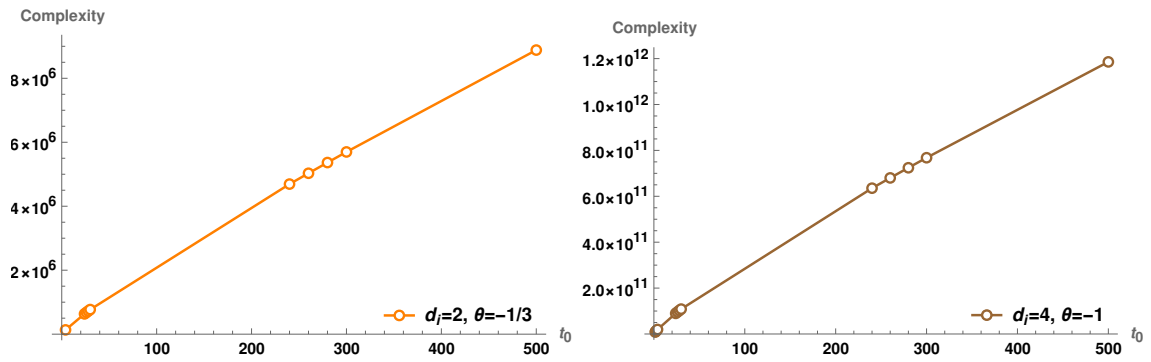

Figure 3.9: Numerical plots of holographic complexity versus t_0 for $d_i = 2,\ \theta = -1/3$ and $d_i = 4,\ \theta = -1$ cosmologies.

3.4 Complexity: isotropic Lifshitz Kasner cosmologies

The 2-dim dilaton gravity formulation [113] led to new Kasner cosmologies with Lifshitz asymptotics. The equations of motion are rather constraining however admitting only certain values for the various exponents: in particular the cosmological solutions turn out to have $\theta = 0$ so $\gamma = 0$ with Lifshitz exponent $z = d_i$. In 2-dim form, they are described by the 2-dim dilaton gravity action (3.6) with dilaton potential, parameters, and the (t, r)-scaling exponents in (3.7) below. Also given below is the higher dimensional Lifshitz Kasner cosmology:

$$
\begin{aligned}
U = \phi^{1/d_i}\Big(-c_1 + \frac{c_2}{\phi^2} e^{\lambda\Psi}\Big)\,, \quad \lambda = -\sqrt{\frac{2d_i}{d_i-1}}\,, \quad c_1 = \frac{2(2d_i-1)}{d_i} \quad c_2 = \frac{2(d_i-1)}{d_i}\,,\\
ds^2 = R^2\left(-\frac{dt^2}{r^{2z}} + \frac{dr^2}{r^2} + t^{2/d_i}\frac{dx_i^2}{r^2}\right), \qquad e^{\Psi} = t^{\alpha} r^{-\alpha}\,, \quad z = d_i\,,\\
k = 1, \quad m = -1\,, \quad a = \frac{d_i-1}{d_i}\,, \quad b = -3 + \frac{1}{d_i}\,, \quad -\beta = \alpha = -\sqrt{\frac{2(d_i-1)}{d_i}}\,.
\end{aligned}
\tag{3.56}
$$

Here R is the analog of the AdS scale, and we are suppressing an additional scale in g_{tt} arising due to the nontrivial Lifshitz scaling. The nonrelativistic time-space scaling implies that lightlike trajectories have $dt^2 = r^{2z-2}dr^2$ so to identify lightlike limits it is convenient to use (t, ρ) coordinates with $\rho \sim r^z$. To illustrate this and study complexity, we will focus on the Lifshitz Kasner cosmology with $z = d_i = 2$ and exponents $a = \frac{1}{2}\,,\ b = -\frac{5}{2}$ with metric

$$
ds^2 = R^2\left(-\frac{dt^2}{r^4} + \frac{dr^2}{r^2} + \frac{t}{r^2}\left(dx_1^2 + dx_2^2\right)\right). \tag{3.57}
$$

Redefining $r^2 \sim \rho$ and appropriately absorbing numerical factors redefining the various lengthscales makes lightlike trajectories have $dt^2 = d\rho^2$, with the metric (3.57) recast as

$$
ds^2 = R^2\left(-\frac{dt^2}{\rho^2} + \frac{d\rho^2}{\rho^2} + \frac{t}{\rho}(dx_1^2 + dx_2^2)\right). \tag{3.58}
$$

Parametrizing the complexity surface by $t(\rho)$ gives the complexity volume functional

$$C = \frac{V_2 R^3}{G_4 R} \int_\epsilon d\rho \left(\frac{t(\rho)}{\rho^2} \sqrt{1 - (t'(\rho))^2} \right), \tag{3.59}$$

with $V_2 = \int dx_1 dx_2$. Extremizing for the complexity surface $t(\rho)$ gives the equation of motion

$$\rho\, t(\rho)\, t''(\rho) - 2t(\rho)\, t'(\rho)\big(\big(1 - t'(\rho)^2\big) + \rho\, \big(1 - t'(\rho)^2\big) = 0\,. \tag{3.60}$$

The perturbative solution of (3.60) for the ansatz $t(\rho) = \sum_{n\in\mathbb{Z}_+} c_n \rho^n$ similar to the previous cases up to $\mathcal{O}(\rho^4)$ is given by

$$t(\rho) = t_0 + \frac{\rho^2}{2t_0} - \frac{\rho^4}{8{t_0}^3}\,. \tag{3.61}$$

The behavior of this perturbative solution is qualitatively similar to that in AdS-Kasner and hv-cosmologies, so we suppress these plots here.

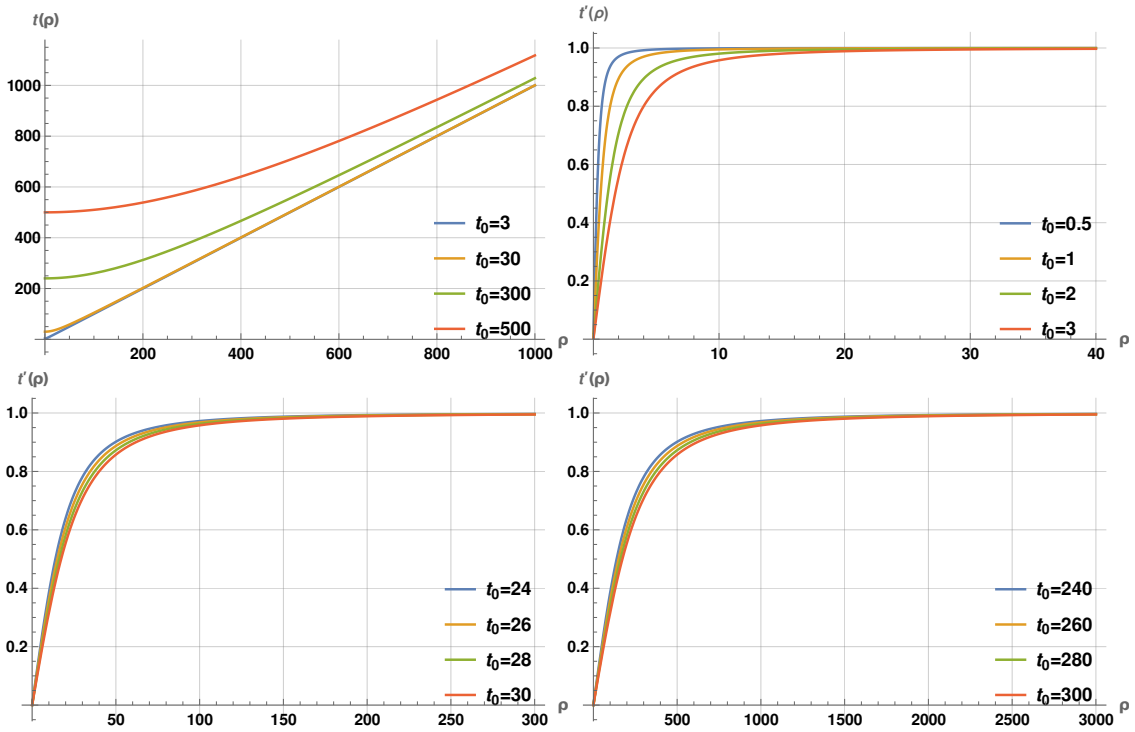

Figure 3.10: Variation of volume complexity surfaces $t(\rho)$ and their derivative $t'(\rho)$ with radial distance ρ for 4-dim Lifshitz Kasner cosmology.

As in the earlier cases, it is instructive to study the complexity surface equation numerically, so we solve (3.60) with boundary conditions for $t(\rho)$ and $t'(\rho)$ at the boundary $\rho = \epsilon_\rho$ with appropriate numerical values for ϵ_ρ, along similar lines as described earlier. The numerical results are shown in Fig. 3.10 which display the variation of the complexity surfaces and their derivatives with ρ for

various t_0 values. The plots show that the transition to the lightlike regime is slower with nontrivial Lifshitz z-exponent (relative to AdS, $z = 1$).

Perturbatively we can compute holographic complexity in the regime $\rho \lesssim t_0$ where $t'(\rho) < 1$, approximating complexity (3.59) as

$$C \sim \frac{V_2 R^2}{G_4} \int_{\epsilon_\rho}^{\rho_\Lambda} d\rho \left[\frac{t(\rho)}{\rho^2} \left(1 - \frac{t'(\rho)^2}{2} \right) \right]. \tag{3.62}$$

For the perturbative solution (3.61), holographic complexity after truncating (3.62) up to next-to-leading-order in t_0 is given by

$$C \approx \frac{V_2 R^2}{G_4} \left[t_0 \left(\frac{1}{\epsilon_\rho} - \frac{1}{\rho_\Lambda} \right) + \frac{(\rho_\Lambda^3 - \epsilon_\rho^3)}{24 t_0^3} + \mathcal{O}\left(\frac{1}{t_0} \right)^5 \right]. \tag{3.63}$$

We have described the $z = 2$ Lifshitz Kasner cosmology so far: other $z = d_i$ cases in $(d_i + 2)$-dims exhibit similar behaviour. The (t, ρ) coordinates with $\rho \sim r^z$ in Lifshitz Kasner cosmologies allow us to conveniently see that the complexity surfaces become lightlike in the bulk. The metric in (3.56) is recast as

$$ds^2 = R^2 \left(-\frac{dt^2}{\rho^2} + \frac{d\rho^2}{\rho^2} + \frac{t^{2/z}}{\rho^{2/d_i}} dx_i^2 \right) \quad \rightarrow \quad C = \frac{V_{d_i} R^{d_i}}{G_{d_i+2}} \int d\rho \, \frac{t(\rho)}{\rho^2} \sqrt{1 - (t'(\rho))^2} \, . \tag{3.64}$$

The leading divergence in C is

$$C \sim \frac{R^{d_i}}{G_{d_i+2}} \frac{V_{d_i}}{\epsilon_r^{d_i}} \, t_0 \, , \qquad \epsilon_\rho = \epsilon_r^z = \epsilon_r^{d_i} \, . \tag{3.65}$$

The above equation shows the linear time growth of complexity in Lifshitz Kasner. Further, from (3.65), we can show that

$$\frac{dC}{dt_0} \sim N_{dof} \, V_{d_i} \Lambda_{UV}^{d_i} \, , \tag{3.66}$$

where $\epsilon_\rho \sim \epsilon_r^{d_i} \equiv \Lambda_{UV}^{d_i}$. The observations in sec. 3.2.1 and sec. 3.2.4 thus apply here as well upon analysing (3.64), and the dual state appears to have vanishingly low complexity as one approaches the singularity. This is vindicated in Fig. 3.11 which shows holographic complexity plotted against t_0 which reveals a linear decrease as the anchoring time slice approaches the singularity, *i.e.* $t_0 \to 0$.

3.5 Holographic entanglement entropy: AdS Kasner etc

We will review the discussion in [43] here. Classical extremal surfaces in cosmological backgrounds are parametrized by $(t(r), x(r))$, $\Delta x = l$, and $t(r) \xrightarrow{r \to 0} t_0$. The time function $t(r)$ exhibits nontrivial bending due to the time-dependence. This extremal surface is located at a constant t slice on the boundary denoted by $t = t_0$ and dips into the bulk up to the turning point and returns to t_0. Here

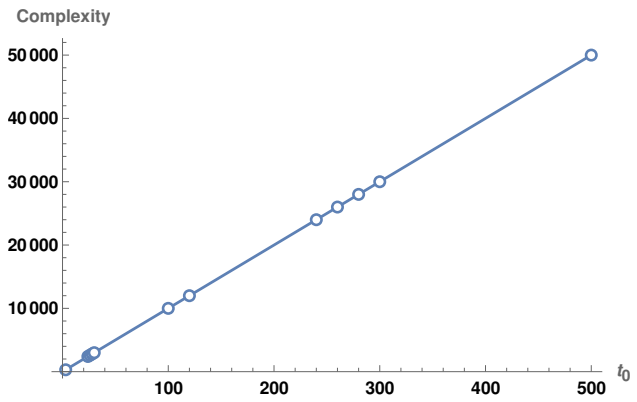

Figure 3.11: Variation of complexity with t_0 for 4-dim Lifshitz Kasner cosmology.

l is the width of the strip along the x direction (taking some $x^1 = x$), and the extremal surface wraps the other $x_{j\neq 1}$ directions. The holographic entanglement entropy is then given by:

$$S_{\rm EE} = \frac{1}{4G_{d_i+2}} \int \prod_{x_j \neq x}^{j=1,2,\ldots,(d_i-1)} \left(\phi^{1/d_i} dx_j\right) \sqrt{\frac{e^f}{\phi^{(d_i-1)/d_i}}(-dt^2 + dr^2) + \phi^{2/d_i} dx^2}\,. \tag{3.67}$$

The absence of $x(r)$ in (3.67) leads to a conserved conjugate momentum: solving for $x'(r)$ gives

$$(x'(r))^2 = A^2 \frac{\frac{e^f}{\phi^{(d_i+1)/d_i}}\left(1 - t'(r)^2\right)}{\phi^2 - A^2}\,. \tag{3.68}$$

Substituting back into (3.67) gives

$$S_{\rm EE} = \frac{V_{d_i-1}}{4G_{d_i+2}} \int dr \left(\frac{e^{f/2}\phi^{(3-1/d_i)/2}}{\sqrt{\phi^2 - A^2}}\right) \sqrt{1 - t'(r)^2}. \tag{3.69}$$

At the turning point, $x'(r) \to \infty$ implying $A = \phi_* = \frac{t_*}{r_*^{|m|}}$ (in the approximation ϕ is nonvanishing and $t'(r) \ll 1$) where $t_* = t(r_*)$ (since, $\phi = t^k r^m$, $k = 1$, $m = -|m| < 0$).

For the AdS Kasner spacetime, (3.68), (3.69), simplify to

$$x'(r)^2 = A^2 \left(\frac{1}{t^{2/d_i}}\right) \frac{1 - t'(r)^2}{\frac{t^2}{r^{2d_i}} - A^2}\,, \qquad S_{\rm EE} = \frac{V_{d_i-1}}{4G_{d_i+2}} \int dr \left(\frac{t^{2-1/d_i}}{r^{2d_i}}\right) \frac{\sqrt{1 - t'(r)^2}}{\sqrt{\frac{t^2}{r^{2d_i}} - A^2}}\,. \tag{3.70}$$

Using $A = \phi_*$, $u = \frac{r}{r_*}$, we find the width scaling

$$\frac{l}{2} = \int_0^{r_*} dr x'(r) = r_* \int_0^1 \frac{du}{t^{1/d_i}} \frac{\sqrt{1 - t'(r)^2}}{\sqrt{(\phi/\phi_*)^2 - 1}} \quad \Rightarrow \quad l \sim r_*\,, \quad A = \phi_* = \frac{t_*}{r_*^{d_i}}\,. \tag{3.71}$$

For a subregion anchored at a time slice $t_0 \gg 0$ far from the singularity, the RT/HRT surface bends in time mildly away from the singularity. The turning point is (t_*, r_*), with $A > 0$ as above for finite size subregions. The IR limit where the subregion becomes the entire space is

defined as $l \to \infty$ and we expect $r_* \to \infty$ so the surface extends deep into the interior: here $A = 0$. In the semiclassical region far from the singularity $t_0 \to \infty$, solving the extremization equation perturbatively for $t(r) = t_0 + \sum_{n\in\mathbb{Z}_+} c_n r^n$ shows that $t_* \gtrsim t_0$ with $t'(r) \ll 1$ for finite subregions [43] (reviewed numerically in App. 6.7). This perturbative analysis is similar to the one for the complexity surface discussed earlier (see Fig. 3.1). Analyzing this in the IR limit is more challenging. In the following, we will analyze this numerically for the entangling RT/HRT surfaces and find results similar to those for the complexity surfaces.

3.6 Entanglement, AdS Kasner: numerical results

In this section, we will numerically analyze the codim-2 RT/HRT surfaces for entanglement entropy, building on the studies in [43], following the same approach as for complexity. First, we obtain the perturbative solution of the equation of motion for $t(r)$ and then use this perturbative solution for boundary conditions to solve numerically. The extremization equation for $t(r)$ following from the entanglement area functional (3.70) is (there is a typo in one of the corresponding equations in [43], but the analysis there is correct):

$$\left(1 - t'(r)^2\right)\left(d_i^2 t'(r) + \frac{r\left(t(r)^2 - A^2 r^{2d_i}\right)}{t(r)^3} - \frac{d_i r}{t(r)}\right) - \frac{\left(t(r)^2 - A^2 r^{2d_i}\right) d_i r t''(r)}{t(r)^2} = 0\,. \tag{3.72}$$

We will focus on solving (3.72) in the IR limit $A = 0$ (3.71) for infinitely wide strip subregions in $AdS_{5,7}$-Kasner spacetimes in sec. 3.6.1 and sec. 3.6.2 respectively. The above equation in the IR limit $A = 0$ becomes

$$d_i\, r\, t(r)\, t''(r) \;-\; \left(1 - t'(r)^2\right)\left(d_i^2\, t(r)\, t'(r) - (d_i - 1) r\right) = 0\,. \tag{3.73}$$

3.6.1 Holographic entanglement entropy in AdS_5-Kasner

For AdS_5-Kasner with $d_i = 3$, the IR limit (3.73) becomes

$$3\, r\, t(r)\, t''(r) \;-\; \left(1 - t'(r)^2\right)\left(9\, t(r)\, t'(r) - 2r\right) = 0\,. \tag{3.74}$$

The perturbative solution of (3.74) using the ansatz $t(r) = t_0 + \sum_{n\in\mathbb{Z}_+} c_n r^n$, after truncating, is

$$t(r) \sim t_0 + \frac{r^2}{6 t_0}\,. \tag{3.75}$$

The numerical solutions of (3.74) and their derivatives are shown in Fig. 3.12. This shows that the behaviour of RT/HRT surfaces is similar to complexity surfaces, as discussed earlier. In particular, the RT/HRT surface for lower t_0 (closer to the singularity) becomes lightlike earlier in comparison to RT surfaces with higher t_0 values. Thus as we approach the singularity with $t_0 \to 0$, entanglement entropy becomes vanishingly small. In particular near the singularity, entanglement

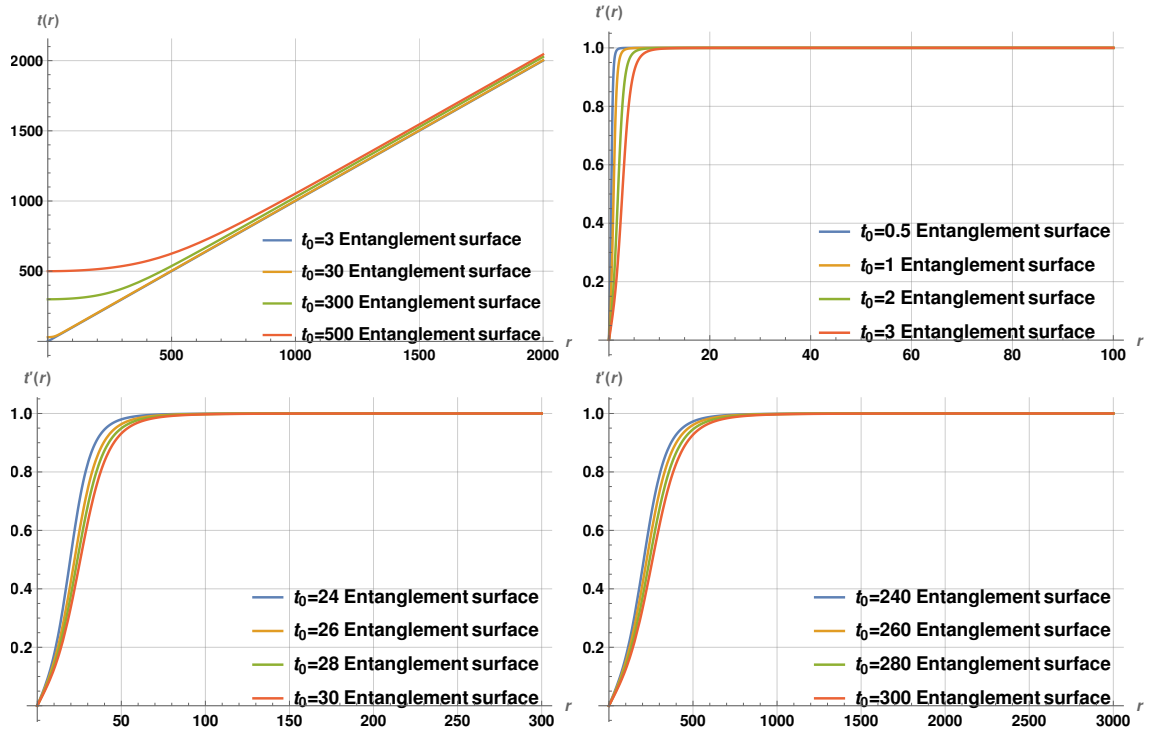

Figure 3.12: Variations of the RT/HRT surface $t(r)$ vs r and $t'(r)$ vs r in AdS_5-Kasner spacetime for various t_0 slices.

entropy vanishes as did complexity. There is an extreme thinning of the degrees of freedom near the singularity.

For AdS_4-Kasner, the results are qualitatively similar but the numerics turn out to not be as clean for just technical rather than physics reasons so we do not discuss this.

3.6.2 Holographic entanglement entropy, AdS_7-Kasner

The $t(r)$ equation of motion in the IR limit (3.73) for AdS_7-Kasner spacetime with $d_i = 5$ is:

$$5\, r\, t(r)\, t''(r) \;-\; \left(1 - t'(r)^2\right)\left(25\, t(r)\, t'(r) - 4r\right) = 0\,. \tag{3.76}$$

The perturbative solution of (3.76) using the ansatz $t(r) = t_0 + \sum_{n\in\mathbb{Z}_+} c_n r^n$ is obtained as:

$$t(r) = t_0 + \frac{r^2}{10 t_0} - \frac{9 r^4}{1000 t_0^3}. \tag{3.77}$$

The numerical solutions of (3.76) and their derivatives are shown in Fig. 3.13: we find the entangling surfaces $t(r)$ have qualitatively similar behaviour as in AdS_5-Kasner.

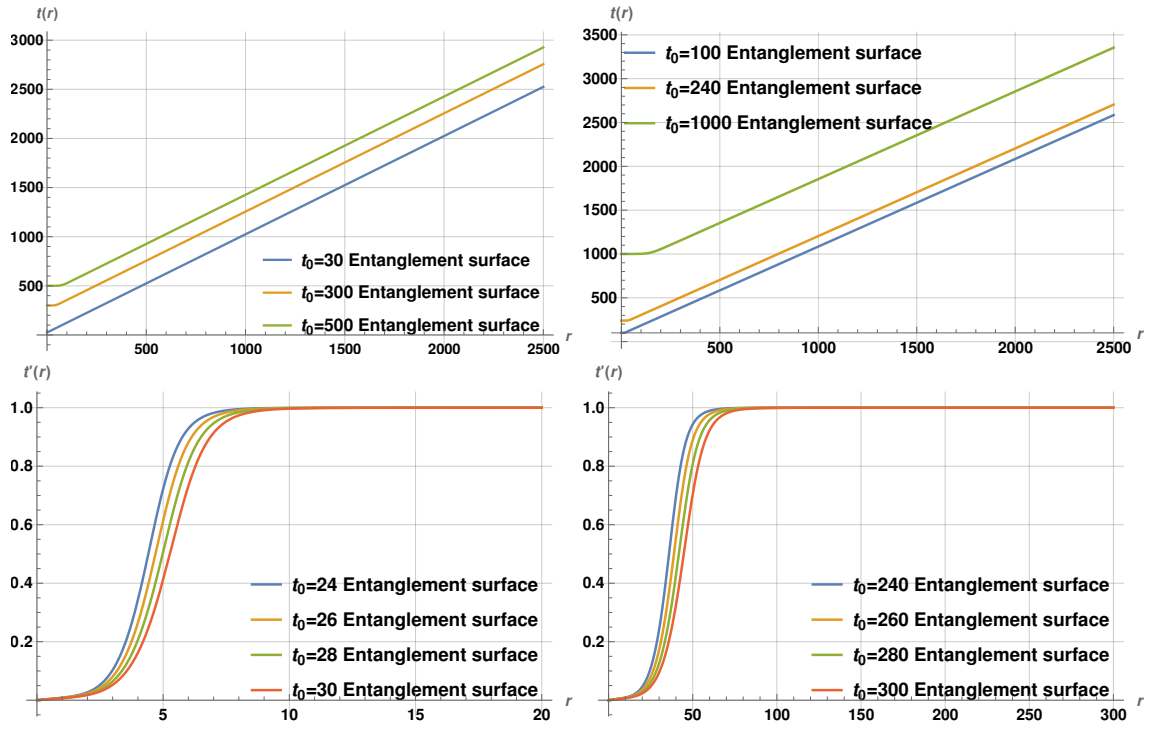

Figure 3.13: Numerical plots of the RT/HRT surfaces $t(r)$ versus r and $t'(r)$ versus r in AdS$_7$-Kasner spacetime for different t_0 slices.

3.6.3 Numerical computation of holographic entanglement entropy

The holographic entanglement entropy (3.70) in the IR limit ($A = 0$) for the AdS_{d_i+2}-Kasner spacetime is given by

$$S_{\rm EE} = \frac{R^{d_i} V_{d_i-1}}{4G_{d_i+2}} \int_\epsilon dr \left(\frac{t(r)^{(d_i-1)/d_i}}{r^{d_i}} \right) \sqrt{1 - t'(r)^2}\,. \tag{3.78}$$

We evaluate the integrals in (3.78) numerically for $AdS_{5,7}$-Kasner spacetimes, setting $\epsilon = 0.01$ and normalizing the length scales R, V_{d_i-1}, G_{d_i+2} to unity. As an order-of-magnitude estimate with $t_0 \sim 1000$, we obtain

$$S_{\rm EE} \sim \frac{t_0^{2/3}}{\epsilon^2} \sim 10^6. \tag{3.79}$$

The variation of entanglement entropy in the IR limit for $AdS_{5,7}$-Kasner spacetimes as a function of t_0 is shown in Fig. 3.14. This indicates that the entanglement entropy in AdS Kasner spacetime decreases as t_0 decreases, eventually vanishing as $t_0 \to 0$. This behavior aligns with our observations in Fig. 3.12, where the entangling surfaces $t(r)$ become lightlike earlier for anchoring time slices t_0 closer to the singularity.

We now compare the IR entangling RT/HRT surfaces for AdS_5-Kasner (Fig. 3.12) and AdS_7-Kasner (Fig. 3.13), as we had done for complexity surfaces in Sec. 3.2.4. We observe that the

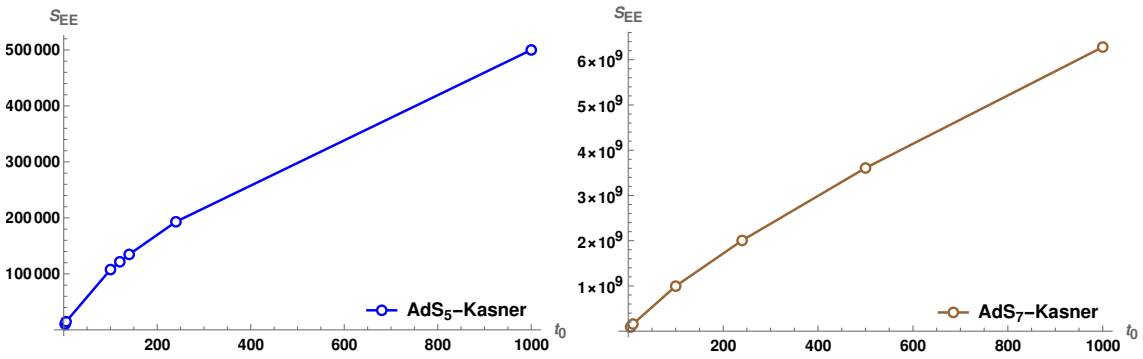

Figure 3.14: Numerical plots of holographic entanglement entropy versus t_0 for $AdS_{5,7}$-Kasner.

surfaces approach the lightlike regime earlier in AdS_7-Kasner relative to AdS_5-Kasner, similar to the complexity surfaces. Once again, this behavior appears to stem from the amplification factor $\frac{1}{r^{d_i-1}}$ of the lightlike term $\sqrt{1-(t')^2}$ in entanglement entropy, leading to a more rapid effective thinning of the degrees of freedom in higher dimensions.

As a mathematical observation, by comparing the $t(r)$ plots in AdS Kasner, we see that the complexity surfaces become lightlike earlier than the entangling RT/HRT surfaces. This follows from the equations of motion, which share a similar structure but differ in the numerical factors that appear. For AdS_5-Kasner, we obtain from (3.74) and (3.15),

$$1-(t')^2 = \frac{\frac{3}{2} r\, t\, t''}{\frac{9}{2} t\, t' - r} \quad [\text{EE}]\,; \qquad 1-(t')^2 = \frac{r\, t\, t''}{4 t\, t' - r} \quad [\text{complexity}]\,. \tag{3.80}$$

Since the denominator factors are comparable, the relative factor of $\frac{3}{2}$ makes $(1-(t')^2)$ larger, resulting in a smaller $t'(r)$ for the entangling surface $t(r)$.

Explicit expressions for holographic entanglement entropy (3.69) can be obtained for hyperscaling violating cosmologies using (3.35). The exponents for $t(r)$ are fairly nontrivial. The r-scalings give the leading divergence as $S_{EE} \sim \frac{V_{d_i-1}}{G_{d_i+2}} \frac{R^{d_i-\theta}}{\epsilon^{d_i-\theta-1}}$ where we have reinstated the dimensionful bulk scale R (which can be done simply on dimensional grounds). This can be recast as

$$S_{EE} \sim \frac{V_{d_i-1}}{G_{d_i+2}} \frac{R^{d_i-\theta}}{\epsilon^{d_i-\theta-1}} \;\sim\; N_{eff}(\epsilon)\, \frac{V_{d_i-1}}{\epsilon^{d_i-1}}\,, \qquad N_{eff}(\epsilon) = \frac{R^{d_i-\theta}}{G_{d_i+2}}\, \epsilon^{\theta}\,, \tag{3.81}$$

where N_{eff} is the effective scale-dependent number of degrees of freedom evaluated at the UV cutoff length ϵ (see [96], [201]). In concrete gauge/string realizations of hyperscaling violating theories obtained by dimensional reduction of nonconformal Dp-branes, it can be seen that the lengthscales in the Dp-brane description reorganize themselves as the above and also match various expectations, including from considerations of the holographic c-function from a 2-dim dilaton gravity point of view [200]. For instance, the $d_i = 2,\ \theta = -\frac{1}{3}$ case corresponding to the D2-brane supergravity phase with $G_4 \sim \frac{G_{10}}{R^6}$ after the transverse sphere reduction gives $N_{eff} = N^2\, (g_{YM}^2 N \epsilon)^{-1/3}$ which

ends up being consistent with the regime of validity of the D2-supergravity phase. By comparison the complexity scalings then are less obvious. The leading divergence of complexity in hyperscaling violating theories can be expressed as

$$C \sim \frac{V_{d_i}}{G_{d_i+2}} \left(\frac{R}{\epsilon}\right)^{d_i-\theta-\frac{\theta}{d_i}} \sim N_{eff}(\epsilon) \frac{V_{d_i}}{\epsilon^{d_i}} \left(\frac{R}{\epsilon}\right)^{-\frac{\theta}{d_i}}, \tag{3.82}$$

using N_{eff} in (3.81). The extra factor $(\frac{R}{\epsilon})^{\frac{-\theta}{d_i}}$ arising from the extra metric factor for codim-1 surfaces (relative to codim-2) cannot be obviously recast in terms of field theory parameters once N_{eff} is pulled out (see [150, 152, 174, 186] for other complexity studies). Of course this can be expressed in terms of some effective UV cutoff $\tilde{\Lambda}^{d_i-\frac{\theta}{d_i}} R^{-\frac{\theta}{d_i}}$. The scalings of complexity with time are also nontrivial. It would be interesting to understand this better.

The numerical plots of the entangling RT/HRT surfaces for the hyperscaling violating cosmology with $d_i = 4,\ \theta = -1$ are qualitatively similar to the above for sufficiently high t_0: away from this, there appear to be some numerical issues (as well as for the $d_i = 2,\ \theta = -\frac{1}{3}$ case), similar to the AdS_4 Kasner case stated earlier. So we do not discuss these in detail.

3.7 Discussion

We have examined holographic volume complexity and entanglement entropy in various families of cosmologies featuring Big-Bang/Crunch singularities, some of which have been previously studied (e.g., [22, 23, 24, 115, 117, 118, 119, 120]). These include AdS Kasner, hyperscaling-violating, and Lifshitz asymptotics. By focusing on isotropic Kasner-like singularities, we demonstrated that higher-dimensional complexity and entanglement can be reformulated in terms of those in two-dimensional dilaton gravity theories obtained via dimensional reduction [113], with the resulting expressions elegantly expressed solely in two-dimensional variables.

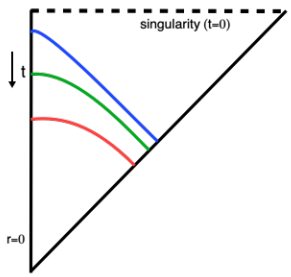

Figure 3.15: Cartoon of complexity and IR entanglement surfaces at various anchoring time slices t on the boundary ($r = 0$) in holographic cosmologies with Kasner-like Big-Crunch singularities. The extremal surfaces bend away from the singularity (dotted line, $t = 0$) and approach lightlike regimes eventually (approaching faster as $t \to 0$).

The equations of motion governing complexity and IR entangling surfaces, derived from the extremization of the respective functionals, can be solved perturbatively near the holographic boundary. This approach allows us to extract boundary conditions for numerical solutions of the surfaces. In the numerics, we impose a near-boundary cutoff ϵ: the interior end approaches a lightlike regime

so no interior regulator is required. The complexity plots appear in Figs. 3.2-3.3, 3.4, 3.5 for $AdS_{5,4,7}$ Kasner, Figs. 3.7, 3.8 for hyperscaling violating cosmologies, and Fig. 3.10 for Lifshitz Kasner, and those of entanglement appear in Fig. 3.12, Fig. 3.13 for $AdS_{5,7}$ Kasner.

Overall this shows that the surfaces begin spacelike near the boundary, bend in the direction away from the location of the singularity and transition to lightlike in the interior (sec. 3.2.1). For instance in (3.80), (i) with $(t')^2 \ll 1$ (spacelike), we see by using a series expansion for $t(r)$ that $t'(r) > 0$, and (ii) with $1 - (t')^2 \sim 0^+$ (lightlike), we see that $t'' > 0$. As the anchoring time slice is moved towards the singularity, the spacelike part shrinks and the transition to lightlike is more rapid. The overall picture depicting a future Big-Crunch singularity is shown in Fig. 3.15 above (which is top-bottom reflected relative to the plots): note that $t \equiv |t|$ here so our analysis applies equally well to past Big-Bang singularities (*e.g.* in (3.80), $t \to -t$ is a symmetry). The complexity and entanglement functionals contain a $\sqrt{1-(t')^2}$ factor so that the lightlike regimes give vanishing contributions: see Figs. 3.6, 3.9, 3.11 (complexity) and Fig. 3.14 (EE). Thus the near singularity region has vanishingly low complexity and entanglement and the "dual Kasner state" in all these theories corresponds to the effective number of qubits being vanishingly low, consistent with spatial volumes undergoing a Crunch. Our results corroborate those in [128] for volume complexity, and in [129] from holographic path integral optimization, in AdS Kasner. However our analysis (in particular numerically) is more detailed and applies to various families of cosmologies which are in the same "universality class" in the scaling behaviour (3.8) near the singularity. Our entanglement analysis develops further the semiclassical perturbative study in [43], where the entangling surfaces were shown to bend away from the singularity (and quantum extremal surfaces are driven far away). Our numerics is consistent with the behaviour of entangling surfaces for finite subregions which only bend mildly (App. 6.7).

This vanishing of holographic complexity and entanglement can be naturally understood from a renormalization group (RG) perspective. As the singularity is approached, the dual field theory undergoes RG flow toward a trivial infrared (IR) fixed point, resulting in a negligible number of effective degrees of freedom. This, in turn, leads to vanishing complexity. The contribution of soft modes to the overall complexity is minimal, as these low-energy excitations dominate in the IR and contribute insignificantly to the complexity. This perspective aligns with the work of Swingle and McGreevy [202], who provided a rigorous RG-based argument for the area law of entanglement entropy in gapped phases of matter. Their framework offers a conceptual foundation for understanding both entanglement and complexity through RG flow. For field theories dual to crunching geometries, the renormalization group (RG) flow traverses all intermediate energy scales—including potential gaps—and ultimately terminates at a trivial infrared (IR) fixed point. This results in a complete suppression of both entanglement and complexity, providing a particularly sharp and illustrative realization of RG-driven vanishing complexity. A more rigorous treatment, including detailed computations and mathematical analysis, is deferred to future work.

It is important to note that in the region very close to the singularity, where the transition to

a lightlike regime occurs rapidly, the anchoring time slice t_0 eventually becomes comparable to the cutoff ϵ, i.e., $t_0 \sim \epsilon$. At this stage, the semiclassical gravity framework employed here likely becomes unreliable. Consequently, when concluding that complexity approaches a vanishingly small value as $t_0 \to 0$, we are effectively extrapolating the observed trend of decreasing complexity into the near-singularity regime. While this extrapolation appears reasonable, a more detailed understanding of the very near-singularity region remains an important open question. At a fundamental level, our analysis of holographic volume complexity and entanglement—building on the work of [43, 127] and [128, 129], as well as studies of the limiting surface in the black hole interior [20]—indicates that such spacelike Kasner cosmological singularities are excluded from the entanglement wedge of observers. This exclusion, determined by extremal surfaces in a self-consistent manner, ensures that they avoid the vicinity of the singularity. We refer to this phenomenon as **"entanglement wedge cosmic censorship"** (thanks to Sumit Das for coining the phrase). In a sense, this is reassuring, since the opposite scenario would imply a breakdown of the semiclassical gravity framework and lead to inconsistencies. It is plausible that the study of null singularities will reveal qualitatively new behavior, particularly in light of the investigations of holographic duals in [115] and quantum extremal surfaces in [127], which tend to bend toward the singularity. The behavior of extremal surfaces bending away from the singularity is reminiscent of the absence of spacelike surfaces anchored at the future boundary in de Sitter space [213]: perhaps more general structures [223, 224] may be of value as near singularity probes.

We have focused on the isotropic Kasner subfamily, which naturally arises in the context of reduction to two dimensions. However, it is likely that more general spacetimes with hyperscaling-violating and Lifshitz asymptotics exist, exhibiting general anisotropic Kasner singularities—analogous to the fully anisotropic Kasner spacetimes in AdS. The constraint $\sum_i p_i = 1$ suggests that holographic volume complexity would remain the same as in our analysis. However, entanglement entropy, which depends on the choice of the boundary spatial subregion, would be sensitive to its spatial orientation.

More general AdS-BKL-type singularities were also studied in [24]. In these cases, spatial curvatures force BKL oscillations between various Kasner regimes (starting with some Kasner exponent negative), which continue indefinitely in the absence of external scalars [203, 204, 205]. In the presence of the scalar Ψ as we have, the BKL oscillations lead to attractor-type basins eventually (with all Kasner exponents positive). Holographic entanglement requires defining a spatial subregion and thus would appear to evolve along BKL oscillations. Since the volume complexity functional for anisotropic AdS-Kasner backgrounds is similar, the evolution of complexity naively appears insensitive to these BKL oscillations, but it would be interesting to explore complexity more carefully to see the role of spatial curvatures.

The effectively 2-dimensional nature of our bulk analysis suggests the existence of effective dual 1-dimensional qubit models governing complexity. In AdS and Lifshitz Kasner spacetimes, the decrease in complexity with time is linear, whereas in hyperscaling-violating theories, it is not.

These latter theories, characterized by a nonzero hyperscaling violation exponent θ, have effective spatial dimensions given by $d_{\text{eff}} = d_i - \theta$. It would be interesting to explore effective 1-dimensional qubit models that simulate this behavior, recalling the general arguments presented in [25].

Finally, it is worth noting that the Kasner singularities we have discussed exhibit time dependence that does not switch off asymptotically. This is reflected in the persistence of the nontrivial Kasner scale t_K appearing in our expressions: for instance (3.33) after reinstating t_K is really $C \sim N_{dof}\, V_{d_i} \Lambda_{UV}^{d_i}\, \frac{t_0}{t_K}$ so this perhaps cannot be extrapolated to asymptotically large timescales $t_0 \gg t_K$. The main merit of these models is the simplicity of the bulk in the vicinity of the singularity. Perhaps, as in [127] for quantum extremal surfaces, asymptotic regions with no time-dependence can be appended beyond $t_0 > t_K$ with appropriate boundary conditions. In this case, the extremal surfaces becoming lightlike hitting the past horizon here (Fig. 3.15) must instead presumably be extended to these asymptotic far-regions (translating the question of the behaviour at the past horizon to the behaviour asymptotically). This hopefully will lead to better understanding of the (non-generic) initial conditions in the asymptotic regions that give rise to this "dual Kasner state" and its low complexity.

Chapter 4

Time entanglement and pseudo-entropy

Our earlier studies focused on extremal surfaces—both quantum extremal surfaces (QES) and complexity surfaces—in the context of AdS/CFT, providing insights into cosmologies exhibiting Big-Crunch singularities. We now turn our attention to a different holographic framework: de Sitter holography, which has been extensively studied in the literature [209]-[226].

In de Sitter space, the holographic dual is a non-unitary Euclidean CFT residing on the future boundary I^+. This departure from AdS/CFT brings fundamentally new challenges in defining and interpreting extremal surfaces [213]. Notably, extremal surfaces anchored at the future boundary (I^+) do not have turning points that connect I^+ to itself. The absence of such $I^+ \to I^+$ returns implies that these surfaces extend inward toward the past. Consequently, they require additional input—either through specifying data in the interior of the spacetime or imposing boundary conditions in the far past—to be properly characterized. One notable scenario involves future-past extremal surfaces [217, 220] that extend from I^+ (the future boundary) to I^- (the past boundary) in fully Lorentzian de Sitter space. These surfaces are entirely timelike, with their area acquiring a factor of $-i$ that reflects their timelike nature. Alternatively, by invoking the Hartle-Hawking no-boundary proposal, one can construct a modified de Sitter geometry, often referred to as no-boundary de Sitter. Here, the extremal surface (no-boundary dS extremal surface) comprises a timelike segment anchored at I^+ and a spacelike segment emerging from a smoothly attached Euclidean hemisphere, resulting in a complex-valued surface [223, 224] (see also [221, 222] for discussions on dS_3/CFT_2) with both real and imaginary contributions to its area. We review the key aspects of extremal surfaces in de Sitter space in Sec. 4.1.

Unlike AdS, where specifying boundary data resolves the extremization problem,
dS extremal surfaces that originate at late times on I^+ do not return. This necessitates the inclusion of additional data for boundary conditions in the far past. As a result, two distinct scenarios arise:

future-past extremal surfaces in entirely Lorentzian dS, and no-boundary dS extremal surfaces, as discussed above. dS extremal surfaces necessarily involve a timelike component, which encodes a novel structure termed 'timelike entanglement', as proposed in [224]. This gives rise to two possible aspects of time-like entanglement: the first is rooted in the thermo-field double state inspired by the timelike future-past surfaces, while the second is based on the time-evolution operator, motivated by the behavior of dS extremal surfaces that require additional boundary conditions in the far past. This behavior is reminiscent of scattering amplitudes, where final states arise from initial states, or equivalently, time evolution. It is thus intriguing to explore entanglement-like structures emerging from the time evolution operator, $\mathcal{U}(t)$, after performing a partial trace over a subsystem. The time evolution operator yields complex-valued entanglement structures. We review various aspects of timelike entanglement in Sec. 4.2. Furthermore, [223] suggests that the entanglement entropy derived from the complex-valued extremal surfaces in no-boundary de Sitter space should be interpreted as pseudo-entropy.

Pseudo-entropy is a generalization of entanglement entropy, defined in terms of a transition matrix rather than a density matrix. The transition matrix is expressed as:

$$T_{F|I} = \frac{|F\rangle \langle I|}{\langle I|F\rangle}\,, \tag{4.1}$$

which reduces to the density matrix for $|F\rangle = |I\rangle$. We now decompose the Hilbert space as $H_A \otimes H_B$. The reduced transition matrix $T^A_{F|I}$ is obtained by tracing out H_B:

$$T^A_{F|I} = \mathrm{Tr}_B(T_{F|I})\,. \tag{4.2}$$

Notably, the transition matrix is non-Hermitian, and its reduced transition matrix may possess complex eigenvalues. The entropy associated with the reduced transition matrix is referred to as pseudo entropy and is defined as:

$$S(T^A_{F|I}) = -\mathrm{Tr}_A(T^A_{F|I} \log T^A_{F|I})\,. \tag{4.3}$$

Pseudo-entropy can generally take complex values. Unlike de Sitter space with its non-unitary CFT dual, the entanglement entropy of a timelike interval, even in unitary CFTs, is complex-valued and should be interpreted as pseudo entropy.

For ordinary unitary two-dimensional conformal field theories (CFTs), the entanglement entropy is given by

$$S = \frac{c}{6} \log \frac{\Delta^2}{\epsilon^2} = \frac{c}{6} \log \frac{-(\Delta t)^2 + (\Delta x)^2}{\epsilon^2}\,. \tag{4.4}$$

For ordinary spacelike intervals with $\Delta^2 > 0$, this reduces to the familiar expression $S = \frac{c}{3} \log \frac{\Delta x}{\epsilon}$. On the other hand, if we rotate the subsystem to be entirely timelike, with a width $\Delta t = T_0$ along the time direction, we obtain [224]

$$S = \frac{c}{3} \log \frac{T_0}{\epsilon} + \frac{c}{6}(i\pi)\,. \tag{4.5}$$

The imaginary part arises from the term $\log(-1)$ due to the timelike separation in the interval. More generally, the real part of the entanglement entropy incorporates the condition $\Delta^2 < 0$.

This result can also be derived by identifying the complex-valued extremal surface in AdS_3. For a detailed discussion, see [223]. Furthermore, pseudo entropy in holographic CFTs can be computed as the area of a minimal surface in a time-dependent Euclidean asymptotically AdS geometry, as illustrated in Figure 4.1. Numerous studies on pseudo-entropy can be found in [227]-[239] (see also [240]). Moreover, recent works [241]-[254] explore various aspects of time entanglement and pseudo-entropy.

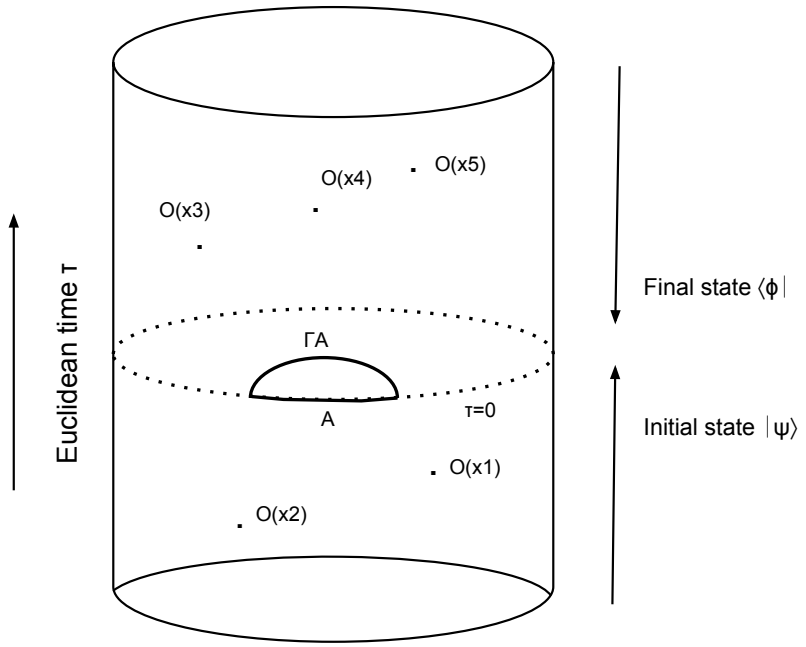

Figure 4.1: A schematic representation of the setup for holographic pseudo-entropy. The minimal surface ΓA is anchored at the boundary of subregion 'A' in a time-dependent Euclidean asymptotically AdS geometry. The dots denote excitations arising from external sources or conformal field theory (CFT) operators.

This Chapter is based on [239] and builds upon the work in [224], exploring the time evolution operator and its associated entanglement-like structures in various quantum systems, treating the operator as a density operator. These structures, involving timelike separations, generally lead to complex-valued entropy, though notable real subfamilies also emerge. This has many parallels and close relations with reduced transition matrices and pseudo-entropy, which we discuss in this study. We also consider time evolution operator along with a projection onto some initial state, which amounts to pseudo-entropy for the initial state and its time-evolved final state. In the time-independent cases studied, the structure of time entanglement exhibits similarities to conventional finite-temperature entanglement but analytically continued to an imaginary temperature, $\beta = it$.

In Sec. 4.8, we extend the analysis to time-dependent interactions, focusing on simple two-qubit systems with δ-function potentials and the resulting time entanglement.

4.1 Review of extremal surfaces in de Sitter space

This section presents a review of the key aspects of dS extremal surfaces discussed in [224, 226].

4.1.1 dS extremal surfaces from I^+, and boundary conditions

The absence of $\mathcal{I}^+ \to \mathcal{I}^+$ turning points is evident in the Poincaré slicing with planar foliations [213]. The metric in this slicing is given as:

$$ds^2_{d+1} = \frac{R^2_{dS}}{\tau^2}\left(-d\tau^2 + dy_i^2\right) = \frac{R^2_{dS}}{\tau^2}\left(-d\tau^2 + dw^2 + dx_i^2\right). \tag{4.6}$$

Here, $w \in y_i$ is singled out as the boundary Euclidean time. This choice is made without loss of generality.

To analyze extremal surfaces, we consider a constant w slice. At $\mathcal{I}^+$, we take a strip-shaped subregion. This subregion is natural for planar symmetries, with its width along $x \in x_i$. Extremal surfaces are anchored at the boundary interfaces of the strip.

The corresponding area functional is:

$$S_{dS} = -i\frac{R^{d-1}_{dS}V_{d-2}}{4G_{d+1}}\int \frac{d\tau}{\tau^{d-1}}\sqrt{1-(\partial_\tau x)^2}. \tag{4.7}$$

Here, V_{d-2} is the transverse volume, and G_{d+1} is the gravitational constant in $(d+1)$ dimensions.

Extremizing this functional yields:

$$(\partial_\tau x)^2 = \frac{B^2\tau^{2d-2}}{1+B^2\tau^{2d-2}}, \tag{4.8}$$

where B^2 is a constant.

A key observation is the sign difference compared to the AdS case. This difference reflects the absence of turning points that would return to $\mathcal{I}^+$. Near the boundary, where $\tau \to 0$, the behavior is:

$$(\partial_\tau x)^2 \ll 1. \tag{4.9}$$

This derivative remains bounded throughout, with $(\partial_\tau x)^2 < 1$, for any real $B^2 > 0$.

For $B^2 < 0$, the surfaces correspond to analytic continuations from AdS Ryu-Takayanagi (RT) surfaces [213, 214, 215, 216].

The absence of $\mathcal{I}^+ \to \mathcal{I}^+$ turning points implies that the surfaces extend inward. In a purely Lorentzian de Sitter space, these surfaces naturally end at $\mathcal{I}^-$. This gives rise to future-past extremal surfaces [217, 220]. These are timelike codimension-2 surfaces stretching from $\mathcal{I}^+$ to $\mathcal{I}^-$.

Alternatively, one can modify the Lorentzian de Sitter geometry using the Hartle-Hawking no-boundary proposal. This replaces the bottom half of dS space with a Euclidean hemisphere. Extremal surfaces then satisfy a no-boundary type condition. These alternatives are discussed in detail in subsequent sections.

4.1.2 Future-past extremal surfaces in dS

In static coordinates, the metric describes static patches with time translation symmetry. These patches allow analytic extensions to the entire de Sitter space. The metric takes the form:

$$ds^2 = -\left(1 - \frac{r^2}{l^2}\right) dt^2 + \frac{dr^2}{1 - \frac{r^2}{l^2}} + r^2 d\Omega_{d-1}^2. \tag{4.10}$$

In the Northern and Southern diamond regions (N and S), these static patches exhibit time translation symmetry, with t serving as the time coordinate. Observers in these regions encounter event horizons at $r = l$, where the area of these cosmological horizons corresponds to the de Sitter entropy. To study the future boundary, we employ the coordinate transformations:

$$\tau = \frac{l}{r}, \qquad w = \frac{t}{l}, \tag{4.11}$$

which recast the metric as:

$$ds^2 = \frac{l^2}{\tau^2}\left(-\frac{d\tau^2}{1-\tau^2} + (1-\tau^2)dw^2 + d\Omega_{d-1}^2\right). \tag{4.12}$$

Here, τ serves as the bulk time, with $\tau = 0$ representing the future and past boundaries. The future and past universes are described by $0 \leq \tau < 1$, and the boundary at $\mathcal{I}^+$ is $R \times S^{d-1}$. The boundary Euclidean time slice can be chosen as any S^{d-1} equatorial plane or as a $w = \text{const}$ slice.

Let us define a subregion on the boundary $\mathcal{I}^+$ as $\Delta w \times S^{d-2}$, with a corresponding subregion at $\mathcal{I}^-$. The area functional is then:

$$S = -i\frac{l^{d-1} V_{S^{d-2}}}{4G_{d+1}} \int \frac{d\tau}{\tau^{d-1}} \sqrt{\frac{1}{f} - f(w')^2}, \tag{4.13}$$

where $f = 1 - \tau^2$. Extremizing this functional leads to:

$$(1-\tau^2)^2 (w')^2 = \frac{B^2 \tau^{2d-2}}{1 - \tau^2 + B^2 \tau^{2d-2}}, \tag{4.14}$$

where $B^2 > 0$ is a constant. The total area is:

$$S = -i\frac{2l^{d-1} V_{S^{d-2}}}{4G_{d+1}} \int_\epsilon^{\tau_*} \frac{d\tau}{\tau^{d-1}} \frac{1}{\sqrt{1 - \tau^2 + B^2 \tau^{2d-2}}}. \tag{4.15}$$

Here, τ_* denotes the turning point, satisfying:

$$1 - \tau_*^2 + B^2 \tau_*^{2d-2} = 0. \tag{4.16}$$

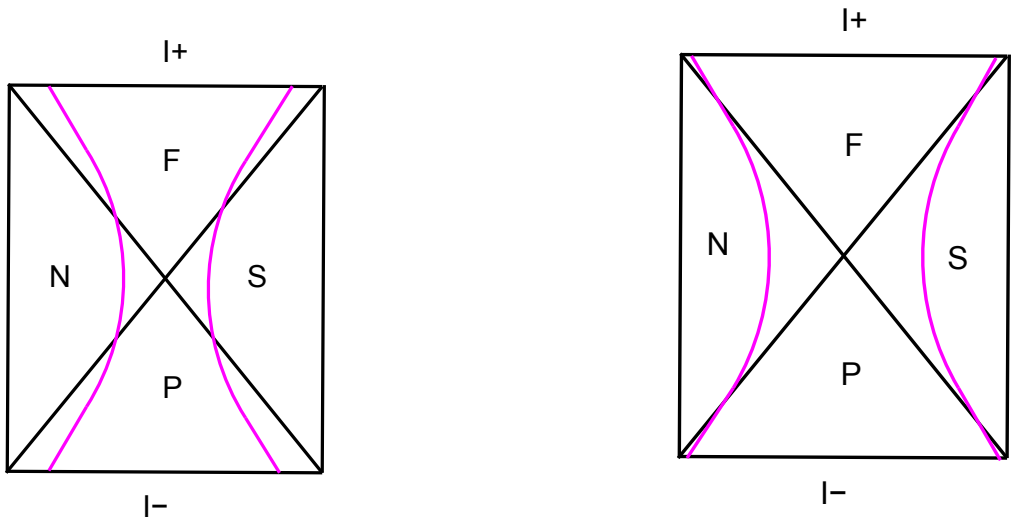

(a) (b)

Figure 4.2: dS future-past extremal surfaces stretching between $I^{\pm}$ on an S^{d-1} equatorial plane. The left panel schematically depicts the extremal surface (shown in magenta) for a generic subregion, whereas the right panel illustrates the extremal surface corresponding to the entire space.

The turning point τ_* lies within the N and S diamond regions, where the extremal surface remains timelike. The surface from $\mathcal{I}^+$ can be joined to an equivalent surface from $\mathcal{I}^-$, resulting in a full, timelike future-past surface [217, 220] stretching from $\mathcal{I}^+$ to $\mathcal{I}^-$, as shown in Figure 4.2. These surfaces are rotated analogs of Hartman-Maldacena surfaces in the eternal AdS black hole [20]. For $\Delta w \to \infty$, the subregion becomes the entire space $\mathcal{I}^{\pm}$. For dS_4, the turning point occurs at $\tau_* = \sqrt{2}$, corresponding to $B \to \frac{1}{2}$. The area of these surfaces exhibits an area-law divergence and a finite part:

$$S^{\text{div}} \sim -i\frac{\pi l^2}{G_4}\frac{l}{\epsilon_c}, \qquad S^{\text{fin}} \sim -i\frac{\pi l^2}{G_4}\Delta w \quad [dS_4]. \tag{4.17}$$

The divergence scales with the de Sitter entropy, $\frac{\pi l^2}{G_4}$, akin to the number of degrees of freedom in the dual CFT.

Alternatively, we can consider cap-like subregions defined by $\theta = \text{const}$ latitudes on S^{d-1} at $\mathcal{I}^+$, with corresponding ones at $\mathcal{I}^-$. The area functional is:

$$S = -i\frac{2l^{d-1}V_{S^{d-2}}}{4G_{d+1}}\int \frac{d\tau}{\tau^{d-1}}(\sin\theta)^{d-2}\sqrt{\frac{1}{1-\tau^2} - (\theta')^2}. \tag{4.18}$$

While analyzing this explicitly for general θ is challenging, for $\theta = \frac{\pi}{2}$, we obtain a future-past extremal surface stretching from a hemispherical cap on S^{d-1} at $\mathcal{I}^+$ to the corresponding cap at $\mathcal{I}^-$. The area in dS_4 is:

$$S = -i\frac{2\pi l^2}{G_4}\int_\epsilon^1 \frac{d\tau}{\tau^3\sqrt{1-\tau^2}} \sim -i\frac{\pi l^2}{G_4}\frac{1}{\epsilon}. \tag{4.19}$$

This result contains no finite part.

In global coordinates, the metric is written as:

$$ds^2_{d+1} = -d\tau^2 + l^2\cosh^2\left(\frac{\tau}{l}\right)d\Omega_d^2. \tag{4.20}$$

The boundary Euclidean time slice can be chosen as any S^d equatorial plane, all of which are equivalent. The area functional, including a factor of 2 for the top and bottom parts, is:

$$S = -i\frac{2l^{d-2}V_{S^{d-2}}}{4G_{d+1}}\int d\tau\,(\cosh\tau)^{d-2}(\sin\theta)^{d-2}\sqrt{1-\cosh^2\tau(\partial_\tau\theta)^2}. \tag{4.21}$$

For $\theta = \frac{\pi}{2}$, the future-past extremal surface stretches from $\mathcal{I}^+$ to $\mathcal{I}^-$. In dS_4, the area is:

$$S = -i\frac{\pi l^2}{G_4}\int_0^{\tau_c/l}\cosh\tau\,d\tau \sim -i\frac{\pi l^2}{2G_4}e^{\tau_c/l} \sim -i\frac{\pi l^2}{2G_4}\frac{l}{T_c}. \tag{4.22}$$

The result exhibits an area-law divergence, similar to the static coordinate case.

4.1.3 dS no-boundary surfaces

In accordance with the Hartle-Hawking no-boundary prescription [255] (see also [256]), global de Sitter space can be split along the $\tau = 0$ time slice. The top half is then joined to a hemisphere in the bottom half, defined by the Euclidean continuation

$$ds^2 = l^2 d\tau_E^2 + l^2\cos^2\tau_E\,d\Omega_d^2\,; \qquad \tau = il\tau_E\,, \quad 0 \le \tau_E \le \frac{\pi}{2}\,. \tag{4.23}$$

Now, consider an S^d equatorial plane and the timelike extremal surface from (4.21) at $\theta = \pi/2$, which represents the IR limit of such surfaces. The top portion of this surface originating from I^+ intersects the $\tau = 0$ mid-slice vertically. This is smoothly joined at $\tau = 0$ with a surface extending over the bottom hemisphere, ensuring consistency with the Hartle-Hawking prescription, as schematically illustrated in Figure 4.3. The IR surface in this configuration is

$$ds^2 = l^2 d\tau_E^2 + l^2\cos^2\tau_E(d\theta^2 + \sin^2\theta\,d\Omega_{d-2}^2)\big|_{\theta=\pi/2} = l^2 d\tau_E^2 + l^2\cos^2\tau_E d\Omega_{d-2}^2\,,$$

with the corresponding area given by

$$\frac{l^{d-1}}{4G_{d+1}}V_{S^{d-2}}\int_0^{\pi/2}d\tau_E\,(\cos\tau_E)^{d-2} = \frac{l^{d-1}}{4G_{d+1}}V_{S^{d-2}}\,\frac{\sqrt{\pi}\,\Gamma\left(\frac{d-1}{2}\right)}{2\,\Gamma\left(\frac{d}{2}\right)} = \frac{1}{2}\frac{l^{d-1}\,V_{S^{d-1}}}{4G_{d+1}}\,. \tag{4.24}$$

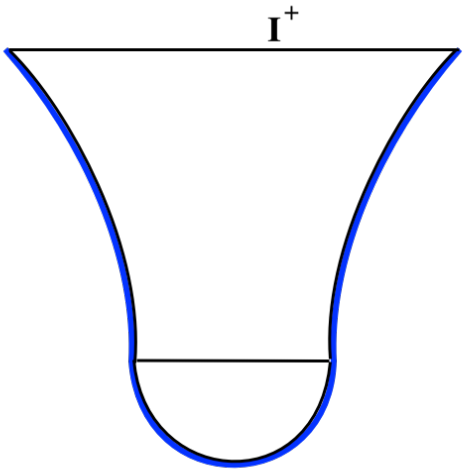

Figure 4.3: A schematic representation of a global dS no-boundary surface. The top portion (timelike) anchored at the future boundary I^+, is smoothly joined to the spatial component that wraps around the hemisphere in the bottom half. In this figure, the no-boundary dS surface corresponds to the IR limit ($\theta = \frac{\pi}{2}$) on an S^d equatorial plane (This figure is adapted from [224], which holds the original credit).

Here, $V_{S^d} = \frac{2\pi^{(d+1)/2}}{\Gamma((d+1)/2)}$ is the volume of a d-sphere. Notably, the real part of the area of this spacelike surface on the hemisphere is precisely half of the de Sitter entropy. This recovery of entropy differs from the interpretation as the area of the cosmological horizon observed in static patches. In this context, one of the hemisphere directions corresponds to the Euclidean continuation of the time direction in the future universe. For dS_4, the total area for the no-boundary surface is the sum of the top timelike part (half of the future-past area from (4.22)) and the hemisphere contribution:

$$S = -i\frac{\pi l^2}{4G_4}\frac{l}{T_c} + \frac{\pi l^2}{2G_4}\,. \tag{4.25}$$

This bears some resemblance to the semiclassical wavefunction $\Psi_{dS} = e^{iS_{cl}}$ for no-boundary dS_4, where S_{cl} represents the action. The Lorentzian top half contributes a real S_{cl}, yielding a pure phase in Ψ_{dS}. In contrast, the bottom hemisphere results from the Euclidean continuation (4.23), with iS_{cl} becoming the Euclidean gravitational action $-\int_{\rm nbp}\sqrt{g}\,(R-2\Lambda)$, evaluated on the hemisphere. For dS_4, this gives $\frac{1}{2}\frac{l^4 V_{S^4}}{16\pi G_4}\cdot\frac{6}{l^2} = \frac{\pi l^2}{2G_4}$, as is well known (see, *e.g.*, [257, 258]).

A similar calculation can be performed for the timelike future-past surface in static coordinates. Here, the boundary is $R_w \times S^{d-1}$, allowing for either S^{d-1} equatorial planes or $w = $ const slices as boundary Euclidean time slices. The Euclidean continuation in this case is

$$ds^2 = l^2(\cos^2\psi\, d\tau_E^2 + d\psi^2 + \sin^2\psi\, d\Omega_{d-1}^2)\,, \qquad t = i\tau_E\,, \quad r = l\sin\psi\,, \tag{4.26}$$

where $\tau_E \in [0, 2\pi l]$ and $0 \leq \psi \leq \pi/2$.

For S^{d-1} equatorial plane surfaces, there is a limiting surface at $\tau_* > 1$ (*e.g.*, $\tau_* = \sqrt{2}$ for dS_4), corresponding to a limiting ψ_* with $\sin\psi_* = r_*/l = 1/\tau_*$:

$$ds^2 = \cos^2\psi_*\, d\tau_E^2 + \sin^2\psi_*\, d\Omega_{d-2}^2\,.$$

The area evaluates to

$$\int_0^{\pi l} \cos\psi_*\, d\tau_E\, (\sin\psi_*)^{d-2}\, V_{S^{d-2}}\, \frac{l^{d-2}}{4G_{d+1}}\,.$$

For dS_4, with $\sin\psi_* = 1/\sqrt{2}$, this yields an area

$$\frac{1}{2}(\pi l)\frac{2\pi l}{4G_4} = \frac{\pi^2 l^2}{4G_4}\,.$$

For $w = \text{const}$ slices (*equivalently,* $\tau_E = \text{const}$), the timelike surface from the $\theta = \pi/2$ cap on S^{d-1} leads to

$$ds^2 = d\psi^2 + \sin^2\psi\, d\Omega_{d-2}^2\,,$$

giving an area identical to that in global de Sitter space (4.24). For dS_4, adding the top timelike part from (4.19), the total area becomes

$$S = -i\frac{\pi l^2}{2G_4}\frac{1}{\epsilon} + \frac{\pi l^2}{2G_4}\,.$$

Finally, note that these no-boundary surfaces turn only in the bottom hemisphere. The top timelike half remains identical to the corresponding future-past surface, with no $I^+ \to I^+$ turning point. For two disjoint subregions, the corresponding no-boundary surfaces are unique, with no additional connected surfaces. As a result, the entropies satisfy

$$S[A \cup B] = S[A] + S[B]\,,$$

implying that mutual information vanishes, similar to the case of future-past surfaces [220]. Furthermore, the entropy for no-boundary de Sitter space is complex-valued, as evident from (4.25). This suggests that it should be interpreted as a pseudo-entropy, as proposed in [223].

4.1.4 dS_3 no-boundary surfaces, and pseudo entropy

Let us now turn our attention to dS_3, which holds special significance for various reasons. In fully Lorentzian global de Sitter space, the future-past surfaces on an S^2 equatorial plane slice (see Eq. 4.21) yield the area:

$$S = -i\frac{l}{G_3}\log\frac{l}{T_c}.$$

In the context of no-boundary dS_3, the total area arises as the sum of contributions from the top timelike segment and the bottom hemisphere (Eq. 4.24), resulting in:

$$S_{dS_3} = -i\frac{l}{2G_3}\log\frac{l}{T_c} + \frac{\pi l}{4G_3}.$$

This expression can be reformulated as:

$$S_{dS_3} = \frac{c_{dS}}{3} \log \frac{l}{T_c} + i\pi \frac{c_{dS}}{6}, \tag{4.27}$$

where $c_{dS} = -i\frac{3l_{dS}}{2G_3}$. The second term, which is real, corresponds to half of the dS_3 entropy, $\frac{\pi l}{2G_3}$. This formulation can be obtained by making the substitutions $\frac{l^2}{\epsilon^2} \to -\frac{l^2}{T_c^2}$ and $c \to c_{dS}$ in the familiar expression $\frac{c}{6} \log \frac{l^2}{\epsilon^2}$ [36, 37, 259]. Here, the CFT_2 dual to dS_3 has the central charge: $c_{dS} = -i\frac{3l_{dS}}{2G_3}$, as established in [211]. One striking feature of Eq. 4.27 is the presence of a real part, originating from the hemisphere contribution. This real part necessitates an additional factor of i, which is a novel characteristic of the Euclidean CFT_{dS_3} dual. This is in contrast to ordinary Euclidean CFTs, which involve purely real spatial lengths and lack temporal components.

4.2 Review of time-entanglement in quantum mechanics

In the previous section, We have reviewed future-past extremal surfaces extending from I^+ to I^-. These surfaces are entirely timelike, resulting in an area that is purely imaginary, differing by an overall factor of $-i$ from the areas of the familiar spacelike RT/HRT surfaces in AdS. Despite this imaginary factor, the magnitude of the area remains real and positive, with $-i$ acting as a uniform multiplier for any subregion at I^+. This is reminiscent of the relationship between the lengths of timelike and spacelike geodesics, where the timelike geodesic length acquires an overall $-i$ factor relative to its spacelike counterpart. Motivated by this analogy, the areas of these timelike future-past extremal surfaces are interpreted as encoding a novel object, *time-entanglement*, as introduced in [224].

The no-boundary surfaces, which are closely related to the timelike future-past surfaces, also exhibit complex-valued areas. These consist of two components: a timelike segment (identical to the top half of the future-past surfaces) contributing a purely imaginary part, and a spacelike segment (arising from the hemisphere) contributing a real part. Together, these components form a complex area.

This notion of *time-entanglement* can be further explored through two perspectives in quantum mechanics, independent of the de Sitter framework. The first perspective involves the thermofield-double-type state discussed in [217, 220]. The second perspective treats the timelike surfaces as representing some form of transition amplitude, related to the time-evolution operator.

A future-past thermofield double state

The entirely timelike future-past surfaces, analogous to the rotated Hartman-Maldacena surfaces [20], suggest a form of entanglement between I^+ and I^-. Consider the state

$$|\psi\rangle_{fp} = \sum \psi^{i_n^F, i_n^P} |i_n\rangle_F |i_n\rangle_P \ , \tag{4.28}$$

as introduced in [217]. This state was proposed as an entirely positive object, entangling identical F (future) and P (past) components, inspired by the thermofield-double (TFD) state for the eternal black hole [260]. A partial trace over the second (P) copy yields a reduced density matrix with nontrivial entanglement entropy.

To illustrate, consider a simple two-state system in ordinary quantum mechanics. The Hamiltonian H acts on the orthogonal basis eigenstates, leading to the time evolution:

$$H|k\rangle = E_k|k\rangle\,, \quad k=1,2\;; \qquad |k\rangle_F \equiv |k(t)\rangle = e^{-iE_k t}|k\rangle_P\;. \qquad [\langle 1|2\rangle = 0] \tag{4.29}$$

The F and P slices are separated by time t, and the F state is obtained from the P state via time evolution through t.

The future-past TFD state in this toy example is given by:

$$|\psi\rangle_{fp} = \frac{1}{\sqrt{2}}|1\rangle_F|1\rangle_P + \frac{1}{\sqrt{2}}|2\rangle_F|2\rangle_P = \frac{1}{\sqrt{2}}e^{-iE_1 t}|1\rangle_P|1\rangle_P + \frac{1}{\sqrt{2}}e^{-iE_2 t}|2\rangle_P|2\rangle_P\;. \tag{4.30}$$

The coefficients are normalized for maximal entanglement at $t=0$. For nonzero t, additional phases arise due to time evolution. However, these phases cancel in the reduced density matrix obtained by tracing over the second copy (P):

$$\rho_{fp} = \mathrm{Tr}_P\big(|\psi\rangle_{fp}\langle\psi|_{fp}\big) = \frac{1}{2}|1\rangle_F\langle 1|_F + \frac{1}{2}|2\rangle_F\langle 2|_F\;. \tag{4.31}$$

As a concrete analogy, consider a two-spin system where $|1\rangle = |++\rangle$ and $|2\rangle = |--\rangle$, representing the two-state subspace $|\pm\pm\rangle$ of two spins with states $|\pm\rangle$. A partial trace over the second spin yields the reduced density matrix:

$$\mathrm{Tr}_2\rho_{fp} = \frac{1}{2}|+\rangle_F\langle +|_F + \frac{1}{2}|-\rangle_F\langle -|_F\;, \tag{4.32}$$

with an entirely positive structure and entropy $\log 2$.

This future-past TFD state, characterized by timelike separation, exhibits a fundamentally distinct nature compared to the standard TFD state. Notably, its positive structure, despite the timelike separation, bears a resemblance to the areas of entirely timelike surfaces when the universal overall factor of $-i$ is disregarded.

Time-evolution and reduced transition amplitudes

Unlike AdS, where specifying boundary data resolves the extremization problem, dS extremal surfaces that start at late times on I^+ do not return. This necessitates additional data for boundary conditions in the far past. Such behavior is reminiscent of scattering amplitudes, i.e., final states arising from initial states, or equivalently, time evolution. It is therefore interesting to explore entanglement-like structures emerging from the time evolution operator $\mathcal{U}(t)$ after performing a partial trace over an environment. In other words, we seek a "reduced transition amplitude" and its associated entropy. Specifically, for a subregion A and an environment B, we define:

$$\rho_t(t) \equiv \frac{\mathcal{U}(t)}{\mathrm{Tr}\,\mathcal{U}(0)} \quad \Rightarrow \quad \rho_t^A = \mathrm{Tr}_B\,\rho_t \quad \Rightarrow \quad S_A = -\mathrm{Tr}\big(\rho_t^A \log \rho_t^A\big). \tag{4.33}$$

The normalization ensures that ordinary entanglement structures are recovered at $t = 0$, as we will explicitly demonstrate.

To illustrate, consider the simple toy example described earlier. For this case, since all components are diagonal, the normalized time evolution operator simplifies to:

$$\mathcal{U}(t) = e^{-iHt} \quad \Rightarrow \quad \rho_t(t) = \frac{1}{2}e^{-iE_1t}|1\rangle_P\langle 1|_P + \frac{1}{2}e^{-iE_2t}|2\rangle_P\langle 2|_P = \frac{1}{2}|1\rangle_F\langle 1|_P + \frac{1}{2}|2\rangle_F\langle 2|_P. \quad (4.34)$$

Using the two-spin analogy, where $|1\rangle = |++\rangle$ and $|2\rangle = |--\rangle$, a partial trace over the second components results in:

$$\rho_t^A = \frac{1}{2}e^{-iE_1t}|+\rangle_P\langle +|_P + \frac{1}{2}e^{-iE_2t}|-\rangle_P\langle -|_P. \quad (4.35)$$

The entropy associated with this is:

$$S_A = -\sum_i \frac{1}{2}e^{-iE_it}\log\left(\frac{1}{2}e^{-iE_it}\right) = \frac{1}{2}\log 2\,(e^{-iE_1t} + e^{-iE_2t}) + \frac{1}{2}iE_1t\,e^{-iE_1t} + \frac{1}{2}iE_2t\,e^{-iE_2t}. \quad (4.36)$$

Normalizing $\mathcal{U}(t)$ by its trace at time t ensures that $\mathrm{Tr}\,\rho_t(t) = 1$ for all t (not just $t = 0$), which modifies (4.80)–(4.36) to:

$$\rho_t(t) \equiv \frac{\mathcal{U}(t)}{\mathrm{Tr}\,\mathcal{U}(t)} \quad \Rightarrow \quad \rho_t(t) = \sum_i p_i|i\rangle_P\langle i|_P, \quad p_i = \frac{e^{-iE_it}}{\sum_j e^{-iE_jt}},$$
$$\rho_t^A = \sum_i p_i'|i'\rangle_P\langle i'|_P \quad \Rightarrow \quad S_A = -\sum_i p_i'\log p_i', \quad (4.37)$$

where $H|i\rangle = E_i|i\rangle$. The second line follows after taking a partial trace. These structures share similarities with pseudo-entropy [227], though their details differ. The time entanglement (entanglement-like structures derived from the time evolution operator treated as a density operator) and pseudo-entropy exhibit intriguing interrelations, which we explore in the subsequent sections.

At $t = 0$, ρ_t^A resembles an ordinary maximally entangled state. For $t \neq 0$, the entropy S_A generally becomes complex-valued. However, certain cases, such as (4.38) for the two-state system, involve a single phase $e^{-i(E_2-E_1)t}$, yielding a real entropy. Additionally, different normalizations yield varying results, as demonstrated in the examples above. Overall, these structures bear a resemblance to mixed-state entanglement at finite temperature, but with an imaginary temperature, i.e., $\beta = it$. Several related quantities can also be constructed. For instance, the time evolution operator $\mathcal{U}(t)$, combined with a projection operator onto a generic state $|I\rangle$, leads to:

$$\mathcal{U}(t)|I\rangle\langle I| = |F_I(t)\rangle\langle I|,$$

where $|F_I(t)\rangle$ is the future state obtained by time-evolving the initial state $|I\rangle$. Normalizing at time t and performing a partial trace yields a reduced transition matrix, resembling that in pseudo-entropy [227], but specifically tied to the time-evolved future state. Similarly, normalizing at $t = 0$ produces different structures. For instance, projections onto Hamiltonian eigenstates $|E_I\rangle$, followed by a partial trace, result in simple phases for $\rho_t^{A,I}$ (essentially components of (4.35)), with corresponding entropy forms such as $iE_It\,e^{-iE_It}$.

4.3 Summary: time evolution and pseudo-entropy

Our investigations, following [224], are based on treating the time evolution operator as a density operator, performing partial traces over subsystems, and evaluating the corresponding von Neumann entropy. The time evolution operator $\mathcal{U}(t) = e^{-iHt}$ for a system with Hamiltonian H (time-independent) can be written in terms of Hamiltonian eigenstates $|i\rangle$, which are defined on some past time slice P. The time evolution operator normalized at an arbitrary time t gives:

$$\begin{aligned} \mathcal{U}(t) = e^{-iHt} = \sum_i e^{-iE_i t}|i\rangle\langle i| &= \sum_i |i\rangle_t \, \langle i|_P \,, \qquad |i(t)\rangle \equiv |i\rangle_t = e^{-iE_i t}|i\rangle_P \,; \\ \rho_t(t) \equiv \frac{\mathcal{U}(t)}{\mathrm{Tr}\mathcal{U}(t)} \quad &\Rightarrow \quad \rho_t(t) = \sum_i p_i \, |i\rangle_P \langle i|_P \,, \qquad p_i = \frac{e^{-iE_i t}}{\sum_j e^{-iE_j t}} \,, \\ \rightarrow \quad \rho_t^A = \mathrm{Tr}_B \rho_t = \sum_i p_i' \, |i'\rangle_P \langle i'|_P \quad &\rightarrow \quad S_A = -\sum_i p_i' \log p_i' \,. \end{aligned} \tag{4.38}$$

As is evident, there are striking parallels with ordinary finite-temperature entanglement structures, except with imaginary temperature $\beta = it$. This connection will repeatedly emerge as a recurring theme throughout much of what follows.

A related quantity involves the time evolution operator with projection onto some state $|i\rangle$,

$$\rho_t^{|i\rangle} = \frac{\rho_t |i\rangle\langle i|}{\mathrm{Tr}(\rho_t |i\rangle\langle i|)} = \frac{|f[i](t)\rangle\langle i|}{\mathrm{Tr}(|f[i](t)\rangle\langle i|)} \,, \qquad |f[i](t)\rangle = e^{-iHt}|i\rangle \,; \qquad \rho_t^{|i\rangle,A} = \mathrm{Tr}_{\,B} \, \rho_t^{|i\rangle} \,. \tag{4.39}$$

The state $|f[i]\rangle$ is the final state obtained by time-evolving the initial state $|i\rangle$. We obtain

$$|i\rangle = \sum c_n |n\rangle \;; \qquad \rho_t^{|i\rangle} = \frac{1}{\sum_k e^{-iE_k t}|c_k|^2} \sum_{k,m} e^{-iE_k t} c_k c_m^* |k\rangle\langle m| \tag{4.40}$$

for a general (non-eigen)state $|i\rangle$. At $t = 0$, the time evolution operator is just the identity operator, a sum over all the eigenstate projection operators, while the time evolution operator with projection becomes simply the density matrix for the initial state $|i\rangle$. For any nonzero time t, there is timelike separation between the initial states $|\psi\rangle_P$ and the eventual states $|\psi\rangle_t$. These entanglement structures involving timelike separations and time evolution have close parallels with pseudo-entropy [227] obtained from the reduced transition matrix for two arbitrary states $|i\rangle, |f\rangle$:

$$\mathcal{T}^A_{f|i} = \mathrm{Tr}_B \left(\frac{|f\rangle\langle i|}{\mathrm{Tr}(|f\rangle\langle i|)} \right) . \tag{4.41}$$

To summarize in generality, consider a bipartite system where the Hilbert space is characterized by Hamiltonian eigenstates $|i, i'\rangle$ with energies $E_{i,i'}$. The normalized time evolution operator (4.38) and its partial trace over $B \equiv \{i'\}$ are

$$\rho_t = \frac{1}{\sum_{i,i'} e^{-iE_{i,i'}t}} \sum_{i,i'} e^{-iE_{i,i'}t} \, |i,i'\rangle\langle i,i'| \quad \rightarrow \quad \rho_t^A = \frac{1}{\sum_{i,i'} e^{-iE_{i,i'}t}} \Big(\sum_{i'} e^{-iE_{i,i'}t} \Big) \, |i\rangle\langle i| \,. \tag{4.42}$$

The time evolution operator with projection onto state $|I\rangle$ is

$$|I\rangle = \sum_{k,k'} c_{k,k'}|k,k'\rangle\,, \qquad \rho_t^{|I\rangle} = \frac{1}{\sum_{i,i'}|c_{i,i'}|^2 e^{-iE_{i,i'}t}} \sum_{i,i',j,j'} c_{i,i'}c^*_{j,j'}e^{-iE_{i,i'}t}|i,i'\rangle\langle j,j'|\,,$$
$$\rho_t^{|I\rangle,A} = \frac{1}{\sum_{i,i'}|c_{i,i'}|^2 e^{-iE_{i,i'}t}} \sum_{i,j}\big(\sum_{i'} c_{i,i'}c^*_{j,i'}e^{-iE_{i,i'}t}\big)|i\rangle\langle j|\,. \tag{4.43}$$

The reduced transition matrix for pseudo-entropy is obtained as

$$|I\rangle = c_{i,i'}|i,i'\rangle, \quad |F\rangle = c'_{i,i'}|i,i'\rangle\,; \qquad \mathcal{T}_{F|I} = \frac{1}{\sum_{i,i'} c'_{i,i'}c^*_{i,i'}} \sum_{i,i',j,j'} c'_{i,i'}c^*_{j,j'}\,|i,i'\rangle\langle j,j'|\,,$$
$$\mathcal{T}^A_{F|I} = \frac{1}{\sum_{i,i'} c'_{i,i'}c^*_{i,i'}}\big(\sum_{i'} c'_{i,i'}c^*_{j,i'}\big)\,|i\rangle\langle j|\,. \tag{4.44}$$

It is clear that the time evolution operator with projection (4.43) is derived from the pseudo-entropy reduced transition matrix (4.44) by restricting the final state to be the time-evolved initial state, *i.e.* $|F\rangle = \mathcal{U}(t)|I\rangle$.

4.3.1 The time evolution operator and the transition matrix

With a single Hilbert space, the structure of the reduced transition matrix appears different in detail from that of the reduced time evolution operator. This distinction is evident in bipartite systems from (4.42), (4.43), and (4.44). However, there should be a close connection between the time evolution operator and the transition matrix, as both pertain to time evolution—particularly when focusing on final states as time-evolved initial states.

Towards studying this, let us first recall that a special class of states comprises thermofield-double type states $|I\rangle_{TFD} = \sum_k c_{k,\{k\}}|k,\{k\}\rangle$, with only diagonal components (a further special subclass comprises maximally entangled TFD states, with all $c_{k,\{k\}}$ equal).

Towards mapping time evolution and the transition matrix, consider doubling the Hilbert space at both initial and final times: *i.e.* extend the Hilbert state $\mathscr{H} \equiv \mathscr{H}_1$ to $\mathscr{H}_1 \otimes \mathscr{H}_2$, where the Hilbert space $\mathscr{H}_2$ is an identical copy of $\mathscr{H}_1$. Now consider thermofield-double type initial and final states:

$$|\psi_I\rangle = \sum_i c_i^I\,|i\rangle_1|i\rangle_2\,, \qquad |\psi_F\rangle = \sum_i c_i^F\,|i\rangle_1|i\rangle_2\,, \tag{4.45}$$

where $\{|i\rangle\}$ is a basis of states. The (un-normalized) transition matrix is

$$\mathcal{T}_{F|I} = |\psi_F\rangle\langle\psi_I| = \sum_{i,j} c_i^F c_j^{I\,*}\;|i\rangle_1|i\rangle_2\;\langle j|_1\langle j|_2\,. \tag{4.46}$$

Performing a partial trace over copy-2 gives

$$\mathrm{Tr}_2\,\mathcal{T}_{F|I} = \sum_i c_i^F c_i^{I\,*}\;|i\rangle_1\langle i|_1\,. \tag{4.47}$$

For this to equal the time evolution operator, we require

$$\mathrm{Tr}_2\,\mathcal{T}_{F|I} = \mathcal{U}(t) = \sum_i e^{-iE_it}\,|i\rangle\langle i| \qquad \Rightarrow \qquad c_i^F\,c_i^{I\,*} = e^{-iE_it}\ . \tag{4.48}$$

A "symmetric" solution is

$$\begin{aligned} c_i^I &= e^{iE_it/2}\ : \qquad |\psi_I\rangle = \sum_i e^{iE_it/2}\,|i\rangle_1|i\rangle_2\,, \\ c_i^F &= e^{-iE_it/2}\ : \qquad |\psi_F\rangle = \sum_i e^{-iE_it/2}\,|i\rangle_1|i\rangle_2\,. \end{aligned} \tag{4.49}$$

These can be regarded as obtained from a continuation $\beta \to it$ of the usual finite temperature thermofield-double type states $e^{-\beta E_i/2}|i\rangle|i\rangle$. There are of course less symmetric solutions $c_i^I,\ c_i^F$, describing the initial and final states. However the symmetric solution reduces to ordinary entanglement when the initial and final states are the same, *i.e.* $|\psi_I\rangle = |\psi_F\rangle$ (*i.e.* at $t = 0$), the transition matrix becomes the usual density matrix $\mathcal{T}_{F|I} = |\psi_I\rangle\langle\psi_I| = \rho_I$ for the state $|\psi_I\rangle$. Thus the time evolution operator can be regarded as a particular reorganization of the transition matrix appearing in pseudo-entropy.

It is worth noting that for systems with infinite towers of states, the trace of the time evolution operator contains highly oscillatory terms and therefore requires a regulator to be well-defined. This will be seen explicitly in the case of the harmonic oscillator later; see (4.70).

Single qubit: This simple case serves to illustrate the above. In this case (described by (4.53)), we have $H\,|1\rangle = E_1\,|1\rangle\,,\ H\,|2\rangle = E_2\,|2\rangle$, with H the Hamiltonian. Let us take

$$|\psi_F\rangle = \sum_{n=1,2} e^{-\frac{i\,E_nt}{2}}\,|n\rangle_1 \otimes |n\rangle_2\ , \qquad |\psi_I\rangle = \sum_{m=1,2} e^{\frac{i\,E_mt}{2}}\,|m\rangle_1 \otimes |m\rangle_2\ . \tag{4.50}$$

Here the subscript 2 stands for the second auxiliary system with the identical Hilbert space $\mathscr{H}_2$. Then the unnormalised transition matrix $T = |\psi_F\rangle\,\langle\psi_I|$ is

$$T_{F|I} = |\psi_F\rangle\,\langle\psi_I| = \sum_{n,m=1,2} e^{\frac{-i(E_n+E_m)t}{2}}\,|n\rangle_1\,|n\rangle_2\,\langle m|_1\,\langle m|_2\ . \tag{4.51}$$

Taking a partial trace over the second component gives

$$T^1_{F|I} = Tr_2(T_{F|I}) = \sum_{n=1,2} e^{-i\,E_nt}\,|n\rangle_1\,\langle n|_1\ = e^{-iHt}\,, \tag{4.52}$$

thus obtaining the time evolution operator. This illustrates the general discussion earlier in this simple case.

4.4 Time evolution operator, entanglement: examples

In this section, we study various examples of finite quantum systems to explore the entanglement structure of the time evolution operator.

4.4.1 2-qubit systems

For a 2-state system,

$$H|k\rangle = E_k|k\rangle\,, \quad k=1,2\;; \qquad |k\rangle_F \equiv |k(t)\rangle = e^{-iE_kt}|k\rangle_P\;. \qquad [\langle 1|2\rangle = 0] \tag{4.53}$$

we obtain $\rho_t(t)$ using (4.38). Now, imagining a 2-spin analogy $|1\rangle \equiv |{+}{+}\rangle$, $|2\rangle \equiv |{-}{-}\rangle$, performing a partial trace over the second spins gives

$$\begin{aligned}
\rho_t^A &= \frac{1}{1+e^{i\theta}}\big(|+\rangle_P\langle +|_P + e^{i\theta}|-\rangle_P\langle -|_P\big), \qquad \theta = -(E_2-E_1)t\,,\\
S_A &= -\mathrm{tr}\big(\rho_t^A \log \rho_t^A\big) = -\frac{1}{1+e^{i\theta}}\log\frac{1}{1+e^{i\theta}} - \frac{1}{1+e^{-i\theta}}\log\frac{1}{1+e^{-i\theta}}\,,
\end{aligned} \tag{4.54}$$

so the von Neumann entropy, recast as $\alpha+\alpha^*$, is real-valued in this special case. We see that S_t^A grows large as $\theta \to (2n+1)\pi$. Further ρ_t^A and S_t^A are periodic in θ and so in time t (simplifying S_t^A shows terms containing $\log\big(e^{i\theta/2}\big)$ which we retain as it is, rather than $\frac{i\theta}{2}$, so as to avoid picking specific branches of the logarithm, thereby losing manifest periodicity; within one θ-cell the simplified expression for S_t^A coincides with the corresponding one in [227]).

Now consider two qubits, each being $|1\rangle, |2\rangle$, with a more general Hamiltonian

$$H = E_{11}|11\rangle\langle 11| + E_{22}|22\rangle\langle 22| + E_{12}\big(|12\rangle\langle 12| + |21\rangle\langle 21|\big) \tag{4.55}$$

that is diagonal in this basis. It is reasonable to take $E_{12}=E_{21}$. So the normalized time evolution operator (4.38) becomes

$$\begin{aligned}
\rho_t = \sum_{i,j}\frac{e^{-iE_{ij}t}}{\sum_{kl}e^{-iE_{kl}t}}\,|ij\rangle\langle ij| \;&=\; \frac{\big(|11\rangle\langle 11| + e^{i\theta_1}|22\rangle\langle 22| + e^{i\theta_2}(|12\rangle\langle 12| + |21\rangle\langle 21|)\big)}{1+e^{i\theta_1}+2e^{i\theta_2}}\;;\\
\theta_1 \equiv -(E_{22}-E_{11})t\,, &\qquad \theta_2 \equiv -(E_{12}-E_{11})t\,.
\end{aligned} \tag{4.56}$$

(At $t=0$, the θ_i vanish and this is the normalized identity operator.) A partial trace over the 2nd component gives the reduced time evolution operator,

$$\rho_t^A = \frac{1}{1+e^{i\theta_1}+2e^{i\theta_2}}\Big(\big(1+e^{i\theta_2}\big)|1\rangle\langle 1| + \big(e^{i\theta_1}+e^{i\theta_2}\big)|2\rangle\langle 2|\Big) \tag{4.57}$$

which generically has complex-valued von Neumann entropy. It is clear that this matches ordinary finite temperature entanglement, except with imaginary temperature $\beta = it$.

Now let us impose an exchange symmetry $|1\rangle \leftrightarrow |2\rangle$: this occurs for instance if we consider two spins $|\pm\rangle$ with nearest neighbour interaction $H = -Js_z^1 s_z^2$. This restriction now implies $E_{22}=E_{11}$ thereby reducing (4.57) to (4.54) earlier, with just one nontrivial phase, giving real entropy.

Qubit chains: In Appendix 6.9, we study finite and infinite chains of qubits with nearest neighbour interactions, towards understanding the reduced time evolution operator for a single qubit, after partial trace over all other qubits. This also reveals interesting complex-valued entropy in general,

obtainable as a finite temperature system but with imaginary temperature. We also find a real-valued slice when the system enjoys $|1\rangle \leftrightarrow |2\rangle$ exchange symmetry.

To illustrate obtaining the time evolution operator (4.56) from the doubled transition matrix as in (4.48), (4.49), we write

$$|\psi_F\rangle = \sum_{n,m=1,2} e^{-\frac{i\,E_{nm}t}{2}}\,|nm\rangle_1 \otimes |nm\rangle_2\ , \qquad |\psi_I\rangle = \sum_{n,m=1,2} e^{\frac{i\,E_{nm}t}{2}}\,|nm\rangle_1 \otimes |nm\rangle_2\ . \tag{4.58}$$

Then the unnormalized transition matrix $T = |\psi_F\rangle\,\langle\psi_I|$ after partial trace over the second component gives

$$T^1_{F|I} = \mathrm{Tr}_2\Big(\sum_{n,m,p,q=1,2} e^{-\frac{iE_{nm}t}{2}} e^{-\frac{iE_{pq}t}{2}}\,|nm\rangle_1\,|nm\rangle_2\,\langle pq|_1\,\langle pq|_2\Big) = \sum_{n,m=1,2} e^{-i\,E_{nm}t}\,|nm\rangle_1\,\langle nm|_1\ , \tag{4.59}$$

so this reduced transition matrix is the same as the unnormalized time evolution operator.

Mutual information

Mutual information defined as $I[A,B] = S[A]+S[B]-S[A\cup B]$ can be studied for the time evolution operator as well. In the general 2-qubit case (4.55), (4.56), above, we can calculate $\rho^1_t = \mathrm{Tr}_2\rho_t$ and $\rho^2_t = \mathrm{Tr}_1\rho_t$, which then leads to the von Neumann entropies S^1_t and S^2_t respectively. The time evolution operator ρ_t itself leads to $S_t = -\mathrm{tr}\big(\rho_t \log \rho_t\big)$. It is straightforward to see that $\rho^{1,2}_t$ are of the same form as ρ^A_t in (4.57), which alongwith ρ_t in (4.56) gives

$$\begin{aligned} S^{1,2}_t &= -\frac{1+e^{i\theta_2}}{1+e^{i\theta_1}+2e^{i\theta_2}}\,\log\frac{1+e^{i\theta_2}}{1+e^{i\theta_1}+2e^{i\theta_2}} - \frac{e^{i\theta_1}+e^{i\theta_2}}{1+e^{i\theta_1}+2e^{i\theta_2}}\,\log\frac{e^{i\theta_1}+e^{i\theta_2}}{1+e^{i\theta_1}+2e^{i\theta_2}}\ , \\ S_t &= -\frac{1}{1+e^{i\theta_1}+2e^{i\theta_2}}\,\log\frac{1}{1+e^{i\theta_1}+2e^{i\theta_2}} - \frac{e^{i\theta_1}}{1+e^{i\theta_1}+2e^{i\theta_2}}\,\log\frac{e^{i\theta_1}}{1+e^{i\theta_1}+2e^{i\theta_2}} \\ &\quad - \frac{2e^{i\theta_2}}{1+e^{i\theta_1}+2e^{i\theta_2}}\,\log\frac{e^{i\theta_2}}{1+e^{i\theta_1}+2e^{i\theta_2}}\ , \end{aligned} \tag{4.60}$$

so the mutual information is

$$I[A,B] = S^1_t + S^2_t - S_t\ . \tag{4.61}$$

In general this is nonzero and complex since the entropies are complex in general. However there are special cases: for instance if all energy eigenvalues are identical, then

$$\theta_{1,2} = 0\ : \qquad S^{1,2}_t = \log 2\,,\quad S_t = 2\log 2 \quad\Rightarrow\quad I[A,B] = 0\ , \tag{4.62}$$

although the time evolution is nontrivial since each phase e^{-iEt} is nonzero.
Likewise the 2-state subcase (4.53) is obtained by setting $e^{i\theta_2} = 0$ which gives $S^{1,2}_t, S_t$ of the same real-valued form as in (4.54), so $I[A,B] = S^1_t$.

These expressions above can also be viewed as arising from the finite temperature results for inverse temperature β continued to $\beta = it$. From that point of view, the high temperature limit

$\beta \to 0$ gives vanishing mutual information: this limit has $\beta E_i \to 0$ which is mathematically equivalent to the $\theta_{1,2} = 0$ subcase earlier, with $I[A,B] \to 0$. In the present context, this is $t \to 0$, and we again obtain vanishing mutual information, $I[A,B] \to 0$.

4.4.2 2-qutrit systems

Consider now two qutrits, $|i\rangle,\ i = 0,1,2$: the Hamiltonian (in eigenstate basis) and the normalized time evolution operator are

$$H = \sum E_{ij} |ij\rangle\langle ij| \,, \qquad E_{ij} = \{E_{00}, E_{11}, E_{22}, E_{01}, E_{02}, E_{12}\} \ , \tag{4.63}$$
$$\rho_t = \frac{e^{-iE_{ij}t}}{\sum_{ij} e^{-iE_{ij}t}} \, |ij\rangle\langle ij| \ = \ \frac{e^{-iE_{ij}t}}{e^{-iE_{00}t} + e^{-iE_{11}t} + e^{-iE_{22}t} + 2e^{-iE_{01}t} + 2e^{-iE_{02}t} + 2e^{-iE_{12}t}} \, |ij\rangle\langle ij|,$$

again with $E_{ij} = E_{ji}$. The reduced time evolution operator tracing over the second qutrit is

$$(\rho_t^A)_{ij} = (\rho_t)_{ijkl}\delta^{kl} \,; \qquad \rho_t^A = \frac{1}{\sum_{ij} e^{-iE_{ij}t}} \sum_{i=0,1,2} \big(\sum_j e^{-iE_{ij}t}\big) |i\rangle\langle i| \ . \tag{4.64}$$

In general this leads to complex-valued entropy as before, with multiple distinct phases. Imposing exchange symmetry between the qutrits, *i.e.* $|0\rangle \leftrightarrow |1\rangle \leftrightarrow |2\rangle$, this reduces to a single independent phase controlled by $-(E_{01} - E_{00})t$ which then gives real entropy.

4.4.3 Two uncoupled oscillators

We consider two uncoupled harmonic oscillators: the Hamiltonian is

$$H = \sum E_{n_1 n_2} \, |n_1, n_2\rangle\langle n_1, n_2| \,, \qquad E_{n_1 n_2} = \omega(n_1 + n_2 + 1) \ . \tag{4.65}$$

The normalized time evolution operator then becomes

$$\rho_t = \sum \frac{e^{-iE_{n_1 n_2}t}}{\sum e^{-iE_{n_1 n_2}t}} \, |n_1, n_2\rangle\langle n_1, n_2| \tag{4.66}$$

The normalization evaluates to

$$\sum_{1,2} e^{-iE_{n_1 n_2}t} = e^{-i\omega t} \sum_{1,2} e^{-i\omega n_1 t} \ e^{-i\omega n_2 t} = \frac{e^{-i\omega t}}{(1 - e^{-i\omega t})^2} \ . \tag{4.67}$$

Now, tracing over the second oscillator, we obtain

$$\rho_t^A = \sum_{n_2=0}^{\infty} \rho_t = \sum_{n_1} \frac{e^{-i\omega n_1 t}}{1/(1 - e^{-i\omega t})} \, |n_1\rangle\langle n_1| \tag{4.68}$$

with the von Neumann entropy

$$S_t^A = -\sum_n \frac{e^{-i\omega n t}}{1/(1 - e^{-i\omega t})} \, \log \frac{e^{-i\omega n t}}{1/(1 - e^{-i\omega t})} = -\log\big(1 - e^{-i\omega t}\big) + \frac{i\omega t \, e^{-i\omega t}}{1 - e^{-i\omega t}} \ , \tag{4.69}$$

which is the usual entropy for a single oscillator at finite temperature with $\beta = it$. In general this is complex-valued. The zero temperature limit gives $S \sim \beta E\, e^{-\beta E}$ which here gives $S \sim it\omega\, e^{-i\omega t}$.

In evaluating the normalization (4.67), it is important to note that this sum over the infinite tower of states (and similar quantities involving any infinite tower of states) is not strictly convergent as an infinite series since this complex expression is highly oscillatory for high energy states, although the sum and its closed form expression are formally true. This is also true for the single oscillator expression (4.68) obtained as the reduced time evolution operator, whose normalization is $\sum_{n_1} e^{-i\omega n_1 t} = 1/(1-e^{-i\omega t})$. Towards rendering this well-defined as a series, one can introduce a small regulator either in ω or in t (giving time a tiny regulating Euclidean component) which then makes it converge: *e.g.* a small Euclidean time component gives

$$\sum_{n_1} e^{-i\omega n_1 (t-i\epsilon)} = \sum_{n_1} e^{-i\omega n_1 t} e^{-n_1 \omega \epsilon} = \frac{1}{1-e^{-i\omega(t-i\epsilon)}}\,, \tag{4.70}$$

which defines the sum. An alternative way to view it is to start with the (convergent) finite temperature partition function $\sum_n e^{-\beta E_n}$ and then perform analytic continuation to imaginary temperature $\beta = it$.

It is also interesting to study two coupled harmonic oscillators with the Hamiltonian

$$H = \frac{1}{2}\,(p_A^2 + p_B^2) + \frac{k_1}{2}\,(x_A^2 + x_B^2) \,+\, \frac{k_2}{2}\,(x_A - x_B)^2\ . \tag{4.71}$$

We describe this in detail in Appendix 6.10. The resulting entropy from the time evolution operator can be interpreted as arising from an imaginary temperature.

4.5 The time evolution operator with projections

As we have seen, the entanglement structures arising from the time evolution operator involve the entire space of states, as the time evolution operator behaves like a full density matrix. To better understand its various components, it is desirable to isolate a "part" of the time evolution operator. This motivates appending projections onto individual states.

With this in mind, we now consider the time evolution operator along with a projection operator onto some state $|i\rangle$, as in (4.39):

$$\rho_t^{|i\rangle} = \frac{\rho_t |i\rangle\langle i|}{\mathrm{Tr}(\rho_t |i\rangle\langle i|)} = \frac{|f[i]\rangle\langle i|}{\mathrm{Tr}(|f(i)\rangle\langle i|)}\ , \qquad |f[i]\rangle = e^{-iHt}|i\rangle\ . \tag{4.72}$$

(The projection here is from the right: at the calculational level, projecting from the left is similar but leads to complex conjugate expressions in general.) The state $|f[i]\rangle$ is the final state obtained by time-evolving the initial state $|i\rangle$. If $|i\rangle$ is a Hamiltonian eigenstate, then $\rho_t^{|i\rangle}$ reduces to just a single component $|i\rangle\langle i|$ (the phase coefficient cancels upon normalizing), *i.e.* the usual density matrix for $|i\rangle$. This is also true at $t = 0$ for a generic state $|i\rangle$: here $\rho_t^{|i\rangle}|_{t=0} = \frac{|i\rangle\langle i|}{\mathrm{Tr}(|i\rangle\langle i|)}$ which gives ordinary entanglement structures at $t = 0$.

For a generic state $|i\rangle$, we obtain (4.43). As a simple concrete example, consider the 2-state system (4.53) earlier with a generic initial state:

$$|i\rangle = c_1|1\rangle + c_2|2\rangle \quad (|c_1|^2 + |c_2|^2 = 1) \qquad \to \qquad |f[i]\rangle = c_1 e^{-iE_1 t}|1\rangle + c_2 e^{-iE_2 t}|2\rangle\,;$$
$$\rho_t^{|i\rangle} = \mathcal{N}^{-1}\Big(|c_1|^2 e^{-iE_1 t}|1\rangle\langle 1| + |c_2|^2 e^{-iE_2 t}|2\rangle\langle 2| + c_1 c_2^* e^{-iE_1 t}|1\rangle\langle 2| + c_2 c_1^* e^{-iE_2 t}|2\rangle\langle 1|\Big), \quad (4.73)$$

where $\mathcal{N} = \mathrm{Tr}(|f\rangle\langle i|)$ is the normalization. Now taking $|1\rangle \equiv |{+}{+}\rangle$ and $|2\rangle \equiv |{-}{-}\rangle$ and performing a partial trace over the second component gives

$$\rho_t^{|i\rangle,A} = \frac{1}{|c_1|^2 + |c_2|^2 e^{i\theta}}\Big(|c_1|^2|+\rangle\langle +| + |c_2|^2 e^{i\theta}|-\rangle\langle -|\Big), \qquad \theta = -(E_2 - E_1)t\,,$$
$$S_t^{|i\rangle,A} = -\frac{|c_1|^2}{|c_1|^2 + |c_2|^2 e^{i\theta}} \log \frac{|c_1|^2}{|c_1|^2 + |c_2|^2 e^{i\theta}} - \frac{|c_2|^2 e^{i\theta}}{|c_1|^2 + |c_2|^2 e^{i\theta}} \log \frac{|c_2|^2 e^{i\theta}}{|c_1|^2 + |c_2|^2 e^{i\theta}}\,. \quad (4.74)$$

At $t = 0$, the von Neumann entropy above is ordinary entanglement entropy for the generic state $|i\rangle$ (obtained from $\rho_A = \mathrm{Tr}_B\,|i\rangle\langle i|$). For general timelike separation t, the entropy S_A is real-valued only if $|c_1|^2 = |c_2|^2$, *i.e.* maximal entanglement at $t = 0$ (or $\theta = 0$).

Consider now two qubits, each $|1\rangle, |2\rangle$, with a general Hamiltonian (4.55) as before. For a generic state

$$|I\rangle = \sum_{ij} c_{ij}|ij\rangle\,, \quad (4.75)$$

with the basis $|ij\rangle = \{|11\rangle, |22\rangle, |12\rangle, |21\rangle\}$, and the time evolution operator with projection can be evaluated as (4.43). Performing a partial trace over the second component here gives

$$\begin{aligned}
\rho_t^{|I\rangle,A} &= \frac{1}{\sum_{ij}|c_{ij}|^2 e^{-iE_{ij}t}} \sum_{i,k=1}^{2} \big(\sum_j c_{ij} c_{kj}^* e^{-iE_{ij}t}\big)|i\rangle\langle k| \\
&= \frac{1}{\sum_{ij}|c_{ij}|^2 e^{-iE_{ij}t}}\Big(\big(|c_{11}|^2 e^{-iE_{11}t} + |c_{12}|^2 e^{-iE_{12}t}\big)|1\rangle\langle 1| \\
&\qquad + \big(c_{11}c_{21}^* e^{-iE_{11}t} + c_{12}c_{22}^* e^{-iE_{12}t}\big)|1\rangle\langle 2| + \big(c_{21}c_{11}^* e^{-iE_{12}t} + c_{22}c_{12}^* e^{-iE_{22}t}\big)|2\rangle\langle 1| \\
&\qquad + \big(|c_{21}|^2 e^{-iE_{12}t} + |c_{22}|^2 e^{-iE_{22}t}\big)|2\rangle\langle 2|\Big) \qquad (4.76)
\end{aligned}$$

At $t = 0$, this is ordinary entanglement for the generic state $|I\rangle$. There are special subcases with interesting structure, some of which we will discuss soon.

For 3-qubits with Hamiltonian (C2) with energies E_{ijk} for eigenstates $|ijk\rangle$ (alongwith the symmetry-based simplifications there), we obtain

$$|I\rangle = \sum_{i,j,k=1}^{2} c_{ijk}|ijk\rangle : \qquad \rho_t^{|I\rangle} = \frac{1}{\sum_{ijk}|c_{ijk}|^2 e^{-iE_{ijk}t}} \sum_{i,j,k,l,m,n=1}^{2} c_{ijk}c_{lmn}^* e^{-iE_{ijk}t}|ijk\rangle\langle lmn|\,,$$
$$\rho_t^{|I\rangle,A} = \frac{1}{\sum_{ijk}|c_{ijk}|^2 e^{-iE_{ijk}t}} \sum_{j,m=1}^{2} \big(\sum_i \sum_k c_{ijk}c_{imk}^* e^{-iE_{ijk}t}\big)|j\rangle\langle m|\,, \quad (4.77)$$

where the last line is the reduced transition matrix for the middle qubit, arising after a partial trace over the 1st and 3rd components $(\rho_t^A)_{jm} = (\rho_t)_{ijk,lmn}\delta^{il}\delta^{kn}$.

4.5.1 Thermofield-double type states

It is interesting to focus on thermofield-double type initial states with only "diagonal" components: then for 2-qubits, using (4.76) we obtain

$$|I\rangle = \sum_{i=1,2} c_{ii}|ii\rangle \; : \qquad \rho_t^{|I\rangle} = \frac{1}{\sum_i |c_{ii}|^2 e^{-iE_{ii}t}} \sum_{i,k=1}^{2} c_{ii}c_{kk}^* e^{-iE_{ii}t}|ii\rangle\langle kk|,$$
$$\rho_t^{|I\rangle,A} = \frac{1}{|c_{11}|^2 e^{-iE_{11}t} + |c_{22}|^2 e^{-iE_{22}t}} \Big(|c_{11}|^2 e^{-iE_{11}t}|1\rangle\langle 1| + |c_{22}|^2 e^{-iE_{22}t}|2\rangle\langle 2| \Big) . \quad (4.78)$$

This is identical to (4.74). To elaborate a little, the initial state is $|I\rangle = c_{11}|11\rangle + c_{22}|22\rangle$ and its time-evolved final state is $|F\rangle = c_{11}e^{-iE_{11}t}|11\rangle + c_{22}e^{-iE_{22}t}|22\rangle$, and the reduced time evolution operator with projection, $\rho_t^{|I\rangle,A}$ above, is the normalized reduced transition matrix for $|I\rangle$, $|F\rangle$, with the corresponding (in general complex-valued) pseudo-entropy (4.41).

Now restricting further to maximally entangled states with $|c_{11}|^2 = |c_{22}|^2 = \frac{1}{2}$ simplifies this to just a single nontrivial phase $e^{i\theta} = e^{-i\Delta E\, t}$ where $\Delta E = E_{22} - E_{11}$, thereby leading to the entanglement structure (4.54) of the time evolution operator for the 2-state case, *i.e.* $S_t^{|I\rangle,A} = -\frac{1}{1+e^{i\theta}} \log \frac{1}{1+e^{i\theta}} - \frac{1}{1+e^{-i\theta}} \log \frac{1}{1+e^{-i\theta}}$. The states in question here can be regarded as maximally entangled Bell pairs and the entropy can be regarded as pseudo-entropy for the Bell pair initial state $|I\rangle$ and its time-evolved final state $|F\rangle$. As noted there, this is a real-valued entropy, oscillating in time with periodicity set by ΔE, growing unbounded at specific time values where $t = \frac{(2n+1)\pi}{\Delta E}$. Note also that specific time values $t = \frac{2n\pi}{\Delta E}$ lead to the minimum value $S_A = \log 2$, which is simply the ordinary entanglement entropy of the maximally entangled initial state. The fact that this time entanglement entropy can be unbounded is a novel feature compared with ordinary entanglement entropy for ordinary quantum systems.

For an n-qubit system comprising basis states $|\{i_1, \ldots, i_n\}\rangle$, with $i_k = 1, 2$, the time evolution operator with projection onto generic initial states gives complicated entanglement structure. However projecting onto thermofield double type initial states, we obtain

$$|I\rangle = \sum_{i=1,2} c_{ii\ldots i}|ii\ldots i\rangle \; : \qquad \rho_t^{|I\rangle,A} = \frac{1}{\sum_i |c_{ii\ldots i}|^2 e^{-iE_{ii\ldots i}t}} \sum_{i=1}^{2} |c_{ii\ldots i}|^2 e^{-iE_{ii\ldots i}t}|i\rangle\langle i| \,, \quad (4.79)$$

which is identical to the 2-qubit case. It is clear that any qubit system has identical entanglement structure for the time evolution operator with projection onto thermofield double type states. Now if we additionally restrict to maximal entanglement, we have both $|c_{ii\ldots i}|^2$ equal so $|c_{ii\ldots i}|^2 = \frac{1}{2}$. This again contains just one nontrivial phase thereby leading to the entanglement structure of the time evolution operator for the 2-state case, *i.e.* (4.54).

4.6 Time evolution operator, normalized at $t = 0$

In this section, we will discuss aspects of the time evolution operator with normalization at $t = 0$ (rather than at general time t), following [224]. This gives

$$\rho_t^0(t) \equiv \frac{\mathcal{U}(t)}{\mathrm{Tr}\mathcal{U}(0)} \quad \rightarrow \quad \rho_t^{0,A} = tr_B\, \rho_t \quad \rightarrow \quad S_A = -tr(\rho_t^A \log \rho_t^A)\ . \tag{4.80}$$

The normalization ensures that we obtain ordinary entanglement structures at $t = 0$. In this case $\mathrm{Tr}\,\rho_t(t) = 1$ at $t = 0$ but not at general t. This gives quite different entanglement structures, as we will see.

Since $\mathcal{U}(0) = \sum_I |I\rangle\langle I| = \mathbf{1}$ *i.e.* the identity operator made up as a sum over all eigenstate projection operators, the normalization factor is $\mathrm{Tr}\,\mathcal{U}(0) = N$, the dimension of the Hilbert space, constant in time. Thus for a general bipartite system we obtain

$$\rho_t^0(t) = \frac{1}{N}\sum_{i,i'} e^{-iE_{i,i'}t}|i,i'\rangle\langle i,i'| \quad \rightarrow \quad \rho_t^{0,A} = \frac{1}{N}\sum_i \big(\sum_{i'} e^{-iE_{i,i'}t}\big)|i\rangle\langle i|\,, \tag{4.81}$$

differing from (4.42) only in the normalization. A general 2-qubit system (4.55) now gives

$$\rho_t^0(t) = \frac{1}{4}\sum_{ij} e^{-iE_{ij}t}\,|ij\rangle\langle ij| \tag{4.82}$$

and taking a partial trace over the second component gives

$$\begin{aligned}
\rho_t^{0,A} &= \frac{1}{4}\Big(\big(e^{-iE_{11}t} + e^{-iE_{12}t}\big)|1\rangle\langle 1| + \big(e^{-iE_{21}t} + e^{-iE_{22}t}\big)|2\rangle\langle 2|\Big) \\
S_t^{0,A} &= -\frac{1}{4}\big(e^{-iE_{11}t} + e^{-iE_{12}t}\big)\log\Big(\frac{1}{4}\big(e^{-iE_{11}t} + e^{-iE_{12}t}\big)\Big) \\
&\quad - \frac{1}{4}\big(e^{-iE_{21}t} + e^{-iE_{22}t}\big)\log\Big(\frac{1}{4}\big(e^{-iE_{21}t} + e^{-iE_{22}t}\big)\Big).
\end{aligned} \tag{4.83}$$

In general $S_t^{0,A}$ is a complicated complex entropy. However there are special cases. If all energy values are the same, this simplifies to

$$\begin{aligned}
E_{ij} = E_0: \qquad \rho_t &= \frac{e^{-iE_0t}}{4}\sum_{ij}|ij\rangle\langle ij|\,, \quad \rho_t^{0,A} = \frac{e^{-iE_0t}}{2}\sum_{i=1,2}|i\rangle\langle i|\,, \\
S_t^{0,A} &= -e^{-iE_0t}\log\Big(\frac{1}{2}e^{-iE_0t}\Big) = (\log 2 + iE_0t)\ e^{-iE_0t}\ .
\end{aligned} \tag{4.84}$$

Appending a projection operator for a state $|i\rangle$ as in sec. 4.5, we obtain

$$\rho_t^{0,|i\rangle} = \frac{\rho_t^0\,|i\rangle\langle i|}{\mathrm{Tr}(\rho_t^0\,|i\rangle\langle i|)} = \frac{|f[i](t)\rangle\langle i|}{\mathrm{Tr}\,(\mathcal{U}(0)|i\rangle\langle i|)} = \frac{|f[i](t)\rangle\langle i|}{\mathrm{Tr}(|i\rangle\langle i|)}\,, \tag{4.85}$$

since $\mathcal{U}(0)$ is the identity operator. This is similar to (4.39), but differs in normalization. So if the initial state is unit-normalized, the normalization factor is a trivial 1. This is not ordinary

entanglement even if the state is an eigenstate since the nontrivial time evolution phase remains. For instance a 2-qubit system (4.55) gives

$$|i\rangle = |11\rangle \; : \quad \rho_t^{0,|i\rangle} = \frac{\mathcal{U}(t)|11\rangle\langle 11|}{\mathrm{Tr}(|11\rangle\langle 11|)} = e^{-iE_{11}t}|11\rangle\langle 11|\,, \tag{4.86}$$

after projecting onto a simple eigenstate $|11\rangle$. The partial trace then gives

$$\rho_t^{0,|i\rangle,A} = \mathrm{Tr}_2 \rho_t^{0,|i\rangle} = e^{-iE_{11}t}|1\rangle\langle 1| \quad \Rightarrow \quad S_t^{0,|i\rangle,A} = -e^{-iE_{11}t}\,\log\left(e^{-iE_{11}t}\right) = iE_{11}t\,e^{-iE_{11}t}\,. \tag{4.87}$$

The normalization at $t = 0$ distinguishes this from ordinary mixed-state entanglement structures at finite temperature, though it still bears a resemblance to imaginary temperature structures. Although it might seem natural to normalize at general t, part of the motivation here, following [224], is that the time evolution only enters via the final state in (4.85), which apart from this is akin to the pseudo-entropy (4.39), (4.72). This appears to help isolate the timelike characteristics, as in (4.87) where the leading time-dependence is manifestly pure imaginary: it would be interesting to explore this further.

4.7 2-dim CFTs and timelike intervals

The studies of dS_3 extremal surfaces in [221, 222, 223, 224], led to studies of timelike entanglement in ordinary 2-dim CFT (in particular (4.95)): we now elaborate on this (there are parallels with some discussions in [236] which appeared as we were finalizing this paper).

We want to consider the time evolution operator as a density operator towards exploring entanglement-like structures: towards this we define

$$\rho_t[\{\phi(x)\}|\{\phi(x')'\}] = \frac{1}{Z_t}\,\langle\{\phi(x)\}|e^{-itH}|\{\phi(x')\}\rangle \tag{4.88}$$

with $Z_t = \mathrm{Tr}\; e^{-itH}$. However rendering this well-defined is best done in the Euclidean path integral formulation, defining the ground state wavefunction for the configuration $\phi(x')$ as

$$\Psi[\{\phi(x')\}] = \int_{t_E=-\infty}^{\phi(t_E=0,x)=\phi(x')} D\phi\, e^{-S_E} = \int_{t_E=-\infty}^{t_E=0} D\phi\, e^{-S_E} \prod_x \delta(\phi(t_E=0,x) - \phi(x')) \tag{4.89}$$

with S_E the Euclidean action for the field $\phi(t_E, x)$ (we model this discussion along the lines of [36, 37, 96], and [259]). Now the reduced density matrix for the interval A is obtained from $\rho_t[\phi_0(x)|\phi_0'(x')]$ above by performing a partial trace over the environment B setting $\phi_0(x) = \phi_0'(x)$. This becomes

$$\rho[\phi(x)_{0^+}|\phi(x)_{0^-}] = \frac{1}{Z}\int_{t_E=-\infty}^{t_E=\infty} D\phi\, e^{-S_E(\phi)} \prod_{x\in A} \delta(\phi(0^+,x) - \phi(x)_{0^+})\;\delta(\phi(0^-,x) - \phi(x)_{0^-}) \tag{4.90}$$

In this form there is no sacrosanct meaning to what we define as Euclidean time: the differences for a timelike interval only enter in the analytic continuation to Lorentzian signature eventually.

For a free massless 2-dim scalar, the action is $S_E = \int dt_E dx\,((\partial_{t_E}\phi)^2 + (\partial_x\phi)^2)$ and Euclidean evolution appears symmetric between t_E, x. For the usual spacelike interval, the reduced density matrix involves Euclidean time evolution along t_E: for a timelike interval on the other hand, the reduced density matrix involves Euclidean time evolution along x which is regarded as Euclidean time now calculationally. So we have

$$\rho_t[\phi(t_E)_{0^+}|\phi(t_E)_{0^-}] = \frac{1}{Z_{t_E}}\int_{x=-\infty}^{x=\infty} D\phi\, e^{-S_E(\phi)} \prod_{t_E\in A} \delta(\phi(t_E,0^+) - \phi(t_E)_{0^+})\ \delta(\phi(t_E,0^-) - \phi(t_E)_{0^-}) \tag{4.91}$$

Apart from $x \leftrightarrow t_E$, this is equivalent to (4.90).

Let us now discuss this in terms of Hamiltonians for a free massless scalar: note that Euclidean and Lorentzian times are related as $t_E = it$. For the usual time coordinate t, the Hamiltonian is $H_t^+ = \int dx\,((\partial_t\phi)^2 + (\partial_x\phi)^2) = \int dx\,(-(\partial_{t_E}\phi)^2 + (\partial_x\phi)^2)$: this is positive definite. Now compactifying t_E can be used to obtain the reduced density matrix $\mathrm{Tr}_B\, e^{-\beta_t H}$ at finite temperature for an interval with width Δx. With x taken as Euclidean time, we obtain the Hamiltonian $H_x = \int dt_E\,((\partial_{t_E}\phi)^2 - (\partial_x\phi)^2)$. Now compactifying x with periodicity β_x and considering a timelike interval with width Δt, the reduced density matrix becomes

$$H_x = \int dt_E\,(-(\partial_x\phi)^2 + (\partial_{t_E}\phi)^2) = -i\int dt\,((\partial_x\phi)^2 + (\partial_t\phi)^2) \equiv -iH_x^+\,;$$
$$\rho_t^A = \mathrm{Tr}_B\, e^{-\beta_x H_x} = \mathrm{Tr}_B\, e^{i\beta_x H_x^+}\,, \tag{4.92}$$

so that in terms of the positive definite Hamiltonian H_x^+, this resembles a thermal reduced density matrix but with imaginary temperature.

The usual replica formulation of entanglement entropy for a single interval proceeds by picking some Euclidean time direction τ_E and the interval $\Delta x \equiv [u,v]$ on that slice, then constructing n replica copies of the space glued at the interval endpoints and evaluating $\mathrm{Tr}\rho_A^n$. The reduced density matrix for the ground state is formulated as above, via Euclidean time evolution, with appropriate boundary conditions for the fields on the replica sheets. Then $\mathrm{Tr}\rho_A^n$ in the replica space can be mapped to the twist operator 2-point function at the interval endpoints which implement the boundary conditions across the sheets. This finally leads to

$$S_A = -\lim_{n\to 1}\partial_n \mathrm{Tr}\rho_A^n \ \to\ \frac{c}{6}\log\frac{(\Delta x)^2}{\epsilon^2}\,. \tag{4.93}$$

The only data that enters this is the central charge of the CFT and the interval in question. When we consider a timelike interval, the above formulation goes through with the only change being that the Euclidean time slice we pick is the spatial slice $x = const$ with the interval being $\Delta t \equiv [u_t, v_t]$. However now when we continue back to Lorentzian time, we must rotate u_t, v_t accordingly, so the spacetime interval is

$$\Delta^2 = -(\Delta t)^2 = -(v_t - u_t)^2\,, \tag{4.94}$$

and the entanglement entropy becomes

$$S_A = \frac{c}{6}\log\frac{\Delta^2}{\epsilon^2} = \frac{c}{6}\log\frac{-(\Delta t)^2}{\epsilon^2} = \frac{c}{3}\log\frac{\Delta t}{\epsilon} + \frac{c}{6}(i\pi)\ , \tag{4.95}$$

with the imaginary part arising as $i\pi = \log(-1)$. Note that imaginary values also arise in studies of quantum extremal surfaces in de Sitter with regard to the future boundary [98, 127], stemming from timelike-separations.

The discussions above are formulated in terms of Euclidean path integrals with an eventual analytic continuation to obtain timelike interval entanglement. Along the lines of our finite quantum system descriptions, one could consider Lorentzian time evolution explicitly. Towards this consider a CFT on a cylinder, with time running along the axis. The Hamiltonian is $H_{cyl} = \frac{\pi}{l}(L_0 + \bar{L}_0 - \frac{c+\bar{c}}{24})$ and the unnormalized time evolution operator becomes $e^{-iH_{cyl}t} \sim q^{\sum_n nN_n}|N_n\rangle\langle N_n|$ with $q = e^{-2it/l}$ for both left/right modes, and the normalization becomes $\mathrm{Tr}\, q^{\sum_n nN_n} = \prod_{n=1}^{\infty}\frac{1}{1-q^n}$ (the $\frac{c+\bar{c}}{24}$ factor cancels with normalization). In the momentum basis, the time evolution operator is an infinite sum of decoupled oscillators. Recalling the case of two uncoupled oscillators (4.66), tracing out all higher mode oscillators leaving only the lowest frequency $n = 1$ oscillator mode naively gives $\rho_t^A = \sum_n \frac{q^n}{1/(1-q)}|n\rangle\langle n|$ and $S_t^A = -\log(1-q) - \frac{q\log q}{1-q}$, with appropriate limits as described after (4.68). Also, along the lines of sec. 4.5, we can study aspects of the time evolution operator along with projection onto initial states. We leave these and related investigations for the future.

4.8 Time entanglement, time-dependent interactions

So far, we have considered time-independent Hamiltonians, where the time evolution operator can be related to the thermal density matrix through the analytic continuation $\beta \to it$. This aligns with the expectation that time independence corresponds to thermal equilibrium. In this section, we explore specific examples of time-dependent Hamiltonians. In such cases, we anticipate that the time evolution operator will not admit a simple mapping to a thermal density matrix, as no thermal equilibrium is present.

We obtain the time evolution operator in the interaction picture by solving the Schrodinger time evolution equations, evolving the state by the time evolution operator

$$|\alpha, t\,; t_0\rangle_I = U_I(t, t_0)\ |\alpha, t_0; t_0\rangle_I = \sum c_{ij}(t)\,|ij\rangle\ . \tag{4.96}$$

This enables to determine the time evolution operator, where $|ij\rangle$ are the eigenstates of H_0 (and $t_0 = 0$). Our conventions are those of [261], with the interaction picture time evolution equations of the form $i\hbar\frac{d}{dt}c_N(t) = \sum_M V_{NM}e^{i\omega_{NM}t}c_M(t)$ with $\omega_{NM} = E_N - E_M$.

As a toy example, consider a 2-state system with states $|1\rangle, |2\rangle$, and energies E_1, E_2: then a δ-function interaction $V_{12} = V\delta(t-\epsilon)$ (with $\epsilon > 0$ an infinitesimal regulator) gives the interaction

picture evolution equations (with $\dot{c}_i = \frac{d}{dt}c_i$)

$$\begin{aligned} i\hbar\dot{c}_1 &= V_{12}e^{i\omega_{12}t}c_2\,, \qquad & i\hbar\dot{c}_2 &= V_{21}e^{i\omega_{21}t}c_1\,; \\ i\hbar c_1(t) &= Vc_2(\epsilon) + i\hbar c_1(0)\,, \qquad & i\hbar c_2(t) &= Vc_1(\epsilon) + i\hbar c_2(0)\,, \end{aligned} \tag{4.97}$$

where the second line is obtained by integrating across the interaction support at $t = \epsilon$ (and the phases $e^{i\omega_{12}t}$ are trivial). Since the time dependence is only nontrivial for $t = \epsilon$, we see that $c_i(t) = c_i(\epsilon)$, *i.e.* the coefficients remain unchanged for $t \geq \epsilon$. Solving for $c_1(t), c_2(t)$ gives $\binom{c_1(t)}{c_2(t)} = \rho_{t,I}\binom{c_1(0)}{c_2(0)}$ with generic initial state $c_1(0), c_2(0)$, where the interaction picture time evolution operator is $\rho_{t,I} = \frac{1}{1+\frac{V^2}{\hbar^2}}\big(|1\rangle\langle 1| + \frac{V}{i\hbar}|1\rangle\langle 2| + + \frac{V}{i\hbar}|2\rangle\langle 1| + |2\rangle\langle 2|\big)$ (this can also be seen to agree with time dependent perturbation theory). We now generalize this sort of delta-function coupling interaction to a system of two qubits to study time entanglement.

Consider a simple system of two qubits with the time-dependent interaction

$$V_I(t) = V\delta(t-\epsilon)\left(\,|11\rangle\,\langle 12| \,+\, |12\rangle\,\langle 11|\,\right), \tag{4.98}$$

with an infinitesimal regulator $\epsilon > 0$ (so the impulse interaction is just after $t = 0$). The Hamiltonian H_0 before turning on the interaction ($t \leq 0$) has eigenstates $|11\rangle$, $|22\rangle$, $|12\rangle$, $|21\rangle$, and eigenvalues E_{11}, E_{22}, E_{12}, $E_{21} = E_{12}$, respectively. The time evolution equations for the coefficients (suppressing the phases), and their integrated versions, are (with $\hbar = 1$)

$$\begin{aligned} \frac{d}{dt}c_{11}(t) &= -iV\,\delta(t-\epsilon)\,c_{12}(t)\ , \qquad & \frac{d}{dt}c_{12}(t) &= -iV\,\delta(t-\epsilon)\,c_{11}(t)\,, \\ \frac{d}{dt}c_{21}(t) &= 0 \qquad\qquad\ , \qquad & \frac{d}{dt}c_{22}(t) &= 0\,, \\ \Rightarrow \qquad c_{11}(t) &= c_{11}(0) - iV\,c_{12}(\epsilon) \quad , \qquad & c_{12}(t) &= c_{12}(0) - iV\,c_{11}(\epsilon), \\ c_{21}(t) &= c_{21}(0) \qquad\qquad , \qquad & c_{22}(t) &= c_{22}(0)\,. \end{aligned} \tag{4.99}$$

We now note that the $c_{ij}(t) = c_{ij}(\epsilon)$ for the impulse interaction, where $t \geq \epsilon$, since there is no nontrivial time dependence after $t = \epsilon$. This then gives

$$\begin{aligned} c_{11}(t) &= \frac{1}{1+V^2}\Big(c_{11}(0) - iV\,c_{12}(0)\Big)\ , \qquad & c_{12}(t) &= \frac{1}{1+V^2}\Big(c_{12}(0) - iV\,c_{11}(0)\Big), \\ c_{21}(t) &= c_{21}(0) \qquad\qquad\qquad\qquad , \qquad & c_{22}(t) &= c_{22}(0)\,. \end{aligned} \tag{4.100}$$

This gives the interaction picture time evolution operator $U_I(t, t_0)$ (with $t_0 = 0$ and $t > 0$) which maps $\binom{c_{11}(t)}{c_{12}(t)} = U_I(t)\binom{c_{11}(0)}{c_{12}(0)}$ in the $\{|11\rangle, |12\rangle\}$ subspace, using (4.96). Then the time evolution operator $U(t) \equiv \tilde{\rho}_t$ in the Schrödinger picture is (with ρ_t the normalized one)

$$\begin{aligned} \tilde{\rho}_t = e^{-iH_0t}\,U_I(t) = \frac{1}{1+V^2}\Big(&e^{-iE_{11}t}\,|11\rangle\,\langle 11| \,-\, iVe^{-iE_{11}t}\,|11\rangle\,\langle 12| \,-\, iV\,e^{-iE_{12}t}\,|12\rangle\,\langle 11| \\ &+\, e^{-iE_{12}t}\,|12\rangle\,\langle 12|\,\Big) \,+\, e^{-iE_{12}t}\,|21\rangle\,\langle 21| \,+\, e^{-iE_{22}t}\,|22\rangle\,\langle 22|\,, \\ \rho_t = \mathcal{N}_V\tilde{\rho}_t\,, \qquad \mathcal{N}_V^{-1} \equiv \mathrm{Tr}(\tilde{\rho}_t) &= \frac{1}{1+V^2}\big(e^{-iE_{11}t} + e^{-iE_{12}t}\big) + e^{-iE_{12}t} + e^{-iE_{22}t}\,. \end{aligned} \tag{4.101}$$

We now find the reduced time evolution operator by tracing out a qubit. ρ_t^A arises from tracing out the second qubit in ρ_t, and ρ_t^B from tracing out the first qubit:

$$\begin{aligned}
\mathcal{N}_V^{-1}\rho_t^A &= \frac{1}{1+V^2}\left(e^{-iE_{11}t} + e^{-iE_{12}t}\right)|1\rangle\langle 1| + \left(e^{-iE_{12}t} + e^{-iE_{22}t}\right)|2\rangle\langle 2|\,, \\
\mathcal{N}_V^{-1}\rho_t^B &= \frac{1}{1+V^2}\Big(e^{-iE_{11}t}\,|1\rangle\langle 1| - iVe^{-iE_{11}t}\,|1\rangle\langle 2| - iV\,e^{-iE_{12}t}\,|2\rangle\langle 1| \\
&\qquad + e^{-iE_{12}t}\,|2\rangle\langle 2|\Big) + e^{-iE_{12}t}\,|1\rangle\langle 1| + e^{-iE_{22}t}\,|2\rangle\langle 2|\,. \qquad (4.102)
\end{aligned}$$

Note that $\rho_t^A = \rho_t^B$ for $V = 0$ is in agreement with sec. 4.4 for the 2-qubit system. The entropy associated with ρ_t^A or ρ_t^B is complex-valued in general.

Consider now the same 2-qubit system but a more general impulse interaction

$$V_I(t) = V\delta(t-\epsilon)\left(|11\rangle\langle 12| + |12\rangle\langle 11| + |21\rangle\langle 22| + |22\rangle\langle 21|\right). \qquad (4.103)$$

Using (4.96), the interaction picture time evolution equations and the integrated versions are

$$\begin{aligned}
&\frac{d}{dt}c_{11}(t) = -iV\,\delta(t-\epsilon)\,c_{12}(t)\,, \qquad \frac{d}{dt}c_{12}(t) = -iV\,\delta(t-\epsilon)\,c_{11}(t)\,, \\
&\frac{d}{dt}c_{21}(t) = -iV\,\delta(t-\epsilon)\,c_{22}(t)\,, \qquad \frac{d}{dt}c_{22}(t) = -iV\,\delta(t-\epsilon)\,c_{21}(t)\,, \\
\Rightarrow\quad &c_{11}(t) = c_{11}(0) - iV\,c_{12}(\epsilon)\,, \qquad c_{12}(t) = c_{12}(0) - iV\,c_{11}(\epsilon)\,, \\
&c_{21}(t) = c_{21}(0) - iV\,c_{22}(\epsilon)\,, \qquad c_{22}(t) = C_{22}(0) - iV\,c_{21}(\epsilon)\,. \qquad (4.104)
\end{aligned}$$

These are the analogs for the interaction (4.103) of (4.99) with the simpler interaction (4.98). As before, we have $c_{ij}(t) = c_{ij}(\epsilon),\ t \geq \epsilon$, since there is no nontrivial time dependence after the impulse at $t = \epsilon$. Solving for $c_{ij}(t)$ leads here to the Schrödinger picture time evolution operator $U(t) \equiv \tilde{\rho}_t$ (with ρ_t the normalized one)

$$\begin{aligned}
\tilde{\rho}_t = e^{-iH_0t}\,U_I(t) = \frac{1}{1+V^2}\Big(&e^{-iE_{11}t}\,|11\rangle\langle 11| - iVe^{-iE_{11}t}\,|11\rangle\langle 12| - iV\,e^{-iE_{12}t}\,|12\rangle\langle 11| \\
&+ e^{-iE_{12}t}\,|12\rangle\langle 12| + e^{-iE_{12}t}\,|21\rangle\langle 21| - iVe^{-iE_{12}t}\,|21\rangle\langle 22| \\
&- iV\,e^{-iE_{22}t}\,|22\rangle\langle 21| + e^{-iE_{22}t}\,|22\rangle\langle 22|\Big)\,, \\
\rho_t = \mathcal{N}_V\tilde{\rho}_t \qquad \mathcal{N}_V^{-1} \equiv \mathrm{Tr}(\tilde{\rho}_t) &= \frac{1}{1+V^2}\left(e^{-iE_{11}t} + 2e^{-iE_{12}t} + e^{-iE_{22}t}\right). \qquad (4.105)
\end{aligned}$$

Tracing out either the second qubit or the first gives ρ_t^A or ρ_t^B:

$$\begin{aligned}
\rho_t^A &= \mathcal{N}_V\,\frac{1}{1+V^2}\left((e^{-iE_{11}t} + e^{-iE_{12}t})\,|1\rangle\langle 1| + (e^{-iE_{12}t} + e^{-iE_{22}t})\,|2\rangle\langle 2|\right), \\
\rho_t^B &= \mathcal{N}_V\,\frac{1}{1+V^2}\Big((e^{-iE_{11}t} + e^{-iE_{12}t})\,|1\rangle\langle 1| - iV(e^{-iE_{11}t} + e^{-iE_{12}t})\,|1\rangle\langle 2| \\
&\qquad - iV(e^{-iE_{12}t} + e^{-iE_{22}t})\,|2\rangle\langle 1| + (e^{-iE_{12}t} + e^{-iE_{22}t})\,|2\rangle\langle 2|\Big)\,. \qquad (4.106)
\end{aligned}$$

Note that here the $\frac{1}{1+V^2}$ factors cancel with that in $\mathcal{N}_V$ (which is an accident; this would not occur if the interaction strengths in (4.103) were not uniformly V for all matrix elements). As for

(4.102), we see that these reduced time evolution operators are equal, $\rho_t^A = \rho_t^B$, for $V = 0$, in agreement with sec. 4.4. These give complex-valued entropy in general, although there are special cases with real entropy: *e.g.* for $E_{11} = E_{22} = E_{12}$ we obtain $\rho_t^B = \frac{1}{2}\left(\begin{smallmatrix} 1 & -iV \\ -iV & 1 \end{smallmatrix}\right)$ with eigenvalues $\lambda_k = \frac{1}{2}(1 \pm iV)$: then the entropy $S_t^B = -\sum_k \lambda_k \log \lambda_k$ becomes real-valued giving $S_t^B = \log 2 - \frac{1}{2}(1+iV)\log(1+iV) - \frac{1}{2}(1-iV)\log(1-iV)$.

We now look at this time evolution operator with projection onto some initial state, along the lines of sec. 4.5. First consider a thermofield-double type initial state $|I\rangle = \sum_{i=1,2} c_{ii}|ii\rangle$ as in sec. 4.5.1: this gives (with $\mathcal{N}$ the normalization)

$$\mathcal{N}\rho_t|I\rangle\langle I| = \frac{\mathcal{N}}{1+V^2}\big(\rho_t|I\rangle\langle I|\big)\big|_{V=0} - \mathcal{N}\,\frac{iV\,e^{-iE_{12}t}}{1+V^2}\Big(|c_{11}|^2|12\rangle\langle 11| + c_{11}c_{22}^*|12\rangle\langle 22| + c_{11}^* c_{22}|21\rangle\langle 11| + |c_{22}|^2|21\rangle\langle 22|\Big). \tag{4.107}$$

A partial trace over the second or first qubit gives, respectively,

$$\rho_{t,I}^A = \mathcal{N}\,\frac{1}{1+V^2}\,\rho_t^A\big|_{V=0} - \mathcal{N}\,\frac{iV\,e^{-iE_{12}t}}{1+V^2}\Big(c_{11}c_{22}^*|1\rangle\langle 2| + c_{11}^* c_{22}|2\rangle\langle 1|\Big),$$
$$\rho_{t,I}^B = \mathcal{N}\,\frac{1}{1+V^2}\,\rho_t^B\big|_{V=0} - \mathcal{N}\,\frac{iV\,e^{-iE_{12}t}}{1+V^2}\Big(|c_{11}|^2|2\rangle\langle 1| + |c_{22}|^2|1\rangle\langle 2|\Big). \tag{4.108}$$

This thus leads to nontrivial contributions to the complex-valued entropy stemming from the impulse interaction controlled by the strength V. For special cases the entropy is real: *e.g.* $E_{11} = E_{22} = E_{12}$ with maximally entangled initial state $c_{11} = c_{22} = \frac{1}{\sqrt{2}}$ gives $\rho_{t,I}^A = \rho_{t,I}^B = \frac{1}{2}\left(\begin{smallmatrix} 1 & -iV \\ -iV & 1 \end{smallmatrix}\right)$ with eigenvalues $\lambda_k = \frac{1}{2}(1 \pm iV)$ leading to real entropy $S_t^B = -\sum_k \lambda_k \log \lambda_k$.

This is essentially the pseudo-entropy for the initial state $|I\rangle = c_{11}|11\rangle + c_{22}|22\rangle$ and its time evolved final state using $\tilde{\rho}_t$ in (4.105)

$$|F\rangle = \tilde{\rho}_t|I\rangle = \frac{1}{1+V^2}\Big(e^{-iE_{11}t}c_{11}|11\rangle + e^{-iE_{22}t}c_{22}|22\rangle - iV\,e^{-iE_{12}t}c_{11}|12\rangle - iV\,e^{-iE_{12}t}c_{22}|21\rangle\Big). \tag{4.109}$$

If on the other hand, one considers some initial state within the $\{|11\rangle, |12\rangle\}$ subspace, then it turns out that $\rho_{t,I}^A \propto |1\rangle\langle 1|$ while $\rho_{t,I}^B$ has eigenvalues $0, 1$ (perhaps this is not surprising since any state in this subspace is of a factorized form $|1\rangle_A(a|1\rangle + b|2\rangle)_B$). This leads to vanishing pseudo entropy for $\rho_{t,I}^A$ and $\rho_{t,I}^B$.

We have illustrated the time evolution operator and its time entanglement structure, focusing on simple 2-qubit examples involving an impulse δ-function interaction. We obtained the time evolution operator by solving the time evolution Schrödinger equation for the state coefficients. The time dependence of the interaction introduces a nontrivial dependence on the interaction strength V, in addition to its dependence on the energy eigenvalues and the timelike separation t. Unlike the discussions in the rest of the study, which involve time-independent quantum systems, no simple continuation via some imaginary temperature exists here. It is likely that general time-dependent quantum systems will exhibit similar features. Perhaps there are deeper ways to formulate timelike entanglement that make a partial trace over time paths or histories more explicit.

4.9 Discussion

We have explored various aspects of entanglement like structures with timelike separations arising from the time evolution operator when regarded as a density operator, as discussed in [224]. There are close parallels with pseudo-entropy [227] as we have seen. The entropy from the time evolution operator alongwith projection onto some initial state as we have seen in sec. 4.5 is identical to pseudo-entropy for the initial state and its time-evolved final state. More broadly, there are large parallels of the investigations here and in [224] with corresponding ones in [223, 236]. In general, the non-Hermitian structures discussed yield complex-valued entropy; however, there are several notable real-valued subfamilies, for example, (4.54), special cases of (4.57) and (4.78), as well as qubit chains (see App.6.9) exhibiting the $|1\rangle \leftrightarrow |2\rangle$ exchange symmetry, and so on. The behaviour of this entropy is quite different from usual spatial entanglement entropy: for instance, (4.54) oscillates in time and appears to grow large at specific time values. Correspondingly at other specific periodic time values the entropy acquires its minimum value, coinciding with ordinary entanglement entropy for the initial state (see sec. 4.5.1 in the context of thermofield-double states, akin to Bell pair states). Overall these appear to be new entanglement-like measures involving timelike separations, likely with many new aspects open for exploring further. (It is also worth noting other work *e.g.* [262, 263, 264, 265], which may have bearing on this broad circle of ideas.)

Although a more detailed understanding and physical interpretation of time entanglement remain to be developed, mapping it to pseudo-entropy establishes connections with previously studied quantities. Pseudo-entropy originates from the transition matrix $\mathcal{T}_{F|I}$ in (4.41) and (4.44), which is treated as a generalized density operator incorporating both a preparation state and a postselected state. Related quantities include weak values of operators, defined as $\mathcal{O}_w = \mathrm{Tr}\big(\mathcal{T}_{F|I}\,\mathcal{O}\big)$. In general, these weak values are complex-valued, which is unsurprising given that the transition matrix is not a Hermitian object (in contrast to conventional Hermitian density matrices). See *e.g.* [266, 267] for more on postselected states, conditional entropy and weak values (including some experimental aspects). In the current context, components of the time evolution operator can be isolated via projections onto specific initial states as we have seen in sec. 4.5: this then maps onto the corresponding pseudo-entropy. Thus time entanglement with projection onto initial state $|I\rangle$ dovetails with postselected states being the corresponding time-evolved states. We hope to obtain more refined understanding of these interrelations in the future.

The finite quantum systems we have examined permit analysis through Hamiltonian eigenstates, making them inherently straightforward. Time-independent Hamiltonians enable the mapping of the time evolution operator to a thermal density matrix via the analytic continuation $\beta \to it$, aligning with the expectation that time independence corresponds to thermal equilibrium. We expect that in cases with nontrivial time dependence, these time-entanglement structures will become more intricate with no natural imaginary temperature analytic continuation: along the lines of studies of scattering amplitudes, we expect that analogs of the interaction picture will be useful in organizing these time entanglement structures. All these are vindicated in the simple

2-qubit examples with δ-function impulse potentials (sec. 4.8), where we solve explicitly for the nontrivial time evolution operator and the corresponding time entanglement structures. Related, complementary studies (including holographic ones) appear in [223], [227]-[238]. We hope to report further on these in the future.

Furthermore, recent studies have examined quantum entanglement in scattering processes from both theoretical and experimental perspectives. Notably, key experimental results from the LHC during 2023–2024 have confirmed the generation of quantum entanglement in high-energy scattering events. These include findings from the ATLAS Collaboration [268], the CMS Collaboration [269] , and the CMS Update on the High-Mass Regime [270]. These experiments reveal spatial entanglement, inferred through spin correlations among decay products. However, they have not yet measured timelike entanglement—such as entanglement between different temporal instances—or entanglement characterized via pseudo-entropy across time evolution. On the theoretical front, a number of studies have investigated entanglement in scattering processes, with notable contributions spanning both spatial and temporal aspects [271]–[276]. While most of these works focus on spatial entanglement, only a few—such as [271] and [275]—explicitly address temporal entanglement within the scattering framework. To date, no dedicated study has directly applied pseudo-entropy to scattering amplitude matrices. Existing analyses of temporal entanglement typically employ standard entropy measures—such as the von Neumann and second-order Rényi entropies—defined via density matrices, rather than pseudo-entropy derived from transition matrices or the time evolution operator. Our work, together with related research, seeks to establish a foundational framework for applying pseudo-entropy to scattering processes through the use of the scattering amplitude matrix or the time evolution operator. Further investigation into this direction remains an open and important area for future research.

It would also be of interest to explore connections between the present work and the principle of entanglement minimization, which has recently emerged as a promising bootstrap criterion (see, e.g., [277]). Nonetheless, a natural extension of this work would be to define a timelike entanglement power (EP) via the Schmidt decomposition of the time-evolution operator. This would yield a real-valued quantity that characterizes the entanglement generated as a system evolves in time. Such a formulation could offer valuable insights into the role of entanglement minimization within S-matrix bootstrap frameworks. Moreover, it holds the potential to track the buildup of entanglement during scattering processes—not only between asymptotic states but also throughout the interaction itself. A detailed investigation of this direction is left for future work.

We now make a few remarks on de Sitter extremal surfaces anchored at the future boundary, which have timelike components, in particular paraphrasing some discussions in [226]. The dS/CFT dictionary [211] $Z_{CFT} = \Psi_{dS}$ implies that boundary entanglement entropy is bulk pseudo-entropy (since a replica formulation on Z_{CFT} amounts to one on Ψ_{dS}, *i.e.* single ket rather than a density matrix). Among other things this leads to novel entropy relation/inequalities based on the complex-valued dS extremal surface areas. This is put in perspective by comparing with

time-entanglement/pseudo-entropy in qubit systems, using the analyses in this paper, in particular sec. 4.5: this reveals striking differences for mutual time-information, tripartite information and strong subadditivity (see sec.2.5 in [226]). The dS areas give definite signs for these quantities relative to those obtained from time-entanglement/pseudo-entropy for qubit systems (with the final state being time-evolved from the initial state). Since the dS areas are analytic continuations from AdS, these differences are perhaps not surprising in light of the studies in [278] (which reveal definite signs the AdS RT surface area inequalities compared with those for entanglement entropy in qubit systems), but they are striking. Overall, the entanglement structures observed here arise from timelike separations. We anticipate that this study, along with related ongoing research, will provide deeper insights into both quantum information and holography.

Chapter 5

Conclusion

In this thesis, we primarily explored various aspects of quantum extremal surfaces (QES) and holographic volume complexity within cosmological models that exhibit Big-Crunch singularities, all of which can be represented as two-dimensional cosmologies. In addition, we investigated the structure of timelike entanglement by treating the time evolution operator as a density operator and examining its connection with pseudo-entropy. Below, we summarize the key findings and results of our studies.

In Chapter 2, we examined various aspects of quantum extremal surfaces (QES) in cosmologies exhibiting Big-Crunch singularities. These cosmologies include isotropic AdS Kasner, general Kasner cosmologies with holographic interpretations, and null Kasner cosmologies obtained via dimensional reduction from higher-dimensional spacetimes. To gain insights into these cosmologies, we computed the quantum extremal surfaces by extremizing the generalized entropy, S_{gen}, whose extrema yield the QES. The generalized entropy comprises two components: a classical term and a quantum bulk entanglement entropy term. For simplicity, we assume that the bulk matter is in its ground state—a reasonable approximation in the semiclassical region far from the singularity—modeled by a two-dimensional conformal field theory (CFT_2). In the AdS Kasner case, the quantum extremal surface is consistently driven away from the near-singularity region. The QES, denoted by (r_*, t_*), asymptotically approaches $r_* \to \infty$ and $t_* \to \infty$ with $t_* \sim t_0$. To regularize the extremization solution, we introduce a spatial cutoff $r_* = R \to \infty$. This procedure allows us to associate the temporal location of the QES with the observer's time slice t_0, implying that the QES lags behind the observer O (situated at t_0) in the direction away from the singularity. Moreover, we observed that the generalized entropy decreases over time as the singularity is approached, a behavior that mirrors findings in holographic complexity studies of these cosmologies and suggests a state of low complexity near the singularity. Although an island solution initially appears to emerge, a detailed analysis of the extremization equations reveals it to be inconsistent. This observation is consistent with existing literature, which shows that these cosmologies lack horizons and are not entangled

with "elsewhere." General Kasner cosmologies exhibit similar behavior.

In the next section, we analyze a class of null cosmologies that admit a two-dimensional null reduction. These null cosmologies encapsulate holomorphic structures, as suggested by their null backgrounds. Interestingly, the quantum extremal surface in these cases can approach the null singularity region. However, the on-shell generalized entropy becomes singular in this regime, rendering the semiclassical analysis unreliable near the singularity. Nevertheless, the semiclassical analysis provides an intriguing result: the quantum extremal surfaces tend to approach the singularity. To probe the near-singularity regime more reliably, a more fundamental framework—such as string theory or a complete theory of quantum gravity—is required, as the semiclassical approximation breaks down in this region.

In Chapter 3, we analyzed the holographic volume complexity for various families of holographic cosmologies with Kasner-like singularities, specifically focusing on AdS Kaner, hyperscaling violating, and Lifshitz geometries. First, we derived the extremization equations by extremizing the codimension-1 volume functional for these cosmologies. Subsequently, we conducted an extensive numerical analysis of these equations, employing appropriate boundary conditions. Our results reveal that the complexity surface consistently bends away from the singularity, transitioning from spacelike near the boundary to lightlike in the interior. Notably, as the boundary anchoring time slice approaches the singularity, this transition to lightlike becomes more abrupt, with the spacelike region diminishing. In the vicinity of the singularity, the complexity functional receives negligible contributions from the lightlike region, resulting in a vanishing complexity near the singularity. This suggests that the dual Kasner state exhibits low complexity, corresponding to an effectively negligible number of qubits, which is consistent with the spatial volume undergoing a crunch. For AdS Kasner and isotropic Lifshitz Kasner cosmologies, the holographic complexity exhibits linear scaling with the anchoring time slice t_0. In contrast, hyperscaling violating theories demonstrate a nonlinear dependence of holographic complexity on the anchoring time slice. Additionally, our study further refines prior investigations of extremal surfaces for holographic entanglement entropy, revealing that their behavior in the IR limit aligns closely with that observed for complexity.

In Chapter 4, we explored various aspects of entanglement like structures with timelike separations, by treating the time evolution operator as a density operator. The relationship between the time evolution operator and the reduced transition matrix is detailed in Sec. 4.3.1. Furthermore, this approach has a close connection to pseudo-entropy. We analyzed several examples of simple quantum systems to investigate the time entanglement structure arising from the time evolution operator. In general, the corresponding entanglement entropy is complex; however, certain subfamilies exhibit real values, which are explored in detail in this study. A key finding is that time entanglement matches the usual finite-temperature entanglement entropy evaluated at an imaginary temperature, with $\beta \to it$, for systems with time-independent interactions. Additionally, we examined the entanglement structure of the time evolution operator when projected onto an initial state. This is exactly equivalent to the transition matrix, where the final state is time-evolved from the initial state. In this case, the corresponding entanglement entropy is identified as the pseudo-entropy. We further extended our analysis to systems with time-dependent interactions, which introduce a more intricate time entanglement structure.

Chapter 6

Appendix

6.1 Computation of renormalized on-shell gravitational action for two-point correlators in $\mathbf{AdS}_{d+1}$

Consider a free scalar field Φ in Euclidean poincare AdS_{d+1}, the action is given by

$$S = -\frac{1}{2}\int d^{d+1}x\,\sqrt{g}\,g^{MN}\partial_M\Phi\partial_N\Phi\,. \tag{6.1}$$

The equation of motion is

$$z^{d+1}\partial_z\left(z^{1-d}\partial_z\phi_k\right) - z^2k^2\phi_k - m^2R^2\phi_k = 0\,. \tag{6.2}$$

The solution for the scalar field Φ reads as:

$$\Phi_k(z) = z^{d/2}\left[B(k)I_\nu(kz) + A(k)K_\nu(kz)\right] \quad ; \quad \nu = \sqrt{\frac{d^2}{4} + m^2R^2}\,. \tag{6.3}$$

$I_\nu(kz)$ diverges as $z \to \infty$, requiring that the solution of Φ is regular in the interior as $z \to \infty$. This forces the condition $B(k) = 0$, Φ_k is then expressed as

$$\Phi_k(z) = A(k)z^{d/2}K_\nu(kz)\,. \tag{6.4}$$

The scalar field ϕ takes the form

$$\Phi(z,x) \sim \int dk\,e^{ikx}z^{d/2}A(k)K_\nu(kz)\,. \tag{6.5}$$

We now normalize the scalar field such that $\Phi(z=\epsilon,x) = A(x)$, and $\phi_0(k) = A(k)$. Φ is then expressed as:

$$\Phi(z,x) \sim \int dk\,e^{ikx}\,\frac{\phi_0(k)z^{d/2}K_\nu(kz)}{\epsilon^{d/2}K_\nu(k\epsilon)}\,. \tag{6.6}$$

(6.1) can be recast as:

$$S = -\frac{1}{2}\int d^{d+1}x \left[\partial_M\left(\sqrt{g}\, g^{MN}\Phi\partial_N\Phi\right) - \Phi\partial_M\left(\sqrt{g}\, g^{MN}\partial_N\Phi\right)\right] . \tag{6.7}$$

After using the scalar equation of motion for Φ, obtaining $S_{o.s}[\Phi_c]$ as:

$$S_{o.s}[\Phi_c] = -\frac{1}{2}\int d^d x\, \partial_M\left(\sqrt{g}\, g^{MN}\Phi\partial_N\Phi\right) . \tag{6.8}$$

Extracting the relevant part of the action (source $\phi_0(x)$ dependent) which contributes to the two-point function after performing the integral, $S_{o.s}$ is then given by

$$S_{o.s}[\Phi_c] = -\frac{1}{2}\int d^d x\, [\sqrt{g}g^{zz}\Phi\,\partial_z\Phi]_{z=\infty}^{z=\epsilon} . \tag{6.9}$$

After putting the metric coefficients, the above expression becomes

$$\begin{aligned} S_{o.s}[\Phi_c] &= -\frac{1}{2}\int d^d x \left[\frac{R^{d-1}}{z^{d-1}}\Phi\,\partial_z\Phi\right]_{z=\epsilon}^{z=\infty} , \\ &\sim \int d^d x \frac{R^{d-1}}{\epsilon^{d-1}}\left[\Phi\,\partial_z\Phi\right]\Big|_{z=\epsilon} . \end{aligned} \tag{6.10}$$

Here, we are interested in the on-shell $S_{o.s}$ with the source $\Phi_0(x)$. Therefore, dropping a term at $z=\infty$, which is not relevant in computing the two-point function. We now insert the classical solution (6.6) into (6.10), after some simplification, $S_{o.s}[\Phi_c]$ takes the form as follows:

$$S_{o.s}[\Phi_c] \sim \int d^d k\, \frac{R^{d-1}}{\epsilon^{d-1}}\phi_0(k)\phi_0(-k)\, \frac{\left[\partial_z\left(z^{\frac{d}{2}}\, K_\nu(kz)\right)\right]_{z=\epsilon}}{\epsilon^{\frac{d}{2}}\, K_\nu(k\epsilon)} . \tag{6.11}$$

We can compute the on-shell action $S_{o.s}$ explicitly for AdS_4 using $\nu = \frac{3}{2}$, d=3, and

$$K_{\frac{3}{2}}(z) = \sqrt{\frac{\pi}{2z}}e^{-z}\left(1+\frac{1}{z}\right) . \tag{6.12}$$

Then, the on-shell action reads as:

$$S_{o.s}[\Phi_c] \sim R^2\int d^3k\, \phi_0(k)\phi_0(-k)\left[-\frac{k^2}{\epsilon}+k^3\right] . \tag{6.13}$$

First term in (6.13) is divergent, it can be cancelled by adding a local-counterterm in (6.13) of the form, $S_{\text{counterterm}} \sim \int d^3x\sqrt{\gamma}\,\gamma^{ij}\partial_i\phi_0\,\partial_j\phi_0$. The renormalised on-shell action is given by:

$$S_{o.s}^{ren.}[\Phi_c] \sim R^2\int d^3k\, \phi_0(k)\phi_0(-k)\, k^3 . \tag{6.14}$$

Two-point correlator is then computed as:

$$\langle O(k)O(-k)\rangle \sim k^3 . \tag{6.15}$$

In the position space, the two-point correlator is expressed as:

$$\langle O(x)O(0)\rangle \sim \frac{1}{|x|^6}\,. \tag{6.16}$$

In general dimensions, the two-point correlator is given by:

$$\langle O(x)O(0)\rangle \sim \frac{1}{|x|^{2\Delta}}\,, \tag{6.17}$$

where $\Delta = \nu + \frac{d}{2}$ is the scaling dimension of the operator O.

6.2 Black hole near-horizon geometry and Rindler time

Consider the metric for a 4-dimensional black hole given by:

$$ds^2 = -f(r)\,dt^2 + \frac{dr^2}{f(r)} + r^2 d\Omega^2\,, \tag{6.18}$$

where $f(r)$ is the black hole's redshift factor, and $f(r_h) = 0$ defines the horizon at $r = r_h$. Here, $d\Omega^2$ represents the metric of a unit 2-sphere.

Near the horizon ($r \approx r_h$), $f(r)$ can be expanded as:

$$f(r) \approx f'(r_h)(r - r_h)\,. \tag{6.19}$$

The surface gravity κ is defined as:

$$\kappa = \frac{f'(r_h)}{2}\,. \tag{6.20}$$

Thus, the function $f(r)$ can be approximated as:

$$f(r) \approx 2\kappa(r - r_h)\,. \tag{6.21}$$

Substituting this into the metric (6.18), we obtain:

$$ds^2 \approx -2\kappa(r - r_h)\,dt^2 + \frac{dr^2}{2\kappa(r - r_h)} + r^2 d\Omega^2\,. \tag{6.22}$$

To further simplify the metric near the horizon, we introduce a new radial coordinate:

$$\rho = \sqrt{\frac{2}{\kappa}(r - r_h)}\,, \tag{6.23}$$

and rescale the time coordinate as $\tau = \kappa t$. Substituting these into the metric, we get:

$$ds^2 \approx -\rho^2\,d\tau^2 + d\rho^2 + r(\rho)^2 d\Omega^2\,. \tag{6.24}$$

For the Euclidean near-horizon geometry, we perform a Wick rotation, $\tau \to i\tau_E$, where τ_E is the Euclidean time. The metric becomes:

$$ds^2 \approx \rho^2\, d\tau_E^2 + d\rho^2 + r(\rho)^2 d\Omega^2\,. \tag{6.25}$$

To avoid a conical singularity at $\rho = 0$, the Euclidean time τ_E must be periodic with a period:

$$\tau_E \sim \tau_E + \frac{2\pi}{\kappa}\,. \tag{6.26}$$

This periodicity implies that the surface gravity κ is related to the Hawking temperature T_H of the black hole:

$$T_H = \frac{\kappa}{2\pi}\,. \tag{6.27}$$

The near-horizon geometry of a black hole (non-extremal) takes the universal form (6.24), where the two-dimensional part describes the Rindler wedge (a region of Minkowski space). In this setup, τ corresponds to the Rindler time, and the metric:

$$ds^2 = -\rho^2\, d\tau^2 + d\rho^2\,, \tag{6.28}$$

describes the Rindler patch, with a uniformly accelerating observer at a constant ρ.

6.3 Some details: 2-dim gravity, extremal surfaces

The equations of motion following from the 2-dim effective action (2.2) are

$$\begin{aligned} &g_{\mu\nu}\nabla^2\phi - \nabla_\mu\nabla_\nu\phi + \frac{g_{\mu\nu}}{2}\Big(\frac{\phi}{2}(\partial\Psi)^2 + U\Big) - \frac{\phi}{2}\partial_\mu\Psi\partial_\nu\Psi = 0\,, \\ &\mathcal{R} - \frac{\partial U}{\partial\phi} - \frac{1}{2}(\partial\Psi)^2 = 0\,, \qquad\qquad \frac{1}{\sqrt{-g}}\partial_\mu(\sqrt{-g}\,\phi\partial^\mu\Psi) - \frac{\partial U}{\partial\Psi} = 0\,. \end{aligned} \tag{6.29}$$

In conformal gauge $g_{\mu\nu} = e^f\eta_{\mu\nu}$ these give

$$\begin{aligned} (tr) \qquad & \partial_t\partial_r\phi - \frac{1}{2}f'\partial_t\phi - \frac{1}{2}\dot f\partial_r\phi + \frac{\phi}{2}\dot\Psi\Psi' = 0\,, \\ (rr+tt) \qquad & -\partial_t^2\phi - \partial_r^2\phi + \dot f\partial_t\phi + f'\partial_r\phi - \frac{\phi}{2}(\dot\Psi)^2 - \frac{\phi}{2}(\Psi')^2 = 0, \\ (rr-tt) \qquad & -\partial_t^2\phi + \partial_r^2\phi + e^f U = 0\,, \\ (\phi) \qquad & \big(\ddot f - f''\big) - \frac{1}{2}(-(\dot\Psi)^2 + (\Psi')^2) - e^f\frac{\partial U}{\partial\phi} = 0, \\ (\Psi) \qquad & -\partial_t(\phi\partial_t\Psi) + \partial_r(\phi\partial_r\Psi) - e^f\frac{\partial U}{\partial\Psi} = 0\,. \end{aligned} \tag{6.30}$$

The severe (singular) time-dependence in the vicinity of the singularity implies that time-derivative terms are dominant while other terms, in particular pertaining to the dilaton potential, are irrelevant there: solving these leads to a "universal" subsector

$$\phi \sim t, \quad e^f \sim t^a, \quad e^\Psi \sim t^\alpha; \qquad a = \frac{\alpha^2}{2}\,, \tag{6.31}$$

which governs the cosmological singularity. Analysing these equations in more detail can be done using the ansatz (2.3), giving *e.g.* the AdS Kasner cosmology (2.4) as well as various others, some of which have nonrelativistic (hyperscaling violating Lifshitz) asymptotics. For instance, flat space has $U = 0$, giving

$$\phi = t, \quad ds^2 = t^{\alpha^2/2}(-dt^2 + dr^2), \quad e^{\Psi} = t^{\alpha} \ . \tag{6.32}$$

With $t = T^{1-p_1}$, these are the reduction of "mostly isotropic" Kasner singularities $ds^2 = -dt^2 + t^{2p_1} dx_1^2 + t^{2p_2} \sum_i dx_i^2$. Hyperscaling violating cosmologies comprise backgrounds (2.3) with exponents and parameters:

$$\begin{aligned} U(\phi, \Psi) &= 2\Lambda \phi^{\frac{1}{d_i}} e^{\gamma \Psi} \ , \quad \Lambda = -\frac{1}{2}(d_i + 1 - \theta)(d_i - \theta), \quad \gamma = \frac{-2\theta}{\sqrt{2d_i(d_i - \theta)(-\theta)}} \ , \\ m &= -(d_i - \theta) \ , \quad b = \frac{m(1 + d_i)}{d_i} \ , \quad \beta = -m\gamma \, , \\ k &= 1, \quad a = \frac{\alpha^2}{2} \, , \quad \alpha = -\gamma \pm \sqrt{\gamma^2 + \frac{2(d_i - 1)}{d_i}} \ . \end{aligned} \tag{6.33}$$

Here $\theta < 0$, $\gamma > 0$. The higher dimensional backgrounds here can be obtained as certain kinds of cosmological deformations of reductions of nonconformal branes down to D dimensions.
Still more complicated hyperscaling violating Lifshitz cosmologies (with nontrivial Lifshitz exponents z as well) and their 2-dimensional avatars were also obtained in [113]: these have a more complicated dilaton potential. These are more constrained, requiring the conditions $m = -1$, $a = -b - 2$, as well as further relations between other exponents. A simple example has $\theta = 0$, $z = 2$, $d_i = 2$, and $k = 1$, $m = -1$, $a = \frac{1}{2}$, $b = -\frac{5}{2}$, $\beta = -\alpha = 1$, and the dilaton potential is $U = \phi^{1/2}(-3 + \frac{1}{\phi^2} e^{-2\Psi})$.

Extremal (RT/HRT) surfaces: The area functional

$$S = \frac{V_{d_i - 1}}{4G_{d_i + 2}} \int dr \, \phi \sqrt{\frac{e^f}{\phi^{(d_i+1)/d_i}}\big(1 - (\partial_r t)^2\big) + (\partial_r x)^2} \tag{6.34}$$

upon extremizing $x(r)$ gives

$$(\partial_r x)^2 = A^2 \, \frac{\frac{e^f}{\phi^{(d_i+1)/d_i}}\big(1 - (\partial_r t)^2\big)}{\phi^2 - A^2} \ , \qquad S = \frac{V_{d_i - 1}}{4G_{d_i + 2}} \int dr \, \frac{e^{f/2} \, \phi^{(3 - 1/d_i)/2}}{\sqrt{\phi^2 - A^2}} \sqrt{1 - (\partial_r t)^2} \ . \tag{6.35}$$

In the above expressions, A is the turning point $A = \phi_* = \frac{t_*}{r_*^{d_i}}$ for the AdS Kasner case (2.4). Analysing these extremal surfaces is reliable in the semiclassical region far from the singularity at $t = 0$. In this region, a detailed analysis of the time extremization equation leads to (1.61): the surface lies almost on a constant time slice ($t'' \ll 1$) and can be shown to bend in the direction away from the singularity, as depicted in Figure 1.2.

6.4 Some details on 2d CFT and entanglement entropy

Any 2-dim metric is conformally flat so $ds^2 = e^f \eta_{\mu\nu} dx^\mu dx^\nu$. We can then modify the Calabrese-Cardy result [36, 37], in particular taking the ground state entanglement in flat space and then incorporating the effects of the conformal transformation e^f as in [15]. The twist operator 2-point function scales under a conformal transformation as

$$\langle \sigma(x_1)\,\sigma(x_2)\rangle_{e^f g} = e^{-\Delta_n f/2}|_{x_1}\, e^{-\Delta_n f/2}|_{x_2}\, \langle \sigma(x_1)\,\sigma(x_2)\rangle_g \ , \qquad \Delta_n = \frac{c}{12}\frac{n^2-1}{n} \ . \tag{6.36}$$

Since the partition function in the presence of twist operators scales as the twist operator 2-point function, the entanglement entropy becomes

$$S^{12}_{e^f g} = -\lim_{n\to 1} \partial_n \langle \sigma(x_1)\,\sigma(x_2)\rangle_{e^f g} = S^{12}_g + \frac{c}{6}\sum_{endpoints} \log e^{f/2} \ . \tag{6.37}$$

For a bulk interval, this gives

$$S^{12}_g = \frac{c}{6}\log\left(\frac{\Delta^2}{\epsilon^2_{UV}}\right) \quad \to \quad S^{12}_{e^f g} = \frac{c}{6}\log\left(\frac{\Delta^2}{\epsilon^2_{UV}}\, e^{f/2}|_1\, e^{f/2}|_2\right) \tag{6.38}$$

while for a CFT with boundary, we have essentially half the flat space answer (with one end of the interval at the boundary), thus obtaining

$$S^{10}_g = \frac{c}{12}\log\left(\frac{\Delta^2}{\epsilon^2_{UV}}\right) \quad \to \quad S^{10}_{e^f g} = \frac{c}{12}\log\left(\frac{\Delta^2}{\epsilon^2_{UV}}\, e^f|_1\right) \tag{6.39}$$

We have used the latter in the AdS cases which include the presence of the AdS boundary, while for the bulk cases we use the former expression.

6.5 Holographic cosmologies $\to$ 2-dim

Time-dependent non-normalizable deformations of AdS/CFT were studied in [22, 23, 24, 115] towards gaining insights via gauge/gravity duality into cosmological (Big-Bang or -Crunch) singularities. The bulk gravity theory exhibits a cosmological Big-Crunch (or -Bang) singularity and breaks down while the holographic dual field theory (in the AdS_5 case) subject to a severe time-dependent gauge coupling $g^2_{YM} = e^\Psi$ (and living on a time-dependent base space) may be hoped to provide insight into the dual dynamics: in this case the scalar Ψ controls the gauge/string coupling. There is a large family of such backgrounds exhibiting cosmological singularities. Among the simplest are AdS-Kasner theories

$$ds^2 = \frac{R^2_{AdS}}{r^2}(-dt^2 + \sum_i t^{2p_i} dx_i^2 + dr^2), \quad e^\Psi = t^\alpha \ ; \qquad \sum_i p_i = 1 \ , \quad \sum_i p_i^2 = 1 - \frac{1}{2}\alpha^2 \ . \tag{A1}$$

For constant scalar Ψ with $\alpha = 0$, the Kasner space is necessarily anisotropic: the p_i cannot all be equal. In this case, the gauge theory lives on a time-dependent space but the gauge coupling is

not time-dependent. The isotropic subfamily requires a nontrivial scalar source Ψ as well. More general backgrounds can also be found involving AdS-FRW and AdS-BKL spacetimes [23, 24], all of which have spacelike singularities. There are also backgrounds with null singularities [115]. Similar Kasner deformations exist for $AdS_4 \times X^7$ and $AdS_7 \times X^4$. For generic spacelike singularities, the gauge theory response appears singular [24] while null singularities appear better behaved [115]. Some of these spacelike singularities were further investigated in [117, 118, 119, 120]

These arise in higher dimensional theories of Einstein gravity with scalar Ψ, a potential V, and action

$$S = \frac{1}{16\pi G_D} \int d^D x \sqrt{-g^{(D)}} \left(\mathcal{R} - \frac{1}{2}(\partial\Psi)^2 - V \right) . \tag{A2}$$

We allow the potential V to also contain metric data, *i.e.* it is a function $V(g, \Psi)$. Under dimensional reduction with ansatz (3.5), we obtain the 2-dim action (3.6) (see the general reviews [206, 207, 208], of 2-dim dilaton gravity theories and dimensional reduction). In general these sorts of generic 2-dim dilaton gravity theories encapsulate various aspects of the higher dimensional gravity theories, and are perhaps best regarded as effective holographic models [112]. These sorts of theories were considered in [200] towards understanding holographic c-functions from the 2-dim dilaton gravity point of view. The 2-dim equations of motion following from (3.6) were solved in [113] with various families of asymptotics (flat, AdS, hyperscaling violating and Lifshitz) to obtain various classes of 2-dim cosmologies with Kasner-like Big-Bang/Crunch singularities.

We now review a little more from [113]. With AdS asymptotics, we have $V = 2\Lambda$ giving the dilaton potential in (3.6) as $U = 2\Lambda\phi^{1/d_i}$ (3.13) independent of the scalar Ψ. Hyperscaling violating asymptotics $ds^2 = \frac{R^2 r^{2\theta/d_i}}{r^2}(-dt^2 + dr^2 + dx_i^2)$ with nontrivial exponent θ arise [198] from dimensional reductions of nonconformal Dp-branes [199]: after reduction over the transverse sphere we obtain a (d_i+2)-dim action of the form (A2) with $V = 2\Lambda\, e^{\gamma\Psi}$, which after reduction over the d_i spatial dimensions gives (3.6) with U in (3.35), and the corresponding parameters for the on-shell backgrounds. Lifshitz asymptotics $ds^2 = R^2(-\frac{dt^2}{r^{2z}} + \frac{dr^2}{r^2} + \frac{dx_i^2}{r^2})$ with nontrivial exponent z requires a further gauge field strength, which on-shell leads to an action (A2) with effective potential of the form $V = \phi^{-1/d_i} U$ with U in (3.56). Hyperscaling violating Lifshitz theories contain both nontrivial z and θ exponents.

Cosmological deformations of the isotropic Kasner kind were found in [113] by solving the 2-dim theories obtained by reduction over the transverse d_i-space. The power law ansatz (3.7) for the 2-dim fields $\phi,\ e^f,\ e^\Psi$ describes the vicinity of the singularity. The exponents, fixed by the 2-dim equations, with various asymptotics are in (3.13), (3.35) and (3.56). The asymptotics are the same as those in the absence of the time-dependence. For the AdS and hyperscaling violating cases, the solutions for the t- and r-parts of the equations of motion end up being compatible (they are roughly independent). In general however, the time-dependent backgrounds are more constraining, particularly in the Lifshitz case where the equations couple the t- and r-exponents forcing $\theta = 0$ and $z = d_i$.

As in AdS_5 Kasner, the scalar e^Ψ controls the gauge coupling in nonconformal brane theories

as well. Taking the exponent $\alpha > 0$ in (3.35) amounts to taking the gauge coupling to vanish at $t = 0$ which then leads to diverging $(\dot{\Psi})^2 \sim \frac{1}{t^{\#}}$ and thence a bulk singularity.

6.6 g_i, s_i, y_i, v_i

- The iterative solution of (3.15) up to $O(r^{30})$ is given as:

$$t(r) = t_0 + \frac{r^2}{6t_0} - \frac{7r^4}{216t_0^3} + \frac{5r^6}{3888t_0^5} - \frac{23r^8}{31104t_0^7} + \frac{5671r^{10}}{125971200t_0^9} - \frac{193157r^{12}}{31744742400t_0^{11}} - \frac{1451389r^{14}}{571405363200t_0^{13}}$$
$$+\frac{126271147r^{16}}{60340406353920t_0^{15}} - \frac{171499492421r^{18}}{211794826302259200t_0^{17}} + \frac{2509650528887r^{20}}{7624613746881331200t_0^{19}}$$
$$-\frac{23544237318388621r^{22}}{213870415600021340160000t_0^{21}} + \frac{74037865493904302737r^{24}}{204802309978580435337216000t_0^{23}}$$
$$-\frac{27221138559698748551r^{26}}{24576277197429652240465920000t_0^{25}} + \frac{204069246505971511844537 9r^{28}}{64099846186336018973583212544000 0t_0^{27}}$$
$$-\frac{41412040443643818046045477 1r^{30}}{48074884639752014230187409408000000 0t_0^{29}}\,. \tag{B1}$$

  Likewise (3.19), (3.31), (3.42), (3.44), (3.49), (3.51), (3.61) display truncated solutions analogous to (3.17). The numerical plots do not change much with the truncation.

- $g_{2,4}$ appearing in (3.42) are given as:

$$g_2 = \frac{15 - 2\sqrt{2}}{70t_0}, \quad g_4 = \frac{5036\sqrt{2} - 25835}{343000t_0^3}. \tag{B2}$$

- $s_{2,4}$ appearing in (3.44) are given as:

$$s_2 = \frac{15 - 2\sqrt{2}}{70t_0}, \quad s_4 = \frac{-233 - 60\sqrt{2}}{1960t_0^3}. \tag{B3}$$

- $y_{2,4}$ appearing in (3.49) are given as:

$$y_2 = \frac{17}{210t_0}, \quad y_4 = -\frac{597941}{120393000t_0^3}. \tag{B4}$$

- $v_{2,4}$ appearing in (3.51) are given as:

$$v_2 = \frac{17}{210t_0}, \qquad v_4 = -\frac{289}{54600t_0^3}. \tag{B5}$$

In general, the coefficients in the series expansion (3.16) (and similar other places in the paper), scale as $c_n \sim \#\frac{1}{t_0^{n-1}}$, with "#" is some numerical coefficient that becomes an increasingly bigger (more unwieldy) fraction at higher order n.

6.7 EE, finite subregions ($A \neq 0$), AdS_5 Kasner

Here we give a brief description of the entangling RT/HRT surface for finite subregions, *i.e.* finite A, developing numerically the studies in [43]. The equation of motion for the entangling RT/HRT surface for finite A in AdS_5 Kasner spacetime is given by (3.72) with $d_i = 3$.

The perturbative solution of this equation is the same as (3.75) for $A = 0$. For nonzero A, we solve numerically for $t(r)$ up to the turning point r_* determined by the condition (see (3.70), (3.71))

$$A = \phi_* = \frac{t(r_*)}{r_*^{d_i}} \,. \tag{C1}$$

The perturbative solution (3.75) simplifies (C1) with $d_i = 3$ to

$$6Ar_*^3 t_0 - r_*^2 - 6t_0^2 = 0 \,. \tag{C2}$$

This can be solved for r_* (with one real solution) but in perturbation theory, it is consistent to take $r_* \sim At_0^{1/d_i}$ since $t(r_*) \sim t_0$, *i.e.* the surface is approximately on the t_0 constant time slice (the surface bends very little, as we confirm below). The $t(r)$-equation (3.72) with $d_i = 3$ is solved

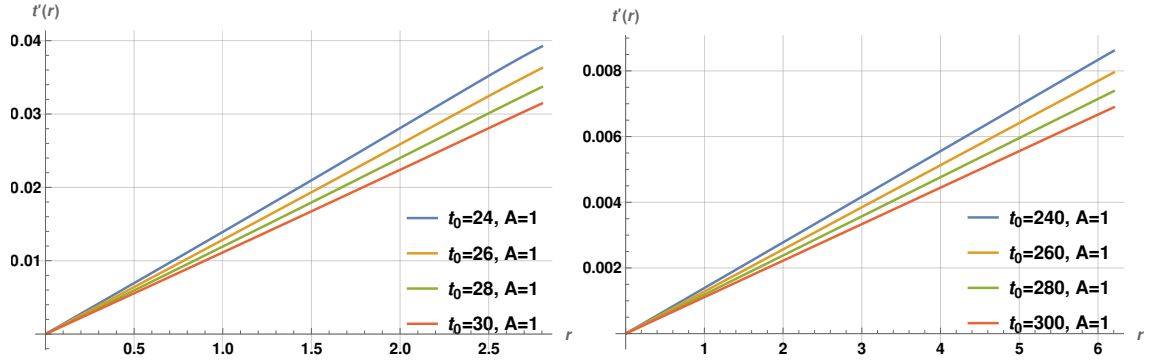

Figure 6.1: Numerical plots of $t'(r)$ with r in AdS_5 Kasner for different t_0 slices with $A = 1$.

numerically for the boundary conditions extracted from the perturbative solution (3.75). The numerical solution for the surface only makes sense upto the turning point r_*. We illustrate this fixing $A = 1$ so $r_* \sim t_0^{1/3}$ here, with the results plotted in Fig. 6.1. It is clear that the bending is always small, *i.e.* $t'(r) \ll 1$ over the entire surface as expected: the $t'(r)$ values in Fig. 6.1 are in approximate agreement with the semiclassical $t' \sim \frac{r}{3t_0}$ in (3.75). No lightlike limit arises here as expected (see Fig. 1 of [127] for a qualitative picture of the surface). This shows consistency of our techniques and analysis throughout the paper where the numerics for complexity and entanglement for large subregions with $A = 0$ (Fig. 3.12) exhibits clear lightlike limits.

6.8 Time evolution, pseudo-entropy: special cases

Consider now the pseudo-entropy transition matrix (4.41) for the 2-state case (4.53), with arbitrary initial state $|i\rangle$ and arbitrary final state $|f\rangle$,

$$\begin{aligned}&|i\rangle = c_1|1\rangle + c_2|2\rangle\,, \quad |f\rangle = c'_1|1\rangle + c'_2|2\rangle\,;\\ &\mathcal{T}_{f|i} = \frac{1}{c'_1c^*_1 + c'_2c^*_2}\Big(c'_1c^*_1|1\rangle\langle 1| + c'_2c^*_2|2\rangle\langle 2| + c'_1c^*_2|1\rangle\langle 2| + c'_2c^*_1|2\rangle\langle 1|\Big)\,.\end{aligned} \tag{C1}$$

With $|1\rangle \equiv |++\rangle, |2\rangle \equiv |--\rangle$, a partial trace over the second component gives

$$\mathcal{T}^A_{f|i} = \frac{1}{c'_1c^*_1 + c'_2c^*_2}\Big(c'_1c^*_1|+\rangle\langle +| + c'_2c^*_2|-\rangle\langle -|\Big) \tag{C2}$$

as the reduced transition matrix. To compare with entanglement for the time evolution operator, we take the final state to be time-evolved from some other initial state $|i'\rangle$ so

$$|f\rangle = c'_1e^{-iE_1t}|1\rangle + c'_2e^{-iE_2t}|2\rangle \quad \to \quad \mathcal{T}^A_{f|i} = \frac{\big(c'_1c^*_1|+\rangle\langle +| + c'_2c^*_2e^{i\theta}|-\rangle\langle -|\big)}{c'_1c^*_1 + c'_2c^*_2e^{i\theta}}\,, \tag{C3}$$

with $\theta = -(E_2 - E_1)t$. Then we see that:

- using (4.54) for the time evolution operator, $\mathcal{T}^A_{f|i} = \rho^A_t$ if $c_1 = c'_1 = \frac{1}{\sqrt{2}}$, $c_2 = c'_2 = \frac{1}{\sqrt{2}}$, *i.e.* the initial and final states are identical maximally entangled states.
- using (4.74) for the time evolution operator with projection, $\mathcal{T}^A_{f|i} = \rho^{|i\rangle}_t$ if $c'_1 = c_1$, $c'_2 = c_2$, *i.e.* $|f\rangle = |f[i]\rangle$ *i.e.* the final state is time-evolved from the initial state $|i'\rangle = |i\rangle$.

This structure of mapping $\mathcal{T}^A_{f|i} = \rho^A_t$ however is not true more generally. For instance, consider two qubits more generally, as in (4.55). Then the pseudo-entropy transition matrix (4.41) becomes

$$|I\rangle = \sum_{i,j=1}^{2} c_{ij}|ij\rangle\,, \quad |F\rangle = \sum_{i,j=1}^{2} c'_{ij}|ij\rangle\,; \qquad \mathcal{T}_{F|I} = \frac{1}{\sum_{ij} c'_{ij}c^*_{ij}}\sum_{i,j,k,l=1}^{2} c'_{ij}c^*_{kl}\,|ij\rangle\langle kl| \tag{C4}$$

and partial trace over the 2nd component gives the reduced transition matrix as

$$\begin{aligned}\mathcal{T}^A_{F|I} = \frac{1}{\sum_{ij} c'_{ij}c^*_{ij}}\sum_{i,k=1}^{2}\Big(\sum_j c'_{ij}c^*_{kj}\Big)\,|i\rangle\langle k| \;=\; &\frac{1}{\sum_{ij} c'_{ij}c^*_{ij}}\Big((c'_{11}c^*_{11} + c'_{12}c^*_{12})|1\rangle\langle 1| + \\ &(c'_{11}c^*_{21} + c'_{12}c^*_{22})|1\rangle\langle 2| + \;(c'_{21}c^*_{11} + c'_{22}c^*_{12})|2\rangle\langle 1| + (c'_{21}c^*_{21} + c'_{22}c^*_{22})|2\rangle\langle 2|\Big).\end{aligned} \tag{C5}$$

Towards comparing with the time evolution operator, we think of the future state as time-evolved from some initial state, *i.e.* $|F\rangle = \sum_{ij} c'_{ij}e^{-iE_{ij}t}|ij\rangle$. It is then clear that pseudo-entropy via the reduced transition matrix matches time entanglement via the normalized time evolution operator with projection onto $|i\rangle$, *i.e.* $\mathcal{T}^A_{f|i'} = \rho^{|i\rangle,A}_t$ if the final state is taken to be time-evolved from the initial state, *i.e.* $|F\rangle = \mathcal{U}(t)|I\rangle$ so $c'_{ij} = c_{ij}e^{-iE_{ij}t}$. However, in contrast with (C3), the fact that there are off-diagonal terms in (C5) makes the structure different from the reduced time evolution operator. To set the off-diagonal terms to vanish, we could consider specializing to maximally

entangled thermofield-double type initial and final states, and with $|F\rangle$ time-evolved from $|I\rangle$, *i.e.* $|I\rangle = \sum_{ii} c_{ii}|ii\rangle$ with $c_{ij}, c'_{ij} = 0,\ i \neq j,\ c_{ii} = c_{jj}\ \forall\ i, j$, and $|F\rangle = \sum_{ii} c'_{ii}|ii\rangle = \mathcal{U}(t)|I\rangle$. In this case, we find that all the off-diagonal terms vanish and we obtain the reduced transition matrix to be of the same form as in (C3). On the other hand the reduced time evolution operator for the general 2-qubit case is (4.57), which has two distinct phases in general. Thus the reduced transition matrix differs from the reduced time evolution operator. One can engineer special energy values E_{ij} where the two coincide (although this appears ad hoc).

Of course, these structures are with a single Hilbert space for constructing both initial and final states. Doubling the Hilbert spaces directly enables a map from the transition matrix to the time evolution operator in general, as in sec. 4.3.1.

6.9 Qubit chains

Now we consider qubit chains to understand time entanglement structures. For any nearest neighbour 2-qubit pair, we impose nearest-neighbour interactions, with

$$\begin{aligned} s|q\rangle = a_q|q\rangle\,, \quad |q\rangle = \{|1\rangle, |2\rangle\}\,; \qquad H = -Js_1s_2\,, \\ H[11] = E_{11} = -Ja_1^2\,, \quad H[22] = E_{22} = -Ja_2^2\,, \quad H[12] = H[21] = E_{12} = -Ja_1a_2\,. \end{aligned} \tag{C1}$$

In the first line, we are defining operators s_i with action as above (the i being the site label), that give the qubit Hamiltonian action elaborated on in the second line. This Hamiltonian generalizes the 2-qubit case (4.55) earlier. (Imposing a $|1\rangle \leftrightarrow |2\rangle$ exchange symmetry simplifies this to Ising-like interactions, as we will discuss later.)

3-qubit chain: Consider now a chain of 3 qubits with Hamiltonian based on the nearest neighbour 2-qubit interaction above. This gives the 3-qubit chain Hamiltonian as

$$\begin{aligned} H &= -J(s_1s_2 + s_2s_3)\ , \\ H \equiv E_I|I\rangle\langle I| &= E_1|111\rangle\langle 111| + E_2|222\rangle\langle 222| + E_5\big(|121\rangle\langle 121| + |212\rangle\langle 212|\big) \\ &\quad + E_3\big(|112\rangle\langle 112| + |211\rangle\langle 211|\big) + E_4\big(|122\rangle\langle 122| + |221\rangle\langle 221|\big)\,, \\ E_1 &= -2Ja_1^2 = 2E_{11}\,, \quad E_2 = -2Ja_2^2 = 2E_{22}\,, \quad E_5 = -2Ja_1a_2 = 2E_{12}\,, \\ E_3 &= -Ja_1^2 - Ja_1a_2 = E_{11} + E_{12}\,, \quad E_4 = -Ja_1a_2 - Ja_2^2 = E_{22} + E_{12}\,, \\ E_4 - E_3 &= \frac{1}{2}(E_2 - E_1)\,, \quad E_1 + E_5 = 2E_3\,, \quad E_2 + E_5 = 2E_4\,. \end{aligned} \tag{C2}$$

Then the time evolution operator $\mathcal{U}(t)$ after normalizing becomes

$$\rho_t = \frac{1}{e^{-iE_1t} + e^{-iE_2t} + 2e^{-iE_3t} + 2e^{-iE_4t} + 2e^{-iE_5t}} \sum_I e^{-iE_It}|I\rangle\langle I| \equiv \mathcal{N}\sum_I e^{-iE_It}|I\rangle\langle I|\ . \tag{C3}$$

Now tracing out the 1st and 3rd qubit states gives the reduced time evolution operator

$$(\rho_t^A)_{11} = \mathcal{N}\left(e^{-iE_1t} + 2e^{-iE_3t} + e^{-iE_5t}\right)\ , \qquad (\rho_t^A)_{22} = \mathcal{N}\left(e^{-iE_2t} + 2e^{-iE_4t} + e^{-iE_5t}\right)\ , \tag{C4}$$

for the middle qubit. Using the relations between the E_i in (C2) simplifies this to

$$(\rho_t^A)_{11} = \mathcal{N}\left(e^{-iE_{11}t} + e^{-iE_{12}t}\right)^2, \qquad (\rho_t^A)_{22} = \mathcal{N}\left(e^{-iE_{22}t} + e^{-iE_{12}t}\right)^2,$$
$$\mathcal{N}^{-1} = \mathrm{Tr}\,\mathcal{U}(t) = \left(e^{-iE_{11}t} + e^{-iE_{12}t}\right)^2 + \left(e^{-iE_{22}t} + e^{-iE_{12}t}\right)^2 . \tag{C5}$$

In general, this is a function of three independent parameters E_{11}, E_{22}, E_{12} (or equivalently E_1, E_2, E_5) so it is a complex-valued function of three phases in general. A straightforward real slice is obtained when there is a $|1\rangle \leftrightarrow |2\rangle$ exchange symmetry as we will discuss later.

5-qubit chain: the configurations and their energies are

$$\begin{aligned}
&|11111\rangle, \;\; 4E_{11}; \qquad |22222\rangle, \;\; 4E_{22}; \qquad |12121\rangle, \;\; |21212\rangle, \;\; 4E_{12};\\
&|11112\rangle, \;\; |11122\rangle, \;\; |11222\rangle, \;\; |12222\rangle, \;\; 3E_{11} + E_{12};\\
&|22221\rangle, \;\; |22211\rangle, \;\; |22111\rangle, \;\; |21111\rangle, \;\; 3E_{22} + E_{12};\\
&|11121\rangle, \;\; |11211\rangle, \;\; |12111\rangle, \;\; |21112\rangle, \;\; 2E_{11} + 2E_{12};\\
&|12221\rangle, \;\; |22212\rangle, \;\; |22122\rangle, \;\; |21222\rangle, \;\; 2E_{22} + 2E_{12};\\
&|11221\rangle, \;\; |12211\rangle, \;\; |22112\rangle, \;\; |21122\rangle, \;\; E_{11} + E_{22} + 2E_{12};\\
&|11212\rangle, \;\; |12112\rangle, \;\; |21211\rangle, \;\; |21121\rangle, \;\; E_{11} + 3E_{12};\\
&|12122\rangle, \;\; |12212\rangle, \;\; |22121\rangle, \;\; |21221\rangle, \;\; E_{22} + 3E_{12};
\end{aligned} \tag{C6}$$

Tracing over all but the middle (3rd) qubit gives the reduced time evolution operator as

$$\begin{aligned}
(\tilde{\rho}_t)^{(3)}_{11} &= e^{-i(4E_{11})t} + e^{-i(4E_{12})t} + 2e^{-i(3E_{11}+E_{12})t} + 2e^{-i(3E_{22}+E_{12})t} + 2e^{-i(E_{11}+E_{22}+2E_{12})t}\\
&\quad + 3e^{-i(2E_{11}+2E_{12})t} + e^{-i(2E_{22}+2E_{12})t} + 2e^{-i(E_{11}+3E_{12})t} + 2e^{-i(E_{22}+3E_{12})t},\\
(\tilde{\rho}_t)^{(3)}_{22} &= e^{-i(4E_{22})t} + e^{-i(4E_{12})t} + 2e^{-i(3E_{22}+E_{12})t} + 2e^{-i(3E_{11}+E_{12})t} + 2e^{-i(E_{11}+E_{22}+2E_{12})t}\\
&\quad + 3e^{-i(2E_{22}+2E_{12})t} + e^{-i(2E_{11}+2E_{12})t} + 2e^{-i(E_{22}+3E_{12})t} + 2e^{-i(E_{11}+3E_{12})t},
\end{aligned} \tag{C7}$$

where the tilde denotes un-normalized. The normalization of the time evolution operator here becomes

$$\mathcal{N}_5^{-1} = \mathrm{Tr}\,\tilde{\rho}_t^{(3)} = \mathrm{Tr}\,\mathcal{U}(t) = (\tilde{\rho}_t)^{(3)}_{11} + (\tilde{\rho}_t)^{(3)}_{22} \tag{C8}$$

In general the resulting von Neumann entropy is a complicated complex-valued function of the three energy parameters E_{11}, E_{22}, E_{12}.

There are parallels between our discussions here on qubit chain configurations and those in [279] on ghost-spin chains (although the context is different).

Infinite qubit chain: Consider now an infinite 1-dim chain of qubits, again with only nearest-neighbour interactions, the Hamiltonian being

$$H = -J\sum_n s_n s_{n+1} = \ldots - Js_{-1}s_0 - Js_0s_1 + \ldots \tag{C9}$$

We can focus on the qubit at location $n = n_0$ as the subsystem in question, tracing over all the other qubits in the chain. The reduced time evolution operator is

$$\rho_t = \frac{1}{\sum_I e^{-iE[I]t}} \sum_{n_0=1,2} \Big(\sum_{I;\ n\neq 0} e^{-iE[I]t} \Big) |n_0\rangle\langle n_0| \tag{C10}$$

This is a complicated object in general, although still simply a complex-valued function of the three energy parameters E_{11}, E_{22}, E_{12}. Since this qubit only interacts directly with its two neighbours, the effective system has some parallels with the 3-qubit chain above: but the detailed structure is complicated, as already evident in the 5-qubit case earlier.

$|1\rangle \leftrightarrow |2\rangle$ exchange symmetry: In the simple subcase enjoying $|1\rangle \leftrightarrow |2\rangle$ exchange symmetry, there are substantial simplifications in (C1): this is when there is an Ising-like structure, with

$$a_1 = -a_2 = 1\,; \qquad E_{11} = E_{22} = -E_{12} = -J\ . \tag{C11}$$

For instance the 3-qubit case (C5) simplifies to

$$\mathcal{N}_3^{-1} = 2\big(e^{iJt} + e^{-iJt}\big)^2\,, \qquad (\rho_t^A)_{11} = (\rho_t^A)_{22} = \mathcal{N}_3\left(e^{iJt} + e^{-iJt}\right)^2 = \frac{1}{2}\ , \tag{C12}$$

which thus gives von Neumann entropy $\log 2$. Likewise the 5-qubit (C7) case can be seen to simplify to

$$\mathcal{N}_5^{-1} = 2\big(e^{iJt} + e^{-iJt}\big)^4\,, \qquad (\rho_t^A)_{11} = (\rho_t^A)_{22} = \mathcal{N}_5\left(e^{iJt} + e^{-iJt}\right)^4 = \frac{1}{2}\ , \tag{C13}$$

so the middle qubit has identical structure. For an infinite qubit chain with this Ising-like $\mathbb{Z}_2$ symmetry, we expect translation invariance in the "bulk" so we expect that the reduced time evolution operator has again similar structure. Considering an N-qubit chain (towards large N), the configurations can be organized similar to (C6). It is then clear that the ground states are $|11\ldots11\rangle$, $|22\ldots22\rangle$, with energy $-(N-1)J$. The first excited states comprise "one kink" states with exactly one 12- or 21-interface with energy $-(N-3)J$ and degeneracy $2(N-1)$. The next set of excited states contain two kinks, so the energy is $-(N-5)J$ with degeneracy $4(N-2)$. Higher excited states contain multiple 12- or 21-interfaces. The two highest energy states have maximally alternating $1, 2$s, *i.e.* $|12121..\rangle, |21212..\rangle$: there are $(N-1)$ interfaces giving energy $(N-1)J$. Furthermore, every energy E (with corresponding configurations) comes in pairs, *i.e.* there are corresponding configurations with energy $-E$. This can be seen above, with the ground states and highest energy states: likewise, corresponding to the one kink states, we have states with energy $(N-3)J$ obtained by transforming one of the 12- or 21-interfaces in the highest energy states to 11 or 22, which then lowers the energy precisely by $2J$ (and their degeneracy can be checked easily). Thus the normalization of the time evolution operator (akin to the partition function) is $\mathcal{N}_N^{-1} = \mathrm{Tr}\,\tilde{\rho}_t$, *i.e.*

$$\mathcal{N}_N^{-1} = 2\big(e^{iJt(N-1)} + (N-1)e^{iJt(N-3)} + \ldots + (N-1)e^{-iJt(N-3)} + e^{-iJt(N-1)}\big) = 2\big(e^{iJt} + e^{-iJt}\big)^{N-1}\ . \tag{C14}$$

Each component of the reduced time evolution operator for some bulk qubit can be explicitly seen to receive contributions equally from half these states: so we obtain

$$(\rho_t^A)_{11} = (\rho_t^A)_{22} = \mathcal{N}_N \left(e^{iJt} + e^{-iJt}\right)^{N-1} = \frac{1}{2} \,, \tag{C15}$$

which is identical to the structure of the middle qubit in the previous finite qubit cases.

Note that it is adequate to require $E_{11} = E_{22}$ to implement this $|1\rangle \leftrightarrow |2\rangle$ exchange symmetry: then shifting the energies arrives at the symmetric values in (C11). However if keep E_{12} independent of $E_{11} = E_{22}$ then there are apparently two independent parameters: however it is straightforward to see that the reduced time evolution operator, wbile non-Hermitian, nevertheless leads to real-valued von Neumann entropy. It is likely that similar studies can be extended for "ghost-spin" models such as those in [279, 280].

All of the above structures can be seen to match ordinary finite temperature entanglement, except with imaginary temperature $\beta = it$.

6.10 Two coupled oscillators

We consider the following Hamiltonian H with unit masses $m_A = m_B = 1$,

$$H = \frac{1}{2}\,(p_A^2 + p_B^2) + \frac{k_1}{2}\,(x_A^2 + x_B^2) \,+\, \frac{k_2}{2}\,(x_A - x_B)^2 \,. \tag{C1}$$

This is slightly different from the coupled oscillators case discussed in [227]. We diagonalise the Hamiltonian in a coordinate basis $\{y_1, y_2\}$ as below. Then the hamiltonian (C1) becomes

$$\begin{aligned} H &= (\,\frac{1}{2}\,p_1^2 + \frac{1}{2}\,\Omega_1^2\,y_1^2\,) + (\,\frac{1}{2}\,p_2^2 \,+\, \frac{1}{2}\,\Omega_2^2\,y_2^2\,)\,, \\ y_1 &= \frac{(x_A + x_B)}{\sqrt{2}}\;; \quad y_2 = \frac{(x_A - x_B)}{\sqrt{2}}\;, \end{aligned} \tag{C2}$$

where $\Omega_1 = \sqrt{k_1}\,,\ \Omega_2 = \sqrt{k_1 + 2k_2}$. The energy eigenvalues and eigenfunctions of (C2) are labelled by $E_{n_1 n_2}$, and $\phi_{n_1 n_2}(y_1, y_2)$ respectively,

$$E_{n_1 n_2} = (n_1 + \frac{1}{2})\Omega_1 + (n_2 + \frac{1}{2})\Omega_2 \,=\, E_{n_1} + E_{n_2}\,; \quad \phi_{n_1 n_2}(y_1, y_2) = \phi_{n_1}(y_1)\,\phi_{n_2}(y_2)\,, \tag{C3}$$

where n_1,n_2 take values from 0 to ∞ and $E_{n_1} = (n_1 + \frac{1}{2})\Omega_1\,,\ E_{n_2} = (n_2 + \frac{1}{2})\Omega_2\,.$

We now write the time evolution operator in its eigenbasis as follows

$$e^{-iHt} = \rho(t) = \sum_{n_1, n_2} \,e^{-i\,E_{n_1 n_2} t}\ |\phi_{n_1 n_2}\rangle\,\langle\phi_{n_1 n_2}|\ . \tag{C4}$$

In position space

$$\begin{aligned} \rho(y_1, y_2; y_1', y_2', t) &= \sum_{n_1, n_2} \,e^{-i\,E_{n_1 n_2} t}\,\phi_{n_1 n_2}(y_1, y_2)\,\phi^*_{n_1 n_2}(y_1', y_2') \quad , \\ &= \sum_{n_1, n_2} \,e^{-i\,(E_{n_1} + E_{n_2})t}\,\phi_{n_1 n_2}(y_1, y_2)\,\phi^*_{n_1 n_2}(y_1', y_2') \ , \\ &= \rho_1(y_1; y_1', t)\,\rho_2(y_2; y_2', t) \ . \end{aligned} \tag{C5}$$

We have applied (C3) in the first line of (C5), and

$$\rho_1(y_1;y_1',t)=\sum_{n_1} e^{-iE_{n_1}t}\,\phi_{n_1}(y_1)\phi^*_{n_1}(y_1')\,;\quad \rho_2(y_2;y_2',t)=\sum_{n_2} e^{-iE_{n_2}t}\,\phi_{n_2}(y_2)\phi^*_{n_2}(y_2')\ . \tag{C6}$$

(C5) shows that the time evolution operator $\rho(t)$ is decomposed as $\rho(t)=\rho_1(t)\otimes\rho_2(t)$. The energy eigenstate for a single harmonic oscillator of frequency Ω (setting $m=1$) is

$$\phi_n(x)=\frac{1}{\sqrt{2^n n!}}\left(\frac{\Omega}{\pi}\right)^{\frac{1}{4}} e^{-\frac{\Omega\,x^2}{2}}\,H_n(\sqrt{\Omega}\,x)\,;\qquad E_n=(n+\frac{1}{2})\Omega\,. \tag{C7}$$

We now use Mehler's formula for Hermite polynomials [281]

$$\sum_{n=0}^{\infty}\frac{(\frac{\alpha}{2})^n}{n!}H_n(X)H_n(Y)\;=\frac{1}{\sqrt{1-\alpha^2}}\,e^{\frac{-\alpha^2\left(X^2+Y^2\right)+2\alpha XY}{1-\alpha^2}}\ . \tag{C8}$$

We now consider the time evolution operator for a single harmonic oscillator of frequency Ω in order to calculate (C5):

$$\rho(x;x',t)=\sum_{n=0}^{\infty} e^{-iE_nt}\,\phi_n(x)\,\phi^*_n(x')\ . \tag{C9}$$

Applying (C7) into (C9)

$$\rho(x;x',t)=\sum_{n=0}^{\infty} e^{-i(n+\frac{1}{2})\Omega t}\,\frac{1}{2^n\,n!}\left(\frac{\Omega}{\pi}\right)^{\frac{1}{2}} e^{-\frac{\Omega}{2}\,(x^2+x'^2)}\,H_n(\sqrt{\Omega}\,x)\,H_n(\sqrt{\Omega}\,x')\ . \tag{C10}$$

We now use (C8) in (C10),

$$\rho(x;x',t)=\frac{\left(\frac{\Omega}{\pi}\right)^{\frac{1}{2}}}{\sqrt{2i\,\sin(\Omega\,t)}}\;e^{-\frac{p\,(x^2+x'^2)}{2}+q\,xx'}\,, \tag{C11}$$

where

$$p(t)=-i\,\Omega\,\cot(\Omega\,t)\ ;\qquad q(t)=\frac{-i\,\Omega}{\sin(\Omega\,t)}\,. \tag{C12}$$

We will not write the t dependence of p and q explicitly, we simply write p and q instead of $p(t)$ and $q(t)$. We now define the normalised time evolution operator as $P(x;x',t)=\frac{\rho(x;x',t)}{\mathrm{Tr}(\rho(x;x',t))}$,

$$P(x;x',t)=\sqrt{\frac{p-q}{\pi}}\,e^{-\frac{p\,(x^2+x'^2)}{2}+q\,xx'}\,. \tag{C13}$$

Note that the normalization $\mathrm{Tr}(\rho(x;x',t))$ using (C11) is $\int_{-\infty}^{\infty}dx\,\rho(x,x,t)$, which is oscillatory (rather than a damped Gaussian), using (C12). To render this well-defined, we insert a small exponentially damping regulator: this is the position space analog of the regularization in (4.70). Similar regulators are required to define various infinite sums/integrals here.

We now find the expressions for $\rho_1(y_1; y_1', t)$ and $\rho_2(y_2; y_2', t)$ appearing in (C5) using (C11),

$$\rho_1(y_1; y_1', t) = \frac{\left(\frac{\Omega_1}{\pi}\right)^{\frac{1}{2}}}{\sqrt{2i\,\sin(\Omega_1\, t)}}\; e^{-\frac{p\,(y_1^2 + {y_1'}^2)}{2} + q\, y_1 y_1'}\,,$$
$$\rho_2(y_2; y_2', t) = \frac{\left(\frac{\Omega_2}{\pi}\right)^{\frac{1}{2}}}{\sqrt{2i\,\sin(\Omega_2\, t)}}\; e^{-\frac{r\,(y_2^2 + {y_2'}^2)}{2} + s\, y_2 y_2'}\,, \tag{C14}$$

where

$$p = -i\,\Omega_1\,\cot(\Omega_1\, t)\,; \quad q = \frac{-i\,\Omega_1}{\sin(\Omega_1\, t)}\,; \quad r = -i\,\Omega_2\,\cot(\Omega_2\, t)\,; \quad s = \frac{-i\,\Omega_2}{\sin(\Omega_2\, t)}\,. \tag{C15}$$

We define the normalised time evolution operator as $P(y_1, y_2; y_1', y_2', t) = \frac{\rho(y_1, y_2; y_1', y_2', t)}{Tr(\rho(y_1, y_2; y_1', y_2', t))}$,

$$P(y_1, y_2; y_1', y_2', t) = \sqrt{\frac{p-q}{\pi}}\,\sqrt{\frac{r-s}{\pi}}\, e^{-\frac{p\,(y_1^2 + {y_1'}^2)}{2} + q\, y_1 y_1'}\;\; e^{-\frac{r\,(y_2^2 + {y_2'}^2)}{2} + s\, y_2 y_2'}\,. \tag{C16}$$

Writing $P(y_1, y_2; y_1', y_2', t)$ in terms of original variables x_A, x_B (C2) gives

$$P(x_A, x_B; x_A', x_B' = x_B, t) = \sqrt{\frac{p-q}{\pi}}\,\sqrt{\frac{r-s}{\pi}}\, e^{-\frac{(p+r)}{4}\,(x_A^2 + {x_A'}^2) + \frac{(q+s)}{2}\, x_A\, x_A'}$$
$$e^{-\frac{x_B^2}{2}\,(p+r-q-s) + x_B\,\frac{(x_A + x_A')}{2}\,(-p-s+q+r)}\,. \tag{C17}$$

We now trace over the 2nd oscillator $P_A(x_A; x_A', t) = Tr_B[P(x_A, x_B; x_A', x_B', t)]$. For this we integrate (C17) over x_B, after performing the integration, we get

$$P_A(x_A; x_A', t) = \sqrt{\frac{\gamma-\beta}{\pi}}\, e^{-\frac{\gamma}{2}(x_A^2 + {x_A'}^2) + \beta\, x_A\, x_A'}\,, \tag{C18}$$

where

$$\gamma = \frac{p+r}{2} - \frac{1}{4}\,\frac{(p+s-q-r)^2}{p+r-q-s}\,; \qquad \beta = \frac{q+s}{2} + \frac{1}{4}\,\frac{(p+s-q-r)^2}{p+r-q-s}\,,$$
$$\gamma - \beta = 2\,\frac{(p-q)(r-s)}{p-q+r-s}\,; \qquad \gamma + \beta = \frac{p+q+r+s}{2}\,. \tag{C19}$$

The entropy associated with the reduced density matrix $P_A(x_A, x_A', t)$ is given by $S_A = -Tr(P_A \log P_A)$. The eigenvalues λ_n and eigenvectors $f_n(x)$ of an operator of the form (C18) are given in [35]: we have $\lambda_n = (1-\zeta)\,\zeta^n$, where $\zeta = \frac{\beta}{\gamma+\alpha}$, $\alpha = \sqrt{\gamma^2 - \beta^2}$, which gives

$$S_A = -\log(1-\zeta) - \frac{\zeta}{1-\zeta}\log\zeta\,. \tag{C20}$$

We see that the entropy S_A is complex valued, recasting ζ in terms of $\gamma+\beta$ and $\gamma-\beta$,

$$\zeta = \frac{\sqrt{\gamma+\beta} - \sqrt{\gamma-\beta}}{\sqrt{\gamma+\beta} + \sqrt{\gamma-\beta}}\,. \tag{C21}$$

The explicit expressions for (C19) in terms of original variables are given by

$$\sqrt{\gamma+\beta}=\Big(-i\Big(\frac{\Omega_1}{2}\cot\frac{\Omega_1 t}{2}+\frac{\Omega_2}{2}\cot\frac{\Omega_2 t}{2}\Big)\Big)^{\frac{1}{2}},\quad \sqrt{\gamma-\beta}=\Big(\frac{2i}{\frac{1}{\Omega_1}\cot\frac{\Omega_1 t}{2}+\frac{1}{\Omega_2}\cot\frac{\Omega_2 t}{2}}\Big)^{\frac{1}{2}}. \quad \text{(C22)}$$

For $\Omega_1=\Omega_2=\omega$ (*i.e.* $k_2=0$), we recover our result for two uncoupled oscillators. Comparing our result with the spacelike entanglement evaluated at finite inverse temperature it, we recover the result in [282] (in particular ζ in (C21) matches with eq.(2.22) in [282]).

Bibliography

[1] J. D. Bekenstein, "Black Holes and Entropy," Phys. Rev. D **7**, 2333-2346 (1973) doi:10.1103/PhysRevD.7.2333

[2] G. 't Hooft, "Dimensional reduction in quantum gravity," Conf. Proc. C **930308**, 284-296 (1993) [arXiv:gr-qc/9310026 [gr-qc]].

[3] L. Susskind, "The World as a hologram," J. Math. Phys. **36**, 6377-6396 (1995) doi:10.1063/1.531249 [arXiv:hep-th/9409089 [hep-th]].

[4] J. M. Maldacena, "The Large N limit of superconformal field theories and supergravity," Adv. Theor. Math. Phys. **2**, 231-252 (1998) doi:10.4310/ATMP.1998.v2.n2.a1 [arXiv:hep-th/9711200 [hep-th]].

[5] O. Aharony, S. S. Gubser, J. M. Maldacena, H. Ooguri and Y. Oz, "Large N field theories, string theory and gravity," Phys. Rept. **323**, 183-386 (2000) doi:10.1016/S0370-1573(99)00083-6 [arXiv:hep-th/9905111 [hep-th]].

[6] I. R. Klebanov, "TASI lectures: Introduction to the AdS / CFT correspondence," doi:10.1142/9789812799630_0007 [arXiv:hep-th/0009139 [hep-th]].

[7] J. M. Maldacena, "TASI 2003 lectures on AdS / CFT," [arXiv:hep-th/0309246 [hep-th]].

[8] J. Polchinski, "Introduction to Gauge/Gravity Duality," doi:10.1142/9789814350525_0001 [arXiv:1010.6134 [hep-th]].

[9] C. P. Herzog, P. Kovtun, S. Sachdev and D. T. Son, "Quantum critical transport, duality, and M-theory," Phys. Rev. D **75**, 085020 (2007) doi:10.1103/PhysRevD.75.085020 [arXiv:hep-th/0701036 [hep-th]].

[10] S. A. Hartnoll, A. Lucas and S. Sachdev, "Holographic quantum matter," [arXiv:1612.07324 [hep-th]].

[11] A. S. T. Pires, "Ads/CFT correspondence in condensed matter," IOP, 2014, ISBN 978-1-62705-310-5 [arXiv:1006.5838 [cond-mat.str-el]].

[12] S. Sachdev, "Condensed Matter and AdS/CFT," Lect. Notes Phys. **828**, 273-311 (2011) doi:10.1007/978-3-642-04864-7_9 [arXiv:1002.2947 [hep-th]].

[13] S. Hawking, "Breakdown of Predictability in Gravitational Collapse," Phys. Rev. D **14** (1976), 2460-2473.

[14] G. Penington, "Entanglement Wedge Reconstruction and the Information Paradox," JHEP **09**, 002 (2020) doi:10.1007/JHEP09(2020)002 [arXiv:1905.08255 [hep-th]].

[15] A. Almheiri, N. Engelhardt, D. Marolf and H. Maxfield, "The entropy of bulk quantum fields and the entanglement wedge of an evaporating black hole," JHEP **12** (2019), 063 [arXiv:1905.08762 [hep-th]].

[16] A. Almheiri, R. Mahajan, J. Maldacena and Y. Zhao, "The Page curve of Hawking radiation from semiclassical geometry," JHEP **03**, 149 (2020) doi:10.1007/JHEP03(2020)149 [arXiv:1908.10996 [hep-th]].

[17] S. Ryu and T. Takayanagi, "Holographic derivation of entanglement entropy from AdS/CFT," Phys. Rev. Lett. **96**, 181602 (2006) doi:10.1103/PhysRevLett.96.181602 [arXiv:hep-th/0603001 [hep-th]].

[18] V. E. Hubeny, M. Rangamani and T. Takayanagi, "A Covariant holographic entanglement entropy proposal," JHEP **07**, 062 (2007) doi:10.1088/1126-6708/2007/07/062 [arXiv:0705.0016 [hep-th]].

[19] V. E. Hubeny, "Extremal surfaces as bulk probes in AdS/CFT," JHEP **07**, 093 (2012) doi:10.1007/JHEP07(2012)093 [arXiv:1203.1044 [hep-th]].

[20] T. Hartman and J. Maldacena, "Time Evolution of Entanglement Entropy from Black Hole Interiors," JHEP **05**, 014 (2013) doi:10.1007/JHEP05(2013)014 [arXiv:1303.1080 [hep-th]].

[21] A. V. Frolov, "Kasner-AdS space-time and anisotropic brane world cosmology," Phys. Lett. B **514**, 213-216 (2001) doi:10.1016/S0370-2693(01)00844-9 [arXiv:gr-qc/0102064 [gr-qc]].

[22] S. R. Das, J. Michelson, K. Narayan and S. P. Trivedi, "Time dependent cosmologies and their duals," Phys. Rev. D **74**, 026002 (2006) doi:10.1103/PhysRevD.74.026002 [arXiv:hep-th/0602107 [hep-th]].

[23] A. Awad, S. R. Das, K. Narayan and S. P. Trivedi, "Gauge theory duals of cosmological backgrounds and their energy momentum tensors," Phys. Rev. D **77**, 046008 (2008) doi:10.1103/PhysRevD.77.046008 [arXiv:0711.2994 [hep-th]].

[24] A. Awad, S. R. Das, S. Nampuri, K. Narayan and S. P. Trivedi, "Gauge Theories with Time Dependent Couplings and their Cosmological Duals," Phys. Rev. D **79**, 046004 (2009) doi:10.1103/PhysRevD.79.046004 [arXiv:0807.1517 [hep-th]].

[25] L. Susskind, "Computational Complexity and Black Hole Horizons," Fortsch. Phys. **64**, 24-43 (2016) doi:10.1002/prop.201500092 [arXiv:1403.5695 [hep-th]].

[26] D. Stanford and L. Susskind, "Complexity and Shock Wave Geometries," Phys. Rev. D **90**, no.12, 126007 (2014) doi:10.1103/PhysRevD.90.126007 [arXiv:1406.2678 [hep-th]].

[27] A. R. Brown, D. A. Roberts, L. Susskind, B. Swingle and Y. Zhao, "Holographic Complexity Equals Bulk Action?," Phys. Rev. Lett. **116**, no.19, 191301 (2016) doi:10.1103/PhysRevLett.116.191301 [arXiv:1509.07876 [hep-th]].

[28] A. R. Brown, D. A. Roberts, L. Susskind, B. Swingle and Y. Zhao, "Complexity, action, and black holes," Phys. Rev. D **93**, no.8, 086006 (2016) doi:10.1103/PhysRevD.93.086006 [arXiv:1512.04993 [hep-th]].

[29] J. Couch, W. Fischler and P. H. Nguyen, "Noether charge, black hole volume, and complexity," JHEP **03**, 119 (2017) doi:10.1007/JHEP03(2017)119 [arXiv:1610.02038 [hep-th]].

[30] A. Belin, R. C. Myers, S. M. Ruan, G. Sárosi and A. J. Speranza, "Does Complexity Equal Anything?," Phys. Rev. Lett. **128**, no.8, 081602 (2022) doi:10.1103/PhysRevLett.128.081602 [arXiv:2111.02429 [hep-th]].

[31] A. Belin, R. C. Myers, S. M. Ruan, G. Sárosi and A. J. Speranza, "Complexity equals anything II," JHEP **01**, 154 (2023) doi:10.1007/JHEP01(2023)154 [arXiv:2210.09647 [hep-th]].

[32] M. Van Raamsdonk, "Comments on quantum gravity and entanglement," [arXiv:0907.2939 [hep-th]].

[33] M. Van Raamsdonk, "Building up spacetime with quantum entanglement," Gen. Rel. Grav. **42**, 2323-2329 (2010) doi:10.1142/S0218271810018529 [arXiv:1005.3035 [hep-th]].

[34] E. Witten, "A Mini-Introduction To Information Theory," Riv. Nuovo Cim. **43**, no.4, 187-227 (2020) doi:10.1007/s40766-020-00004-5 [arXiv:1805.11965 [hep-th]].

[35] M. Srednicki, "Entropy and area," Phys. Rev. Lett. **71**, 666-669 (1993) doi:10.1103/PhysRevLett.71.666 [arXiv:hep-th/9303048 [hep-th]].

[36] P. Calabrese and J. L. Cardy, "Entanglement entropy and quantum field theory," J. Stat. Mech. **0406**, P06002 (2004) doi:10.1088/1742-5468/2004/06/P06002 [arXiv:hep-th/0405152 [hep-th]].

[37] P. Calabrese and J. Cardy, "Entanglement entropy and conformal field theory," J. Phys. A **42**, 504005 (2009) doi:10.1088/1751-8113/42/50/504005 [arXiv:0905.4013 [cond-mat.stat-mech]].

[38] M. M. Wolf, F. Verstraete, M. B. Hastings and J. I. Cirac, "Area Laws in Quantum Systems: Mutual Information and Correlations," Phys. Rev. Lett. **100**, no.7, 070502 (2008) doi:10.1103/PhysRevLett.100.070502 [arXiv:0704.3906 [quant-ph]].

[39] H. Casini and M. Huerta, "Entanglement entropy in free quantum field theory," J. Phys. A **42**, 504007 (2009) doi:10.1088/1751-8113/42/50/504007 [arXiv:0905.2562 [hep-th]].

[40] M. Headrick, "Lectures on entanglement entropy in field theory and holography," [arXiv:1907.08126 [hep-th]].

[41] T. Nishioka, S. Ryu and T. Takayanagi, J. Phys. A **42**, 504008 (2009) doi:10.1088/1751-8113/42/50/504008 [arXiv:0905.0932 [hep-th]].

[42] M. Rangamani and T. Takayanagi, "Holographic Entanglement Entropy," Lect. Notes Phys. **931**, pp.1-246 (2017) Springer, 2017, doi:10.1007/978-3-319-52573-0 [arXiv:1609.01287 [hep-th]].

[43] A. Manu, K. Narayan and P. Paul, "Cosmological singularities, entanglement and quantum extremal surfaces," JHEP **04**, 200 (2021) doi:10.1007/JHEP04(2021)200 [arXiv:2012.07351 [hep-th]].

[44] K. Narayan, H. K. Saini and G. Yadav, "Cosmological singularities, holographic complexity and entanglement," JHEP **07**, 125 (2024) doi:10.1007/JHEP07(2024)125 [arXiv:2404.00761 [hep-th]].

[45] T. Faulkner, A. Lewkowycz and J. Maldacena, "Quantum corrections to holographic entanglement entropy," JHEP **11**, 074 (2013) doi:10.1007/JHEP11(2013)074 [arXiv:1307.2892 [hep-th]].

[46] N. Engelhardt and A. C. Wall, "Quantum Extremal Surfaces: Holographic Entanglement Entropy beyond the Classical Regime," JHEP **01**, 073 (2015) doi:10.1007/JHEP01(2015)073 [arXiv:1408.3203 [hep-th]].

[47] Claude E. Shannon, "A Mathematical Theory of Communication," The Bell System Technical Journal, vol. 27, no. 3, pp. 379–423, 1948.

[48] Richard Feynman, "Simulating physics with computers", International Journal of Theoretical Physics, 21(6/7):467–488, 1982.

[49] David Deutsch "Quantum theory, the Church–Turing principle and the universal quantum computer", In Proceedings of the Royal Society of London A: Mathematical, Physical and Engineering Sciences, volume 400, pages 97–117, 1985.

[50] Peter W. Shor, "Algorithms for quantum computation: discrete logarithms and factoring," Proceedings of the 35th Annual Symposium on Foundations of Computer Science (FOCS), pp. 124–134, 1994.

[51] Adriano Barenco, Charles H. Bennett, Richard Cleve, David P. DiVincenzo, Norman Margolus, Peter Shor, Tycho Sleator, John A. Smolin, and Harald Weinfurter, "Elementary gates for quantum computation," Physical Review A, vol. 52, no. 5, pp. 3457–3467, Nov. 1995.

[52] Michael A. Nielsen and Isaac L. Chuang, *Quantum Computation and Quantum Information*, Cambridge University Press, 1st edition, 2000.

[53] S. Chapman, H. Marrochio and R. C. Myers, "Complexity of Formation in Holography," JHEP **01**, 062 (2017) doi:10.1007/JHEP01(2017)062 [arXiv:1610.08063 [hep-th]].

[54] S. Chapman, M. P. Heller, H. Marrochio and F. Pastawski, "Toward a Definition of Complexity for Quantum Field Theory States," Phys. Rev. Lett. **120**, no.12, 121602 (2018) doi:10.1103/PhysRevLett.120.121602 [arXiv:1707.08582 [hep-th]].

[55] D. Carmi, S. Chapman, H. Marrochio, R. C. Myers and S. Sugishita, "On the Time Dependence of Holographic Complexity," JHEP **11**, 188 (2017) doi:10.1007/JHEP11(2017)188 [arXiv:1709.10184 [hep-th]].

[56] M. Moosa, "Evolution of Complexity Following a Global Quench," JHEP **03**, 031 (2018) doi:10.1007/JHEP03(2018)031 [arXiv:1711.02668 [hep-th]].

[57] R. Q. Yang, "Complexity for quantum field theory states and applications to thermofield double states," Phys. Rev. D **97**, no.6, 066004 (2018) doi:10.1103/PhysRevD.97.066004 [arXiv:1709.00921 [hep-th]].

[58] R. Khan, C. Krishnan and S. Sharma, "Circuit Complexity in Fermionic Field Theory," Phys. Rev. D **98**, no.12, 126001 (2018) doi:10.1103/PhysRevD.98.126001 [arXiv:1801.07620 [hep-th]].

[59] S. Chapman, J. Eisert, L. Hackl, M. P. Heller, R. Jefferson, H. Marrochio and R. C. Myers, "Complexity and entanglement for thermofield double states," SciPost Phys. **6**, no.3, 034 (2019) doi:10.21468/SciPostPhys.6.3.034 [arXiv:1810.05151 [hep-th]].

[60] S. Chapman, H. Marrochio and R. C. Myers, "Holographic complexity in Vaidya spacetimes. Part I," JHEP **06**, 046 (2018) doi:10.1007/JHEP06(2018)046 [arXiv:1804.07410 [hep-th]].

[61] S. Chapman, H. Marrochio and R. C. Myers, "Holographic complexity in Vaidya spacetimes. Part II," JHEP **06**, 114 (2018) doi:10.1007/JHEP06(2018)114 [arXiv:1805.07262 [hep-th]].

[62] P. Caputa and J. M. Magan, "Quantum Computation as Gravity," Phys. Rev. Lett. **122**, no.23, 231302 (2019) doi:10.1103/PhysRevLett.122.231302 [arXiv:1807.04422 [hep-th]].

[63] M. Guo, J. Hernandez, R. C. Myers and S. M. Ruan, "Circuit Complexity for Coherent States," JHEP **10**, 011 (2018) doi:10.1007/JHEP10(2018)011 [arXiv:1807.07677 [hep-th]].

[64] J. M. Magán, "Black holes, complexity and quantum chaos," JHEP **09**, 043 (2018) doi:10.1007/JHEP09(2018)043 [arXiv:1805.05839 [hep-th]].

[65] K. Goto, H. Marrochio, R. C. Myers, L. Queimada and B. Yoshida, "Holographic Complexity Equals Which Action?," JHEP **02**, 160 (2019) doi:10.1007/JHEP02(2019)160 [arXiv:1901.00014 [hep-th]].

[66] A. R. Brown and L. Susskind, "Complexity geometry of a single qubit," Phys. Rev. D **100**, no.4, 046020 (2019) doi:10.1103/PhysRevD.100.046020 [arXiv:1903.12621 [hep-th]].

[67] T. Ali, A. Bhattacharyya, S. S. Haque, E. H. Kim, N. Moynihan and J. Murugan, "Chaos and Complexity in Quantum Mechanics," Phys. Rev. D **101**, no.2, 026021 (2020) doi:10.1103/PhysRevD.101.026021 [arXiv:1905.13534 [hep-th]].

[68] E. Caceres, S. Chapman, J. D. Couch, J. P. Hernandez, R. C. Myers and S. M. Ruan, "Complexity of Mixed States in QFT and Holography," JHEP **03**, 012 (2020) doi:10.1007/JHEP03(2020)012 [arXiv:1909.10557 [hep-th]].

[69] N. Chagnet, S. Chapman, J. de Boer and C. Zukowski, "Complexity for Conformal Field Theories in General Dimensions," Phys. Rev. Lett. **128**, no.5, 051601 (2022) doi:10.1103/PhysRevLett.128.051601 [arXiv:2103.06920 [hep-th]].

[70] S. Chapman and G. Policastro, "Quantum computational complexity from quantum information to black holes and back," Eur. Phys. J. C **82**, no.2, 128 (2022) doi:10.1140/epjc/s10052-022-10037-1 [arXiv:2110.14672 [hep-th]].

[71] P. Caputa and S. Liu, "Quantum complexity and topological phases of matter," Phys. Rev. B **106**, no.19, 195125 (2022) doi:10.1103/PhysRevB.106.195125 [arXiv:2205.05688 [hep-th]].

[72] R. Jefferson and R. C. Myers, "Circuit complexity in quantum field theory," JHEP **10**, 107 (2017) doi:10.1007/JHEP10(2017)107 [arXiv:1707.08570 [hep-th]].

[73] J. Erdmenger, M. Flory, M. Gerbershagen, M. P. Heller and A. L. Weigel, "Exact Gravity Duals for Simple Quantum Circuits," SciPost Phys. **13**, no.3, 061 (2022) doi:10.21468/SciPostPhys.13.3.061 [arXiv:2112.12158 [hep-th]].

[74] S. Baiguera, R. Berman, S. Chapman and R. C. Myers, "The cosmological switchback effect," JHEP **07**, 162 (2023) doi:10.1007/JHEP07(2023)162 [arXiv:2304.15008 [hep-th]].

[75] S. Baiguera and R. Berman, "The cosmological switchback effect. Part II," JHEP **08**, 086 (2024) doi:10.1007/JHEP08(2024)086 [arXiv:2406.04397 [hep-th]].

[76] L. Susskind, "Three Lectures on Complexity and Black Holes," Springer, 2020, ISBN 978-3-030-45108-0, 978-3-030-45109-7 doi:10.1007/978-3-030-45109-7 [arXiv:1810.11563 [hep-th]].

[77] M. A. Nielsen, "A geometric approach to quantum circuit lower bounds," Quant. Inf. Comput. **6**, no.3, 213-262 (2006) doi:10.26421/QIC6.3-2 [arXiv:quant-ph/0502070 [quant-ph]].

[78] M. A. Nielsen, M. R. Dowling, M. Gu and A. C. Doherty, "Quantum Computation as Geometry," Science **311**, no.5764, 1133-1135 (2006) doi:10.1126/science.1121541 [arXiv:quant-ph/0603161 [quant-ph]].

[79] M. R. Dowling and M. A. Nielsen, "The geometry of quantum computation," Quant. Inf. Comput. **8**, no.10, 0861-0899 (2008) doi:10.26421/QIC8.10-1 [arXiv:quant-ph/0701004 [quant-ph]].

[80] E. Jørstad, R. C. Myers and S. M. Ruan, "Complexity=anything: singularity probes," JHEP **07**, 223 (2023) doi:10.1007/JHEP07(2023)223 [arXiv:2304.05453 [hep-th]].

[81] M. T. Wang, H. Y. Jiang and Y. X. Liu, "Generalized volume-complexity for RN-AdS black hole," JHEP **07**, 178 (2023) doi:10.1007/JHEP07(2023)178 [arXiv:2304.05751 [hep-th]].

[82] S. E. Aguilar-Gutierrez, M. P. Heller and S. Van der Schueren, "Complexity equals anything can grow forever in de Sitter space," Phys. Rev. D **110**, no.6, 6 (2024) doi:10.1103/PhysRevD.110.066009 [arXiv:2305.11280 [hep-th]].

[83] X. Wang, R. Li and J. Wang, "Generalized volume complexity in Gauss-Bonnet gravity: Constraints and phase transitions," Phys. Rev. D **108**, no.12, 126018 (2023) doi:10.1103/PhysRevD.108.126018 [arXiv:2307.12530 [hep-th]].

[84] S. E. Aguilar-Gutierrez, "C=Anything and the switchback effect in Schwarzschild-de Sitter space," JHEP **03**, 062 (2024) doi:10.1007/JHEP03(2024)062 [arXiv:2309.05848 [hep-th]].

[85] M. Zhang, J. Sun and R. B. Mann, "Generalized holographic complexity of rotating black holes," JHEP **09**, 050 (2024) doi:10.1007/JHEP09(2024)050 [arXiv:2401.08571 [hep-th]].

[86] S. E. Aguilar-Gutierrez, "Holographic complexity of axion-de Sitter universes," [arXiv:2401.00851 [hep-th]].

[87] R. C. Myers and S. M. Ruan, "Complexity Equals (Almost) Anything," [arXiv:2403.17475 [hep-th]].

[88] S. E. Aguilar-Gutierrez, S. Baiguera and N. Zenoni, "Holographic complexity of the extended Schwarzschild-de Sitter space," JHEP **05**, 201 (2024) doi:10.1007/JHEP05(2024)201 [arXiv:2402.01357 [hep-th]].

[89] M. Emami and S. Parvizi, "Generalized volume-complexity for Lovelock black holes," [arXiv:2409.13899 [hep-th]].

[90] G. Penington, S. H. Shenker, D. Stanford, Z. Yang, "Replica wormholes & the black hole interior," [arXiv:1911.11977[hep-th]].

[91] A. Almheiri, T. Hartman, J. Maldacena, E. Shaghoulian and A. Tajdini, "Replica Wormholes and the Entropy of Hawking Radiation," JHEP **05**, 013 (2020) [arXiv:1911.12333 [hep-th]].

[92] A. Almheiri, T. Hartman, J. Maldacena, E. Shaghoulian and A. Tajdini, "The entropy of Hawking radiation," [arXiv:2006.06872 [hep-th]].

[93] S. Raju, "Lessons from the Information Paradox," [arXiv:2012.05770 [hep-th]].

[94] B. Chen, B. Czech and Z. z. Wang, "Quantum Information in Holographic Duality," [arXiv:2108.09188 [hep-th]].

[95] T. Kibe, P. Mandayam and A. Mukhopadhyay, "Holographic spacetime, black holes and quantum error correcting codes: A review," [arXiv:2110.14669 [hep-th]].

[96] S. Ryu and T. Takayanagi, "Aspects of Holographic Entanglement Entropy," JHEP **0608**, 045 (2006) [hep-th/0605073].

[97] V. E. Hubeny, M. Rangamani and T. Takayanagi, "A Covariant holographic entanglement entropy proposal," JHEP **0707** (2007) 062 [arXiv:0705.0016 [hep-th]].

[98] Y. Chen, V. Gorbenko and J. Maldacena, "Bra-ket wormholes in gravitationally prepared states," [arXiv:2007.16091 [hep-th]].

[99] T. Hartman, Y. Jiang and E. Shaghoulian, "Islands in cosmology," JHEP **11**, 111 (2020) doi:10.1007/JHEP11(2020)111 [arXiv:2008.01022 [hep-th]].

[100] C. Krishnan, "Critical Islands," JHEP **01**, 179 (2021) doi:10.1007/JHEP01(2021)179 [arXiv:2007.06551 [hep-th]].

[101] M. Van Raamsdonk, "Comments on wormholes, ensembles, and cosmology," arXiv:2008.02259[hep-th].

[102] V. Balasubramanian, A. Kar and T. Ugajin, "Islands in de Sitter space," [arXiv:2008.05275 [hep-th]].

[103] W. Sybesma, "Pure de Sitter space and the island moving back in time," [arXiv:2008.07994 [hep-th]].

[104] S. Choudhury, S. Chowdhury, N. Gupta, A. Mishara, S. P. Selvam, S. Panda, G. D. Pasquino, C. Singha and A. Swain, "Circuit Complexity From Cosmological Islands," Symmetry **13**, 1301 (2021) doi:10.3390/sym13071301 [arXiv:2012.10234 [hep-th]].

[105] R. Bousso and A. Shahbazi-Moghaddam, "Island Finder and Entropy Bound," Phys. Rev. D **103**, no.10, 106005 (2021) doi:10.1103/PhysRevD.103.106005 [arXiv:2101.11648 [hep-th]].

[106] H. Geng, Y. Nomura and H. Y. Sun, "Information paradox and its resolution in de Sitter holography," Phys. Rev. D **103**, no.12, 126004 (2021) doi:10.1103/PhysRevD.103.126004 [arXiv:2103.07477 [hep-th]].

[107] S. Fallows and S. F. Ross, "Islands and mixed states in closed universes," JHEP **07**, 022 (2021) doi:10.1007/JHEP07(2021)022 [arXiv:2103.14364 [hep-th]].

[108] D. Giataganas and N. Tetradis, "Entanglement entropy in FRW backgrounds," Phys. Lett. B **820**, 136493 (2021) doi:10.1016/j.physletb.2021.136493 [arXiv:2105.12614 [hep-th]].

[109] L. Aalsma, A. Cole, E. Morvan, J. P. van der Schaar and G. Shiu, "Shocks and information exchange in de Sitter space," JHEP **10**, 104 (2021) doi:10.1007/JHEP10(2021)104 [arXiv:2105.12737 [hep-th]].

[110] K. Langhoff, C. Murdia and Y. Nomura, "Multiverse in an inverted island," Phys. Rev. D **104**, no.8, 086007 (2021) doi:10.1103/PhysRevD.104.086007 [arXiv:2106.05271 [hep-th]].

[111] S. E. Aguilar-Gutierrez, A. Chatwin-Davies, T. Hertog, N. Pinzani-Fokeeva and B. Robinson, "Islands in Multiverse Models," [arXiv:2108.01278 [hep-th]].

[112] K. Narayan, "On aspects of two-dimensional dilaton gravity, dimensional reduction, and holography," Phys. Rev. D **104**, no.2, 026007 (2021) doi:10.1103/PhysRevD.104.026007 [arXiv:2010.12955 [hep-th]].

[113] R. Bhattacharya, K. Narayan and P. Paul, "Cosmological singularities and 2-dimensional dilaton gravity," JHEP **08**, 062 (2020) doi:10.1007/JHEP08(2020)062 [arXiv:2006.09470 [hep-th]].

[114] D. Grumiller, R. Ruzziconi, C. Zwikel, "Generalized dilaton gravity in 2d," [arXiv:2109.03266 [hep-th]].

[115] S. R. Das, J. Michelson, K. Narayan and S. P. Trivedi, "Cosmologies with Null Singularities and their Gauge Theory Duals," Phys. Rev. D **75**, 026002 (2007) doi:10.1103/PhysRevD.75.026002 [arXiv:hep-th/0610053 [hep-th]].

[116] K. Madhu and K. Narayan, "String spectra near some null cosmological singularities," Phys. Rev. D **79**, 126009 (2009) doi:10.1103/PhysRevD.79.126009 [arXiv:0904.4532 [hep-th]].

[117] N. Engelhardt, T. Hertog and G. T. Horowitz, "Holographic Signatures of Cosmological Singularities," Phys. Rev. Lett. **113**, 121602 (2014) doi:10.1103/PhysRevLett.113.121602 [arXiv:1404.2309 [hep-th]].

[118] N. Engelhardt, T. Hertog and G. T. Horowitz, "Further Holographic Investigations of Big Bang Singularities," JHEP **1507**, 044 (2015) doi:10.1007/JHEP07(2015)044 [arXiv:1503.08838 [hep-th]].

[119] N. Engelhardt and G. T. Horowitz, "Holographic Consequences of a No Transmission Principle," Phys. Rev. D **93**, no.2, 026005 (2016) doi:10.1103/PhysRevD.93.026005 [arXiv:1509.07509 [hep-th]].

[120] N. Engelhardt and G. T. Horowitz, "New Insights into Quantum Gravity from Gauge/gravity Duality," Int. J. Mod. Phys. D **25**, no.12, 1643002 (2016) [arXiv:1605.04335 [hep-th]].

[121] B. Craps, "Big Bang Models in String Theory," Class. Quant. Grav. **23**, S849-S881 (2006) doi:10.1088/0264-9381/23/21/S01 [arXiv:hep-th/0605199 [hep-th]].

[122] C. Burgess and L. McAllister, "Challenges for String Cosmology," Class. Quant. Grav. **28**, 204002 (2011) doi:10.1088/0264-9381/28/20/204002 [arXiv:1108.2660 [hep-th]].

[123] N. Engelhardt and G. T. Horowitz, "Entanglement Entropy Near Cosmological Singularities," JHEP **1306**, 041 (2013) doi:10.1007/JHEP06(2013)041 [arXiv:1303.4442 [hep-th]].

[124] Raghu Mahajan, "A tutorial on entanglement island computations", Aug 2020, ICTS Bangalore String Seminars, `https://www.youtube.com/watch?v=7wmpBWGAp44&t=1816s` .

[125] A. Almheiri, R. Mahajan and J. Maldacena, "Islands outside the horizon," [arXiv:1910.11077 [hep-th]].

[126] H. Geng, A. Karch, C. Perez-Pardavila, S. Raju, L. Randall, M. Riojas and S. Shashi, "Inconsistency of Islands in Theories with Long-Range Gravity," [arXiv:2107.03390 [hep-th]].

[127] K. Goswami, K. Narayan and H. K. Saini, "Cosmologies, singularities and quantum extremal surfaces," JHEP **03**, 201 (2022) doi:10.1007/JHEP03(2022)201 [arXiv:2111.14906 [hep-th]].

[128] J. L. F. Barbon and E. Rabinovici, "Holographic complexity and spacetime singularities," JHEP **01**, 084 (2016) doi:10.1007/JHEP01(2016)084 [arXiv:1509.09291 [hep-th]].

[129] P. Caputa, D. Das and S. R. Das, "Path Integral Complexity and Kasner singularities," [arXiv:2111.04405 [hep-th]].

[130] G. T. Horowitz and A. R. Steif, "Space-Time Singularities in String Theory," Phys. Rev. Lett. **64**, 260 (1990) doi:10.1103/PhysRevLett.64.260

[131] B. Craps, S. Sethi and E. P. Verlinde, "A Matrix big bang," JHEP **10**, 005 (2005) doi:10.1088/1126-6708/2005/10/005 [arXiv:hep-th/0506180 [hep-th]].

[132] C. S. Chu and P. M. Ho, "Time-dependent AdS/CFT duality and null singularity," JHEP **04**, 013 (2006) doi:10.1088/1126-6708/2006/04/013 [arXiv:hep-th/0602054 [hep-th]].

[133] F. L. Lin and W. Y. Wen, "Supersymmetric null-like holographic cosmologies," JHEP **05**, 013 (2006) doi:10.1088/1126-6708/2006/05/013 [arXiv:hep-th/0602124 [hep-th]].

[134] B. Craps, F. De Roo and O. Evnin, "Can free strings propagate across plane wave singularities?," JHEP **03**, 105 (2009) doi:10.1088/1126-6708/2009/03/105 [arXiv:0812.2900 [hep-th]].

[135] J. Maldacena and L. Susskind, "Cool horizons for entangled black holes," Fortsch. Phys. **61**, 781-811 (2013) doi:10.1002/prop.201300020 [arXiv:1306.0533 [hep-th]].

[136] L. Susskind and Y. Zhao, "Switchbacks and the Bridge to Nowhere," [arXiv:1408.2823 [hep-th]].

[137] D. A. Roberts, D. Stanford and L. Susskind, "Localized shocks," JHEP **03**, 051 (2015) doi:10.1007/JHEP03(2015)051 [arXiv:1409.8180 [hep-th]].

[138] L. Susskind, "Entanglement is not enough," Fortsch. Phys. **64**, 49-71 (2016) [arXiv:1411.0690 [hep-th]].

[139] L. Susskind, "The Typical-State Paradox: Diagnosing Horizons with Complexity," Fortsch. Phys. **64**, 84-91 (2016) doi:10.1002/prop.201500091 [arXiv:1507.02287 [hep-th]].

[140] M. Alishahiha, "Holographic Complexity," Phys. Rev. D **92**, no.12, 126009 (2015) doi:10.1103/PhysRevD.92.126009 [arXiv:1509.06614 [hep-th]].

[141] R. Q. Yang, "Strong energy condition and complexity growth bound in holography," Phys. Rev. D **95**, no.8, 086017 (2017) doi:10.1103/PhysRevD.95.086017 [arXiv:1610.05090 [gr-qc]].

[142] H. Huang, X. H. Feng and H. Lu, "Holographic Complexity and Two Identities of Action Growth," Phys. Lett. B **769**, 357-361 (2017) doi:10.1016/j.physletb.2017.04.011 [arXiv:1611.02321 [hep-th]].

[143] D. Carmi, R. C. Myers and P. Rath, "Comments on Holographic Complexity," JHEP **03**, 118 (2017) doi:10.1007/JHEP03(2017)118 [arXiv:1612.00433 [hep-th]].

[144] A. Reynolds and S. F. Ross, "Divergences in Holographic Complexity," Class. Quant. Grav. **34**, no.10, 105004 (2017) doi:10.1088/1361-6382/aa6925 [arXiv:1612.05439 [hep-th]].

[145] P. Caputa, N. Kundu, M. Miyaji, T. Takayanagi and K. Watanabe, "Anti-de Sitter Space from Optimization of Path Integrals in Conformal Field Theories," Phys. Rev. Lett. **119**, no.7, 071602 (2017) [arXiv:1703.00456 [hep-th]].

[146] S. Chapman, M. P. Heller, H. Marrochio and F. Pastawski, "Toward a Definition of Complexity for Quantum Field Theory States," Phys. Rev. Lett. **120**, no.12, 121602 (2018) doi:10.1103/PhysRevLett.120.121602 [arXiv:1707.08582 [hep-th]].

[147] D. Carmi, S. Chapman, H. Marrochio, R. C. Myers and S. Sugishita, "On the Time Dependence of Holographic Complexity," JHEP **11**, 188 (2017) doi:10.1007/JHEP11(2017)188 [arXiv:1709.10184 [hep-th]].

[148] W. Cottrell and M. Montero, "Complexity is simple!," JHEP **02**, 039 (2018) [arXiv:1710.01175 [hep-th]].

[149] J. Couch, S. Eccles, W. Fischler and M. L. Xiao, "Holographic complexity and noncommutative gauge theory," JHEP **03**, 108 (2018) doi:10.1007/JHEP03(2018)108 [arXiv:1710.07833 [hep-th]].

[150] B. Swingle and Y. Wang, "Holographic Complexity of Einstein-Maxwell-Dilaton Gravity," JHEP **09**, 106 (2018) doi:10.1007/JHEP09(2018)106 [arXiv:1712.09826 [hep-th]].

[151] S. Bolognesi, E. Rabinovici and S. R. Roy, "On Some Universal Features of the Holographic Quantum Complexity of Bulk Singularities," JHEP **06**, 016 (2018) doi:10.1007/JHEP06(2018)016 [arXiv:1802.02045 [hep-th]].

[152] M. Alishahiha, A. Faraji Astaneh, M. R. Mohammadi Mozaffar and A. Mollabashi, "Complexity Growth with Lifshitz Scaling and Hyperscaling Violation," JHEP **07**, 042 (2018) doi:10.1007/JHEP07(2018)042 [arXiv:1802.06740 [hep-th]].

[153] C. A. Agón, M. Headrick and B. Swingle, "Subsystem Complexity and Holography," JHEP **02**, 145 (2019) doi:10.1007/JHEP02(2019)145 [arXiv:1804.01561 [hep-th]].

[154] A. Bhattacharyya, P. Caputa, S. R. Das, N. Kundu, M. Miyaji and T. Takayanagi, "Path-Integral Complexity for Perturbed CFTs," JHEP **07**, 086 (2018) doi:10.1007/JHEP07(2018)086 [arXiv:1804.01999 [hep-th]].

[155] S. Chapman, H. Marrochio and R. C. Myers, "Holographic complexity in Vaidya spacetimes. Part I," JHEP **06**, 046 (2018) doi:10.1007/JHEP06(2018)046 [arXiv:1804.07410 [hep-th]].

[156] P. Caputa and J. M. Magan, "Quantum Computation as Gravity," Phys. Rev. Lett. **122**, no.23, 231302 (2019) doi:10.1103/PhysRevLett.122.231302 [arXiv:1807.04422 [hep-th]].

[157] H. A. Camargo, P. Caputa, D. Das, M. P. Heller and R. Jefferson, "Complexity as a novel probe of quantum quenches: universal scalings and purifications," Phys. Rev. Lett. **122**, no.8, 081601 (2019) doi:10.1103/PhysRevLett.122.081601 [arXiv:1807.07075 [hep-th]].

[158] S. Chapman, J. Eisert, L. Hackl, M. P. Heller, R. Jefferson, H. Marrochio and R. C. Myers, "Complexity and entanglement for thermofield double states," SciPost Phys. **6**, no.3, 034 (2019) doi:10.21468/SciPostPhys.6.3.034 [arXiv:1810.05151 [hep-th]].

[159] A. R. Brown, H. Gharibyan, H. W. Lin, L. Susskind, L. Thorlacius and Y. Zhao, "Complexity of Jackiw-Teitelboim gravity," Phys. Rev. D **99**, no.4, 046016 (2019) doi:10.1103/PhysRevD.99.046016 [arXiv:1810.08741 [hep-th]].

[160] A. Akhavan, M. Alishahiha, A. Naseh and H. Zolfi, "Complexity and Behind the Horizon Cut Off," JHEP **12**, 090 (2018) doi:10.1007/JHEP12(2018)090 [arXiv:1810.12015 [hep-th]].

[161] A. Belin, A. Lewkowycz and G. Sárosi, "Complexity and the bulk volume, a new York time story," JHEP **03**, 044 (2019) doi:10.1007/JHEP03(2019)044 [arXiv:1811.03097 [hep-th]].

[162] S. Chapman, D. Ge and G. Policastro, "Holographic Complexity for Defects Distinguishes Action from Volume," JHEP **05**, 049 (2019) doi:10.1007/JHEP05(2019)049 [arXiv:1811.12549 [hep-th]].

[163] K. Goto, H. Marrochio, R. C. Myers, L. Queimada and B. Yoshida, "Holographic Complexity Equals Which Action?," JHEP **02**, 160 (2019) doi:10.1007/JHEP02(2019)160 [arXiv:1901.00014 [hep-th]].

[164] A. Bernamonti, F. Galli, J. Hernandez, R. C. Myers, S. M. Ruan and J. Simón, "First Law of Holographic Complexity," Phys. Rev. Lett. **123**, no.8, 081601 (2019) doi:10.1103/PhysRevLett.123.081601 [arXiv:1903.04511 [hep-th]].

[165] T. Ali, A. Bhattacharyya, S. S. Haque, E. H. Kim, N. Moynihan and J. Murugan, "Chaos and Complexity in Quantum Mechanics," Phys. Rev. D **101**, no.2, 026021 (2020) doi:10.1103/PhysRevD.101.026021 [arXiv:1905.13534 [hep-th]].

[166] R. J. Caginalp, "Holographic Complexity in FRW Spacetimes," Phys. Rev. D **101**, no.6, 066027 (2020) doi:10.1103/PhysRevD.101.066027 [arXiv:1906.02227 [hep-th]].

[167] Y. S. An, R. G. Cai, L. Li and Y. Peng, "Holographic complexity growth in an FLRW universe," Phys. Rev. D **101**, no.4, 046006 (2020) doi:10.1103/PhysRevD.101.046006 [arXiv:1909.12172 [hep-th]].

[168] P. Braccia, A. L. Cotrone and E. Tonni, "Complexity in the presence of a boundary," JHEP **02**, 051 (2020) doi:10.1007/JHEP02(2020)051 [arXiv:1910.03489 [hep-th]].

[169] M. Doroudiani, A. Naseh and R. Pirmoradian, "Complexity for Charged Thermofield Double States," JHEP **01**, 120 (2020) doi:10.1007/JHEP01(2020)120 [arXiv:1910.08806 [hep-th]].

[170] L. Schneiderbauer, W. Sybesma and L. Thorlacius, "Holographic Complexity: Stretching the Horizon of an Evaporating Black Hole," JHEP **03**, 069 (2020) doi:10.1007/JHEP03(2020)069 [arXiv:1911.06800 [hep-th]].

[171] A. Bhattacharyya, S. Das, S. Shajidul Haque and B. Underwood, "Cosmological Complexity," Phys. Rev. D **101**, no.10, 106020 (2020) doi:10.1103/PhysRevD.101.106020 [arXiv:2001.08664 [hep-th]].

[172] R. G. Cai, S. He, S. J. Wang and Y. X. Zhang, "Revisit on holographic complexity in two-dimensional gravity," JHEP **08**, 102 (2020) doi:10.1007/JHEP08(2020)102 [arXiv:2001.11626 [hep-th]].

[173] A. Bhattacharyya, S. Das, S. S. Haque and B. Underwood, "Rise of cosmological complexity: Saturation of growth and chaos," Phys. Rev. Res. **2**, no.3, 033273 (2020) doi:10.1103/PhysRevResearch.2.033273 [arXiv:2005.10854 [hep-th]].

[174] K. X. Zhu, F. W. Shu and D. H. Du, "Holographic complexity for nonlinearly charged Lifshitz black holes," Class. Quant. Grav. **37**, no.19, 195023 (2020) doi:10.1088/1361-6382/aba843 [arXiv:2007.11759 [hep-th]].

[175] S. Choudhury, S. Chowdhury, N. Gupta, A. Mishara, S. P. Selvam, S. Panda, G. D. Pasquino, C. Singha and A. Swain, "Circuit Complexity from Cosmological Islands," Symmetry **13**, no.7, 1301 (2021) doi:10.3390/sym13071301 [arXiv:2012.10234 [hep-th]].

[176] A. Bhattacharya, A. Bhattacharyya, P. Nandy and A. K. Patra, "Islands and complexity of eternal black hole and radiation subsystems for a doubly holographic model," JHEP **05**, 135 (2021) doi:10.1007/JHEP05(2021)135 [arXiv:2103.15852 [hep-th]].

[177] S. Jiang and J. Jiang, "Holographic complexity in charged accelerating black holes," Phys. Lett. B **823**, 136731 (2021) doi:10.1016/j.physletb.2021.136731 [arXiv:2106.09371 [hep-th]].

[178] N. Engelhardt and Å. Folkestad, "General bounds on holographic complexity," JHEP **01**, 040 (2022) doi:10.1007/JHEP01(2022)040 [arXiv:2109.06883 [hep-th]].

[179] A. Bhattacharya, A. Bhattacharyya, P. Nandy and A. K. Patra, "Partial islands and subregion complexity in geometric secret-sharing model," JHEP **12**, 091 (2021) doi:10.1007/JHEP12(2021)091 [arXiv:2109.07842 [hep-th]].

[180] S. Chapman, D. A. Galante and E. D. Kramer, "Holographic complexity and de Sitter space," JHEP **02**, 198 (2022) doi:10.1007/JHEP02(2022)198 [arXiv:2110.05522 [hep-th]].

[181] R. Emparan, A. M. Frassino, M. Sasieta and M. Tomašević, "Holographic complexity of quantum black holes," JHEP **02**, 204 (2022) doi:10.1007/JHEP02(2022)204 [arXiv:2112.04860 [hep-th]].

[182] E. Jørstad, R. C. Myers and S. M. Ruan, "Holographic complexity in dS_{d+1}," JHEP **05**, 119 (2022) doi:10.1007/JHEP05(2022)119 [arXiv:2202.10684 [hep-th]].

[183] K. Adhikari and S. Choudhury, "Cosmological Krylov Complexity," Fortsch. Phys. **70**, no.12, 2200126 (2022) doi:10.1002/prop.202200126 [arXiv:2203.14330 [hep-th]].

[184] Y. S. An, L. Li, F. G. Yang and R. Q. Yang, "Interior structure and complexity growth rate of holographic superconductor from M-theory," JHEP **08**, 133 (2022) doi:10.1007/JHEP08(2022)133 [arXiv:2205.02442 [hep-th]].

[185] T. Mandal, A. Mitra and G. S. Punia, "Action complexity of charged black holes with higher derivative interactions," Phys. Rev. D **106**, no.12, 126017 (2022) doi:10.1103/PhysRevD.106.126017 [arXiv:2205.11201 [hep-th]].

[186] F. Omidi, "Generalized volume-complexity for two-sided hyperscaling violating black branes," JHEP **01**, 105 (2023) doi:10.1007/JHEP01(2023)105 [arXiv:2207.05287 [hep-th]].

[187] S. Chapman, D. A. Galante, E. Harris, S. U. Sheorey and D. Vegh, "Complex geodesics in de Sitter space," JHEP **03**, 006 (2023) doi:10.1007/JHEP03(2023)006 [arXiv:2212.01398 [hep-th]].

[188] R. Auzzi, G. Nardelli, G. P. Ungureanu and N. Zenoni, "Volume complexity of dS bubbles," Phys. Rev. D **108**, no.2, 026006 (2023) doi:10.1103/PhysRevD.108.026006 [arXiv:2302.03584 [hep-th]].

[189] H. Zolfi, "Complexity and Multi-boundary Wormholes in 2 + 1 dimensions," JHEP **04**, 076 (2023) doi:10.1007/JHEP04(2023)076 [arXiv:2302.07522 [hep-th]].

[190] G. Katoch, J. Ren and S. R. Roy, "Quantum complexity and bulk timelike singularities," JHEP **12**, 085 (2023) doi:10.1007/JHEP12(2023)085 [arXiv:2303.02752 [hep-th]].

[191] T. Anegawa, N. Iizuka, S. K. Sake and N. Zenoni, "Is action complexity better for de Sitter space in Jackiw-Teitelboim gravity?," JHEP **06**, 213 (2023) doi:10.1007/JHEP06(2023)213 [arXiv:2303.05025 [hep-th]].

[192] A. Bhattacharya, A. Bhattacharyya and A. K. Patra, "Holographic complexity of Jackiw-Teitelboim gravity from Karch-Randall braneworld," JHEP **07**, 060 (2023) doi:10.1007/JHEP07(2023)060 [arXiv:2304.09909 [hep-th]].

[193] T. Anegawa and N. Iizuka, "Shock waves and delay of hyperfast growth in de Sitter complexity," JHEP **08**, 115 (2023) doi:10.1007/JHEP08(2023)115 [arXiv:2304.14620 [hep-th]].

[194] S. Baiguera, R. Berman, S. Chapman and R. C. Myers, "The cosmological switchback effect," JHEP **07**, 162 (2023) doi:10.1007/JHEP07(2023)162 [arXiv:2304.15008 [hep-th]].

[195] G. Yadav and H. Rathi, "Yang-Baxter deformed wedge holography," Phys. Lett. B **852**, 138592 (2024) doi:10.1016/j.physletb.2024.138592 [arXiv:2307.01263 [hep-th]].

[196] S. E. Aguilar-Gutierrez, A. K. Patra and J. F. Pedraza, "Entangled universes in dS wedge holography," JHEP **10**, 156 (2023) doi:10.1007/JHEP10(2023)156 [arXiv:2308.05666 [hep-th]].

[197] S. E. Aguilar-Gutierrez, B. Craps, J. Hernandez, M. Khramtsov, M. Knysh and A. Shukla, "Holographic complexity: braneworld gravity versus the Lloyd bound," [arXiv:2312.12349 [hep-th]].

[198] X. Dong, S. Harrison, S. Kachru, G. Torroba and H. Wang, "Aspects of holography for theories with hyperscaling violation," JHEP **06**, 041 (2012) doi:10.1007/JHEP06(2012)041 [arXiv:1201.1905 [hep-th]].

[199] N. Itzhaki, J. M. Maldacena, J. Sonnenschein and S. Yankielowicz, "Supergravity and the large N limit of theories with sixteen supercharges," Phys. Rev. D **58**, 046004 (1998) [hep-th/9802042].

[200] K. S. Kolekar and K. Narayan, "On AdS_2 holography from redux, renormalization group flows and c-functions," JHEP **02**, 039 (2019) doi:10.1007/JHEP02(2019)039 [arXiv:1810.12528 [hep-th]].

[201] J. L. F. Barbon and C. A. Fuertes, "Holographic entanglement entropy probes (non)locality," JHEP **0804**, 096 (2008) doi:10.1088/1126-6708/2008/04/096 [arXiv:0803.1928 [hep-th]].

[202] B. Swingle and J. McGreevy, "Renormalization group constructions of topological quantum liquids and beyond," Phys. Rev. B **93**, no.4, 045127 (2016) doi:10.1103/PhysRevB.93.045127 [arXiv:1407.8203 [cond-mat.str-el]].

[203] L.D. Landau and E.M. Lifshitz, Course of Theoretical Physics, Vol. 2, "Classical Theory of Fields", (Pergamon, 1987). This has a transparent treatment of the Bianchi classification of 4-dim cosmologies as well as the BKL analysis.

[204] E. Lifshitz, V. Belinskii and I. Khalatnikov, Adv. Phys. **19** 525(1970).

[205] V. Belinskii and I. Khalatnikov, *Sov. Phys. JETP* **36** (1973) 591.

[206] A. Strominger, "Les Houches lectures on black holes," [arXiv:hep-th/9501071 [hep-th]].

[207] D. Grumiller, W. Kummer and D. V. Vassilevich, "Dilaton gravity in two-dimensions," Phys. Rept. **369**, 327-430 (2002) doi:10.1016/S0370-1573(02)00267-3 [arXiv:hep-th/0204253 [hep-th]].

[208] T. G. Mertens and G. J. Turiaci, "Solvable models of quantum black holes: a review on Jackiw–Teitelboim gravity," Living Rev. Rel. **26**, no.1, 4 (2023) doi:10.1007/s41114-023-00046-1 [arXiv:2210.10846 [hep-th]].

[209] E. Witten, "Quantum gravity in de Sitter space," [hep-th/0106109].

[210] A. Strominger, "The dS / CFT correspondence," JHEP **0110**, 034 (2001) [hep-th/0106113].

[211] J. M. Maldacena, "Non-Gaussian features of primordial fluctuations in single field inflationary models," JHEP **0305**, 013 (2003), [astro-ph/0210603].

[212] D. Anninos, T. Hartman and A. Strominger, "Higher Spin Realization of the dS/CFT Correspondence," Class. Quant. Grav. **34** no.1, 015009 (2017) doi:10.1088/1361-6382/34/1/015009 [arXiv:1108.5735 [hep-th]].

[213] K. Narayan, "de Sitter extremal surfaces," Phys. Rev. D **91**, no.12, 126011 (2015) [arXiv:1501.03019 [hep-th]].

[214] Y. Sato, "Comments on Entanglement Entropy in the dS/CFT Correspondence," Phys. Rev. D **91**, no. 8, 086009 (2015) [arXiv:1501.04903 [hep-th]].

[215] M. Miyaji and T. Takayanagi, "Surface/State Correspondence as a Generalized Holography," PTEP **2015**, no. 7, 073B03 (2015) doi:10.1093/ptep/ptv089 [arXiv:1503.03542 [hep-th]].

[216] K. Narayan, "de Sitter space and extremal surfaces for spheres," Phys. Lett. B **753**, 308 (2016) [arXiv:1504.07430 [hep-th]].

[217] K. Narayan, "On extremal surfaces and de Sitter entropy," Phys. Lett. B **779**, 214 (2018) [arXiv:1711.01107 [hep-th]].

[218] C. Arias, F. Diaz and P. Sundell, "De Sitter Space and Entanglement," Class. Quant. Grav. **37**, no. 1, 015009 (2020) doi:10.1088/1361-6382/ab5b78 [arXiv:1901.04554 [hep-th]].

[219] K. Narayan, "de Sitter entropy as entanglement," Int. J. Mod. Phys. D **28**, no.14, 1944019 (2019) doi:10.1142/S021827181944019X [arXiv:1904.01223 [hep-th]].

[220] K. Narayan, "de Sitter future-past extremal surfaces and the entanglement wedge," Phys. Rev. D **101**, no.8, 086014 (2020) doi:10.1103/PhysRevD.101.086014 [arXiv:2002.11950 [hep-th]].

[221] Y. Hikida, T. Nishioka, T. Takayanagi and Y. Taki, "Holography in de Sitter Space via Chern-Simons Gauge Theory," Phys. Rev. Lett. **129**, no.4, 041601 (2022) [arXiv:2110.03197 [hep-th]].

[222] Y. Hikida, T. Nishioka, T. Takayanagi and Y. Taki, "CFT duals of three-dimensional de Sitter gravity," JHEP **05**, 129 (2022) doi:10.1007/JHEP05(2022)129 [arXiv:2203.02852 [hep-th]].

[223] K. Doi, J. Harper, A. Mollabashi, T. Takayanagi and Y. Taki, "Pseudoentropy in dS/CFT and Timelike Entanglement Entropy," Phys. Rev. Lett. **130**, no.3, 031601 (2023) doi:10.1103/PhysRevLett.130.031601 [arXiv:2210.09457 [hep-th]].

[224] K. Narayan, "de Sitter space, extremal surfaces, and time entanglement," Phys. Rev. D **107**, no.12, 126004 (2023) doi:10.1103/PhysRevD.107.126004 [arXiv:2210.12963 [hep-th]].

[225] J. Cotler and A. Strominger, "Cosmic ER=EPR in dS/CFT," [arXiv:2302.00632 [hep-th]].

[226] K. Narayan, "Further remarks on de Sitter space, extremal surfaces, and time entanglement," Phys. Rev. D **109**, no.8, 086009 (2024) doi:10.1103/PhysRevD.109.086009 [arXiv:2310.00320 [hep-th]].

[227] Y. Nakata, T. Takayanagi, Y. Taki, K. Tamaoka and Z. Wei, "New holographic generalization of entanglement entropy," Phys. Rev. D **103**, no.2, 026005 (2021) [arXiv:2005.13801 [hep-th]].

[228] A. Mollabashi, N. Shiba, T. Takayanagi, K. Tamaoka and Z. Wei, "Pseudo Entropy in Free Quantum Field Theories," Phys. Rev. Lett. **126**, no.8, 081601 (2021) doi:10.1103/PhysRevLett.126.081601 [arXiv:2011.09648 [hep-th]].

[229] A. Mollabashi, N. Shiba, T. Takayanagi, K. Tamaoka and Z. Wei, "Aspects of pseudoentropy in field theories," Phys. Rev. Res. **3**, no.3, 033254 (2021) doi:10.1103/PhysRevResearch.3.033254 [arXiv:2106.03118 [hep-th]].

[230] T. Nishioka, T. Takayanagi and Y. Taki, "Topological pseudo entropy," JHEP **09**, 015 (2021) doi:10.1007/JHEP09(2021)015 [arXiv:2107.01797 [hep-th]].

[231] J. Mukherjee, "Pseudo Entropy in U(1) gauge theory," JHEP **10**, 016 (2022) doi:10.1007/JHEP10(2022)016 [arXiv:2205.08179 [hep-th]].

[232] A. Bhattacharya, A. Bhattacharyya and S. Maulik, "Pseudocomplexity of purification for free scalar field theories," Phys. Rev. D **106**, no.8, 8 (2022) doi:10.1103/PhysRevD.106.086010 [arXiv:2209.00049 [hep-th]].

[233] W. z. Guo, S. He and Y. X. Zhang, "Constructible reality condition of pseudo entropy via pseudo-Hermiticity," [arXiv:2209.07308 [hep-th]].

[234] B. Liu, H. Chen and B. Lian, "Entanglement Entropy in Timelike Slices: a Free Fermion Study," [arXiv:2210.03134 [cond-mat.stat-mech]].

[235] Z.Li, Z.Q.Xiao, R.Q.Yang, "On holographic time-like entanglement entropy," arXiv:2211.14883[hep-th].

[236] K. Doi, J. Harper, A. Mollabashi, T. Takayanagi and Y. Taki, "Timelike entanglement entropy," [arXiv:2302.11695 [hep-th]].

[237] X. Jiang, P. Wang, H. Wu and H. Yang, "Timelike entanglement entropy and $T\bar{T}$ deformation," [arXiv:2302.13872 [hep-th]].

[238] Z. Chen, "Complex-valued Holographic Pseudo Entropy via Real-time AdS/CFT Correspondence," [arXiv:2302.14303 [hep-th]].

[239] K. Narayan and Hitesh K. Saini, "Notes on time entanglement and pseudo-entropy," [arXiv:2303.01307 [hep-th]].

[240] P. Wang, H. Wu and H. Yang, "Fix the dual geometries of $T\bar{T}$ deformed CFT_2 and highly excited states of CFT_2," Eur. Phys. J. C **80**, no.12, 1117 (2020) doi:10.1140/epjc/s10052-020-08680-7 [arXiv:1811.07758 [hep-th]].

[241] S. He, J. Yang, Y. X. Zhang and Z. X. Zhao, "Pseudo entropy of primary operators in $T\overline{T}/J\overline{T}$-deformed CFTs," JHEP **09**, 025 (2023) doi:10.1007/JHEP09(2023)025 [arXiv:2305.10984 [hep-th]].

[242] K. Shinmyo, T. Takayanagi and K. Tasuki, "Pseudo entropy under joining local quenches," JHEP **02**, 111 (2024) doi:10.1007/JHEP02(2024)111 [arXiv:2310.12542 [hep-th]].

[243] W. z. Guo, Y. z. Jiang and Y. Jiang, "Pseudo entropy and pseudo-Hermiticity in quantum field theories," JHEP **05**, 071 (2024) doi:10.1007/JHEP05(2024)071 [arXiv:2311.01045 [hep-th]].

[244] S. He, P. H. C. Lau and L. Zhao, "Detecting quantum chaos via pseudo-entropy and negativity," [arXiv:2403.05875 [hep-th]].

[245] M. Afrasiar, J. K. Basak and D. Giataganas, "Timelike entanglement entropy and phase transitions in non-conformal theories," JHEP **07**, 243 (2024) doi:10.1007/JHEP07(2024)243 [arXiv:2404.01393 [hep-th]].

[246] W. z. Guo, Y. z. Jiang and J. Xu, "Pseudoentropy sum rule by analytical continuation of the superposition parameter," JHEP **11**, 069 (2024) doi:10.1007/JHEP11(2024)069 [arXiv:2405.09745 [hep-th]].

[247] T. Anegawa and K. Tamaoka, "Black hole singularity and timelike entanglement," JHEP **10**, 182 (2024) doi:10.1007/JHEP10(2024)182 [arXiv:2406.10968 [hep-th]].

[248] Y. Singh and R. Banerjee, "SVD Entanglement Entropy of Chiral Dirac Oscillators," [arXiv:2407.10898 [hep-th]].

[249] P. Caputa, S. Purkayastha, A. Saha and P. Sułkowski, "Musings on SVD and pseudo entanglement entropies," JHEP **11**, 103 (2024) doi:10.1007/JHEP11(2024)103 [arXiv:2408.06791 [hep-th]].

[250] K. Goswami, K. Narayan and G. Yadav, "No-boundary extremal surfaces in slow-roll inflation and other cosmologies," [arXiv:2409.14208 [hep-th]].

[251] S. S. Jena and S. Mahapatra, "A note on the holographic time-like entanglement entropy in Lifshitz theory," JHEP **01**, 055 (2025) doi:10.1007/JHEP01(2025)055 [arXiv:2410.00384 [hep-th]].

[252] J. Xu and W. z. Guo, "Imaginary part of timelike entanglement entropy," JHEP **02**, 094 (2025) doi:10.1007/JHEP02(2025)094 [arXiv:2410.22684 [hep-th]].

[253] P. Caputa, B. Chen, T. Takayanagi and T. Tsuda, "Thermal pseudo-entropy," JHEP **01**, 003 (2025) doi:10.1007/JHEP01(2025)003 [arXiv:2411.08948 [hep-th]].

[254] M. Afrasiar, J. K. Basak and D. Giataganas, "Holographic Timelike Entanglement Entropy in Non-relativistic Theories," [arXiv:2411.18514 [hep-th]].

[255] J. B. Hartle and S. W. Hawking, "Wave Function of the Universe," Phys. Rev. D **28**, 2960-2975 (1983) doi:10.1103/PhysRevD.28.2960

[256] J. Maldacena, G. J. Turiaci and Z. Yang, "Two dimensional Nearly de Sitter gravity," JHEP **01**, 139 (2021) doi:10.1007/JHEP01(2021)139 [arXiv:1904.01911 [hep-th]].

[257] R. Bousso and S. W. Hawking, "The Probability for primordial black holes," Phys. Rev. D **52**, 5659-5664 (1995) doi:10.1103/PhysRevD.52.5659 [arXiv:gr-qc/9506047 [gr-qc]].

[258] R. Bousso and S. W. Hawking, "Pair creation of black holes during inflation," Phys. Rev. D **54**, 6312-6322 (1996) doi:10.1103/PhysRevD.54.6312 [arXiv:gr-qc/9606052 [gr-qc]].

[259] C. Holzhey, F. Larsen and F. Wilczek, "Geometric and renormalized entropy in conformal field theory," Nucl. Phys. B **424**, 443 (1994) [hep-th/9403108].

[260] J. M. Maldacena, "Eternal black holes in anti-de Sitter," JHEP **0304**, 021 (2003) [hep-th/0106112].

[261] J. Sakurai, "Modern Quantum Mechanics", Revised edn.

[262] C. Jonay, D. A. Huse and A. Nahum, "Coarse-grained dynamics of operator and state entanglement," [arXiv:1803.00089 [cond-mat.stat-mech]].

[263] L. Castellani, "Entropy of temporal entanglement," [arXiv:2104.05722 [quant-ph]].

[264] A. Lerose, M. Sonner and D. A. Abanin, "Scaling of temporal entanglement in proximity to integrability," Phys. Rev. B **104**, no.3, 035137 (2021) doi:10.1103/PhysRevB.104.035137 [arXiv:2104.07607 [quant-ph]].

[265] N. L. Diaz, J. M. Matera and R. Rossignoli, "Path Integrals from Spacetime Quantum Actions," [arXiv:2111.05383 [quant-ph]].

[266] J. Dressel, M. Malik, F. M. Miatto, A. N. Jordan, R. W. Boyd, "Colloquium: Understanding Quantum Weak Values: Basics and Applications," Rev. Mod. Phys. 86 (2014) 307 [arXiv:1305.7154 [quant-ph]].

[267] S. Salek, R. Schubert, and K. Wiesner, "Negative conditional entropy of postselected states," Phys. Rev. A 90 (2014) 022116 [arXiv:1305.0932 [quant-ph]].

[268] G. Aad *et al.* [ATLAS], Nature **633**, no.8030, 542-547 (2024) doi:10.1038/s41586-024-07824-z [arXiv:2311.07288 [hep-ex]].

[269] A. Hayrapetyan *et al.* [CMS], Rept. Prog. Phys. **87**, no.11, 117801 (2024) doi:10.1088/1361-6633/ad7e4d [arXiv:2406.03976 [hep-ex]].

[270] A. Hayrapetyan *et al.* [CMS], Phys. Rev. D **110**, no.11, 112016 (2024) doi:10.1103/PhysRevD.110.112016 [arXiv:2409.11067 [hep-ex]].

[271] F. Ciccarello, M. Paternostro, G. M. Palma, and M. Zarcone, *Rising time of entanglement between scattering spins*, arXiv:0812.0755 [quant-ph], 2008.

[272] J. Fan, G. M. Deng and X. J. Ren, Phys. Rev. D **104**, no.11, 116021 (2021) doi:10.1103/PhysRevD.104.116021 [arXiv:2112.04254 [hep-th]].

[273] T. Kirchner, W. Elkamhawy and H. W. Hammer, Few Body Syst. **65**, no.2, 29 (2024) doi:10.1007/s00601-024-01897-2 [arXiv:2312.14484 [nucl-th]].

[274] M. Duch, A. Strumia and A. Titov, Eur. Phys. J. C **85**, no.2, 151 (2025) doi:10.1140/epjc/s10052-025-13836-4 [arXiv:2403.14757 [hep-ph]].

[275] I. Low and Z. Yin, [arXiv:2405.08056 [hep-th]].

[276] J. Liu, M. Tanaka, X. P. Wang, J. J. Zhang and Z. Zheng, [arXiv:2505.06001 [hep-ph]].

[277] S. R. Beane, R. C. Farrell, and M. Varma, "Entanglement minimization in hadronic scattering with pions," *Int. J. Mod. Phys. A* **36**, no.30, 2150205 (2021), doi:10.1142/S0217751X21502055, arXiv:2108.00646 [hep-ph].

[278] P. Hayden, M. Headrick and A. Maloney, "Holographic Mutual Information is Monogamous," Phys. Rev. D **87**, no.4, 046003 (2013) doi:10.1103/PhysRevD.87.046003 [arXiv:1107.2940 [hep-th]].

[279] D. P. Jatkar and K. Narayan, "Ghost-spin chains, entanglement and *bc*-ghost CFTs," Phys. Rev. D **96**, no. 10, 106015 (2017) [arXiv:1706.06828 [hep-th]].

[280] K. Narayan, "On dS_4 extremal surfaces and entanglement entropy in some ghost CFTs," Phys. Rev. D **94**, no. 4, 046001 (2016) [arXiv:1602.06505 [hep-th]].

[281] E. Merzbacher, "Quantum Mechanics", 3rd edn.

[282] Katsinis, Dimitrios and Pastras, Georgios, "An Inverse Mass Expansion for the Mutual Information in Free Scalar QFT at Finite Temperature", JHEP **02**, 091 (2020) doi:10.1007/JHEP02(2020)091 [arXiv:1907.08508 [hep-th]].